Investigation of Electronic and Magnetic Properties of On-Surface Metalated Organic Ligands on Various Substrates by SP-STM

Dissertation zur Erlangung des Doktorgrades an der Fakultät für Mathematik, Informatik und Naturwissenschaften im Fachbereich Physik der Universität Hamburg

vorgelegt von

Micha Elsebach

aus Frankenberg

Hamburg, 2021

Gutachter/innen der Dissertation:

Prof. Dr. Roland Wiesendanger
Prof. Dr. Carmen Hermann

Zusammensetzung der Prüfungskommission:

Prof. Dr. Roland Wiesendanger
Prof. Dr. Carmen Hermann
Prof. Dr. Michael Potthoff
Prof. Dr. Michael Thorwart
Dr. Maciej Bazarnik

Vorsitzender der Prüfungskommission:

Prof. Dr. Michael Potthoff

Datum der Disputation:

19.10.2021

Vorsitzender des Fach-Promotionsausschusses PHYSIK:

Prof. Dr. Wolfgang Hansen

Leiter des Fachbereichs PHYSIK:

Prof. Dr. Günter H. W. Sigl

Dekan der Fakultät MIN:

Prof. Dr. Heinrich Graener

Abstract

Molecular chains built from 5,5'-dibromosalophenatocobalt(II) (Co–Sal) molecules in an on-surface Ullmann reaction have a high potential for serving as spin leads for information transport in molecular spintronic devices. The individual Co centers in such chains are antiferromagnetically coupled because of a magnetic superexchange interaction with a strong contribution of the spin-polarization mechanism. To create a spintronic device from single molecules, a proper substrate has to be found that, at the same time, enables the Ullmann reaction, preserves the intramolecular magnetic coupling, and allows access to the magnetic moments of the Co centers. In this thesis, two substrate systems are tested for the creation of $[\text{Co–Sal}]_n$ chains: the $GdAu_2$ surface alloy on Au(111) and Co intercalated graphene on Ir(111) (Gr/Co/Ir(111)). The local electronic and magnetic properties of the chains are investigated in a spin-polarized scanning-tunneling microscopy and spectroscopy (SP-STM/STS) study.

On the $GdAu_2$/Au(111) surface alloy, X-ray magnetic circular dichroism (XMCD) data showed that the average magnetic moment of the molecules is reduced upon polymerization. In the SP-STS study, it was found that the magnetic moment of $[\text{Co–Sal}]_n$ chains is almost completely quenched because of hybridization with the substrate. This strong hybridization is attributed to the affinity of Co–Sal to coordinate additional ligands along the z-axis.

For $[\text{Co-Sal}]_n$ chains on Gr/Co/Ir(111), spin contrast was observed, but the expected antiferromagnetic coupling of the individual centers could not be confirmed. Instead, the results point to either a position-dependent magnetic coupling of the individual members with the substrate or to the formation of a non-collinear spin structure due to a more complex magnetic interaction. Several approaches are suggested to identify the correct interpretation. A comparison with density-functional theory (DFT) data of free-standing Co–Sal showed that the hybridization of the

molecules on Gr/Co/Ir(111) is stronger than expected. To further reduce the influence of the substrate, chains were transferred onto pristine graphene on Ir(111) (Gr/Ir(111)) by tip manipulation. However, magnetic contrast could not be obtained on these chains because of their unstable adsorption configuration. Furthermore, it was found that Co is an imperfect catalyst for the Ullmann reaction since it forms clusters on the surface, strongly interacting with the $[\text{Co–Sal}]_n$ chains and hindering the growth of longer chains.

As an approach to obtain more conclusive SP-STS data on a salophen-based spin lead, the 5,5'-dibromosalophen (H_2–Sal) ligand was metalated with Fe and Cr and subsequently polymerized into molecular chains. In a STS study, the different transition metal–salophen complexes could be identified unequivocally because of their characteristic electronic structures. According to DFT calculations, these complexes have larger magnetic moments, being more accessible in SP-STS experiments.

Zusammenfassung

Molekülketten, synthetisiert in einer oberflächenkatalysierten Ullmann-Reaktion aus 5,5'-dibromosalophenatocobalt(II)-Molekülen (Co–Sal-Molekülen), sind vielversprechende Kandidaten als Informationsträger in Anwendungen der molekülbasierten Spintronik. Die einzelnen Co-Zentren innerhalb der Molekülketten sind durch magnetische Superaustauschwechselwirkung antiferromagnetisch gekoppelt. In dieser Kopplung spielt der sogenannte Spinpolarisationsmechanismus eine besondere Rolle. Um tatsächliche Anwendungen realisieren zu können, benötigt man ein entsprechendes Substrat, das gleichermaßen die Ullmann-Reaktion für die Erzeugung der Molekülketten ermöglicht, wobei die magnetischen Eigenschaften der Moleküle erhalten bleiben müssen, wie auch den Zugang zu den magnetischen Momenten der Moleküle erlaubt. In der vorliegenden Arbeit wurden die lokalen elektronischen und magnetischen Eigenschaften von $[\text{Co–Sal}]_n$-Ketten auf zwei möglichen Substraten, nämlich einer $GdAu_2$/Au(111)-Oberflächenlegierung und auf Co-interkaliertem Graphen auf Ir(111), mithilfe von spinpolarisierter Rastertunnelmikroskopie und -spektroskopie (SP-RTM/RTS) untersucht.

Auf der $GdAu_2$/Au(111)-Oberflächenlegierung zeigte eine Untersuchung mit zirkularem, magnetischem Röntgendichroismus eine Reduktion des durchschnittlichen magnetischen Moments der Co-Zentren nach der Erzeugung der Molekülketten. Die Untersuchung mit SP-RTS zeigte, dass die magnetischen Momente nach der Polymerisierungsreaktion aufgrund von erhöhter Hybridisierung unterdrückt werden. Durch die Affinität von Co–Sal, weitere Atome entlang der z-Achse zu binden, wird die starke Hybridisierung zwischen Molekülen und Oberflächenatomen begünstigt.

Im Gegensatz dazu zeigen $[\text{Co-Sal}]_n$-Molekülketten eindeutigen Spinkontrast im SP-RTM-Experiment. Die erwartete antiferromagnetische Kopplung der einzelnen

Co-Zentren konnte jedoch nicht bestätigt werden. Stattdessen deuten die Ergebnisse entweder auf eine Dominanz der ortsabhängigen Kopplung mit dem magnetischen Substrat oder eine nichtkollineare Spinstruktur innerhalb der Molekülkette hin. Mehrere Ansätze wurden verfolgt, um zu einer korrekten Interpretation zu gelangen. Der Vergleich der experimentellen Daten mit auf Dichtefunktionaltheorie beruhenden Berechnungen zeigte, dass die Hybridisierung zwischen Co–Sal-Molekülen und Co-interkaliertem Graphen die elektronische Struktur der Moleküle stärker beeinflusst als erwartet. Um diesen Einfluss des Substrates weiter zu verringern, wurden Molekülketten durch Spitzenmanipulation in Bereichen positioniert, in denen Graphen direkt auf dem Ir(111)-Kristall liegt. Spinpolarisierte Messungen konnten auf diesem System aufgrund der instabilen Adsorptionskonfiguration der Molekülketten jedoch nicht durchgeführt werden. Zudem zeigten die Experimente, dass Co nicht der ideale Katalysator für die Ullmannreaktion ist, da die starke Bindung zwischen auf der Oberfläche entstehenden Co-Clustern und den Molekülen die Erzeugung längerer Molekülketten verhindert.

Zuletzt wurde der H_2–Sal-Ligand erfolgreich mit Fe und Cr metalliert und Molekülketten aus den so erzeugten Komplexen synthetisiert. Hier zeigte eine RTM/RTS-Studie, dass die verschiedenen Übergangsmetall-Salophen-Komplexe aufgrund ihrer individuellen elektronischen Eigenschaften eindeutig voneinander unterscheidbar sind. Berechnungen mit Dichtefunktionaltheorie zeigten, dass diese Komplexe größere magnetische Momente haben, die besser in SP-RTM/RTS-Experimenten adressiert werden können.

Contents

List of Abbreviations

Notation	Description	Page List
AOM	angular overlap model	39
BS	broken symmetry	51
Br_2Co–Sal	5,5'-dibromosalophenatocobalt(II)	66
Br_2H_2–Sal	5,5'-dibromosalophen	3
Br_3Co_3–Sal	tribromo-triplecobaltsalophen	2
CFT	crystal field theory	36
CI	configuration interaction	54
CVD	chemical vapor deposition	113
Co–Sal	salophenatocobalt(II)	VIII
CoOEP	Co–octaethylporphyrin	120
Cr–Sal	salophenatochromium(II)	154
DFT	density-functional theory	3
DM	Dzyaloshinsky–Moriya	63
DOS	density of states	8
EPR	electron paramagnetic resonance	39
EXAFS	extended X-ray absorption fine structure	21
Fe–Sal	salophenatoiron(II)	154
GGA	generalized gradient approximation	48
Gr/Co/Ir(111)	Co-intercalated graphene on Ir(111)	3

Notation	Description	Page List
Gr/Fe/Ir(111)	Fe-intercalated graphene on Ir(111)	71
Gr/Ir(111)	graphene on Ir(111)	112
HDvV	Heisenberg–Dirac–van-Vleck	51
HOMO	highest occupied molecular orbital	12
IUPAC	International Union of Pure and Applied Chemistry	56
LCAO	linear combination of atomic orbitals	45
LDA	local density approximation	47
LDOS	local density of states	10
LFT	ligand field theory	39
LUMO	lowest occupied molecular orbital	13
MO	molecular orbital	39
MO-LCAO	molecular orbitals—linear combination of atomic orbitals theory	39
PDOS	partial density of states	85
PID controller	proportional-integral-derivative controller	5
PTS	point-tunneling spectroscopy	12
Pc	phthalocyanine	121
RKKY	Ruderman–Kittel–Kasuya–Yosida	65
SLS	Swiss light source	96
SMM	single-molecule magnet	2
SOMO	singly occupied molecular orbital	46
SP-PTS	spin-polarized point-tunneling spectroscopy	84
SP-STM	spin-polarized scanning-tunneling microscopy	3
SP-STS	spin-polarized scanning-tunneling spectroscopy	3
STM	scanning-tunneling microscopy	3

Notation	Description	Page List
STS	scanning-tunneling spectroscopy	3
SUMO	singly unoccupied molecular orbital	46
TMR	tunnel magnetoresistance effect	14
TSP	titanium sublimation pump	77
UHV	ultra-high vacuum	74
XANES	X-ray absorption near edge spectroscopy	21
XAS	X-ray absorption spectroscopy	19
XMCD	X-ray magnetic circular dichroism	3
$\mathrm{d}I/\mathrm{d}U$	differential conductance	11
fcc	face centered cubic	83
hcp	hexagonal close packed	83

List of Symbols

Notation	Description	Page List
E	energy	6
V	potential energy	6
Ψ	wave function	7
k, κ	wave number	7
m_e	electron mass	7
$\hbar$	reduced Planck's constant	7
$\tilde{T}$	transmission coefficient	7
$\tilde{j}$	current density	7
I	tunneling current	8
e	electron charge	9
U	bias voltage	9
$\tilde{M}_{nj}$	tunneling matrix element	9
$f(E)$	Fermi-Dirac function	9
k_B	Boltzmann constant	9
T	temperature	9
R	radius	9
ρ	local density of states	10
E_F	Fermi energy	10
$\boldsymbol{r}$	spatial coordinate	10

Notation	Description	Page List
ω_{mod}	modulation frequency	11
U_{mod}	modulation voltage	11
P	spin polarization	14
$\boldsymbol{M}_{\mathbf{s}}$	single-electron spin magnetic moment	14
$\boldsymbol{s}$	single-electron spin	14
$\boldsymbol{M}$	magnetic moment	14
μ_{B}	Bohr's magneton	14
R	resistance	16
G	conductance	16
Θ	angle	16
$\tilde{\kappa}$	decay length	17
$\tilde{\rho}$	integrated local density of states	17
$\boldsymbol{m}$	local magnetization density of states	17
$\tilde{\boldsymbol{m}}$	integrated local magnetization density of states	17
$\tilde{A}$	magnetic asymmetry	18
$\boldsymbol{H}$	magnetic field	18
μ	absorption coefficient	20
I^{X}	X-ray intensity	20
Y	electron yield	20
Λ	escape length	20
n	principal quantum number	21
j	single-electron total angular momentum quantum number	21
σ_{abs}	absorption cross section	22
N_{A}	Avogadro constant	22
ρ_{m}	mass density	22

Notation	Description	Page List
M_{m}	molar mass	22
$\tilde{T}_{if}$	transition probability	22
Ψ_0^{X}	photon flux	22
$\hat{H}$	Hamiltonian	22
$\hat{\tilde{\boldsymbol{P}}}$	momentum operator	22
$\boldsymbol{\epsilon}$	polarization vector	23
l	single-electron orbital angular momentum quantum number	23
m_{l}	single-electron orbital magnetic quantum number	23
s	single-electron spin quantum number	23
m_s	single-electron spin magnetic quantum number	23
$\boldsymbol{M}_{\mathbf{S}}$	spin magnetic moment	27
$\boldsymbol{M}_{\mathbf{L}}$	orbital magnetic moment	27
$\hat{\boldsymbol{T}}$	magnetic dipole operator	27
$\boldsymbol{M}_{\mathbf{S,eff}}$	effective spin magnetic moment	27
V_{Ne}	nuclear potential energy	35
V_{ee}	electronic potential energy	35
S	spin quantum number	35
L	orbital angular momentum quantum number	35
J	total angular momentum quantum number	36
Δ	crystal/ligand field splitting	40
ϵ_0	permittivity constant	40
∇^2	Laplace operator	40
ρ_{e}	electron density	41
$\boldsymbol{x}$	combined spatial and spin coordinate	42
F_{HK}	Hohenberg-Kohn functional	42

Notation	Description	Page List
J_{C}	Coulomb interaction	43
V_{XC}	exchange-correlation potential	44
g_{s}	Landé factor of the spin magnetic moment	48
M_{s}	single-electron spin magnetic moment quantum number	49
$\boldsymbol{M}_{\mathrm{l}}$	single-electron orbital magnetic moment	49
g_{l}	Landé factor of the orbital magnetic moment	49
$\boldsymbol{l}$	single-electron orbital angular momentum	49
M_{l}	single-electron orbital magnetic moment quantum number	49
s_z	z component of the single-electron spin	49
l_z	z component of the single-electron orbital angular momentum	49
$\boldsymbol{j}$	single-electron total angular momentum	49
$\boldsymbol{J}$	total angular momentum	49
$\boldsymbol{L}$	orbital angular momentum	49
$\boldsymbol{S}$	spin	49
$\boldsymbol{M}_{\mathbf{J}}$	total magnetic moment	49
g_{j}	Landé factor of the total magnetic moment	49
$\widetilde{\boldsymbol{D}}$	anisotropy tensor	50
$\boldsymbol{B}$	magnetic flux	50
$\widetilde{g}$	g-factor	50
J	exchange coupling parameter	51
$\boldsymbol{d}_{12}$	Dzyaloshinskii-Moriya vector	51
Φ	atomic/molecular orbital	53
K_{ab}	exchange integral	53

Notation	Description	Page List
t_{ab}	hopping integral	55
U_{H}	on-site Coulomb repulsion	55
r	distance	55
ΔE_{CT}	single charge transfer excitation energy	56
ΔE_{2CT}	double charge transfer excitation energy	57
$\tilde{S}_{ab}$	overlap integral	57
$\hat{J}_{\mathrm{C}}$	Coulomb operator	61
$\hat{K}$	exchange operator	61
γ	gyromagnetic ratio	64
D	magnetic anisotropy energy	71
$\tilde{g}$	g tensor	71
I_{stab}	stabilization tunneling current	82
T_{C}	Curie temperature	85
U_{stab}	stabilization bias voltage	91

1 Introduction

The capability of atoms to organize in molecular structures is crucial for the world as it is. While life itself could not exist without molecules, life in our modern societies would not be the same without the capability to design new molecules with unique properties almost at will. Chemistry is the science providing the tools to design these basic building blocks, obtaining a plethora of new properties. These open the path to many different research fields interesting not only to chemists but also to biologists and physicists.

Two fields especially interesting for chemists and physicists are molecular electronics [1, 2] and molecular spintronics [3–5]. Next to the smaller conveniences of designed molecular materials, for example, flexibility, transparency, and light weight, used in many applications, they can help to solve major problems of our modern societies. The reduced size of molecular building blocks, compared to classical semiconductor devices, not only helps to continue the trend of miniaturization but will also be important in view of recourse efficiency. Especially in the case of spintronics also the energy efficiency will be improved since the heat dissipation is drastically reduced in these devices compared to traditional devices based on semiconductors [4]. Spintronic devices are also revolutionary in the sense that they do not rely on the charge of a moving electron but use the electron spin as the information carrier. The path toward molecular spintronics was opened with the observation of molecular magnetism.

It can be argued when exactly the research of molecular magnetism started. The first step to mention is probably the observation of unusual behavior of the susceptibility in copper acetate at low temperatures [6]. In 1952, Bleaney and Bowers suggested that copper acetate contains two magnetically coupled Cu centers, which was the first report of intramolecular magnetic exchange interaction [7]. A recent

review on molecular magnetism by Coronado dates the beginning of research in this field back to the 1980s [5]. In this time, a fruitful collaboration of physicists and chemists started, investigating simple model systems to test theoretical models transferred from solid state physics to molecular systems in the 1970s [8, 9].

The next landmark was the discovery of magnetic hysteresis in molecules in the 1990s [10]. With this discovery, the biggest branch of molecular spintronics, focusing on using magnetic molecules for information storage, was initiated. In this field, single-molecule magnets (SMMs) are synthesized, aiming for a large total spin and high anisotropies. Because of the interesting quantum mechanical effects found in SMMs, especially those based on 4f-transition-metal atoms, nowadays, they are also considered for utilization in quantum computation devices [11]. Apart from this, magnetic molecules can also be considered for conventional computation of information. To this end, structures for information transport and logic operations are necessary.

Salophen molecules have been shown to have great potential for such spintronic applications [12]. Salen-type complexes have been proposed for the creation of SMMs by designing multi-center transition metal–organic complexes with ferromagnetic intramolecular coupling [13, 14]. The Co–Sal molecule, as used in this thesis, was shown to form antiferromagnetically coupled multi-center chains upon on-surface Ullmann reaction [15]. Such chains can potentially be used for information transport in a spintronic device. By combining these molecules with tribromo-triplecobaltsalophen (Br_3Co_3–Sal), also a logic gate for information processing can be created [16]. However, it has been shown that, on the Au(111) surface, the magnetic moment of the molecules is screened by conduction electrons of the substrate, which is due to the Kondo effect. Therefore, the magnetic moment of the molecules cannot be addressed by an external magnetic field, which renders this system inappropriate for spintronic applications.

The present thesis is dedicated to the investigation of $[\text{Co–Sal}]_n$ chains on alternative substrates that enable on-surface Ullmann coupling and, at the same time, make the magnetic properties of the chains usable. In Chapter 2 the experimental techniques used for the investigation of the molecules and the preparation of the

samples are introduced. Chapter 3 contains an introduction to density-functional theory (DFT) and an overview of molecular magnetism. The focus was set upon the different mechanisms for intramolecular magnetic exchange interactions and the properties of Co–Sal that make it a possible candidate for the application in spintronic devices. The two scanning-tunneling microscopy (STM) setups and the corresponding preparation utilities used during the study will be introduced in Chapter 4.

Chapter 5 treats $[\text{Co–Sal}]_n$ chains on the $GdAu_2$ surface alloy on Au(111). After introducing the properties of the substrate and the literature on molecules adsorbed on this substrate, the preparation procedure for the samples is presented. This is followed by the results from the STM and scanning-tunneling spectroscopy (STS) studies of the electronic properties of single Co–Sal molecules and $[\text{Co–Sal}]_n$ chains. In the end, the results of an X-ray magnetic circular dichroism (XMCD) investigation are summarized, followed by the spin-polarized scanning-tunneling spectroscopy (SP-STS) study on the local magnetic properties of $[\text{Co–Sal}]_n$ chains on $GdAu_2$.

Analogously, Chapter 6 focuses on $[\text{Co–Sal}]_n$ chains on Co-intercalated graphene on Ir(111) (Gr/Co/Ir(111)). First, the substrate properties and studies on molecules and atoms adsorbed on the substrate are presented, and the procedure for the sample preparation is introduced. The STM/STS study on the $[\text{Co–Sal}]_n$ chains, complemented by DFT calculations of the Co–Sal in its gas phase, is presented afterward. This is followed by an SP-STS study on the local magnetic properties of the system. The chapter also contains a study on $[\text{Co–Sal}]_n$ chains adsorbed on pristine graphene to elucidate the influence of the substrate on the molecules. Finally, a study of the on-surface metalation of 5,5'-dibromosalophen (Br_2H_2–Sal) on Gr/Co/Ir(111) with the transition metals Cr and Fe is presented. These complexes will have higher magnetic moments and, therefore, promise better access by external fields and the spin-polarized scanning-tunneling microscopy (SP-STM) tip.

2 Experimental Methods

In the following, the techniques used for the investigation of the sample systems and the methods used during sample preparation will be introduced. The introduction to STM and STS was adapted from reference [17].

2.1 Scanning Tunneling Microscopy (STM) and Spectroscopy (STS)

STM is a technique providing the ability to investigate electrically conducting surfaces and thin layers of nonconducting materials with atomic resolution. It is based on the so-called quantum tunneling. This phenomenon gives electrons the possibility to overcome a potential barrier, like a thin insulating film or vacuum. Binnig and Rohrer were the first to employ quantum tunneling for the realization of the scanning tunneling microscope [18, 19].

A basic STM setup is depicted schematically in Figure 2.1. To take a topographic STM image, a voltage is applied between the sample and a metallic tip before it is brought into tunneling contact at a distance of a few pm. Usually, the voltage is applied to the sample while the tip is grounded. The tip then scans a predefined surface area line by line. Since the tunneling current between the tip and the sample strongly depends on the distance between those two electrodes, one can — by keeping either the tunneling current or the vertical position of the tip constant — get detailed information about the topography of the surface. If the vertical position of the tip (z-position) is kept constant, which is called constant height mode, the corrugation of the sample surface has to be very small. On a

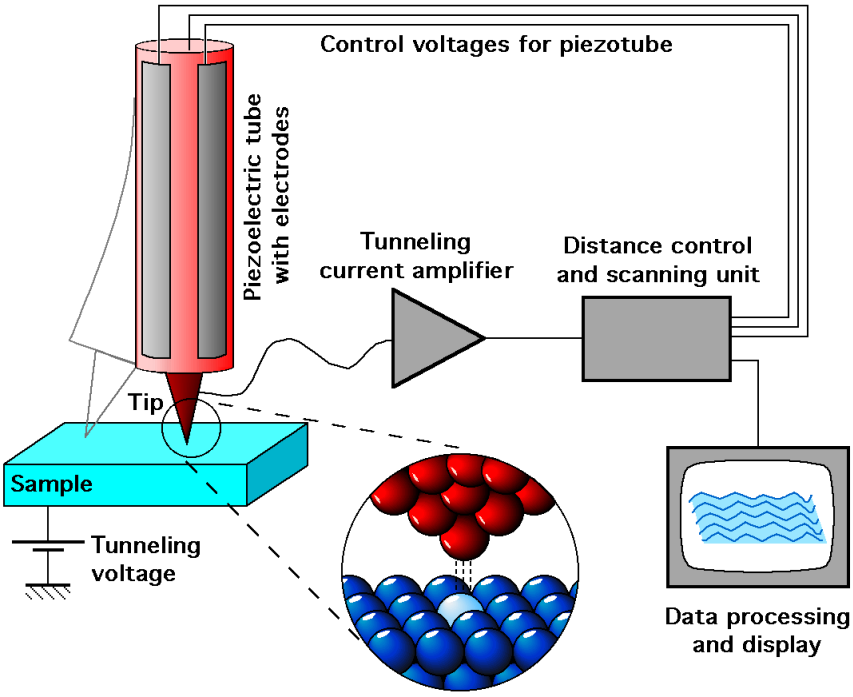

Figure 2.1: Schematic of a basic STM setup. The piezoelectric scanner tube (light red) with two electrodes (grey) moves the tip (dark red) across the sample (blue) to which a voltage is applied. The movement is controlled with a computer that is also used for data recording. To measure the small tunneling currents, they are enhanced by an amplifier.
Figure created by Michael Schmid, TU Wien, reused here under [20].

too rough surface, the tip would either lose the tunneling contact or crash into the surface. In this mode, the current signal is measured and can be interpreted to obtain information about the topography and electronic structure of the sample.

A feedback loop controls the z-position of the tip in the constant current mode. The tunneling current is set to a fixed value (setpoint) of a few pA up to $1\,\mu$A. During the scan, this current is constantly measured. A PID controller adjusts the height of the tip to counteract changes in the measured current. Since the response time is limited, the scanning speed has to be adjusted to fit the settings of the PID controller.

The positioning of the tip is done by piezoelectric materials. If a voltage is applied to a piezoelectric crystal, it responds with deformation. *Vice versa*, if physical stress is applied to the crystal by squeezing or stretching, this will cause creation of an electric field between two opposing faces of the crystal. Since large voltages cause only small deformations, a very precise movement can be realized with piezoelectric materials. For most STM setups, the tip is mounted on a so-called tube scanner similar to the one depicted in Figure 2.1. This tube scanner is made of a piezoelectric material covered with one electrode on the outer face, which is cut into four slices along the axis of the tube and one electrode on the inner face of the tube. Sawtooth voltages of opposite signs are applied to two opposite electrodes causing the movement in the fast scan direction. At the same time, the voltage for the other two electrodes is increased (decreased), step by step with each line, to control the movement in the slow scan direction. The z-position is controlled by applying a bias voltage to the inner electrode versus a bias voltage applied to all of the outer electrodes.

The shape of the tip limits the spatial resolution of the STM. An ideal tip has a cone-like shape with a single atom at the apex. With such shaped tips, one can achieve atomic-resolution STM images because of the properties of the quantum tunneling phenomenon.

2.1.1 One-Dimensional Quantum Tunneling

The simplest model for quantum tunneling is the tunneling through a one-dimensional potential barrier, depicted in Figure 2.2. In this model, the trajectory of a particle with energy E crosses a potential barrier with height $V_0 > E$. From a classical point of view, the particle would simply be reflected by the barrier. An electron, however, is a quantum mechanical object and can be described by a wave function. This wave function is partially transmitted and partially reflected at both borders of the potential barrier.

To solve this problem mathematically, the system is divided into three sections: Before, within, and behind the potential barrier. Each of these regions has a

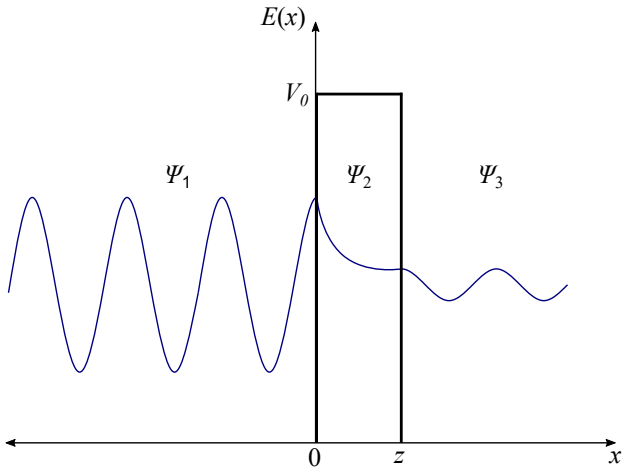

Figure 2.2: Schematic of the one-dimensional tunneling process. Because of the wave–particle duality, a particle with energy E can tunnel through a potential barrier with a height $V_0 > E$ and a width z. The amplitude of the wave function decays exponentially within the barrier region.

different wave function. For the solutions of these wave functions, the following Ansatz can be used:

$$\Psi_1 = A_1 \exp(ikx) + A_1{}' \exp(-ikx), x < 0 \tag{2.1}$$

$$\Psi_2 = A_2 \exp(\kappa x) + A_2{}' \exp(-\kappa x), 0 \leq x \leq z \tag{2.2}$$

$$\Psi_3 = A_3 \exp(ikx) + A_3{}' \exp(-ikx), x > z \tag{2.3}$$

The variables $k^2 = \frac{2m_\mathrm{e}E}{\hbar^2}$ and $\kappa^2 = \frac{2m_\mathrm{e}(V_0-E)}{\hbar^2}$ are the wave numbers in the different regions, with the reduced Planck's constant $\hbar = \frac{h}{2\pi}$ and the electron mass m_e. A_1 can be chosen freely. Since the electron proceeds from left to right, it is set to 1. Also, $A_3{}' = 0$ because there is no electron coming from the right-hand side.

The total wave function has to be continuous. Therefore, four equations are obtained, which can be solved for the transmission coefficient $\tilde{T}$. It is defined as the ratio of transmitted current density $\tilde{j}_\mathrm{t} = \frac{\hbar k}{m_\mathrm{e}}|A_3|^2$ over initial current density $\tilde{j}_\mathrm{i} = \frac{\hbar k}{m_\mathrm{e}}|A_1|^2$ [21]:

$$\tilde{T} = \frac{\tilde{j}_\mathrm{t}}{\tilde{j}_\mathrm{i}} = \left|\frac{A_3}{A_1}\right|^2 = \frac{1}{1 + (k^2+\kappa^2)^2/(4k^2\kappa^2)\sinh^2(\kappa z)} \tag{2.4}$$

For large barriers ($\kappa z >> 1$), this equation can be simplified to [21]:

$$\tilde{T} \approx \frac{16k^2\kappa^2}{\left(k^2+\kappa^2\right)^2} \exp(-2\kappa z) \tag{2.5}$$

This equation shows the exponential dependence of the tunneling current on the width of the tunneling barrier z corresponding to the tip–sample distance. Because of this relation, it is possible that, for a well shaped tip, only one single atom contributes to the tunneling current. This leads to the lateral atomic resolution that is possible with STM.

However, this simple model of one-dimensional tunneling mainly shows the relation between the tunneling current and the distance between tip and sample, while the current also depends on the density of states (DOS) in the tip and the sample. As will be shown in the following, one does not get a pure image of the surface topography but a convolution of the topography and the DOS of both the sample and the tip.

2.1.2 The Tersoff-Hamann Approach to STM

A more profound approach describing tunneling between two three-dimensional metallic electrodes was introduced by Bardeen in 1960 [22]. In the following, a short overview of the main ideas of Bardeen's theory will be given. Detailed discussions can be found in references [21, 23, 24]. Bardeen used a time dependent perturbation theory approach analogous to a theory developed by Oppenheimer for the description of the ionization of H atoms [24, 25]. In this theory, a small overlap between the states of the two tunneling electrodes is assumed, causing a weak coupling of the states. Using Fermi's golden rule, Bardeen derived a formula giving the transfer rate of electrons from a given sample state into tip states of the same energy and of the reversed process. The tunneling current I then corresponds

to the net transfer of electrons between the two electrodes summed over all N tip states and J sample states [24]:

$$I = \frac{2\pi e}{\hbar} \sum_{n,j} \{ f(E_n)(1 - f(E_j + eU)) \\ - (1 - f(E_n)) f(E_j + eU) \} \left| \tilde{M}_{nj} \right|^2 \delta(E_n - (E_j + eU)) \tag{2.6}$$

Here, e is the electron charge, U is the bias voltage applied to the sample, and $f(E) = (1 + exp(\frac{E}{k_\mathrm{B}T}))^{-1}$ is the Fermi–Dirac function with the Boltzmann constant k_B, giving the occupation probability of the tip and sample states at temperature T and energy E. In the equation, the energies are given by the equilibrium energies of the nth or jth state of tip and sample, respectively. For the sample electrode, the energy is lifted by the applied bias voltage. Together with the transition matrix elements $\tilde{M}_{nj}$, the first summand in the braces gives the probability of an electron to tunnel from an occupied tip state into an unoccupied sample state. The second summand gives the probability for the reverse process. The delta function $\delta(E_n - (E_j + eU))$ ensures that only energy conserving tunneling processes are considered.

To calculate the resulting tunneling current, one has to calculate the tunneling matrix elements $\tilde{M}_{nj}$. Bardeen approximated these tunneling matrix elements by integrating the current density between the two electrodes over a freely chosen surface within the area of the tunneling barrier leading to the following expression [21, 22, 24]:

$$\tilde{M}_{nj} = -\frac{\hbar^2}{2m_\mathrm{e}} \int \mathrm{d}\boldsymbol{A}\, \Psi_n^{t\,*} \boldsymbol{\nabla}\, \Psi_j^s - \Psi_j^s \boldsymbol{\nabla}\, \Psi_n^{t\,*} \tag{2.7}$$

Here, Ψ_n^t denotes the nth tip state and Ψ_j^s the jth sample state. Despite the fact that Bardeen's approach presupposes multiple conditions that are not met in every scanning tunneling experiment [24], it is a useful basis for models describing the tunneling current in various situations [23, 24].

While Bardeen formulated his approach for two flat electrodes, it was later applied to STM by Tersoff and Hamann [26, 27]. They solved the problem for a tip with locally round apex and a radius of the curvature R, starting from Equation 2.6.

For the electronic states of the tip, they assumed spherical s-type wave functions.[1] As a result, one gets the following equation for the tunneling current at small bias voltages and temperatures at room temperature or below [24]:

$$I = eU\frac{eh^3}{{m_\mathrm{e}}^2}C^2\rho^\mathrm{t}({E_\mathrm{F}}^s)\rho^\mathrm{s}(\boldsymbol{r}_\mathrm{t}, {E_\mathrm{F}}^s) \tag{2.8}$$

According to this equation, I is proportional to the product of the tip's DOS $\rho^\mathrm{t}({E_\mathrm{F}}^s)$ and the sample's local density of states (LDOS) at the position of the tip $\rho^\mathrm{s}(\boldsymbol{r}_\mathrm{t}, {E_\mathrm{F}}^t + eU)$, both at the quasi Fermi energy of the sample.[2] The constant C characterizes the geometry of the tip and takes the form $C = R\exp(\kappa R)/\sqrt{\frac{4}{3}\pi R^3}$ in the case considered by Tersoff and Hamann. This equation shows that topographic images can be interpreted as a contour plot of constant LDOS of the sample at Fermi energy [30]. Therefore, the gathered data does not correspond directly to the topography of the surface but shows a convolution of the topography and the DOS of tip and sample. This leads to the fact that some protrusions on the surface might be imaged as hollows and *vice versa*. An example for this effect are oxygen atoms adsorbed on a Cu(111) surface [31].

To extend this theory to finite bias voltages, one has to integrate the contribution of all states between Fermi energy E_F and the applied bias voltage [21, 32, 33]. Since the transition matrix elements $\tilde{M}_{nj}$ depend on the bias voltage, a transmission coefficient $\tilde{T}(z, E, eU)$ has to be introduced, accounting for this effect:

$$I \propto \int_{E_\mathrm{F}}^{E_\mathrm{F}+eU} \mathrm{d}E\rho^\mathrm{s}(E)\rho^\mathrm{t}(\boldsymbol{r}_0, E)\tilde{T}(z, E, eU) \tag{2.9}$$

2.1.3 Imaging Electronic States via STM

Topographic imaging is only one of the multiple ways to use a scanning tunneling microscope. Over the years, various STM techniques have been developed to investigate different properties of electrically conducting surfaces [34]. One of

[1] This was later extended to various other wave functions by Chen [28, 29].

[2] The quasi Fermi energy is the energy up to which the sample states are filled, modified by the bias voltage. Since the tunneling process has to be energy conserving, tip and sample states need to have the same energy.

these techniques, the differential conductance ($\mathrm{d}I/\mathrm{d}U$) spectroscopy, can be used to resolve the LDOS in energy. In order to do so, a modulation at a frequency ω_{mod} of typically a few kHz and with an amplitude U_{mod} of a few mV is applied to the bias voltage, using a lock-in amplifier. The modulation of the bias voltage causes an oscillation of the tunneling current with the frequency of the modulation and an amplitude proportional to the $\mathrm{d}I/\mathrm{d}U$. Writing the tunneling current as a Taylor expansion gives the equation [30, 33]:

$$\begin{aligned} I(U + U_{\mathrm{mod}}\cos(\omega_{\mathrm{mod}}t)) = I_0 + \frac{\mathrm{d}I(U)}{\mathrm{d}U}U_{\mathrm{mod}}\cos(\omega_{\mathrm{mod}}t) \\ + \frac{\mathrm{d}^2I(U)}{\mathrm{d}U^2}{U_{\mathrm{mod}}}^2\cos(\omega_{\mathrm{mod}}t)^2 + ... \end{aligned} \tag{2.10}$$

I_0 corresponds to the tunneling current without any applied modulation voltage. By multiplying the current signal with the nth harmonic of the modulation voltage, the lock-in amplifier can filter out the nth derivative of the current.[3]

The question remains as to which information we can get from the differential conductance. From Equation 2.9 one can derive the expression [30, 33, 36]:

$$\begin{aligned} \frac{\mathrm{d}I}{\mathrm{d}U} \propto = \rho^{\mathrm{s}}(E_{\mathrm{F}} + eU)\rho^{\mathrm{t}}(\boldsymbol{r}_{\mathrm{t}}, E_{\mathrm{F}} + eU)\tilde{T}(z, E_{\mathrm{F}} + eU, eU) \\ + \int_{E_{\mathrm{F}}}^{E_{\mathrm{F}}+eU} \mathrm{d}E\rho^{\mathrm{s}}(E)\rho^{\mathrm{t}}(\boldsymbol{r}_{\mathrm{t}}, E)\frac{\mathrm{d}\tilde{T}(z, E, eU)}{\mathrm{d}U} \\ + \int_{E_{\mathrm{F}}}^{E_{\mathrm{F}}+eU} \mathrm{d}E\rho^{\mathrm{s}}(E)\frac{\mathrm{d}\rho^{\mathrm{t}}(\boldsymbol{r}_{\mathrm{t}}, E)}{\mathrm{d}U}\tilde{T}(z, E, eU) \end{aligned} \tag{2.11}$$

Under the assumption that the transmission coefficient and the tip DOS are constant for the energy range of interest given by the modulation energy eU_{mod}, the two integrals equal zero and only the first term remains. The $\mathrm{d}I/\mathrm{d}U$ signal is then proportional to the LDOS of the sample at the bias energy eU with respect to the Fermi energy.

By recording the $\mathrm{d}I/\mathrm{d}U$ signal while taking a topography image, as described above, one can locally resolve the electronic states of the sample at a given energy. The obtained data can be plotted in a so-called $\mathrm{d}I/\mathrm{d}U$ map. In these $\mathrm{d}I/\mathrm{d}U$ maps,

[3] For a more detailed description of lock-in amplifiers and their applications refer to [35]

the finite response time of the feedback-loop can cause artifacts when scanning over step edges or adsorbates. These artifacts can be reduced by averaging over two $\mathrm{d}I/\mathrm{d}U$ maps, one recorded during the forward scan and one during the backward scan of the tip. If not stated otherwise, this was done for all data presented in this thesis. Another technique, point-tunneling spectroscopy (PTS), can be used to resolve the states in energy for a fixed point. For this purpose, the tip is positioned over the sample with a specified tunneling current and bias voltage. Then, the feedback loop is turned off to keep the position of the tip fixed, and the voltage is varied over a specified range. The resolution of this technique is limited by three factors: First, the amplitude of the modulation, which has to be large enough to acquire a signal but small enough to observe the investigated features, second, the step size between the voltages at which the signal is measured, and, third, the temperature broadening. Additionally, finite temperatures lead to a broadening of electronic states due to excitations.

As stated above, the pure $\mathrm{d}I/\mathrm{d}U$ signal is modified by changes in the transmission coefficient and the tip DOS, especially at high bias voltages. While the latter is rather small for metallic tips, the effect of the former can be reduced by normalization of the $\mathrm{d}I/\mathrm{d}U$ signal over I/U [34, 37]. Thereby, background effects caused by the variation of the transmission coefficient are filtered out for positive and small negative bias voltages. However, for large negative voltages the DOS is weakened since the transmission is decreasing and the term proportional to the LDOS is of the same magnitude as the disturbing effects. Also, when approaching $U = 0$ the normalized $\mathrm{d}I/\mathrm{d}U$ signal diverges since the current crosses zero. This effect is particularly dominant with low currents, as often needed for STM measurements on molecular systems. Nevertheless, if a sufficiently high current is used for the spectroscopy, this artifact can be removed by setting the normalized $\mathrm{d}I/\mathrm{d}U$ signal to unity at $U = 0$ [37].

2.1.4 Tunneling Through Molecules

The investigation of molecules with STM produces some surprising results. Since molecules have an energy gap between the highest occupied molecular orbital

(HOMO) and the lowest occupied molecular orbital (LUMO) around Fermi energy, one would expect that the molecule is invisible in STM when scanning with low energies.

The same applies to thin insulating films on surfaces. Those films can be seen in a topographic image taken at a bias energy lying in the band gap of the insulator because they have a different dielectric constant than vacuum. Therefore, they serve as a dielectric lowering the tunneling barrier locally in comparison to vacuum [38]. However, since the tunneling current changes stronger with the width of the tunneling barrier than with its height, the apparent height of an insulating film scanned in the band gap is lower than its real height [39]. The same is true for molecules. They also act as a dielectric and, therefore, change the tunneling current locally. Additionally, the electronic states of a molecule are strongly broadened after adsorption on a metallic surface, which reduces the width of the energy gaps.

Another difference of tunneling through a molecule is that we get two different processes [40]:

One-step process: An electron tunnels directly from one electrode to the other. This is an elastic process in which the electron never occupies a molecular orbital.

Two-step process: This process is constituted by two consecutive tunneling processes, one between tip and molecule and the other between molecule and substrate. The two processes do not need to affect the same electron. During this inelastic tunneling process, the electron is excited.

The two-step process is only possible for energies outside of the HOMO–LUMO gap. Within this gap only one-step processes contribute to the tunneling current. Two-step processes lead to a charging of the molecule for a short period of time. This charge might be either negative, if an electron first tunnels from one electrode to the molecule and then an electron from the molecule to the second electrode, or positive, if the tunneling processes occur in opposite order. Since the molecule's preferred geometry changes for the time it is charged, these processes lead to

vibronic excitations in the molecule. The interaction with the molecule changes the phase of the electron during inelastic tunneling. Therefore, the interference between the two tunneling paths can be either destructive or constructive, and the total tunneling current depends on the phase between the contributions of one-step and two-step processes. A precise description of this phenomenon can be done with a Greens-function approach [41].

2.1.5 Spin-Polarized Scanning Tunneling Microscopy (SP-STM) and Spectroscopy (SP-STS)

The vision of imaging magnetic structures with atomic resolution by utilizing SP-STM was first presented in 1988 by Pierce [42]. Only two years later, in 1990, SP-STM was first introduced by Wiesendanger *et al.* on a Cr(001) surface with antiferromagnetically coupled terraces [43]. SP-STM is based on the tunnel magnetoresistance effect (TMR), which is depicted in Figure 2.3.[4] This effect, first observed by Julliere in 1975 [45], occurs when electrons tunnel between two magnetic electrodes. For STM experiments, these electrodes either inherit magnetic ordering themselves, or they bear a magnetic impurity like a magnetic atom, cluster, or molecule.[5]

For two ferromagnetic, metallic electrodes, spin-polarized tunneling can be explained by the Stoner model [47]. In this model, Stoner considers two sub bands for an electronic band of a metal: One occupied exclusively by spin-up electrons, the other by spin-down electrons. Similarly, the DOS describing a free electron gas can be split into two spin components, as depicted in Figure 2.3. According to the Stoner model, the exchange interaction causes a relative energy shift between these spin components in ferromagnetic metals. The states with the lower energy, the majority states, are occupied by more electrons than the states of the other spin component, the minority states. This creates a spin polarization P of

[4] Note that, due to the relation of the spin magnetic moment for electrons $\boldsymbol{M}_{\mathbf{s}} = -2\mu_B \boldsymbol{s}$, the magnetization directions $\boldsymbol{M}_{\mathrm{s/t}}$ of sample and tip are antiparallel to the spin $\boldsymbol{s}$ of the respective majority electrons [44]. Here, μ_{B} is the Bohr magneton.

[5] In other tunneling-junction experiments also optically pumped semiconductor electrodes or Zeeman split BCS-like superconductors have been utilized as spin-polarized electrodes [46].

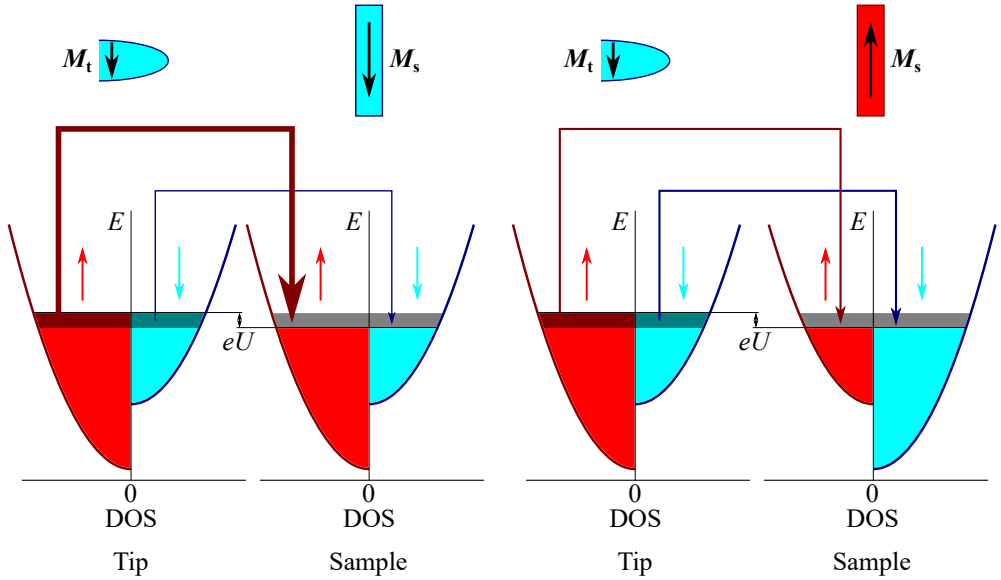

Figure 2.3: Graphical representation of the TMR. The simplified DOS for spin-up (red) and spin-down (blue) electrons are plotted for a ferromagnetic tip and sample with a voltage U applied between the two electrodes. The case for parallel alignment of the magnetic moments of the electrodes is shown on the left; the antiparallel case on the right. The magnetic moments of the electrodes are indicated by black arrows. Because of the applied voltage, electrons from tip states above the sample's Fermi energy (marked by grayed out area) tunnel into unoccupied sample states of the same energy (marked by gray area). The tunneling currents are indicated by colored arrows in darker shades.

the metal, defined as the difference in the DOS of spin-up $\rho_\uparrow$ and spin-down $\rho_\downarrow$ electrons divided over the total DOS of both components:

$$P = \frac{\rho_\uparrow - \rho_\downarrow}{\rho_\uparrow + \rho_\downarrow} \tag{2.12}$$

When neglecting spin flips during tunneling, the tunneling current can be described in the two-current model as the sum of two channels [45]. One being the tunneling between spin-up states and the other tunneling between spin-down states. As depicted in Figure 2.3, in case of a parallel alignment of the magnetic moments of tip and sample there is a relatively large tunneling current between the majority

states and a very small current between the minority states. In the antiparallel case the electrons tunnel from the majority states of the tip into the minority states of the sample and from the minority states of the tip into the majority states of the sample. Both pathways result in a relatively small tunneling current, so that the total current in the antiparallel case is smaller than in the parallel case. This effect is summarized in the tunneling magnetoresistance [46]:

$$R_{\mathrm{TMR}} = \frac{R_{\mathrm{ap}} - R_{\mathrm{p}}}{R_{\mathrm{p}}} = \frac{2P_{\mathrm{t}}P_{\mathrm{s}}}{1 - P_{\mathrm{t}}P_{\mathrm{s}}} \tag{2.13}$$

Here, R_{ap} and R_{p} denote the resistance in the antiparallel and parallel case, respectively, and P_{t} and P_{s} denote the polarization of the tip and the sample, respectively.

Slonczewski formulated a theoretical description of the TMR in the framework of one-dimensional tunneling, as described in Section 2.1.1 [48]. Under use of the free-electron approximation and considering small voltages at zero temperature, the conductance $G = \frac{I}{U}$ of a one-dimensional tunneling barrier can be expressed as:

$$G = G_0(1 + {P_{\mathrm{s}}}^{\mathrm{eff}} {P_{\mathrm{t}}}^{\mathrm{eff}} \cos(\Theta)) \tag{2.14}$$

$$P^{\mathrm{eff}}_{\mathrm{s/t}} = \frac{(k_{\mathrm{s/t}\uparrow} - k_{\mathrm{s/t}\downarrow})}{(k_{\mathrm{s/t}\uparrow} + k_{\mathrm{s/t}\downarrow})} \frac{(\kappa^2 - k_{\mathrm{s/t}\uparrow}k_{\mathrm{s/t}\downarrow})}{(\kappa^2 + k_{\mathrm{s/t}\uparrow}k_{\mathrm{s/t}\downarrow})} \tag{2.15}$$

Here, G_0 denotes the conductance for non-spin-polarized tunneling, $P^{\mathrm{eff}}_{\mathrm{s/t}}$ denotes the effective polarization of the sample and the tip, respectively. The latter are calculated using the wave numbers of the spin-polarized electron wave functions in the sample region and the tip region $k_{\mathrm{s/t}}$, and in the barrier-region κ. Equation 2.14 shows that the tunneling current can be viewed as the sum of the current without spin polarization and a spin-polarized term. The spin-polarized term depends on the angle Θ between the magnetization directions of the tip and the sample. This second term leads to a maximum current for parallel alignment of the magnetic moments and a minimum current for antiparallel alignment.

Wortmann *et al.* adapted the theory developed by Bardeen, and applied to STM by Tersoff and Hamann, to SP-STM [49, 50]. They replaced the non-spin-polarized tip wave function with two spinors, one for the spin-up and one for the spin-down case, and the sample wave function with a spin-mixed wave function. Thereby, they obtained an expression for the tunneling current analogue to Equation 2.14.

$$\begin{aligned} I(\boldsymbol{r}_\mathrm{t}, U, \Theta) &= I_0(\boldsymbol{r}_\mathrm{t}, U) + I_\mathrm{P}(\boldsymbol{r}_\mathrm{t}, U, \Theta) \\ &= \frac{4\pi^3 C^2 \hbar^3 e}{\tilde{\kappa}^2 {m_\mathrm{e}}^2} \left[\rho_\mathrm{t}\tilde{\rho}_\mathrm{s}(\boldsymbol{r}_\mathrm{t}, U) + \boldsymbol{m}_\mathrm{t}\tilde{\boldsymbol{m}}_\mathrm{s}(\boldsymbol{r}_\mathrm{t}, U)\right] \end{aligned} \tag{2.16}$$

For this expression, Wortmann *et al.* introduced the integrated LDOS $\tilde{\rho}_\mathrm{s}(\boldsymbol{r}_\mathrm{t}, U)$ and the integrated local magnetization DOS $\tilde{\boldsymbol{m}}_\mathrm{s}(\boldsymbol{r}_\mathrm{t}, U)$. ρ_t and $\boldsymbol{m}_\mathrm{t}$ denote the regular LDOS and local magnetization DOS of the tip, respectively. Furthermore, $\boldsymbol{r}_\mathrm{t}$ denotes the position of the tip relative to the sample, I_0 denotes the tunneling current neglecting spin polarization, and I_P is the term added to the current by spin polarization effects. The factor outside of the brackets stems from the calculation of the transition matrix elements in the Tersoff–Hamann approach, with the normalization coefficient C and the decay length within the tunneling barrier $\tilde{\kappa}$. Since the tunneling current depends on the integrated LDOS and magnetization DOS of the sample, it is dominated by the non-spin-polarized term I_0. Therefore, it is difficult to extract the spin-polarized information.

To simplify the separation of the spin-polarized information from the non-spin-polarized signal, one can use the differential conductance, which can be expressed by the following equation:

$$\begin{aligned} \frac{\mathrm{d}I}{\mathrm{d}U}(\boldsymbol{r}_\mathrm{t}, U) &\propto \rho_\mathrm{t}\rho_\mathrm{s}(\boldsymbol{r}_\mathrm{t}, E_\mathrm{F} + eU) + \boldsymbol{m}_\mathrm{t}\boldsymbol{m}_\mathrm{s}(\boldsymbol{r}_\mathrm{t}, E_\mathrm{F} + eU) \\ &= \rho_\mathrm{t}\rho_\mathrm{s}(\boldsymbol{r}_\mathrm{t}, E_\mathrm{F} + eU)\left[1 + P_\mathrm{t}P_\mathrm{s}(\boldsymbol{r}_\mathrm{t}, E_\mathrm{F} + eU)\cos(\Theta)\right] \end{aligned} \tag{2.17}$$

The crucial difference compared to the spin-polarized tunneling current is the dependence on the LDOS and on the local magnetization DOS of the sample at the energy $(E_\mathrm{F} + eU)$, instead of the dependence on the analogue integrated parameters.

To further emphasize on the spin-polarized information, one can calculate the magnetic asymmetry of the differential conductance $\tilde{A}(eU, \boldsymbol{r}_\mathrm{t})$, defined as:

$$\tilde{A}(eU, \boldsymbol{r}_\mathrm{t}) = \frac{\left[\frac{\mathrm{d}I}{\mathrm{d}U}(eU, \boldsymbol{r}_\mathrm{t})\right]_\mathrm{a} - \left[\frac{\mathrm{d}I}{\mathrm{d}U}(eU, \boldsymbol{r}_\mathrm{t})\right]_\mathrm{b}}{\left[\frac{\mathrm{d}I}{\mathrm{d}U}(eU, \boldsymbol{r}_\mathrm{t})\right]_\mathrm{a} + \left[\frac{\mathrm{d}I}{\mathrm{d}U}(eU, \boldsymbol{r}_\mathrm{t})\right]_\mathrm{b}} \tag{2.18}$$

Here, $\left[\frac{\mathrm{d}I}{\mathrm{d}U}(eU, \boldsymbol{r}_\mathrm{t})\right]_\mathrm{a}$ is the $\mathrm{d}I/\mathrm{d}U$ signal obtained with a magnetic field $\boldsymbol{H} = H\boldsymbol{e}_\mathrm{H}$ of a certain field strength H applied to the tip–sample system along a well-defined direction ($\boldsymbol{e}_\mathrm{H}$), and $\left[\frac{\mathrm{d}I}{\mathrm{d}U}(eU, \boldsymbol{r}_\mathrm{t})\right]_\mathrm{b}$ is the $\mathrm{d}I/\mathrm{d}U$ signal obtained with the same settings for the STM measurement but in a magnetic field of different strength and/or inverted direction. While in most cases the $\mathrm{d}I/\mathrm{d}U$ data will be obtained in two configurations with fields of the same strength but opposite directions, the exact design of the experiment concerning the sequence of the magnetic field ramps is based on the expected behavior of the tip–sample system.[6] The asymmetry can be calculated from spatially resolved $\mathrm{d}I/\mathrm{d}U$ maps as well as from energy resolved $\mathrm{d}I/\mathrm{d}U$ curves.

It is possible to calculate the polarization of the sample from the asymmetry [46]:

$$P_\mathrm{s}(eU) = \frac{\tilde{A}(eU, \boldsymbol{r}_\mathrm{t})}{P_\mathrm{t}\cos(\Theta)} \tag{2.19}$$

However, as seen from Equation 2.17, the $\mathrm{d}I/\mathrm{d}U$ signal depends on the position of the tip $\boldsymbol{r}_\mathrm{t}$ and, particularly, on the tip-sample distance z. In case of a constant current measurement, in return, the latter depends on the magnitude and relative orientation of tip and sample magnetization. This cross-talk of the tip–sample distance and the spin-polarized $\mathrm{d}I/\mathrm{d}U$ signal always has to be taken into account when interpreting SP-STS data. Over time, SP-STM/STS has been utilized in many different ways to obtain spin-polarized data on magnetic systems. A variety of articles covers the various techniques employed for this research area [46, 51–54].

[6] Details of the SP-STM experiments for this thesis will be given for each experiment individually.

2.2 X-Ray Absorption Spectroscopy (XAS) and the X-Ray Magnetic Circular Dichroism (XMCD)

X-ray absorption spectroscopy (XAS) is a versatile technique that can be used to investigate a variety of different properties of various systems. In the following, this field will be narrowed down to the aspects relevant for this thesis. The focus will be on utilization of the XMCD to investigate magnetic properties. For a more detailed introduction to XMCD please refer to [44, 55–57]. Various introductions to XAS from different points of view can be found in [58] and a comprehensive discussion of X-ray absorption fine structure (XAFS) can be found in [59]. The latter is the theoretical background needed to extract physical information from the measured data.

2.2.1 X-Ray Absorption Spectroscopy

In a general sense, XAS is a surface averaging technique that uses the interaction of light and matter to gather element specific information of various different kinds about the sample. The main interaction process is the absorption of photons by core electrons of sample atoms. Scattering processes such as Compton and Rayleigh scattering can usually be neglected for energies below 20 keV, which is the energy range relevant for XAS [56]. Absorption processes can occur when the photon energy equals or exceeds the binding energy of a core electron. In this case, the photon can be absorbed, and the electron is excited into an empty state above Fermi energy. Due to the short life time of the core level hole, an electron from an occupied state above the now empty core level will fall into this empty state. At the same time, the excess energy of the electron is emitted in form of a photon or by emission of a secondary electron (Auger electron). A specialty of the technique is the possibility to investigate not only surfaces but also bulk properties. Additionally, it can be applied to liquids, gases, as well as solids.

The essential parameter of all XAS experiments is the absorption coefficient $\mu(E)$[7] that characterizes the absorption of light by matter according to Beer's law[8] [55, 56, 62, 63]:

$$\mu(E)z = -ln(\frac{I^{\mathrm{X}}(z,E)}{I_0^{\mathrm{X}}(E)}) \tag{2.20}$$

Here, $I_0^{\mathrm{X}}(E)$ is the intensity of the incident X-ray beam of the energy $E = \hbar\omega$, and $I^{\mathrm{X}}(z,E)$ is the intensity of the beam inside the sample at the distance z from the sample surface along the axis of incidence. The absorption coefficient is a material specific parameter that varies with the energy of the photons.

There are three possible ways to obtain the energy dependence of the absorption coefficient during an XAS experiment. The direct calculation of $\mu(E)$ by the intensity of the transmitted beam requires samples thin enough for the X-ray beam to penetrate the sample. This method is mostly used for gaseous, liquid, or powder samples. A second variant is to measure the intensity of secondary photons, which are emitted during the recombination of excited electrons with the core level hole. However, because of the small probability for the emission of secondary photons, this method suffers from a relatively low signal. In the third variant, the total electron yield caused by the Auger electrons is measured. Since the Auger electrons obtain a finite kinetic energy and need to overcome the work potential of the sample in order to be registered, this method is limiting the potential of XAS to measure bulk properties. The electron yield Y is related to the absorption coefficient by the following equation [57]:

$$Y(E) \propto \int_0^\infty \mathrm{d}z I^{\mathrm{X}}(z,E)\mu(E)\exp(-\frac{z}{\Lambda}) \tag{2.21}$$

Here, Λ is the escape length of the electrons, defining the depth up to which their kinetic energy is large enough to overcome the work function of the sample after losing energy in multiple scattering processes on the way.

[7] H. Wende distinguishes between the absorption coefficient $\mu(E)$ and the attenuation coefficient $\tilde{\mu}(E)$ that includes scattering processes, which can, as stated above, be neglected in the X-ray regime considered for XAS [55]. However, most authors silently apply this assumption to Beer's law and only use the absorption coefficient.

[8] Also known as Bouguer-Lambert-Beer law [60], Lambert-Beer law [61] or other variants.

It remains the question, how to extract physical properties from the energy-dependent absorption coefficient. In general, μ is proportional to $\frac{1}{E^3}$ and, therefore, decreases with rising photon energy [64]. However, every time the energy of the photons reaches a value that equals the binding energy of a core electron of the sample, a new absorption channel becomes available, and a so-called absorption edge appears in the plot of μ versus the energy. Since the core level energies are distinctive for each element, the positions of the edges provide information about the composition of the sample. The edges are labeled according to the shell number n and spin–orbit quantum number j of the excited electrons. For this thesis, the L_{II} ($n = 2, j = 1/2$) and L_{III} ($n = 2, j = 3/2$) edges of Co, and the M_{IV} ($n = 3, j = 3/2$) and M_V ($n = 3, j = 5/2$) edges are relevant. The energy range after each edge is governed by oscillations, which contain further information. One distinguishes between the X-ray absorption near edge spectroscopy (XANES),[9] which considers the energy range from the step up to $\approx 30\,\text{eV}$ above the edge, and the extended X-ray absorption fine structure (EXAFS), which considers the energy range higher than $\approx 30\,\text{eV}$ above the edge. The XANES signal results from excitation of the electrons into bound states and hence contains information about the chemical environment of the atom, e.g. binding partners, and about the atom's magnetic properties, as we will see later in the discussion of the XMCD. For higher energies, the electrons can be excited into continuum or free states. The EXAFS signal therefore depends on interference effects and provides information about the geometrical surroundings of the atom, i.e. the crystallographic structure.

To extract the information about the sample from the behavior of the absorption coefficient in dependence of the photon energy, one has to understand the mechanisms of the interaction of photons with core electrons. Here, the basic physics behind these mechanisms necessary for the interpretation of XMCD data will be introduced.

[9] Sometimes also referred to as near edge X-ray absorption fine structure (NEXAFS).

The probability of a photon to interact with an atom is given by the atom's absorption cross section σ_{abs} related to the absorption coefficient by:

$$\mu(E) = \frac{\rho_m N_{\mathrm{A}}}{M_m} \sigma_{abs}(E) \tag{2.22}$$

Here, N_{A} is the Avogadro constant, ρ_{m} the material specific mass density, and M_{m} the molar mass. In a sample consisting of multiple different elements, μ corresponds to the sum over the absorption cross sections of the individual elements weighted by the respective atomic density within the sample. The absorption cross section is defined as the transition probability $\tilde{T}_{if}$ per unit time and photon flux Ψ_0^{X} and can be calculated by Fermi's golden rule under use of a perturbation approach [61, 65]:

$$\sigma_{abs}(E) = \frac{\tilde{T}_{if}(E)}{\Psi_0^{\mathrm{X}}} = \frac{2\pi}{\hbar \Psi_0^{\mathrm{X}}} \sum_{i,f} |M_{if}|^2 \rho(E_f) \delta(E - (E_f - E_i)) \tag{2.23}$$

Here, $M_{if} = \langle \Phi_f | \hat{H}_{\mathrm{int}} | \Phi_i \rangle$ is the transition matrix element for a transition from the initial state Φ_i to the final state Φ_f mediated by the interaction Hamiltonian $\hat{H}_{\mathrm{int}}$, the term $\rho(E_f)$ is the density of final states, and the delta function describes the energy conservation. The interaction Hamiltonian is based on the electromagnetic nature of the photons, which can be described by the Maxwell equations. For a detailed discussion of the interaction please refer to references [66, 67].

For the purpose of this thesis, several approximations can be made, which will be described in the following. As a first approximation for $\hat{H}_{\mathrm{int}}$, two-photon processes can be neglected. As stated above, scattering processes are not relevant in the energy range of XAS. Furthermore, in this energy regime the terms of $\hat{H}_{\mathrm{int}}$ containing only the B-field of the electromagnetic wave can be neglected. This leads to an interaction Hamiltonian:

$$\hat{H}_{\mathrm{int}}^{\mathrm{approx}} = \boldsymbol{\epsilon} \hat{\hat{\boldsymbol{P}}} \exp(i \boldsymbol{k} \boldsymbol{r}), \tag{2.24}$$

with the polarization of the photon $\boldsymbol{\epsilon}$, the momentum operator $\hat{\vec{\boldsymbol{P}}}$, and the position of the electron $\boldsymbol{r}$. It can be written in a Taylor expansion in the wave vector $\boldsymbol{k}$:

$$\hat{H}_{\text{int}}^{\text{approx}} = \boldsymbol{\epsilon}\hat{\vec{\boldsymbol{P}}} \exp(i\boldsymbol{k}\boldsymbol{r}) \approx \boldsymbol{\epsilon}\hat{\vec{\boldsymbol{P}}} \left[1 + i\boldsymbol{k}\boldsymbol{r} - \frac{1}{2}(\boldsymbol{k}\boldsymbol{r})^2 ...\right] \tag{2.25}$$

In the so-called dipole approximation, only the first term of this expansion is considered [67]. This approximation is valid when the radius of the absorbing atomic shell is small compared to the wave length of the photon, which is the case in the soft X-ray regime (0.12 keV−5 keV). Then the E-field caused by the photon can be considered constant over the shell volume ($\exp(i\boldsymbol{k}\boldsymbol{r}) \approx 1$). Using the relation with the commutator

$$\boldsymbol{\epsilon}\hat{\vec{\boldsymbol{P}}} = \frac{m_{\text{e}}}{i\hbar} \left[\boldsymbol{\epsilon}\boldsymbol{r}, \hat{H}_0\right], \tag{2.26}$$

where m_{e} is the mass of the electron and $\hat{H}_0$ is the Hamiltonian of the unperturbed electron and photon before the interaction, one finds for the transition matrix element:

$$M_{if} = \langle \Phi_f | \hat{H}_{int} | \Phi_i \rangle = i\frac{m_{\text{e}}}{\hbar}(E_f - E_i) \langle \Phi_f | \boldsymbol{\epsilon}\boldsymbol{r} | \Phi_i \rangle \tag{2.27}$$

Here, $E_{f/i}$ are the energy eigenvalues of the initial and final states corresponding to the unperturbed Hamiltonian $\hat{H}_0$. From this the dipole selection rules can be derived. These define the possible transitions the electron can undergo concerning the quantum numbers l and s and their projections [67]:

$$\Delta l = \pm 1 \tag{2.28}$$

$$\Delta m_{\text{l}} = 0, \pm 1 \tag{2.29}$$

$$\Delta s = 0 \tag{2.30}$$

$$\Delta m_s = 0 \tag{2.31}$$

Finally, a one-electron approximation can be applied to further define the meaning of the initial and the final states Φ_i and Φ_f [66, 68]. In reality, these states are multielectronic states describing all electrons within the atom that interacts with the photon. However, in the one-electron approximation these states can be

written as the product of N single electron wave functions $\Phi_{i/f} = \prod_n \varphi_n^{i/f}(r_n)$. Only one of the N core level electrons will interact with the photon, while the other electrons remain passive. Their effect, that is screening of the core hole and a resulting contraction of the final state atomic shell, can be summarized in a simple factor [66]:

$$S_0 = \prod_{n=2,N} \langle \varphi_n^f(r_n) | \varphi_n^i(r_n) \rangle \tag{2.32}$$

Additionally, the passive electrons cause a slight shift in energy of the initial and final state, so that Equation 2.27 becomes:

$$M_{if} = i\frac{m_\mathrm{e}}{\hbar} S_0(E_f - E_i + \Delta E_a) \langle \varphi_1^f | \boldsymbol{\epsilon r} | \varphi_1^i \rangle \,, \tag{2.33}$$

where ΔE_a is the sum of the energy shifts of the initial and final states.

2.2.2 X-Ray Magnetic Circular Dichroism (XMCD)

The term XMCD describes the difference in absorption of left μ_- and right μ_+ circularly polarized light[10] by samples with a magnetic moment in an external magnetic field. The first prediction of XMCD was made by Erskine and Stern in 1975 for the $M_{II,III}$ absorption edges of ferromagnetic Ni [69]. Later, in 1987, the prediction was confirmed experimentally by Schütz *et al.* for ferromagnetic Fe [70].

In 1994, Wu and Stöhr introduced a two-step model based on the one-electron approximation, as discussed above, to describe the mechanism of XMCD [71]. This model is depicted in Figure 2.4. In the first step, the electrons of the spin–orbit split 2p orbital[11] are excited by the incoming photons. During this excitation, the orbital moment of the photon is transferred to the electron. For the configuration

[10] Circularly polarized light is characterized by an electric field of constant magnitude rotating around the propagation direction. The polarization vector for circularly polarized light propagating along the z direction can be written as $\boldsymbol{\epsilon} = \frac{1}{\sqrt{2}} \begin{pmatrix} 1 \\ \pm i \\ 0 \end{pmatrix}$.

[11] The spin–orbit splitting is in fact not a property of the initial state but of the core hole that is created after excitation of an electron.

Table 2.1: Excitation probabilities for L_{II} and L_{III} edges of 3d transition metals:

absorption edge/core level	$L_{\mathrm{II}}/\mathrm{p}_{1/2}$		$L_{\mathrm{III}}/\mathrm{p}_{3/2}$	
helicity	spin-up	spin-down	spin-up	spin-down
$+\hbar$	25.0%	75.0%	62.5%	37.5%
$-\hbar$	75.0%	25.0%	37.5%	62.5%

used to obtain the data presented in this thesis, in which sample magnetization and wave vector are antiparallelly aligned, right-handed circularly polarized photons have a moment of $+\hbar$ and left-handed photons a moment of $-\hbar$. As shown by the dipole selection rules ($\Delta m_s = 0$), the orbital moment of the photon cannot influence the spin state of the excited electron. At the same time, because of spin–orbit coupling, photons excite spin-up and spin-down electrons with a different probability depending on their helicity and on the relative orientation of the electron's spin and orbital moment.

The probability for the excitation of an electron in a certain 2p core-level state can be calculated using Clebsch-Gordan coefficients and the transition matrix elements. This calculation is described in detail by I. Krug [72].[12] To understand the XMCD of the $L_{\mathrm{II/III}}$ edges of 3d transition metals, it is sufficient to know the total probability of a photon with helicity of $\pm\hbar$ to excite either a spin up or spin down electron from the $2\mathrm{p}_{1/2}$ and $2\mathrm{p}_{3/2}$ core levels. These probabilities are summarized in Table 2.1. Note that for the same core level the percentages for spin-up and spin-down electrons are simply exchanged for photons of opposite helicity.

Up to this point, the availability of final states has not been considered. In the second step, the spin- and orbital-momentum polarized, excited electrons probe the available final states. If a ferromagnetic 3d transition metal sample is considered, the final states are represented by the 3d conduction band. For this thesis, the final states will be molecular orbitals formed by the 3d states of the molecules spin center and the ligand orbitals as well as conduction bands formed by two atomic grids in

[12] The dissertation by I. Krug also contains a detailed depiction of the two-step model, similar to Figure 2.4. However, the high detail of the figure is unnecessary for the purpose of the thesis at hand.

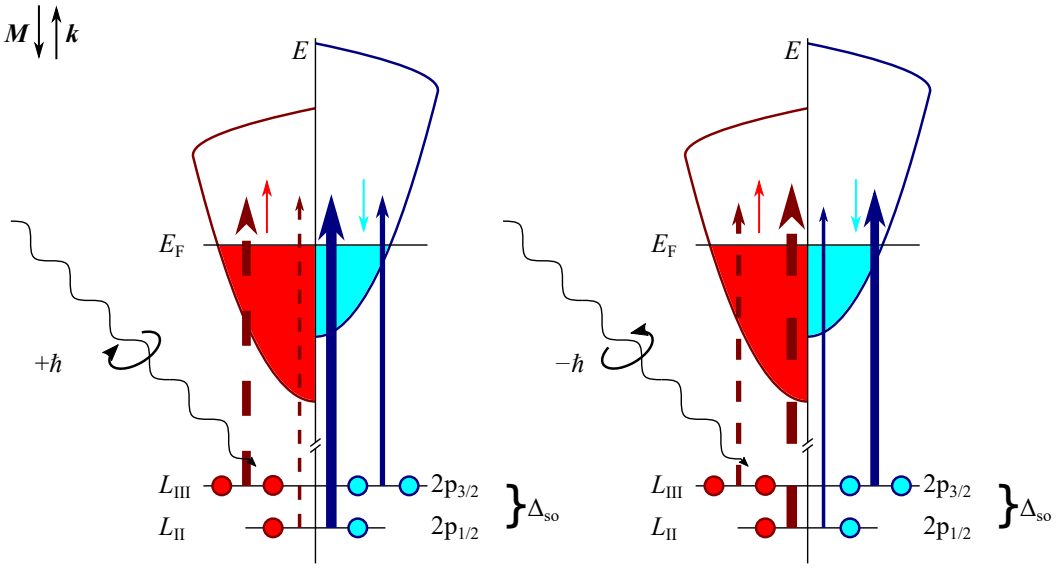

Figure 2.4: Graphical representation of XMCD in the two-step model introduced by Wu and Stöhr. On the left, the case for right-handed circular polarized light is shown and, on the right, for left-handed circular polarized light. The spin–orbit coupled core level $2p$ states for one atom of a ferromagnetic, metallic sample are shown. The $2p_{3/2}$ state is occupied by two spin-up (red) electrons and two spin-down (blue) electrons, while the $2p_{1/2}$ is occupied by only one electron of each spin state. Above the core level states, the simplified DOS for spin-up (red) and spin-down (blue) states of the quasi-free conduction electrons is plotted. Sample magnetization $\boldsymbol{M}$ and wave vector of the photons $\boldsymbol{k}$ are parallel. The colored arrows indicate possible excitations, with their thickness related to the probability of the excitation independent of the density of available final states (compare Table 2.1). Dotted arrows indicate excitation pathways that are suppressed due to a lower density of final states.

a $GdAu_2$/Au(111) surface alloy. Any polarization in spin or orbital momentum of these states will cause XMCD.

The theoretical background for the interpretation of XMCD data was developed by Thole *et al.* and Carra *et al.* with the so-called magneto-optical sum rules [73, 74]. In these sum rules, Thole, Carra, and coworkers harnessed the fact that the spin polarization of the excited electrons is opposite for the L_{II} and L_{III} edges, while the orbital momentum polarization is the same. They can be used to separately calculate the components of the spin magnetic moment $\boldsymbol{M}_{\mathbf{S}}$ and the orbital magnetic moment $\boldsymbol{M}_{\mathbf{L}}$ parallel to the incident X-ray beam [55, 75]:

$$\boldsymbol{M}_{\mathbf{S}||}\hbar = -3N_{\mathrm{h}}\frac{\int_{L_{\mathrm{III}}}(\mu_+ - \mu_-)\mathrm{d}E - 2\int_{L_{\mathrm{II}}}(\mu_+ - \mu_-)\mathrm{d}E}{\int_{\mathrm{L_{III}+L_{II}}}(\mu_+ + \mu_- + \mu_0)\mathrm{d}E}\mu_{\mathrm{B}} + 7\left\langle\hat{\boldsymbol{T}}_{||}\right\rangle\mu_{\mathrm{B}} \tag{2.34}$$

$$\boldsymbol{M}_{\mathbf{L}||}\hbar = -2N_{\mathrm{h}}\frac{\int_{L_{\mathrm{III}}}(\mu_+ - \mu_-)\mathrm{d}E + \int_{L_{\mathrm{II}}}(\mu_+ - \mu_-)\mathrm{d}E}{\int_{\mathrm{L_{III}+L_{II}}}(\mu_+ + \mu_- + \mu_0)\mathrm{d}E}\mu_{\mathrm{B}} \tag{2.35}$$

Here, μ_+, μ_-, and μ_0 are the measured absorption coefficients with the photon angular momentum vector parallel, antiparallel, and perpendicular to the magnetic field, respectively. The integral of all three absorption coefficients in the denominator gives the unpolarized X-ray-absorption spectrum. The integrals in the nominator are over the energy range of the L_{II} or the L_{III} edge; the integral in the denominator over both. μ_{B} denotes Bohr's magneton and N_{h} the number of available final states per atom, which is in case of a 3d transition metal the total number of 3d states minus the number of occupied 3d states. To obtain the spin magnetic moment, the expectation value of the magnetic dipole operator's component parallel to the incident X-ray beam $\left\langle\hat{\boldsymbol{T}}_{||}\right\rangle$ has to be known. This term is accounting for a possible asphericity of the spin density distribution and a resulting anisotropy of the spin magnetization. It can be caused either by spin-orbit coupling or field effects due to charges surrounding the investigated ion, i.e. crystal- or ligand-field effects. If the value of $\left\langle\hat{\boldsymbol{T}}_{||}\right\rangle$ is not known, usually an effective spin magnetic moment $\boldsymbol{M}_{\mathbf{S,eff}} = \boldsymbol{M}_{\mathbf{S}||} - 7\left\langle\hat{\boldsymbol{T}}_{||}\right\rangle\mu_{\mathrm{B}}$ is calculated in experiments.

In an experiment, one must consider several approximations that were made by Thole and Carra as well as artifacts in the data. For example, the excited electrons do not probe the 3d electrons exclusively but also higher lying states. Usually, this

is taken into account by subtracting step functions from the measured absorption coefficient before integration. Another source of error might be too small spin–orbit splitting, insufficient to totally separate the two absorption edges. However, a detailed discussion of these considerations would go beyond the scope of this thesis, but an overview can be found in the work by Chen *et al.* [76].

Since the XMCD depends on the relative orientation of the photons' helicity and the sample magnetization, it is arbitrary if the experiment is carried out by reversing the X-ray beam's polarization or the sample's magnetization. The sensitivity of the XMCD on in-plane or out-of-plane magnetization can be tuned by changing the incidence axis. Normal incidence leads to an out-of-plane contrast, while a gracing incidence with a small angle between the sample and the X-ray beam maximizes the sensitivity towards an in-plane magnetic moment. It has to be noted, however, that a measurement of the pure in-plane magnetization is not possible.

2.3 On-Surface Chemistry

On-surface chemistry is a wide field covering a plethora of processes in biology, chemistry, and physics. A general overview of this field and its impact on industry and research can be found in the review article by Somorjai and Li [77]. While in general on-surface chemistry includes solid–liquid interfaces, these will be neglected here. First aimed at harnessing catalytic properties of surfaces or modifying and functionalizing surfaces by adsorption of molecules in a structured manner, it soon became apparent that on-surface chemistry has multiple advantages for the synthesis of novel molecular complexes. Due to advances in investigation techniques especially on small scales, as for example STM, the understanding of chemical processes at the molecular level got enhanced. This led to the development of on-surface coordination chemistry [78, 79].

Compared to the traditional wet synthesis, on-surface chemical reactions provide several advantages. Typically, on-surface chemical reactions are done *in situ* under ultra-high vacuum conditions. Therefore, the cleanness of the sample can be easily controlled. Difficult processes needed to separate the product from solvents

as well as the exposure to an ambient environment, possibly causing impurities, are avoided. Furthermore, deposition procedures supposing a risk of defragmentation, especially for large, complex structures, are performed on the more robust precursors instead of the typically more complex products.

The main feature of on-surface coordination chemistry, however, is the discovery of new reaction pathways. The surface stabilizes metastable states that would not be stable in a solution. Moreover, it allows for a wider range of reaction temperatures since solvent decomposition is no problem. Therefore, on-surface chemistry gives access to new materials as for example two-dimensional organic or organometallic networks. The following chapter will focus on two processes of on-surface chemistry, i.e. Ullmann reactions and metalation. The section about on-surface metalation will be partly adapted from [80].

2.3.1 The Ullmann Reaction

The Ullmann reaction, discovered by F. Ullmann in 1901 [81], originally employed Cu powder to synthesize biaryls from aryl halides. However, multiple techniques of aryl–aryl bond formation using different metals have been developed over time [82]. For this work, the on-surface Ullmannn reaction, as first reported by Xi and Bent, is the most relevant [83, 84]. Today, this variant of the Ullmann reaction is widely known and used for example to create polymeric chains, organic networks, and graphene nanoribbons on various surfaces [85–90].

For this type of reaction, the precursors are deposited onto a surface under vacuum or ambient conditions or at a solid-liquid interface. A catalyst is provided either in form of surface atoms or co-adsorbed adatoms. Most common catalysts are the coinage metals Au, Ag, and Cu, usually presented as surface atoms of a metallic crystal, but also Pt, Pd, Ni, and Co have been used to catalyze Ullmann reactions. The activation energy can be provided by an electric pulse from an STM tip [91], by annealing of the sample [92], or by light [93, 94]. The amount of activation energy needed depends on the used catalyst, the halogen, and the structure of the surface, e.g. surface reconstructions, number of defects, and step edges. In some cases,

e.g. 3,9–diiododinaphtho[2,3–b:2',3'–d]thiophene on Ag(111), a partial Ullmann reaction can even occur on cold surfaces (below 150 K) without any further energy input [95]. On Co islands on Cu(111), cleavage of Br from benzylbromide has been observed already at temperatures of 80 K and even C–C bonds have been observed for a small fraction of molecules at this temperature [96]. In this case, the Ullmann reaction was found to be completed at 160 K. Due to the differences in energy needed for the cleavage of the different halogen atoms, it is possible to design sequential reactions to have an increased control over the product of the reactions [97].

Usually, the reaction is described as a two-step process: First the cleavage of the halide from the aryl and second the bond formation between the two aryls. However, the exact mechanism depends on the choice of the precursors and the catalyzing metal [98, 99]. The crucial point is whether a metastable metal–organic phase is formed or not. In this phase, the aryls are bonding to metal atoms, forming C–metal bonds. The stability of the metal–organic phase depends on the energy barriers of the two reaction steps [98]. If the barrier that needs to be overcome to cleave the halide from the aryl halides is larger than the energy barrier to form the aryl–aryl bond, which is typically the case on Au(111), the metal–organic phase will be quasi nonexistent. At the same time, if the barrier for the formation of the aryl–aryl bond is very large, the formation of a stable metal–organic phase is destined.

If a metastable metal–organic phase is created during the reaction, the question remains in which configuration it is formed. The organic radicals can either bond to an atom embedded into the top layer of the substrate or the atom can be dragged out of the surface into the plane of the two molecules [99]. Metastable metal–organic phases are typically formed on Ag(111) substrates [95] as well as on Cu(111) substrates [100, 101] and on Co islands on Cu(111) [96]. The occurrence of a metal–organic phase and its geometrical configuration can have a large impact on the formation of a polymer or organic network. If the molecules are bonded to atoms embedded into the substrate surface, their mobility is strongly decreased, which reduces the size of the obtained products. If the metal–organic phase is energetically preferred instead, the aryl–aryl bond formation can be completely

suppressed as shown for Dy catalyzed dehalogenation of 4,4"–dibromo–p–terphenyl on Ag(111) [102].

Another interesting aspect are the whereabouts of the halide atoms after the reaction. In many cases the atoms will desorb from the surface due to the annealing needed for the activation of the Ullmann reaction. However, in some cases, where the interaction of the halides with the sample is strong enough, they might cause pollution of the sample and even intercalate the created organic networks [103].

Recently, Ullmann reactions for two precursors have been reported for a $GdAu_2$/Au(111) surface alloy [104]. Following this publication, Que *et al.* reported Ullmann coupling of precursors for the creation of graphene nanoribbons and a consecutive cyclodehydrogenation on a $TbAu_2$/Au(111) surface alloy [105]. For the sake of completeness, it has to be noted that an Ullmann-like coupling reaction has been reported for the bulk insulator calcite without any metallic catalyst [106]. However, for this reaction relatively high temperatures of 520 K are needed. Because of this high temperature in combination with the typically low desorption energies of molecules on insulating substrates, complicated anchoring groups are required to stably adsorb the molecules.

2.3.2 On-Surface Metalation of Organic Molecules

Metalation is the reaction of individual organic molecules with single metal atoms to form organo-metallic complexes. The on-surface pathway of metalation is a redox reaction in which a metal atom is embedded into the ligand, while two hydrogen atoms are released as H_2. The first on-surface-metalation experiments were reported by Gottfried *et al.* in 2006 [107] and by Auwärter *et al.* in 2007 [108].

In the beginning, metalation studies concentrated on porphyrins [107–109], phthalocyanines [110], and their derivatives. An extensive review of the research on these molecules has been given by Gottfried [111] with chapter six being dedicated to on-surface metalation. Lately, also pyrphyrins [112], corroles [113], and salophens [80] have been metalated successfully. The vast majority of metalation experiments were performed with transition metals but also metalation with rare

earth metals such as Ce is possible [114, 115]. There are four methods to supply the metal for the metalation: Firstly, one being the so-called self-metalation of organic molecules with atoms from the substrate surface [112, 116, 117], secondly, the metalation with a metal atom from a STM tip [118], and two others by metalating molecules with either pre- [116, 119] or postdeposited [107–109, 113, 116, 119] metal atoms.[13]

Metalation reactions were found to occur at different temperatures. While some reactions occurred already at room temperature [109, 117] or even below [122], a temperature of up to 500 K has been necessary for the creation of double-decker complexes [123]. To understand these differences, the mechanism of the on-surface metalation reaction has been investigated by Shubina *et al.* in a DFT study for the metalation of porphyrin in its gas phase with various metals [109]. They found that the metal atom first binds to the N atoms of the porphyrin after which the H atoms consecutively bind to the metal atom before they desorb as H_2. In this mechanism, the intramolecular transfer of the H atoms from the ligand to the metal atom has the highest activation barrier and is therefore the limiting step.

Later, Bao *et al.* did simulations including a Ag(111) surface for the on-surface metalation of phthalocyanine-based molecules and found that the surface takes part in the stabilization of the H-atoms during the reaction and the release from the complex [124]. They found that in a so-called 'dropping-down' pathway the metal can react with the ligand molecule without overcoming an activation energy barrier. Therefore, depositing the metal onto a sample of the prepared ligand would require lower temperatures to activate the metalation reaction. However, while in their calculations the metal atom was placed directly above the cavity of the phthalocyanine, in a real experiment most of the atoms will need to diffuse towards this position after hitting the sample in a random place. Their calculations showed that in the latter case the metal atoms need to overcome an energy barrier caused by the molecule hindering the diffusion of the atom into the position of the molecule's cavity. Nevertheless, it remains an important finding that the surface can help in the release of the H atoms. The temperature needed for the reaction is

[13] In some cases the metal atoms are provided embedded in an organo-metallic complex [120, 121].

therefore mainly determined by the ability of the metal center and the substrate to remove the hydrogen atoms from the complex and the energy needed by the metal atom to diffuse to the cavity of the molecule. So far metalation has only been reported on metal and oxide surfaces with a lower yield on the oxide surfaces [125, 126]. For the sake of completeness, it has to be mentioned that demetalation [127] or the exchange of an established metal center with a different metal [128], despite being rare, have been observed.

3 Magnetism in Molecules

The vast majority of molecules are diamagnetic, meaning they have an even number of electrons, which form pairs with their spins antiparallelly aligned. For the field of molecular spintronics, molecules that bear a magnetic moment caused by one or more unpaired electrons are needed. These can be purely organic radicals or metal–organic complexes containing transition metals or rare-earth elements as magnetic centers. In this thesis, only metal–organic molecules with 3d transition metals will be investigated. The present chapter will give a brief introduction to the description of 3d transition metal–organic complexes and their properties, focusing on magnetic properties and intramolecular magnetic interactions. Additionally, theories for the description of the electronic structure, mainly of molecular systems but also of solids, will be presented, in particular DFT. In the last section, salophen complexes will be introduced. These complexes stand in the focus of this thesis. A more detailed general overview of the magnetic and electronic properties of molecules can be found in reference [129, 130], on which the present chapter is based. Additional introductions focused on magnetic properties can also be found in [131] and for metal–organic compounds of 4f metals in [132].

3.1 Atomic Orbitals

Electrons in a free atom can be described by the following Hamiltonian, written in atomic units:

$$\hat{H} = -\frac{1}{2}\sum_i \nabla_i^2 + \sum_i V_{Ne}(\boldsymbol{r}_i) + \sum_{i\neq j} V_{ee}(\boldsymbol{r}_i, \boldsymbol{r}_j) \tag{3.1}$$

Here, the first sum represents the kinetic energy of the electrons, the second sum gives the potential energy due to the interaction with the nucleus, and the third term adds the potential energy resulting from the interaction of the electrons with each other. V_{Ne} is the nuclear potential energy and V_{ee} the electron potential energy. This Hamiltonian is obtained from the Hamiltonian describing a system consisting of N electrons and M nuclei, which will be later described in Section 3.3, by considering only one nucleus and adapting the Born-Oppenheimer approximation [133, 134]. This approximation states that because of the high mass of the atomic nucleus compared to the electron mass their positions are fixed in space. Therefore, the kinetic energy of the nuclei is assumed to be zero, and the potential they create for the electrons is considered to be constant.

The possible solutions for the resulting Schrödinger equation are wave functions characterized by the quantum numbers n, l, and m_{l}, which correspond to the number of the shell (principal quantum number), the orbital angular moment (azimuthal quantum number), and the z-component of the orbital moment (orbital magnetic quantum number), respectively. The orbital angular moment of a given shell with the principal quantum number n can take values from $l = 0$ to $l = n - 1$ and the value of m_{l} can range from $-l$ to l. Figure 3.1 shows a graphical representation of s, p, and d orbitals, with $l = 0, 1, 2$, respectively. It should be noted that these are very simplified depictions of atomic orbitals, which are not scientifically correct. However, they help to understand the spatial orientation of the individual orbitals. Each atomic orbital can be occupied by a maximum of two electrons with antiparallelly aligned spins, following the Pauli principle. For a free atom, all states with the same quantum numbers n and l are degenerate.

The order in which the atomic orbitals are filled is given by the so-called Hund's rules [135, 136]:

- In the ground state, the atomic spin quantum number S is maximized.
- In the ground state with maximum S, the atomic angular momentum quantum number L is maximized.

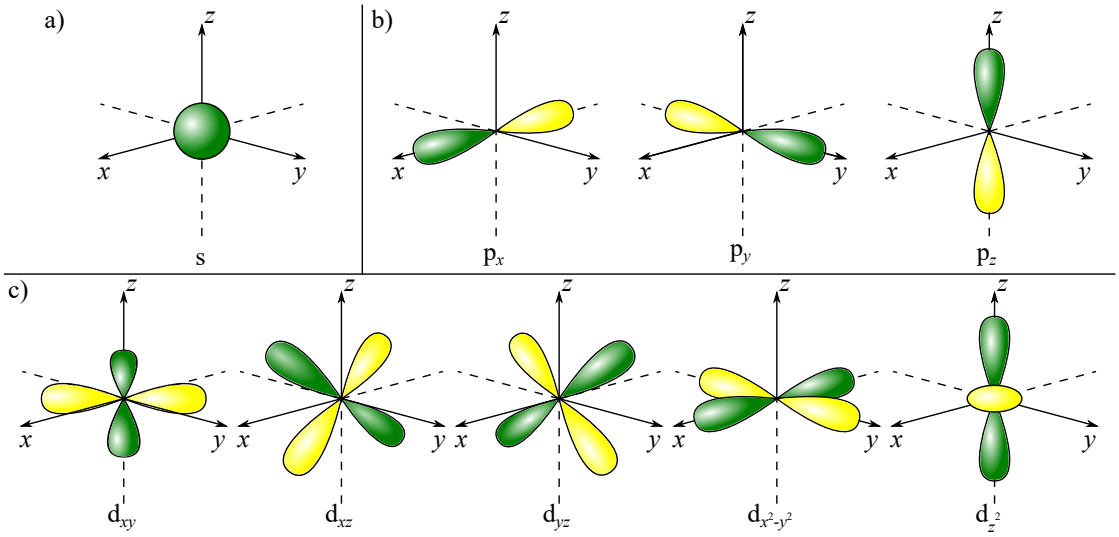

Figure 3.1: Schematic representations of atomic s, p, and d orbitals. Green and yellow colors indicate different phases of the spatial wave functions.

- In the ground state, $J = |L + S|$ is minimized if the shell is less than half-full and maximized if the shell is more than half-full.

Here, $L = \sum_i l_i$ and $S = \sum_i s_i$ are the atomic azimuthal and the atomic spin quantum number obtained by summing over the respective quantum numbers of the individual electrons within an atom. J is the atomic total angular momentum quantum number defined as the sum over the spin and orbital quantum numbers. It should be noted here that the physics causing the first rule by Hund will be important for the discussion of intramolecular magnetic exchange in Section 3.5.1. However, in the case of a metal atom embedded in an organic ligand, the ligand has a big impact on the energies of the electronic states of the metal atom and, therefore, on the filling order and the resulting magnetic moment.

3.2 Crystal Field Theory and Ligand Field Theory

A first approximation of the effect a ligand has on the 3d states of a metal atom can be obtained in the framework of purely electrostatic crystal field theory (CFT), based on the work of Bethe in 1929 [137]. More detailed introductions can be

found in references [138–140] and reference [141] in chapter 1.6. In CFT, each ligand atom bonded to the metal atom is represented by a local negative charge acting on the electrons in the 3d metal atomic orbitals. These negative charges destabilize the electronic states of the metal atom depending on their symmetry. In Figure 3.2, the effect is shown for a metal atom in an octahedral and a square-planar configuration, with six and four identical ligand atoms, respectively.

The octahedral configuration leads to a larger destabilization of the d_{z^2} and the $d_{x^2-y^2}$ orbital compared to the d_{xy}, d_{xz}, and d_{yz} orbital. While the two first-mentioned orbitals are aligned along the main axes pointing directly towards the ligand atoms, the other three are positioned at 45° off the main axes (compare Figure 3.1). Therefore, these three orbitals avoid the ligand atoms and their repelling effect.

In the square-planar configuration, the ligand atoms on the z-axis are removed. Because of the reduced total charge acting on the electrons of the metal ion, the center of gravity of the 3d-orbital energies[1] is shifted by only two thirds of the shift it experiences in the octahedral configuration. Furthermore, the energies of the orbitals with a large z-component, i.e. the d_{z^2}, the d_{xz}, and the d_{yz} orbital, are lowered. At the same time, the positive effective charge of the metal's nucleus is increased because of the removal of the negative charges on the z-axis. This leads to a narrowing of the distances between the metal atom and the ligand atoms. Therefore, the d orbitals strongly interacting with the remaining ligand atoms, i.e. $d_{x^2-y^2}$ and d_{xy}, experience an increase in energy. It has to be noted that the orientation of the complex versus the coordinate system is arbitrary. The geometry presented in Figure 3.2 is most common in literature, but also a geometry rotated by 45° can frequently be encountered. This can be seen for example when comparing Figure 1 of reference [142], where the traditional orientation is used, with Figure 1 of references [143] or [144], where the rotated orientation is used.

However, CFT is an approximation not taking into account the overlap of the metal and ligand orbitals as well as the delocalization of the electrons. A more

[1] The center of gravity, in this context, describes the energy the orbitals would have in a spherically symmetric charge distribution.

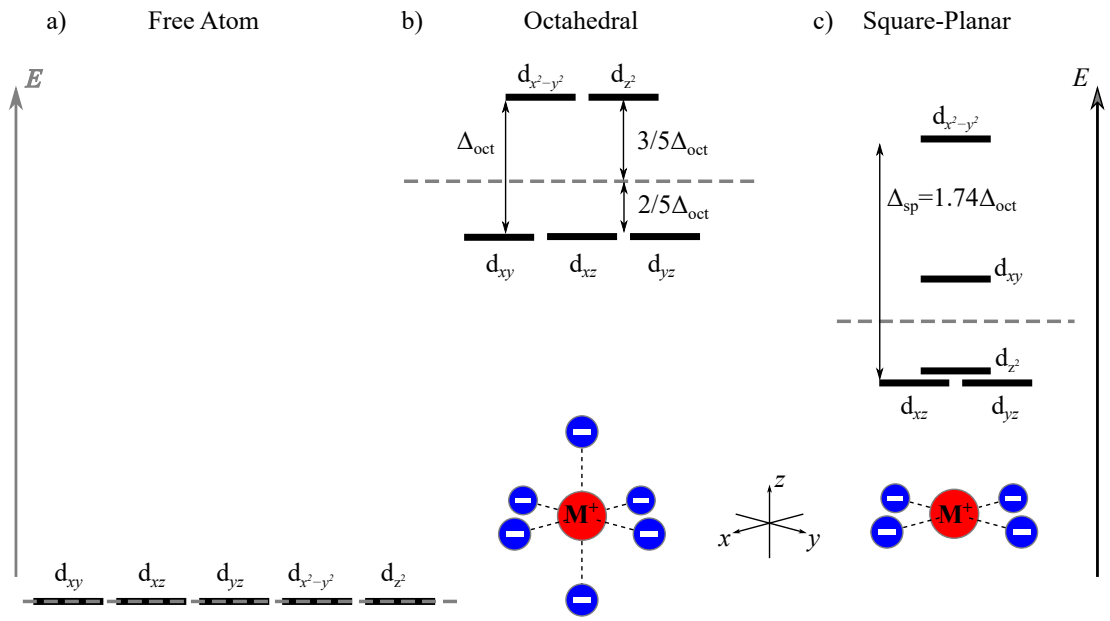

Figure 3.2: Crystal field effects on the 3d orbitals of a) a free metal ion, b) a metal ion in an octahedral ligand, and c) in a square-planar ligand. Dashed lines indicate the centers of gravity (energy in a spherically symmetric charge distribution) of the 3d orbital energies. Note the different energy scales for the position of the centers of gravity and the splitting of the orbitals. This means that when looking at the different configurations a), b), and c), one can only compare the difference in energy of the individual states but not their absolute position. Graphical depictions of the octahedral and the square-planar geometry and the chosen coordinate system are shown in the lower right.

exact description of the problem is provided by ligand field theory (LFT),[2] which is based on the molecular orbitals—linear combination of atomic orbitals theory (MO-LCAO). This theory was developed originally by Hund and Mulliken [145]. Exhaustive introductions to LFT can be found in references [138, 140] and chapter 1.3.6 of reference [129].

In this theory, orbitals of the metal atom are combined with orbitals of the ligand to form molecular orbitals (molecular orbitals (MOs)). Each combination of a metal and a ligand orbital leads to the formation of a bonding MO, with an energy below both of the individual orbitals, and an antibonding MO, with a higher energy. Since the ligand orbitals typically are lower in energy than the orbitals of the metal atom, bonding MOs have a higher electron density on the ligand and antibonding MOs on the metal atom. For transition metals with the nth d shell being the open shell, always the nd, $(n+1)$s, and $(n+1)$p orbitals are taken into account for the calculation of the MOs. The choice of the ligand orbitals depends on the character of the ligand. In the simplest case of a purely σ-type bonding ligand, only σ orbitals are taken into account. For ligands with a π-donator or π-acceptor character, also the respective ligand orbitals have to be considered. The possible combinations of metal and ligand orbitals are defined by the symmetry properties of the atomic orbitals.

The energies of the MOs can be calculated by using the angular overlap model (AOM) [140, 146, 147]. Since these calculations are usually challenging and can lead to different results, they are combined with experimental studies as for example electron paramagnetic resonance (EPR)[3] [148] and electronic spectroscopy [140], in which the distances in energy between the states can be determined. For coordination complexes with high symmetry, i.e. octahedral and tetrahedral symmetry, CFT and LFT give results of good qualitative agreement concerning the order of the predominantly metallic states around Fermi energy. However, especially for complexes of lower symmetry, LFT gives better solutions for the energies of the orbitals.

[2] It has to be noted that the term ligand field theory is also used to describe the whole field of theories describing ligand effects in coordination chemistry. Some authors even refer to crystal field theory as a ligand field theory.

[3] Sometimes also named ESR for 'electron spin resonance'.

The filling sequence of the states is governed by two competing effects. On the one hand side, the electrons tend to occupy different states with their spins aligned parallelly (compare Hund's first rule, Chapter 3.1). On the other hand, the electrons fill the states with lower energy first. Which of the two competing effects governs the filling order is determined by the resulting energy differences between the states, which is called crystal field splitting or ligand field splitting Δ. For a large splitting, the electrons tend to occupy the low lying states (low spin regime) and, for a small splitting, the electrons will distribute among all states before forming pairs due to Hund's first rule. The magnitudes of the splitting energies depend on the metal ion and the ligand. A so-called spectrochemical series sets different ligands into relation with their respective crystal field splittings.

Nowadays, with DFT, a tool is available to *ab initio* calculate the MOs and their energy eigenvalues in form of Kohn–Sham orbitals, as will be described in the following section. However, also DFT relies on experimental data to validate the results. The filling order for the electrons defines the magnetic moment of the molecule since it is caused by the sum of the spin and orbital magnetic moment of the electrons.

3.3 Density Functional Theory (DFT)

To describe a system consisting of N electrons and M nuclei, one can use the following Hamiltonian:

$$\begin{aligned}\hat{H} = &-\frac{\hbar^2}{2m_\mathrm{e}}\sum_i^N \nabla_i^2 - \frac{\hbar^2}{2}\sum_\alpha^M \frac{1}{m_\alpha}\nabla_\alpha^2 \\ &-\sum_i^N\sum_\alpha^M \frac{e^2}{4\pi\epsilon_0}\frac{Z_\alpha}{r_{i\alpha}} + \frac{1}{2}\sum_{i\neq j}^N \frac{e^2}{4\pi\epsilon_0}\frac{1}{r_{ij}} + \frac{1}{2}\sum_{\alpha\neq\beta}^M \frac{e^2}{4\pi\epsilon_0}\frac{Z_\alpha Z_\beta}{r_{\alpha\beta}}\end{aligned} \tag{3.2}$$

Here, $\nabla_{i/\alpha}^2$ denotes the Laplacian operator with respect to the coordinates of the ith electron or the αth nucleus, m_α the mass of the αth nucleus, Z_α the number of protons in the nucleus, and ϵ_0 the permittivity constant. The values r_{ij}, $r_{\alpha\beta}$, and $r_{i\alpha}$ denote the distances between the electrons and nuclei indicated by the

indices i/j and α/β, respectively. In literature, the Hamiltonian in Equation 3.2 is often written in atomic units rather than SI-units [134]. The notation in atomic units will also be applied in the remainder of this section. As mentioned above, the Hamiltonian can be simplified by using the Born-Oppenheimer approximation [133, 134]. This approximation states that, due to the high mass of the atomic nuclei compared to the electron mass, their positions are fixed in space. Therefore, the kinetic energy of the nuclei is assumed to be zero, and the potential they create for the electrons is considered to be constant, which has to be added to the electronic energy to obtain the total energy of the system.

The main difficulty in calculating solutions to Schrödinger's equation with the above Hamiltonian, after applying the Born–Oppenheimer approximation, is given by the term describing the electron–electron interactions. A lot of effort has been put into finding proper approximations to solve these equations. There are two main branches of theories focusing on calculating the correct wave functions, the valence bond theories and the molecular orbital theories. An overview of these theories can be found in [129]. A prominent example is the Hartree–Fock method [134].

DFT, instead, uses the electron density $\rho_\mathrm{e}(\boldsymbol{r})$[4] as the central quantity. The advantage of this theory is the limited dimensionality of the problem. While the wave function, describing a system with N electrons, depends on $3N$ spatial coordinates plus N spin coordinates, the electron density is always three-dimensional. Therefore, the computational effort is drastically reduced compared to the wave-function-based approaches. The electron density is defined as the integral of the wave function, over all spatial coordinates but one and over all spin coordinates of the N electrons of the system, multiplied with the number of electrons [149]:[5]

$$\rho_\mathrm{e}(\boldsymbol{r}) = N \int |\psi(\boldsymbol{x}_1, \boldsymbol{x}_2, ...\boldsymbol{x}_N)|^2 \, \mathrm{d}s_1 \mathrm{d}\boldsymbol{x}_2 ... \mathrm{d}\boldsymbol{x}_N \tag{3.3}$$

[4]The subscript is introduced to distinguish the electron density from the DOS used in previous sections.

[5]In literature, the electron density is sometimes written as $n(\boldsymbol{r})$. In the same instance, the electrons' spin degree of freedom often is neglected and the integral (compare Equation 3.3) is only over the $N-1$ spatial coordinates $\boldsymbol{r}_i$. This is for example the case in the two cited review articles [150, 151].

Here, $\boldsymbol{x}_i \equiv \boldsymbol{r}_i, s_i$ is the combined spatial and spin coordinate of the ith electron. The value of $\rho_\mathrm{e}(\boldsymbol{r})$ is never negative and gives the probability to find any single electron of the system at position $\boldsymbol{r}$. It has maxima at the positions of the nuclei and decreases exponentially with the distance to them. Integrating the electron density over the whole space gives the total number of electrons. Another aspect is that the electron density can be measured for example by X-ray diffraction.

Historically, the first model of a DFT was introduced by Thomas and Fermi [152–154]. While the Thomas-Fermi model never attracted a lot of interest – due to its inaccuracy – it was the first theory to formulate an expression for the atomic energy solely depending on the electron density. However, at that time it had not been proven that the electron density sufficiently defines the system to derive all properties for it.

In the following, the key points of the modern DFT will be summarized. For a comprehensive introduction, please refer to [154, 155] or the review articles [150, 151]. DFT, as it is used today, is based on the work by Hohenberg and Kohn [156] and Kohn and Sham [157]. In their publication from 1964, Hohenberg and Kohn introduced two theorems which are forming the basis of DFT. The first theorem states that for each system of interacting bound electrons there exists a functional of the electron density $F_\mathrm{HK}\left[\rho_\mathrm{e}\right]$ which, up to a constant, uniquely defines the external potential V_ext. Furthermore, the Hamiltonian and, therefore, the ground state energy E_0 of the system are defined by fixing the external potential. They proved this theorem for ground states ψ_0 by a simple *reductio ad absurdum*, which can be found in the various cited references and will not be reproduced here [155, 156].

Following these considerations, the ground state energy can be written as a functional of the electron density, consisting of the three contributions remaining after the Born–Oppenheimer approximation:

$$E_0\left[\rho_\mathrm{e}\right] = E_{Ne}\left[\rho_\mathrm{e}\right] + E_\mathrm{kin}\left[\rho_\mathrm{e}\right] + E_{ee}\left[\rho_\mathrm{e}\right] = \int \rho_\mathrm{e}(\boldsymbol{r}) V_{Ne}(\boldsymbol{r}) \mathrm{d}\boldsymbol{r} + F_\mathrm{HK}\left[\rho_\mathrm{e}\right] \tag{3.4}$$

Here, E_{Ne} is the potential energy related to the external potential V_{Ne} created by the nuclei, E_kin is the kinetic energy and E_{ee} is the potential energy due to electron–electron interaction. The so-called Hohenberg-Kohn functional $F_\mathrm{HK}\left[\rho_\mathrm{e}\right]$

summarizes the contributions that are independent of the external potential and therefore universal for any system. It is often referred to as 'The holy grail of DFT', since an exact expression of this functional would enable to calculate exact solutions of the Schrödinger equation with DFT.

The second theorem states that the sum of $F_{\mathrm{HK}}[\rho_{\mathrm{e}}]$ and $E_{Ne}[\rho_{\mathrm{e}}]$ gives the ground state energy of the system only when the electron density equals the electron density of the ground state. This follows simply from the application of the well-known variational principle to $F_{\mathrm{HK}}[\rho_{\mathrm{e}}]$ [158]:[6]

$$E_0 \leq E[\tilde{\rho}_{\mathrm{e}}] = E_{Ne}[\tilde{\rho}_{\mathrm{e}}] + E_{\mathrm{kin}}[\tilde{\rho}_{\mathrm{e}}] + E_{ee}[\tilde{\rho}_{\mathrm{e}}] \tag{3.5}$$

This means that the energy obtained for a randomly guessed electron density $\tilde{\rho}_{\mathrm{e}}$ gives an upper boundary for the ground state energy. With this proof confirming that the idea behind DFT — to get all information about a system of bound electrons from the electron density — is correct, one can now proceed to search for strategies enabling to find the correct ρ_{e} and a proper approximation for $F_{\mathrm{HK}}[\rho_{\mathrm{e}}]$.

With their publication from 1965, Kohn and Sham introduced an approach to obtain an approximation of $F_{\mathrm{HK}}[\rho_{\mathrm{e}}]$ [157]. The central idea revolves around an expression for the kinetic energy part $E_{\mathrm{kin}}[\rho_{\mathrm{e}}]$ of $F_{\mathrm{HK}}[\rho_{\mathrm{e}}]$ leaving only an expression of small contribution behind to be approximated.

They started from an expression that stood at the end of the previous work by Hohenberg and Kohn:

$$E_0[\rho_{\mathrm{e}}] = \int \rho_{\mathrm{e}}(\boldsymbol{r}) V_{Ne}(\boldsymbol{r}) \mathrm{d}\boldsymbol{r} + \frac{1}{2} \int\int \frac{\rho_{\mathrm{e}}(\boldsymbol{r}_1)\rho_{\mathrm{e}}(\boldsymbol{r}_2)}{r_{12}} \mathrm{d}\boldsymbol{r}_1 \mathrm{d}\boldsymbol{r}_2 + E_{\mathrm{kin}}[\rho_{\mathrm{e}}] + E_{\mathrm{ncl}}[\rho_{\mathrm{e}}] \tag{3.6}$$

Compared to Equation 3.4, here, the electron-electron interaction energy $E_{ee}[\rho_{\mathrm{e}}]$ is split into the classical Coulomb interaction $J_{\mathrm{C}}[\rho_{\mathrm{e}}]$, which equals the second summand of the equation, and the non-classical remainder $E_{\mathrm{ncl}}[\rho_{\mathrm{e}}]$. Next, they suggested to approximate the kinetic energy $E_{\mathrm{kin}}[\rho_{\mathrm{e}}]$ by the kinetic energy of a

[6] It has to be noted that the variational principle only holds for an exact $F_{\mathrm{HK}}[\rho_{\mathrm{e}}]$, which is a major problem since an exact expression for the Hohenberg-Kohn functional has not been found up to today.

non-interacting system but with the same electron density $E_{\mathrm{kin}}^{\mathrm{S}}[\rho_{\mathrm{e}}]$.[7] This energy can be calculated exactly by using one-electron wave functions ϕ_i, also known as Kohn–Sham orbitals:

$$E_{\mathrm{kin}}^{\mathrm{S}} = -\frac{1}{2}\sum_{i}^{N}\langle\phi_i|\nabla^2|\phi_i\rangle \tag{3.7}$$

As a result, they got the expression for the ground state energy:

$$E_0[\rho_{\mathrm{e}}] = E_{Ne}[\rho_{\mathrm{e}}] + J_{\mathrm{C}}[\rho_{\mathrm{e}}] + E_{\mathrm{kin}}^{\mathrm{S}}[\rho_{\mathrm{e}}] + E_{\mathrm{XC}}[\rho_{\mathrm{e}}] \tag{3.8}$$

All unknown terms are then summarized in the exchange-correlation energy:

$$E_{\mathrm{XC}}[\rho_{\mathrm{e}}] = (E_{\mathrm{kin}}[\rho_{\mathrm{e}}] - E_{\mathrm{kin}}^{\mathrm{S}}[\rho_{\mathrm{e}}]) + (E_{ee}[\rho_{\mathrm{e}}] - J_{\mathrm{C}}[\rho_{\mathrm{e}}]) \tag{3.9}$$

From this, the so-called Kohn–Sham equation can be deduced, which can be interpreted as a one-electron Schrödinger-like equation [159]:

$$(-\frac{1}{2}\nabla^2 + [\int\frac{\rho_{\mathrm{e}}(\boldsymbol{r}_2)}{r_{12}}\mathrm{d}\boldsymbol{r}_2 + V_{\mathrm{XC}}(\boldsymbol{r}_1) - \sum_{\alpha}^{M}\frac{Z_\alpha}{r_{1\alpha}}])\phi_i = (-\frac{1}{2}\nabla^2 + V_{\mathrm{S}}(\boldsymbol{r}_1))\phi_i = \epsilon_i\phi_i \tag{3.10}$$

Here, ϵ_i is the energy of the Kohn–Sham orbital ϕ_i, V_{XC} is the exchange-correlation potential, and Z_α is the number of protons in the αth nucleus of the system. The terms in the brackets can be summarized in the potential V_{S} which serves as an effective one-electron potential for the Kohn–Sham orbitals.

It can easily be seen that this equation has to be solved iteratively since V_{S} depends solely on the electron density that is defined by the orthonormal Kohn–Sham orbitals:

$$\rho_{\mathrm{e}}(\boldsymbol{r}) = \sum_{i}^{N}|\phi_i|^2 \tag{3.11}$$

$$\langle\phi_i|\phi_j\rangle = \delta_{ij} \tag{3.12}$$

These Kohn–Sham orbitals, in return, depend on V_{S} and can be calculated by solving the Kohn–Sham Equation 3.10.

[7] The superscript S indicates that it is a single electron kinetic energy.

Since there is still no expression for $V_{\mathrm{XC}}(\boldsymbol{r})$, it is defined as the derivative of the exchange correlation energy:

$$V_{\mathrm{XC}}(\boldsymbol{r}) = \frac{\delta E_{\mathrm{XC}}\left[\rho_{\mathrm{e}}\right]}{\delta \rho_{\mathrm{e}}(\boldsymbol{r})} \tag{3.13}$$

In summary, the work by Hohenberg and Kohn proved that a system of bound electrons moving in an external potential can be described throughout and uniquely by the electron density of the system's ground state. Furthermore, Kohn and Sham developed a recipe for obtaining the ground state electron density iteratively from an initial guess. The initial guess defines the first V_{S} from which the Kohn–Sham orbitals can be calculated, which in return define a new electron density to calculate V_{S}. This procedure is repeated until the result converges and the total energy $E\left[\rho_{\mathrm{e}}\right]$ can be calculated.

In the following, a few remarks on the practical use of DFT concerning the approximation of the $E_{\mathrm{XC}}\left[\rho_{\mathrm{e}}\right]$ and the nature of the Kohn–Sham orbitals ϕ_i will be given. Despite a long debate about the physical meaning of the Kohn–Sham orbitals, it is widely accepted nowadays that Kohn–Sham orbitals of a molecular system are a good approximation of the system's MOs [160–165]. In such molecular systems, usually, the linear combination of atomic orbitals (LCAO) expansion of the Kohn–Sham orbitals is used. This means that the Kohn–Sham orbitals are defined by a basis set consisting of L basis functions η [166]:

$$\phi_i = \sum_{\mu=1}^{L} c_{\mu i}\eta_{\mu} \tag{3.14}$$

Each basis function η_{μ} is weighted by a coefficient $c_{\mu i}$.

The minimum number of basis functions is given by the number of occupied atomic orbitals. However, a multiple of this number is normally chosen to give the algorithm more freedom to find the best solution. For example, L equals twice the number of atomic orbitals in a so-called double zeta basis set. The appearance of the basis functions is not restricted to real atomic orbitals, as they were originally, but can have different forms chosen to fit the described system. Additionally, one

can add so-called polarization orbitals which allow for a better adaption of valence orbitals to molecular orbitals in contrast to atomic orbitals with fewer nodes. By using this LCAO expansion, the complicated optimization problem constituted by the Kohn–Sham Equation 3.10 is simplified to a linear problem and can be solved as described in reference [166].

A large variety of different approximations exists for the exchange-correlation term. A good overview is given in [160]. However, there are two main approximations from which most of the others are derived, which will be shortly presented here. In this vein, the unrestricted or spin-polarized DFT can be introduced. For unrestricted DFT, the electron density is split into two spin densities, each describing only electrons of like spin:

$$\rho_\mathrm{e} = \rho_\mathrm{e}{}^{\alpha} + \rho_\mathrm{e}{}^{\beta} \tag{3.15}$$

The difference between these two spin densities gives the so-called polarization density, which will be useful later when discussing the spin polarization mechanism for intramolecular magnetic interactions. The Kohn–Sham equation (see equation 3.10), then, needs to be solved for each of the spin densities. At the same time, for the Coulomb interaction, all electrons must be considered, which interconnects the two equations.

If the external potential has no spin-dependent contribution, all terms in principle only depend on the total electron density. However, especially in open-shell systems using the two spin densities for the calculation of the exchange correlation energy leads to better results. In restricted DFT, electrons will be paired into spin singlets with both electrons having identical spatial wave functions. If unrestricted DFT is used, paired electrons can have spatial wave functions with different geometries. Furthermore, the energy eigenvalues of the spin orbitals of the two paired electrons can be different. Therefore, the singly occupied molecular orbital (SOMO) of a magnetic molecule will be divided into two spin parts. One of them will be occupied with an energy below Fermi energy and one will be unoccupied and above Fermi energy. While the occupied one can still be called SOMO, the other one can be called singly unoccupied molecular orbital (SUMO).[8]

[8]The term is relatively uncommon, but examples for its usage can be found [167, 168].

The increased flexibility in unrestricted DFT allows for a more realistic description of open-shell systems such as paramagnetic molecules. It is essential for the calculation of intramolecular magnetic coupling by the broken-symmetry approach, which will be introduced in Section 3.5. The calculated Kohn–Sham orbitals as well as the spin polarization of a system can be plotted together with the atomic structure of the system, to visualize its electronic structure.[9]

Many approximations of the exchange correlation energy are based on the local density approximation (LDA). The use of this approximation has already been proposed in the original paper by Kohn and Sham [157]. It is based on the description of a uniform electron gas. In this model, the electrons move in front of a background formed by a positive potential. The whole system has a net charge of zero. In this picture, the exchange correlation energy is given by an integral over the single electron exchange correlation energy $\epsilon_{\mathrm{XC}}(\rho(\boldsymbol{r}))$ of a homogenous electron gas of density $\rho_{\mathrm{e}}(\boldsymbol{r})$:

$$E_{\mathrm{XC}}^{\mathrm{LDA}}\left[\rho_{\mathrm{e}}\right] = \int \rho_{\mathrm{e}}(\boldsymbol{r})\epsilon_{\mathrm{XC}}(\rho_{\mathrm{e}}(\boldsymbol{r}))\mathrm{d}\boldsymbol{r} \tag{3.16}$$

$\epsilon_{\mathrm{XC}}(\rho(\boldsymbol{r}))$ is weighted by the probability to find an electron at this position given by the electron density $\rho_{\mathrm{e}}(\boldsymbol{r})$. The exchange correlation energy can be split into two contributions: The exchange part ϵ_{X} and the correlation part ϵ_{C}. The first one of these is known exactly:

$$\epsilon_{\mathrm{X}} = -\frac{3}{4}\left(\frac{3\rho(\boldsymbol{r})}{\pi}\right)^{1/3} \tag{3.17}$$

The correlation term ϵ_{C} can be obtained from Monte-Carlo simulations of the homogenous electron gas, as performed by Ceperly and Alder [170]. Modern LDA approximations are using more sophisticated fits to this data to obtain ϵ_{C}. While the model is of some use for metal systems, it is far from reality for molecular systems.

[9] All images presented in this thesis containing DFT-calculated data were prepared using VESTA [169].

The second approximation on which many of the modern approximations are based is the generalized gradient approximation (GGA). This approximation has more relevance in view of molecular systems. The main idea is to include the local gradient of the electron density to accommodate for discontinuities. In general, it can be expressed as:

$$E_{\mathrm{XC}}^{\mathrm{GGA}}\left[\rho_{\mathrm{e}}\right] = \int f(\rho_{\mathrm{e}}, \nabla\rho_{\mathrm{e}})\mathrm{d}\boldsymbol{r} \tag{3.18}$$

Furthermore, in this approximation the term is often split into an exchange term $E_{\mathrm{X}}^{\mathrm{GGA}}$ and a correlation term $E_{\mathrm{C}}^{\mathrm{GGA}}$. The expressions for these two terms are usually designed in view of the best possible result rather than in view of representing physical meaning.

For the formulation of LDA as well as GGA in the unrestricted case, the respective expressions for the exchange correlation energy are altered to be dependent on both spin densities:

$$E_{\mathrm{XC}}^{\mathrm{LDA}}[{\rho_{\mathrm{e}}}^{\alpha}, {\rho_{\mathrm{e}}}^{\beta}] = \int \rho_{\mathrm{e}}(\boldsymbol{r})\epsilon_{XC}({\rho_{\mathrm{e}}}^{\alpha}(\boldsymbol{r}), {\rho_{\mathrm{e}}}^{\beta}(\boldsymbol{r}))\mathrm{d}\boldsymbol{r} \tag{3.19}$$

$$E_{\mathrm{XC}}^{\mathrm{GGA}}[{\rho_{\mathrm{e}}}^{\alpha}, {\rho_{\mathrm{e}}}^{\beta}] = \int f({\rho_{\mathrm{e}}}^{\alpha}, {\rho_{\mathrm{e}}}^{\beta}, \nabla{\rho_{\mathrm{e}}}^{\alpha}, \nabla{\rho_{\mathrm{e}}}^{\beta})\mathrm{d}\boldsymbol{r} \tag{3.20}$$

3.4 The Magnetic Moment of One-Center Magnetic Molecules

In this section, the description of magnetic moments in multielectronic systems will be briefly summarized. A more detailed discussion can be found in reference [130]. As mentioned above, the magnetic moment of paramagnetic molecules is caused by electrons singly occupying an orbital without another antiparallelly aligned electron. These electrons have a spin $\boldsymbol{s}$ that is not compensated by the spin of a second electron in the same orbital. The spin causes a magnetic moment of the electron:

$$\boldsymbol{M}_{\mathbf{s}} = -g_{\mathrm{s}}\mu_{\mathrm{B}}\boldsymbol{s} \tag{3.21}$$

Here, $g_\mathrm{s} \approx 2$ is the Landé factor (g-factor) of the spin magnetic moment and $\mu_\mathrm{B} = \frac{e\hbar}{2m_\mathrm{e}}$ is Bohr's magneton. Note that $\boldsymbol{M}_\mathbf{s}$ and $\boldsymbol{s}$ can be read as classical vectors or as quantum mechanical operators with eigenvalues M_s and $s = \pm\frac{1}{2}$ [171].

In addition, the electron can have a orbital angular momentum caused by its movement. It depends on the character of the orbital the electron occupies and is represented by the previously introduced azimuthal quantum number l. This movement of the electron causes an orbital magnetic moment:

$$\boldsymbol{M}_\mathbf{l} = -g_\mathrm{l}\mu_\mathrm{B}\boldsymbol{l} \tag{3.22}$$

The Landé factor of the orbital magnetic moment has a value of $g_\mathrm{l} = 1$. Again, $\boldsymbol{M}_\mathbf{l}$ and $\boldsymbol{l}$ can be read as vectors or operators. Their eigenvalues are the quantum numbers M_l and l. The spin and the orbital angular momentum and the corresponding magnetic moments can be measured along a well-defined axis. Therefore, the z-component operators s_z and l_z with the respective magnetic quantum numbers m_s and m_l are defined.

The spin magnetic moment and the orbital magnetic moment of an electron can interact with each other. This leads to spin–orbit coupling, and the individual angular moments combine to the single-electron total angular momentum $\boldsymbol{j} = \boldsymbol{l}+\boldsymbol{s}$. Spin–orbit coupling is stronger in heavier atoms. For a molecule with multiple electrons in a single 3d transition metal as the magnetic center and therefore weak spin–orbit coupling, the spin and the orbital angular momentum are first summed up over all electrons and then combined to the total angular momentum:

$$\boldsymbol{J} = \boldsymbol{L} + \boldsymbol{S} = \sum_i \boldsymbol{l}_i + \sum_i \boldsymbol{s}_i \tag{3.23}$$

This is called Russell-Saunders coupling.[10] The total magnetic moment of a multi-electron system is then:

$$\boldsymbol{M}_\mathbf{J} = \mu_\mathrm{B}(\boldsymbol{L} + g_\mathrm{s}\boldsymbol{S}) = -g_\mathrm{j}\mu_\mathrm{B}\boldsymbol{J}, \tag{3.24}$$

[10] If the spin–orbit coupling is strong, the single-electron total angular momentum has to be calculated for each electron individually before summing over the electrons. This is called j–j coupling and will be neglected here since it is only relevant for heavy elements.

with the new Landé factor:

$$g_{\mathrm{j}} = 1 + \frac{J(J+1) + S(S+1) - L(L+1)}{2J(J+1)} \tag{3.25}$$

Here, J, S, and L are the total angular momentum quantum number, spin quantum number, and orbital momentum quantum number of the multi-electron system ${}^{2\mathrm{S}+1}L_J$. In addition to spin–orbit coupling, the nuclear spin of the atom can cause hyperfine coupling, which will be neglected here.

In 3d transition metals, spin–orbit coupling is usually small and can be treated as a perturbation. Therefore, a one-center magnetic molecule with a 3d transition metal center can be described with the spin Hamiltonian that was originally introduced by Pryce, who thereby described paramagnetic ions in a crystal [171, 172]:

$$\hat{H} = \boldsymbol{S}\widetilde{\boldsymbol{D}}\boldsymbol{S} + \mu_{\mathrm{B}}\boldsymbol{B}\tilde{g}\boldsymbol{S} \tag{3.26}$$

Here, the first term is the zero-field splitting with the tensor $\widetilde{\boldsymbol{D}}$ describing the anisotropy of the molecule's spin $\boldsymbol{S}$. Zero-field splitting causes the magnetism of so-called SMMs [10, 173]. The second term is the Zeeman term describing the interaction with a magnetic field with flux $\boldsymbol{B}$. Additional terms, for example related to the nuclear spin, are neglected in this spin Hamiltonian. The spin–orbit coupling is treated as a perturbation and affects the appearance of $\widetilde{\boldsymbol{D}}$, $\tilde{g}$, and $\boldsymbol{B}$.

3.5 Intramolecular Magnetic Interactions

When discussing magnetic interactions in molecules, many different aspects have to be taken into account. The interactions can be mediated via different pathways, as depicted for a two-center magnetic molecule in Figure 3.3. Interactions via the ligand and through space have to be considered in all systems, although the latter are usually rather small. The interaction pathway via the substrate is especially relevant on non-insulating substrates, as it is usually mediated via delocalized electrons. On magnetic substrates, also the direct interaction of the magnetic centers with the substrate has to be taken into account. For each of these pathways,

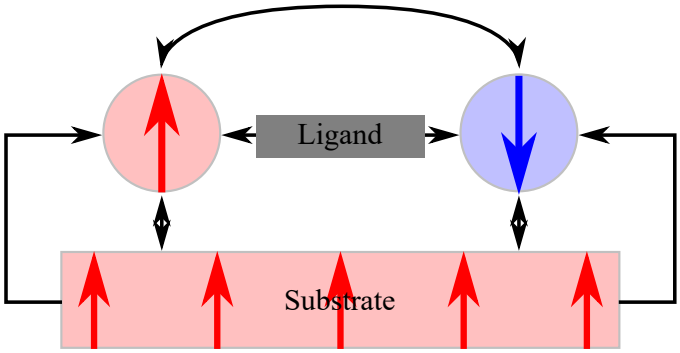

Figure 3.3: Visualisation of different interaction pathways of magnetic centers within a metal–organic complex on a ferromagnetic substrate. The two circles depict two magnetic centers. In this example the magnetic moments are aligned antiparallelly, as indicated by the colored arrows. Possible interaction pathways are marked by black arrows.

a variety of different interaction mechanisms is possible causing different relative alignments of the individual spins.

The interaction of two spins $\boldsymbol{S}_1$ and $\boldsymbol{S}_2$ within a molecule can be described by the following interaction Hamiltonian, as presented in reference [130] Section 2.5.2:

$$\hat{H} = -J\boldsymbol{S}_1\boldsymbol{S}_2 + \boldsymbol{S}_1\widetilde{\boldsymbol{D}}_{12}\boldsymbol{S}_2 + \boldsymbol{d}_{12}\boldsymbol{S}_1\times\boldsymbol{S}_2 \tag{3.27}$$

The first term of this Hamiltonian, also known as the Heisenberg–Dirac–van-Vleck (HDvV) Hamiltonian, is usually the strongest of the three. It describes the isotropic or scalar interaction of two interacting spins, which is either ferromagnetic, if $J > 0$, or antiferromagnetic, if $J < 0$. The value of J is defined as the difference of the energies of the singlet and the triplet state ($J = E_\mathrm{S} - E_\mathrm{T}$)[11] and can be calculated theoretically by a so-called broken symmetry (BS) approach. In this approach, introduced by Noodleman in 1981 [174–177], the coupling constant

[11] The Heisenberg–Dirac–van-Vleck-Hamiltonian can also be defined as $\hat{H}_\mathrm{HDvV} = -2J\boldsymbol{S}_1\boldsymbol{S}_2$. In this case $J = \frac{1}{2}(E_\mathrm{S} - E_\mathrm{T})$. Also the definition $\hat{H}_\mathrm{HDvV} = J\boldsymbol{S}_1\boldsymbol{S}_2$ can be found.

J is related to the difference between the energies of the high-spin state E_{HS} and a so-called BS state E_{BS} [176, 178, 179]:[12]

$$J = \frac{E_{\mathrm{BS}} - E_{\mathrm{HS}}}{2|\boldsymbol{S}_1||\boldsymbol{S}_2|} \tag{3.28}$$

For a system of two spins $|\boldsymbol{S}_1| = |\boldsymbol{S}_2| = \frac{1}{2}$, this equation resembles the above mentioned definition of J, as the difference of the energies of the triplet and the singlet state. The only difference is a factor two because the BS state is not the real singlet state of the system, i.e. it is not an eigenfuction of the Hamiltonian and has an energy of $E_{BS} = \frac{1}{2}(E_{\mathrm{S}} + E_{\mathrm{T}})$. The second term of the interaction Hamiltonian describes anisotropic interactions characterized by the tensor $\widetilde{\boldsymbol{D}}_{12}$. It results in the preferred orientation of the spins in a certain spatial direction. This term is very similar to the first term of the one-center spin Hamiltonian in Equation 3.26, but here the anisotropy tensor describes the coupling between two different spin centers, as indicated by the additional subscripts of the tensor. The third term describes the antisymmetric Dzyaloshinsky-Moriya interaction, which prefers a 90° angle between the interacting spins and a perpendicular orientation of the spins towards the vector $\boldsymbol{d}_{12}$ [180, 181]. It will be described in more detail below.

In the case of multiple spin centers, one has to take into account all interactions between possible pairs of centers. However, the interaction of direct neighbors usually dominates over the next nearest neighbor and higher-order indirect interactions. The spin Hamiltonian in Equation 3.26 summarizes the possible effects on the alignment of the spins, but it does not give any information about the interaction mechanisms. These will be discussed in the following.

3.5.1 Magnetic Interaction via an Electronic Bond

The situation of two neighboring, bonded magnetic atoms is uncommon in magnetic molecules. However, in case of molecules adsorbed on a magnetic substrate,

[12] Note that the different notations of the HDvV Hamiltonian also alter the expression for the BS approach.

bonds can be formed between the molecule's spin center and substrate atoms [182, 183]. Furthermore, the physics of the immediate interaction via an electronic bond is also relevant for superexchange, which will be discussed in the next section. The magnetic interaction between two magnetic orbitals on neighboring atoms is constituted of two contributions:

$$J = J_{\mathrm{F}} + J_{\mathrm{AF}} \tag{3.29}$$

The first term is the ferromagnetic direct exchange interaction[13] and the second term is the so-called kinetic exchange, which is antiferromagnetic. In the here described situation of the magnetic interaction between two overlapping orbitals, the direct exchange is typically the dominating effect, and kinetic exchange can often be neglected. Therefore, the expression 'direct exchange' is often used to refer to the total interaction between two bonded atoms.

With an order of magnitude of about 1 eV to 3 eV for the interaction strength [44, 177], direct exchange is one of the strongest contributions to magnetic interactions. Direct exchange for two electrons, 1 and 2, in two orbitals, Φ_a and Φ_b, is characterized by the exchange integral [129]:

$$K_{ab} = \langle \Phi_a(1)\, \Phi_b(2) | \frac{e^2}{r_{12}} | \Phi_a(2)\, \Phi_b(1) \rangle \tag{3.30}$$

K_{ab} is always positive and stabilizes the triplet state of two electrons in Φ_a and Φ_b versus the singlet state by a total of $2K_{ab}$.

Direct exchange is caused by the interplay between the Pauli principle and the Coulomb repulsion between two interacting electrons. The total wave function Ψ, describing the two electrons, has to fulfill the relation $|\Psi(1,2)|^2 = |\Psi(2,1)|^2$, which states that the two electrons are indistinguishable. For electrons, which are fermions, this relation can only be satisfied if the wave function is antisymmetric. The total wave function can be written as a product of a spatial and a spin component. To create an antisymmetric total wave function, one of the two components needs to be antisymmetric, while the other one is symmetric. In case of a

[13] Sometimes also labeled as Coulomb exchange or potential exchange.

symmetric spatial component, both electrons have a large probability in the region between the individual centers. This leads to a higher Coulomb repulsion between the electrons. For the case of an antisymmetric spatial component, the electrons are localized on the individual centers, leading to a larger separation of the two electrons and a lower Coulomb repulsion. This mechanism is also the reason for Hund's first rule since direct exchange also occurs between two magnetic orbitals on the same atom.

The second term of Equation 3.29 was first expressed by Anderson when describing the magnetic interaction in transition metal salts [184, 185]. In this situation, the magnetic atoms are not bonded immediately but interact via a paramagnetic atom. Therefore, Anderson coined the term superexchange. Later it was found that kinetic exchange[14] is also present in the immediate magnetic interaction of two bonded magnetic atoms, yet, in this case, it is usually smaller than the direct exchange, leading to an effective ferromagnetic interaction. However, in some cases it can become the dominant term and cause an effective antiferromagnetic coupling, as for example in layered chromium compounds [186, 187]. Kinetic exchange is due to the lowered energy of a system if the electrons can delocalize over multiple orbitals. Such delocalization is only possible for antiferromagnetic spins since the Pauli principle forbids the simultaneous occupation of a single orbital for like spins. Therefore, kinetic exchange lowers the energy of the singlet state and causes antiferromagnetic coupling.

To get a full expression for the magnetic interaction of two overlapping magnetic orbitals, one can utilize the configuration interaction (CI) method [188, 189]. In CI, a basis of determinants is built, by which each possible electronic configuration of the system can be described. These determinants are related with each other by a so-called CI matrix. CI gives an exact solution of the Schrödinger equation if every possible electronic configuration is considered, which is called full CI. However, because of computational limitations, usually a subspace of the complete basis has to be used for complex systems. In the minimal valence space for two bonded atoms of spin $S = \frac{1}{2}$, only one singly occupied orbital on each atom is considered. This is also called the complete active space, spanned by four determinants. Of these

[14]Kinetic exchange is what Anderson referred to as superexchange or true superexchange.

four determinants, two are neutral determinants, with the two electrons occupying separate orbitals, and two are ionic determinants, with both electrons occupying either orbital a or orbital b.

In this description and using a perturbation approach, CI yields the following expression for the exchange interaction [177, 190]:

$$J = 2K_{ab} - \frac{4{t_{ab}}^2}{U_{\mathrm{H}}} \tag{3.31}$$

Here, K_{ab} is the already known exchange integral, t_{ab} the hopping integral describing the energy gain for electrons hopping between the orbitals a and b, and U_{H} the on-site Coulomb repulsion for two electrons residing on the same atom, known from the Hubbard model. U_{H} is defined as the difference between the Coulomb repulsion term of an ionic ${J_{\mathrm{C}}}^{aa}$ and a neutral ${J_{\mathrm{C}}}^{ab}$ configuration:

$$\begin{aligned} U_{\mathrm{H}} &= {J_{\mathrm{C}}}^{aa} - {J_{\mathrm{C}}}^{ab} \\ &= \langle \Phi_a(1)\,\Phi_a(2)|\frac{e^2}{r_{12}}|\,\Phi_a(1)\,\Phi_a(2)\rangle - \langle \Phi_a(1)\,\Phi_b(2)|\frac{e^2}{r_{12}}|\,\Phi_a(1)\,\Phi_b(2)\rangle \end{aligned} \tag{3.32}$$

The second term in Equation 3.31 is the expression Anderson derived for the kinetic exchange interaction [184]. In case of multiple singly occupied orbitals on each atom, the interaction between each pair of orbitals has to be taken into account. This includes pairs of orbitals residing on the same atom. Also empty orbitals can play a role in the interaction, because of the additional possibilities for delocalization. Additional contributions to the magnetic exchange interaction by higher order excited states of the system can be expressed in form of effective versions of the individual parameters of the interaction, i.e. ${K_{ab}}^{\mathrm{eff}}$,${t_{ab}}^{\mathrm{eff}}$, and ${U_{\mathrm{H}}}^{\mathrm{eff}}$. Such effects have to be considered especially when additional closed shell orbitals of a ligand come into play, as presented in the next section.

For molecules adsorbed on ferromagnetic substrates, ferromagnetic coupling between the molecular magnetic centers and the substrate is usually attributed to direct exchange via an electronic bond between the magnetic center and substrate

atoms. Antiferromagnetic coupling in such systems is usually attributed to a superexchange interaction via the organic ligand of the molecule.

3.5.2 Superexchange

The most important interaction for multi-center magnetic molecules is the magnetic superexchange interaction. According to the International Union of Pure and Applied Chemistry (IUPAC) the term superexchange describes the "electronic interaction between two molecular entities mediated by one or more different molecules or ions" [191]. This includes intramolecular electron transfer processes as well as magnetic coupling of two magnetic moments connected via nonmagnetic atoms. For this thesis, only the latter aspect is relevant.

In literature, the term superexchange is often not used in this general meaning as defined by IUPAC. Instead, it is used to refer to the kinetic exchange interaction as introduced in the last section. A more precise term used synonymously with kinetic exchange is the term Anderson superexchange. This is due to the pioneering research by P. W. Anderson based on the preliminary work of Kramers [184, 185]. He developed a model of superexchange to describe antiferromagnetic interactions in transition-metal salts.

Anderson considered a model system of two singly occupied orbitals on two atoms bridged by a fully occupied orbital in his original paper [184]. This two-band valence bond model led Anderson to the expression for kinetic exchange introduced in Equation 3.31. The difference in the interaction due to the additional passive orbital of the ligand can be expressed in a modification of the hopping integral [190]:

$$t_{ab}^{\text{eff}} = t_{ab} + \frac{t_{la} t_{lb}}{\Delta E_{\text{CT}}} \tag{3.33}$$

Here, t_{la} and t_{lb} are the hopping integrals for electron hopping between the ligand and the two magnetic orbitals and ΔE_{CT} is the excitation energy of the single charge transfer configurations. The added term describes the influence of a single excitation by which one of the ligand electrons is transferred into any of the magnetic orbitals. Additionally, one can consider the influence of the double excitation

by which both ligand electrons are transferred into the magnetic orbitals. This results in an additional term for the exchange coupling parameter [190]:

$$J = 2K_{ab} - \frac{4{t_{ab}^{\mathrm{eff}}}^2}{U_{\mathrm{H}}} - \frac{8{t_{la}}^2{t_{lb}}^2}{{\Delta E_{\mathrm{CT}}}^2 \Delta E_{\mathrm{2CT}}} \tag{3.34}$$

In this term, the excitation energy of the double charge transfer configuration ΔE_{2CT} replaces the on-site Coulomb interaction U_{H}. In superexchange systems, K_{ab} is typically very small with 0.1 meV to 6 meV [8].

Later, models were developed by Kahn and Briat [9] and by Hay *et al.* [8] to describe superexchange in molecules. The model by Kahn and Briat is based on the valence bond model by Heitler and London. In this model, $\Phi_{a,b}$ does not describe atomic orbitals but MOs, i.e. the SOMOs of the molecule. These molecular orbitals are not localized solely on the magnetic centers but also have tails extending onto the ligand. Therefore, the exchange interaction can be related to the overlap between these two orbitals. They obtained the following expression for the exchange interaction [9, 130, 177]:

$$J = 2K_{ab} + 4\beta\tilde{S}_{ab} \tag{3.35}$$

Here, the first term is the direct exchange, which is twice the exchange integral of the two non-orthogonalized molecular orbitals Φ_a and Φ_b. In the second term, β can be interpreted as a one-electron hopping integral weighting the energy gain by virtual hopping of the electrons and $\tilde{S}_{ab}$ is the overlap integral. This term is negative and describes the antiferromagnetic kinetic exchange. If the interacting magnetic orbitals are orthogonal to each other, the overlap integral $\tilde{S}_{ab}$ equals zero.[15] In this case, the direct exchange is dominating the interaction. If the orbitals have a large overlap integral, the kinetic exchange dominates the exchange interaction and the spins couple antiferromagnetically.

[15] Note that the overlap integral can also be zero for overlapping orbitals if contributions of opposite sign cancel each other out.

An alternative description was developed by Hay *et al.* in the frame of molecular orbital theory as developed by Hund and Mulliken [8, 130, 177]:

$$J = 2K_{ab} - \frac{(E_g - E_u)^2}{{J_\mathrm{C}}^{aa} - {J_\mathrm{C}}^{ab}} \tag{3.36}$$

Again, the first term is the ferromagnetic contribution by the direct exchange integral, but in this case, of the two orthogonalized SOMOs Φ_a and Φ_b. The second term relates the kinetic exchange to the energy difference between the symmetry adapted bonding and antibonding MOs built from the SOMOs $E_g - E_u$. The terms ${J_\mathrm{C}}^{aa}$ and ${J_\mathrm{C}}^{ab}$ are the Coulomb integrals of the state with both electrons residing on the same and on different atoms, respectively. Therefore, the difference between these terms is the Coulomb repulsion U_H, as mentioned above.

The qualitative results of the above discussed models can be summarized by the Goodenough–Kanamori rules [192–194].[16] In their original form these are:

- If the M–L–M bond forms a 180° angle, the two spins interact strongly antiferromagnetic.
- If the M–L–M bond forms a 90° angle, the two spins interact weakly ferromagnetic.

Later Anderson revised these rules, saying that antiferromagnetic coupling is achieved in systems where the two singly occupied orbitals have a reasonably large overlap integral [194]. This describes the 180° case in the picture of the models developed by Kahn and Briat and by Hays *et al.*, although Anderson also describes a case in which a 90° angle of the M–L–M bond leads to this situation. Ferromagnetic interaction, according to Anderson, is achieved for two singly occupied orbitals overlapping in a way that the effective overlap integral is zero. Again, this can not only be achieved in a 90° case but also for a 180° case.

An illustration of these rules is depicted in Figure 3.4. These are very simplified depictions of the complicated physical effects of intramolecular magnetic interactions and should be handled with care. The results obtained in these models give

[16] Sometimes also Goodenough–Kanamori–Anderson rules.

a good qualitative estimation of the superexchange in real systems. Especially the relation between the system's geometry and the resulting exchange interaction has been used successfully to design interesting magnetic molecular systems. In fact, a study by Crawford *et al.* showed a change from ferromagnetic to antiferromagnetic interaction in a Cu–O–Cu bond depending on the bonding angle [195]. They found a cancellation of ferromagnetic and antiferromagnetic contributions at 97.4°. However, the models usually give quantitatively bad results, and exceptions for the influence of the geometry on the coupling can be conceived. Therefore, further extensions mainly based on the Anderson model were developed, focusing on the implementation of additional interaction mechanisms apart from the kinetic exchange.

Anderson already distinguished between three contributions to the magnetic interaction in transition-metal salts [185]: The direct exchange due to the exchange integral, the 'true' superexchange[17] or kinetic exchange, and a polarization effect. The last one of these can be further divided into a charge-polarization and a spin-polarization effect. However, Anderson neglects the polarization mechanism as minor contributions. This was certainly correct for the systems Anderson was considering, in which the magnetic centers are relatively close to each other and the exchange interactions are mainly mediated by σ-type overlaps of the magnetic orbitals. Yet he admitted that it might play a role in systems with a larger separation between the magnetic centers and π-overlap.

Generally, the magnetic superexchange interaction, as defined by IUPAC, can have multiple additional mechanisms caused by higher order perturbations due to additional electronic configurations. All possible mechanisms can be described in the framework of CI. The different effects can be classified by the number of excitations needed to obtain the corresponding electronic configuration. These are classified as excitations of lower lying ligand electrons into the magnetic orbitals, called h excitations, excitations of electrons from the magnetic orbitals into higher lying empty orbitals, called p exciations, or a mixture of both [177, 190].[18] In this picture, the

[17] Anderson writes 'true' superexchange to distinguish it from the spin polarization mechanism [185].

[18] The reasoning behind these labels is that h excitations create a **h**ole in the low lying ligand orbitals and p excitations excite **p**articles into higher orbitals.

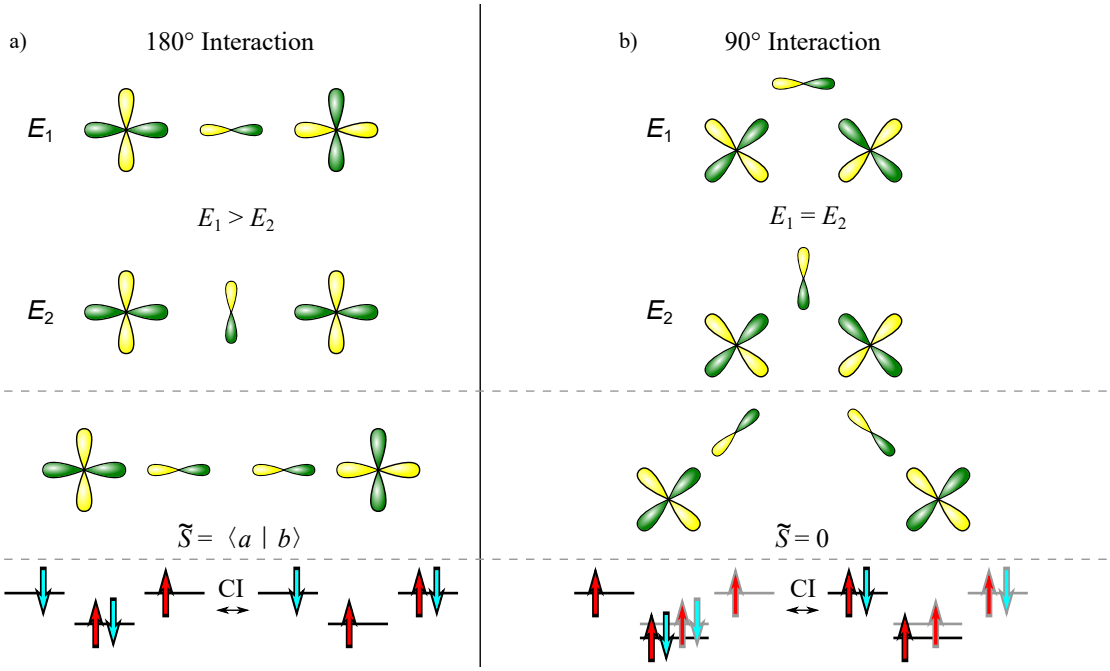

Figure 3.4: Visualization of the Goodenough-Kanamori rules in the framework of different models for a) the 180°-case and b) the 90°-case. The upper part of the figure shows the interactions as in the model by Hays *et al.*, the middle part as in the model of Kahn and Briat, and the bottom part as in a CI picture. Yellow and green parts of the atomic orbitals indicate volumes of the wave functions of different phases. In the CI picture spin-down electrons are represented by blue arrows and spin-up electrons by red arrows. Orbitals represented by lines of different shadings have a zero overlap integral while orbitals of the same shading have a non-zero overlap integral.

correctional term in Equation 3.33 is caused by $1p$ excitations and the correctional term in Equation 3.34 is caused by $2p$ excitations. However, it was shown that their additional effects are very small and only result in a slight stabilization of the singlet state. The same holds true for their h-excitation counterparts [177].

The $1h$-$1p$ excitations are the cause of the aforementioned polarization mechanisms. In these excitations, one electron is excited from the ligand into a magnetic orbital, and one electron from the same magnetic orbital is excited into an empty orbital. If both excited electrons have the same spin, this is causing the dynamic charge polarization, and if the electrons are of opposite spin, it is the so-called spin-polarization mechanism. The former lowers the effective on-site Coulomb repulsion [177, 196]:

$$U_{\mathrm{H}}^{\mathrm{eff}} = U_{\mathrm{H}} - \sum_{hp} \frac{|\langle \Phi_h | (J_{\mathrm{C}}^{a} - J_{\mathrm{C}}^{b}) | \Phi_p \rangle|^2}{U_{\mathrm{H}} + E_p - E_h} \tag{3.37}$$

Here, Φ_h and Φ_p are the occupied and empty ligand orbitals with energies E_h and E_p, respectively. The Coulomb operator $J_{\mathrm{C}}^{a/b}$ describes the electric field created by an electron in orbital $\Phi_{a/b}$. Adding this contribution fixes an often encountered underestimation of antiferromagnetic coupling in transition metal compounds [177].

The other $1h$-$1p$ excitation, which is not spin conserving, is the spin-polarization mechanism. A prominent example of this mechanism is the *meta*-phenylene linkage of organic biradicals [197, 198]. This mechanism is especially important for extended π-systems and can be used to design high-spin SMMs, as suggested by Glaser *et al.* [14]. It is also important for the salophen molecules investigated in this thesis, as will be introduced later in Section 3.6. The non-spin-conserving $1h$-$1p$ excitations lead to configurations in which the two ligand orbitals and the two magnetic orbitals both have a total spin of 1 but with opposite signs, canceling out each other. This effect leads to a polarization of the ligand's spin density and is described by the following correction to the kinetic exchange integral:

$$K_{ab}^{\mathrm{eff}} = K_{ab} + 2 \sum_{hp} \frac{\langle \Phi_h | \hat{K}_a | \Phi_p \rangle \langle \Phi_p | \hat{K}_b | \Phi_h \rangle}{E_p - E_h} \tag{3.38}$$

In this equation, $\hat{K}_i$ is the exchange operator describing the exchange with an electron in orbital Φ_i.

While K_{ab} is always positive, the correctional term can be either negative or positive. It is even possible that the spin polarization results in a total negative value for K_{ab}^{eff}. The sign and value of the correction due to the spin-polarization mechanism depend on the respective ligand. For π-conjugated C systems, an easy rule of thumb exists to determine the sign of the spin polarization mechanism. On each C atom, the spin polarization of the ligand changes its sign. Hence, an even number of C atoms between two magnetic centers leads to antiferromagnetic interaction, while an uneven number of C atoms leads to a ferromagnetic interacion. This is visualized schematically in Figure 3.5 for the example of a *meta*-phenylene diradical compared with the *ortho*- and *para*-phenylene diradicals. A similar visualization is possible by extracting the spin-density distribution of a molecule from DFT calculations, which has been done for many molecules involving π-conjugated C systems [199–201]. In such systems, the spin-polarization mechanism can cause magnetic coupling over long distances, compared to the usual direct exchange and Anderson superexchange. The last possible excitations for a system of two interacting singly occupied orbitals are $2h$-$1p$ and $1h$-$2p$ excitations. However, these do not add new interaction mechanisms but rather enhance the already existing mechanisms [177].

Overall, the interaction strength of the superexchange interaction varies drastically depending on the bridging ligand. Typical values for the interaction strength of intramolecular superexchange are in the range of 0.1 meV to 100 meV [130, 197, 198]. Ferromagnetic interactions usually are at the lower end of this range. Therefore, superexchange, and especially antiferromagnetic superexchange, is the strongest contributing mechanism for intramolecular magnetic coupling since direct exchange usually does not play a role here. Next to the coupling of multiple magnetic centers within a molecule, the superexchange interaction can also couple the molecular spin centers to a magnetic substrate [202, 203].

As mentioned above, the exchange coupling constant J can be calculated by the BS approach, usually without any information about the different mechanisms

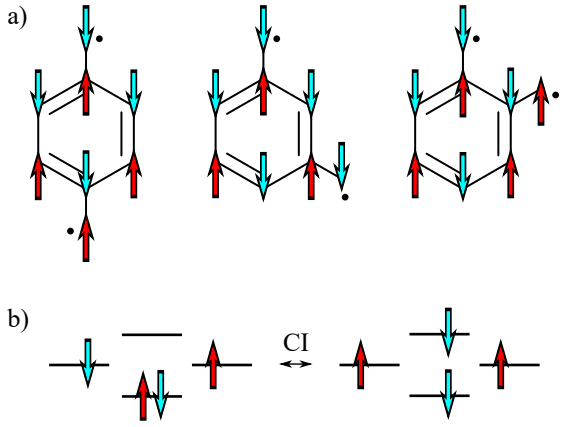

Figure 3.5: Visualization of the spin polarization mechanism. In a) an often encountered schematic visualization of the spin polarization mechanism for the cases of *para*-, *meta*-, and *ortho*-phenylene biradicals is presented. Here, blue and red arrows indicate positive and negative spin polarization on the respective atom. In b) the mechanism is visualized in a CI picture. Spin-down electrons are represented by blue arrows and spin-up electrons by red arrows. Orbitals are represented by black lines.

contributing to the exchange interaction. Recently, a strategy was presented by Coulaud *et al.* to split the coupling constant into the three contributions by direct exchange, kinetic exchange, and the spin-polarization mechanism [204]. An alternative route was proposed by Steenbock *et al.*, who suggested using a Green's-function approach, which also allows identifying individual contributions to the exchange interaction [205].

3.5.3 Dzyaloshinsky–Moriya (DM) Interaction

The non-collinear Dzyaloshinsky–Moriya (DM) interaction has been first postulated by Dzyaloshinsky to describe weakly ferromagnetic phases in antiferromagnetic materials [180]. Later the mathematical basis was contributed by Moriya, who extended Anderson's model of superexchange [181]. Recently, the DM interaction got well known for its effects in metallic layer systems. Here it is responsible for the formation of skyrmions and spin spirals [206–208].

As mentioned earlier, the DM interaction prefers perpendicular alignment of interacting spins toward each other and toward the vector $\boldsymbol{d}_{12}$. The DM interaction is mainly caused by higher order perturbation terms of the kinetic exchange mechanism if the system has no inversion symmetry center between the interacting metals. Therefore, it is small compared to the isotropic interaction represented by the exchange coupling constant J. Typically, the DM interaction results in a deviation of the spins from their collinear alignment by a few degrees, but also larger effects are possible [208].

The direction of $\boldsymbol{d}_{12}$ is determined by the symmetry properties of the system, following the rules listed by Moriya [181]. In molecular systems, this is defined by the bridging ligand. The strength of the interaction is proportional to the spin–orbit coupling in the interacting metal atoms. Moriya estimated the interaction strength by the shift in the gyromagnetic ratio [181]:

$$|\boldsymbol{d}_{12}| \approx \frac{\Delta\gamma}{\gamma}(-\frac{4{t_{ab}}^2}{U_{\mathrm{H}}}) \tag{3.39}$$

This results in an interaction strength of roughly 10 % of the kinetic exchange coupling strength. In molecular systems, the DM interaction influences the properties of multiferroic metal organic frameworks and low-dimensional metal–organic compounds [209, 210].

3.5.4 Dipole–Dipole Interaction

The dipole–dipole interaction is a well-known magnetic through-space interaction with a long range. It couples interacting spins antiferromagnetically. The dipole–dipole interaction strength has an order of magnitude of about 10^{-2} meV and is proportional to $\frac{1}{\boldsymbol{r}^3}$ [44]. Therefore, it is rather weak compared to the other interactions. However, together with direct exchange, it is responsible for the formation of domains in ferromagnetic materials. In isolated spin chains it can induce anisotropic interaction since there are only interaction partners along the chain, and it can contribute to the antisymmetric interaction [131, 181].

3.5.5 RKKY Interaction

On nonmagnetic metallic substrates, the Ruderman–Kittel–Kasuya–Yosida (RKKY) interaction can play a role as a surface mediated interaction [211–213]. Originally, the interaction mechanism was reported by Ruderman and Kittel to explain the interaction of nuclear magnetic moments within metals [211]. Later it was found that the mechanism can also couple magnetic impurities, such as single atoms [214] or molecules [215], on top of a metallic substrate. The magnetic moment of a magnetic impurity polarizes nearby conduction electrons of the substrate antiparallelly. These electrons then interact antiferromagnetically with other conduction electrons further away. This creates an oscillating spin-polarization pattern in the metal substrate. Depending on the relation of the wavelength of the spin pattern and the distance of the magnetic impurities, the interaction is either ferromagnetic or antiferromagnetic. Because of the oscillation of the conduction-electron spins, the interaction strength varies strongly with the distance. However, on the first two maxima (one ferromagnetic, one antiferromagnetic), at distances of about 1 nm to 3 nm, the interaction strength has a magnitude of a few hundred μeV [216, 217].

3.6 Magnetism of Metal-Salophen Complexes

The metal–organic complexes investigated for this thesis are based on the salen type complex 5,5'-dibromosalophen (Br_2H_2–Sal), which has a $C_{2v'}$ symmetry [15, 16, 218]. As a Schiff base ligand, the salophen ligand is easily available and can be modified in various ways. Therefore, salophen complexes have been investigated in view of multiple possible applications [219–222]. In comparison to other salen type complexes, salophen is charactarized by a phenyl ring connected to the two N atoms. This phenyl ring is labeled 'bridge', as indicated in Figure 3.6. Because of this bridge, the backbone of the molecule becomes more stable and organo–metallic complexes based on this ligand are quasi-planar in most cases.

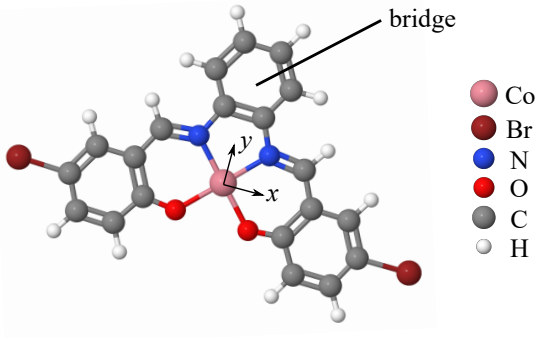

Figure 3.6: Model of 5,5'-dibromosalophenatocobalt(II) (Br_2Co–Sal), extracted from DFT calculations. On the right-hand side of the figure, the different elements are labeled with the respective IUPAC symbol. The phenyl ring identifying the molecule as a salophen is labeled as 'bridge'. The orientations of the x- and y-axis of the coordinate system used for the discussion of the MOs are indicated by black arrows.

Another feature of the salophen ligand used in this study is provided by the two Br atoms, one at each end of the molecule. These Br atoms enable the formation of covalently linked oligomers by use of the on-surface Ullmann reaction introduced in Section 2.3.1 [15, 16, 218, 223]. The covalent bonds formed during the polymerization guarantee that the π-conjugated C system of the phenyl rings is continuous over the whole chain. This conjugated π-system is necessary for the aforementioned spin-polarization mechanism for magnetic superexchange.

Combining Br_2Co–Sal with singly bromated 5-bromosalophenatocobalt(II) helps controlling the length of the created chains [218]. Independent of the metal center, salophen complexes can be identified in STS experiments because of a characteristic electronic state of the ligand. In DFT calculations, performed by Michal Hermanowicz[19] and published in reference [80], this state was calculated to be the LUMO of Co–Sal.[20] The spatial appearance of this state is presented in Figure 3.7. It is characterized by high electron probability on the sides of the bridge and a nodal plane cutting through the bridge and the position of the central cavity. Since

[19]Institute of Physics, Poznan University of Technology, 60-965 Poznan, Poland
[20]Later it will be seen that the calculated LUMO appears at higher energies in experiments and becomes the LUMO+1 or LUMO+2.

this state can be observed in $\mathrm{d}I/\mathrm{d}U$ maps for all salophen complexes studied in this thesis independently of the metal center, it will be called the ligand state.

Salen type complexes like Br_2H_2–Sal provide a central cavity in form of a N_2O_2 pocket that can coordinate various different metals in a square-planar geometry.[21] From solution, salophen complexes with Mn, Co, Ni, Cu, Zn, Pd, and Pt have been reported [222]. These metals are in oxidation state +II if coordinated in the salophen ligand. Complexes with Al, Cr, Fe, Zr, Ru, Cd, and U also have been synthesized [219, 220, 226]. However, these complexes always had additional atoms or groups coordinated to the metal atom. Therefore, they were in an oxidation state higher than +II. Using the on-surface metalation approach introduced in Chapter 2.3.2, the coordination of Cr and Fe in the cavity without further ligands on the metal is possible [80]. The research on these complexes will be the topic of Section 6.6.

The main focus of this thesis will be the investigation of Br_2Co–Sal as shown in Figure 3.6. A Co atom in oxidation state +II (Co(+II)) has seven electrons in the 3d shell. In a square-planar geometry, it will have a spin of $S = \frac{1}{2}$ in its ground state, leading to a spin magnetic moment of $1\,\mu_\mathrm{B}$. It has been debated for a long time which of the five 3d orbitals the single unpaired electron will occupy. To be consistent with previous publications, the orientation of the salophen molecule relative to the coordinate system is set as indicated in Figure 3.6, with the x-axis crossing through the Br atoms. Two orbitals have been considered to be the SOMO: The d_{yz} orbital and the d_{z^2} orbital.

The early stages of this debate are summarized in the works by Hitchman *et al.* [143] and Nishida *et al.* [142].[22] Their studies were focused on the electronic structure of the Co–salen complex and other complexes with the same coordination group. However, the arguments are also valid for Co–Sal since the bridge does influence the coordination of the Co atom apart from the stabilization of the square-planar geometry. The authors of these two papers came to the conclusion

[21] Rare cases of a distortion towards a tetrahedral geometry are known [14, 224, 225].

[22] Because of the chosen orientation of the coordinate system, the d_{xz} orbital in the publication by Hitchman *et al.* will be referred to as d_{yz} orbital and *vice versa*. In the publication by Nishida *et al.* the $\mathrm{d}_{x^2-y^2}$ orbital and the d_{xy} orbital are interchanged.

that for the ground state of the Co–salen complex the unpaired electron occupies the d_{xz} orbital. However, they had to apply some corrections to the AOM method they used for the calculation of the d-orbital energies to fit the results of their calculations to their spectroscopic data.

Later, Ceulemans *et al.* gave a theoretical framework for an amended LFT to describe the ground state of Co–salen and other Co-Schiff base complexes correctly [144].[23] In this paper, a mixed ground state is suggested for Co–salen, composed of the three configurations:

$$\langle {}^2\mathrm{A}_2, xz| = \langle (\mathrm{d}_{yz})^2(\mathrm{d}_{z^2})^2(\mathrm{d}_{xz})^1(\mathrm{d}_{x^2-y^2})^2(\mathrm{d}_{xy})^0| \tag{3.40}$$

$$\langle {}^2\mathrm{A}_1, z^2| = \langle (\mathrm{d}_{yz})^2(\mathrm{d}_{z^2})^1(\mathrm{d}_{xz})^2(\mathrm{d}_{x^2-y^2})^2(\mathrm{d}_{xy})^0| \tag{3.41}$$

$$\langle {}^2\mathrm{B}_1, yz| = \langle (\mathrm{d}_{yz})^1(\mathrm{d}_{z^2})^2(\mathrm{d}_{xz})^2(\mathrm{d}_{x^2-y^2})^2(\mathrm{d}_{xy})^0| \tag{3.42}$$

Among the contributing states, the $\langle {}^2\mathrm{B}_1, yz|$ contribution is minuscule and the $\langle {}^2\mathrm{A}_2, xz|$ configuration is the most dominant since it is the lowest in energy. This electronic structure is caused by three effects: Firstly, the downshift of the d_{z^2} orbital by s-d mixing, secondly, the lifting of the degeneracy between the d_{xz} orbital and the d_{yz} orbital due to the Orgel effect, and, thirdly, the increase in energy of the $\langle {}^2\mathrm{A}_1, x^2 - y^2|$ state due to interelectronic repulsion. Another important remark of the paper by Ceulemans *et al.* is the affinity of Co-salen complexes to coordinate additional ligands along the z-axis. Ligands coordinated in these positions cause a raise in energy of the d_{z^2} orbital.

In recent years, a new tool for the discussion of molecular electronic structures was obtained in DFT. It enables *ab initio* calculations of the MO energies. Various research groups performed DFT calculations of the Co–Sal complex or similar complexes with different software packages. In the Glaser group, research was focused on the design of SMMs from Mn complexes [14]. Only one publication by Oldengott *et al.* considers a Co–Sal complex, the triplesalophen complex [(baron$^{\mathrm{Me}}$)Co_3], as a building block for a SMM [227]. They claim a d_{yz} ground state with the coordinate system aligned along the N–Co–O bonds, as in Figure 1

[23] In the publication by Ceulemans *et al.*, the x-axis and the y-axis were interchanged compared to the geometry considered in this thesis.

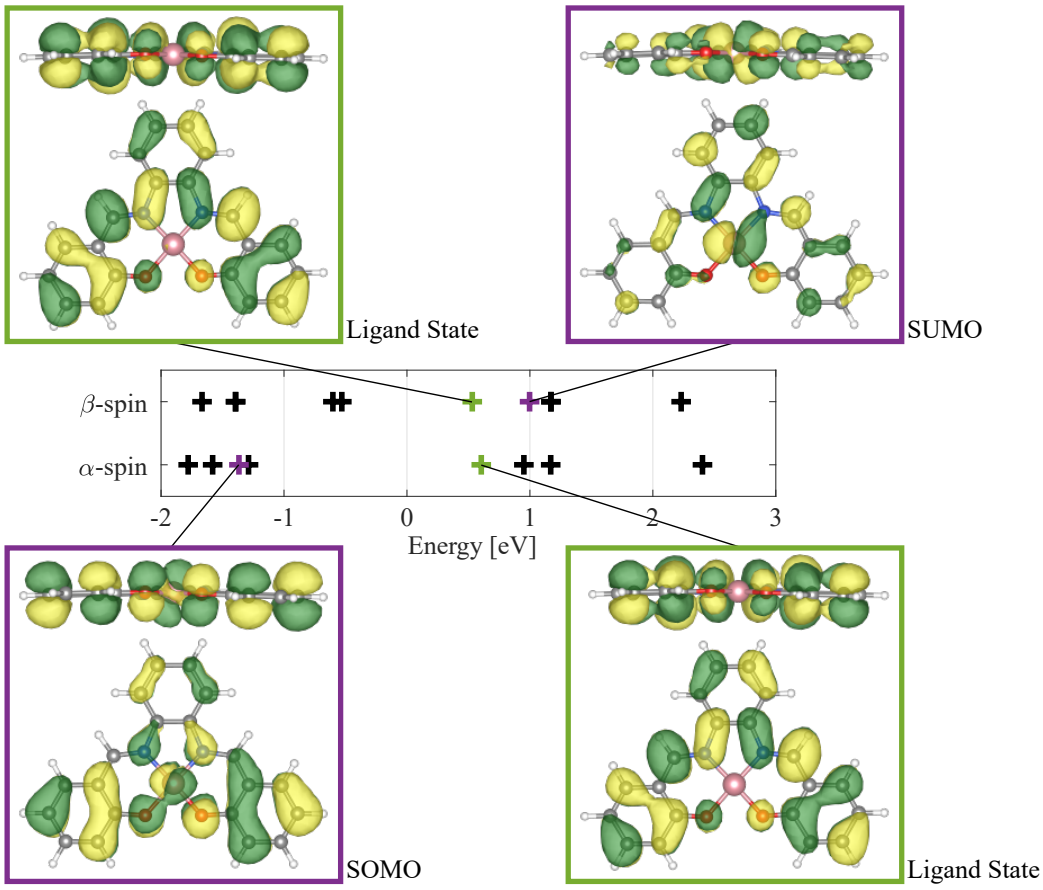

Figure 3.7: DFT calculations of the electronic structure of Co–Sal. For both spin channels the energy eigenvalues for the electronic states around Fermi energy are plotted. For the two LUMO states (green), the SOMO (purple), and the SUMO (purple), the calculated molecular orbitals are presented in a top and a side view. Green and yellow colors indicate different phases of the spatial wave functions.

of [142]. Their claim is supported by a DFT study, of which they present a plot of the SOMO, and by a citation of a publication by Kochem *et al.* [228]. Based on an EPR analysis, Kochem *et al.* actually claim a main d_{z^2} orbital ground state for both complexes investigated in the study.[24] Additionally, Kochem *et al.* presented DFT data pointing to a mixed character of the SOMO with a major contribution of the d_{z^2} state (56 % and 53 % for the two investigated complexes) and an admixed d_{yz} state (40 % and 43 % for the two investigated complexes).

In the Wiesendanger group, three independently performed DFT studies have been presented in different publications [15, 16, 80]. In these studies, very similar results have been obtained, and the SOMO was identified as a MO with mainly d_{xz} character and a strong contribution of ligand orbitals. The SOMO and SUMO, as calculated in the DFT study presented in reference [80], are shown in Figure 3.7. Here, also the distortion of the d_{xz}-type SOMO due to the additional contribution of the d_{z^2} orbital, as described by Kochem *et al.*, can be seen. Furthermore, the figure shows that the orbital identified as the SOMO is not equivalent with the HOMO. This is because the different spin components of the same MO should still have a similar if not the same spatial appearance.

Another study, presenting DFT calculations for infinite chains synthesized from Co–Sal molecules, has been performed by García-Fernández *et al.* [223]. This study is focused on the band structure of [p-phenylene]$_n$ and [Co–Sal]$_n$ chains and the resulting charge transfer properties. Therefore, a discussion of the magnetic properties cannot be found in this paper. However, they present a MO in their Figure 6 b which closely resembles the d_{xz} type MO identified as the SOMO in its spatial appearance, but has a calculated energy closer to Fermi energy.

Overall the good agreement of the individual studies points to a good validity of the data and to a main d_{xz} orbital ground state. The only differences are slight rotations of the d_{xz} orbital contribution around the z-axis and a varying contribution of the d_{z^2} orbital and of ligand orbitals. However, the varying d_{z^2}-orbital contribution is hard to judge without access to the raw data. The relatively

[24] Their complexes differ in the choice of ligand end groups from each other and from the Co–Sal complex studied in this thesis. This should, however, not have an impact on the electronic ground state.

large d_{z^2}-orbital contribution in the study by Kochem *et al.* might be due to the fact that solvent effects were considered in their DFT calculations. DFT calculations of reference [15] were performed for molecules adsorbed on a Au(111) substrate. All other calculations were performed for molecules in the gas phase. The solvent in combination with the affinity of Co–Sal complexes to coordinate additional ligands along the z-axis might cause a higher d_{z^2}-orbital contribution due to the destabilization of the d_{z^2} orbital, as reported by Ceulemans *et al.* [144].

The magnetic anisotropy energy of Co–Sal was calculated by Qu *et al.* to $D \approx -2.4\,\mathrm{meV}$, which results in a preferred in-plane orientation of the spin [229]. This is also in accordance with the values for the $\tilde{g}$ tensor presented by Ceulemans *et al.* for the Co-salen complex [144]: $\tilde{g}_x = 1.66, \tilde{g}_y = 3.81, \tilde{g}_z = 1.74$. Recently, magnetic contrast of Br_2Co–Sal single molecules has been measured using SP-STM on Fe-intercalated graphene on Ir(111) (Gr/Fe/Ir(111)) [230]. The contrast was obtained in magnetic fields too small to affect the magnetic moment of the substrate. Therefore, the contrast could clearly be assigned to the molecular magnetic moment.

The magnetism of $[\text{Co–Sal}]_n$ chains has been investigated in DFT calculations [16]. It was shown that individual Co centers in these chains are coupled antiferromagnetically with an exchange constant of $J = -7.9\,\mathrm{meV}$. Here, the d_{xz} character of the SOMO plays an important role since this orbital can couple with the π-conjugated C system of the ligand via the p_z orbitals of the N and O atoms. For a d_{z^2}-type SOMO, this coupling would likely be lower, and the additional σ-like coupling would be ineffective over the relatively large distance between the magnetic centers. Therefore, the overall magnetic coupling would be weaker. The polarization mechanism was also suggested by Glaser *et al.* for salen type complexes [13, 14, 198]. The mechanism is facilitated by the delocalization of the SOMO over the whole ligand, as can be seen in Figure 3.7. Experimentally, the antiferromagnetic coupling has been proven by DiLullo *et al.*, who investigated Kondo features of $[\text{Co–Sal}]_n$ on Au(111) [15].

For the Br_3Co_3–Sal complex shown in Figure 3.8 b), DFT calculations predict ferromagnetic coupling with a coupling strength of $J = -4.6\,\mathrm{meV}$ via the spin

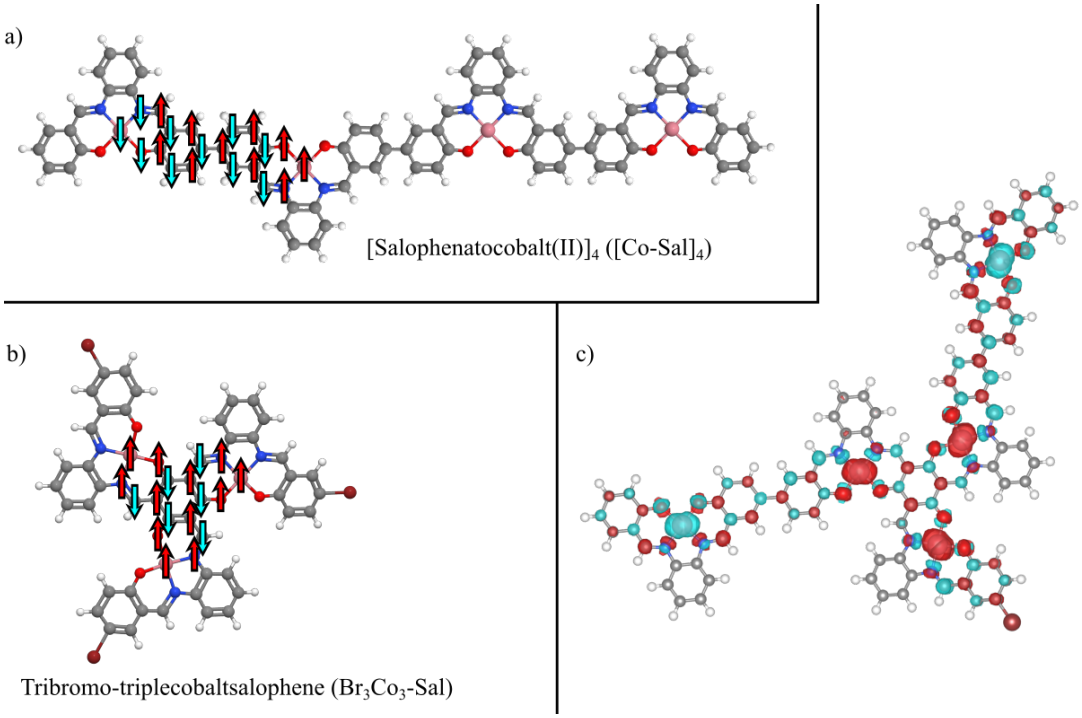

Figure 3.8: Visualization of the polarization mechanism in π-conjugated C systems. In a), the mechanism is depicted for a four membered $[\text{Co-Sal}]_4$-chain and in b) for Br_3Co_3–Sal. The blue and red arrows indicate the local polarization on the corresponding atom site. Panel c) shows a ball-and-stick model of the DFT calculated molecular-device structure consisting of a Br_3Co_3–Sal molecule and two Co–Sal molecules. The spatial distribution of the spin densities is plotted on top. Blue and red colors correspond to opposing spin directions.
Figure in panel c) adapted with permission from [16]. Copyright 2016 American Chemical Society.

polarization mechanism [16]. Based on this complex it is possible to create a prototypical spintronic device on the Au(111) surface [16]. DFT calculations of the spin-polarization in such a device, as shown in Figure 3.8, illustrate the coupling via the spin polarization mechanism. The antiferromagnetically coupled [Co–Sal]$_n$ chains serve as spin leads while Br_3Co_3–Sal serves as a logic gate.

4 Experimental Setups

The main experiments for this thesis were performed with two different STM setups: A variable-temperature STM for fast sample preparation used in the metalation experiments and a low-temperature STM for spin-polarized measurements. Both systems were built at the University of Hamburg and will be introduced here.

4.1 Low-Temperature STM

The low-temperature setup was originally built by Wittneven *et al.* [231]. A schematic of the state of the system during the course of this thesis is presented in Figure 4.1. It consists of three vacuum chambers with the STM chamber in the middle flanked by two preparation chambers. The left preparation chamber is used for the cleaning of samples and tips and the growth of graphene. It is connected to a small load lock for insertion of new samples and tips. Furthermore, the left chamber is equipped with an e-beam stage, a sputter gun, and multiple gas inlets. The setup allows for annealing of samples and tips in ultra-high vacuum (UHV) and O_2 atmosphere to temperatures of up to $\approx 1500\,\mathrm{K}$, as well as the growth of high-quality graphene layers.

The other preparation chamber is used for deposition of molecules and metals. It features an xyz-stage for reproducible positioning of tips and samples during the deposition processes. Via a built-in resistive heater, tip and sample can be heated during depositions.

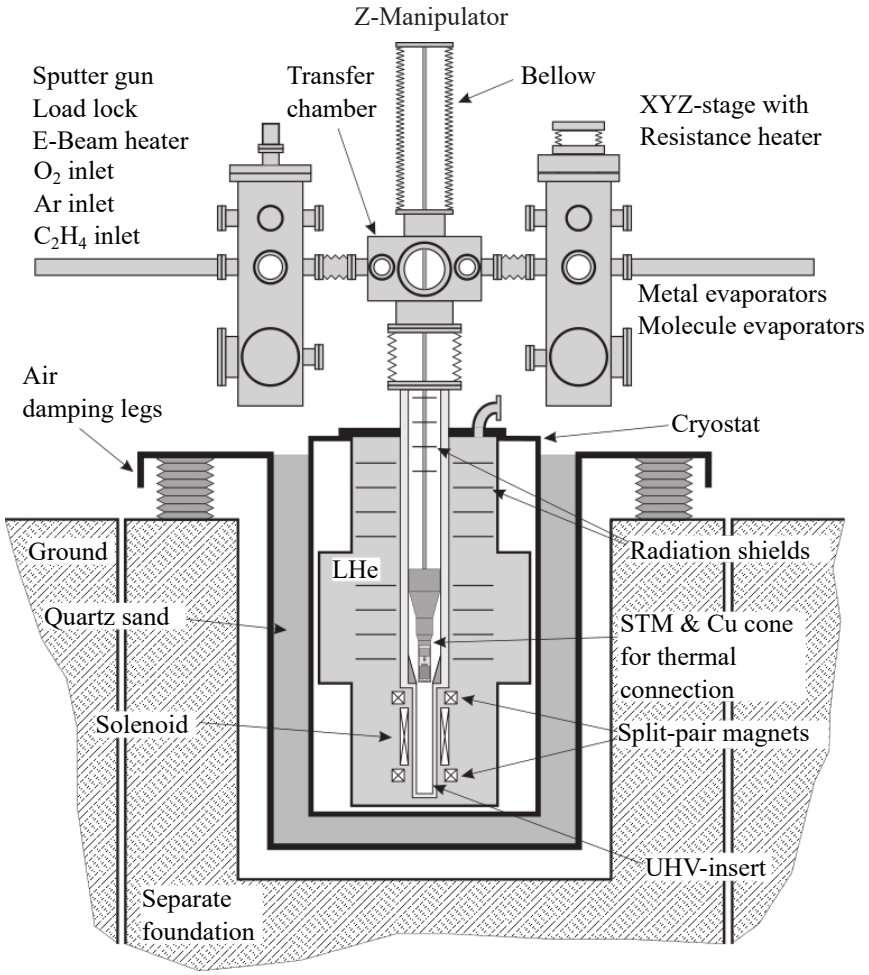

Figure 4.1: Schematic of the vacuum chamber of the low-temperature STM. Reprinted from [231], with the permission of AIP Publishing. New features implemented in the setup were added here and in reference [30].

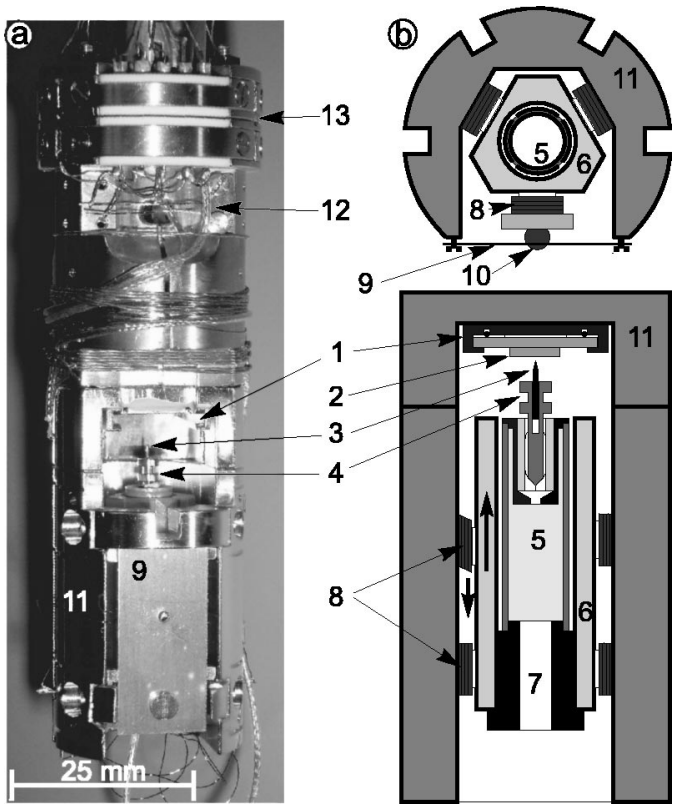

Figure 4.2: Photograph a) and schematics b) of the STM body. The schematics in b) show a top and a front view of the STM body. Individual components are numbered as follows: (1) Sample holder, (2) sample, (3) tip, (4) tip holder (molybdenum), (5) tube scanner, (6) sapphire prism, (7) tube scanner holder (macor), (8) shear-piezo stacks, (9) molybdenum leaf spring, (10) titanium ball, (11) microscope body (phosphorous bronze), (12) Cernox temperature sensor, and (13) electrical connector (OFHC copper).
Reprinted from [232], with the permission of AIP Publishing.

At the bottom, the STM chamber is connected to the bath cryostat, which is positioned inside a pit in the ground. With a capacity of about 90 l of liquid He, the STM can be kept at a temperature of 6.5 K for about three days with one filling. The STM body, depicted in Figure 4.2, is based on a design by Pan [233] and was further developed at the University of Hamburg [232, 234]. It is connected to a Cu cone that rests in a counter cone during measurements. For sample and tip exchanges, the STM has to be raised up into the STM chamber via a z-manipulator. In this position, measurements for a quick characterization of the sample can be performed, but for stable measurements at low temperatures and with magnetic fields the scanner has to be moved down into the cryostat. Thermal contact between the cooling stage with the counter cone and the liquid helium bath is created by N_2 exchange gas. For further stabilization of the temperature, a heater is connected to the STM body. This cooling concept leads to good temperature stability and low thermal drift.

Two superconducting magnets are placed inside the liquid helium bath. A solenoid magnet allows to apply magnetic fields of up to 6 T out-of-plane. Up to 2 T in-plane magnetic field can be created by a split-pair magnet. The whole system is mounted on a damping table supported by four passive damping legs, and is placed on a separate foundation to minimize introduction of noise. To further reduce the noise, the system can be pumped solely by ion pumps, one for each chamber. Additionally, each chamber is equipped with a titanium sublimation pump (TSP). A turbomolecular pump, mounted on the load lock, is only used for pumping down the UHV chamber after it was vented.

4.2 Variable-Temperature STM

The variable-temperature STM was built by Kuck *et al.* [236, 237] and is also based on the design by Pan [233]. Here, a brief summary of the main features of the current setup as presented in Figure 4.3 will be given. The STM chamber is directly connected to two preparation chambers, one at each side. One of these chambers is equipped with an Elion Pure Jet system for electrospray deposition

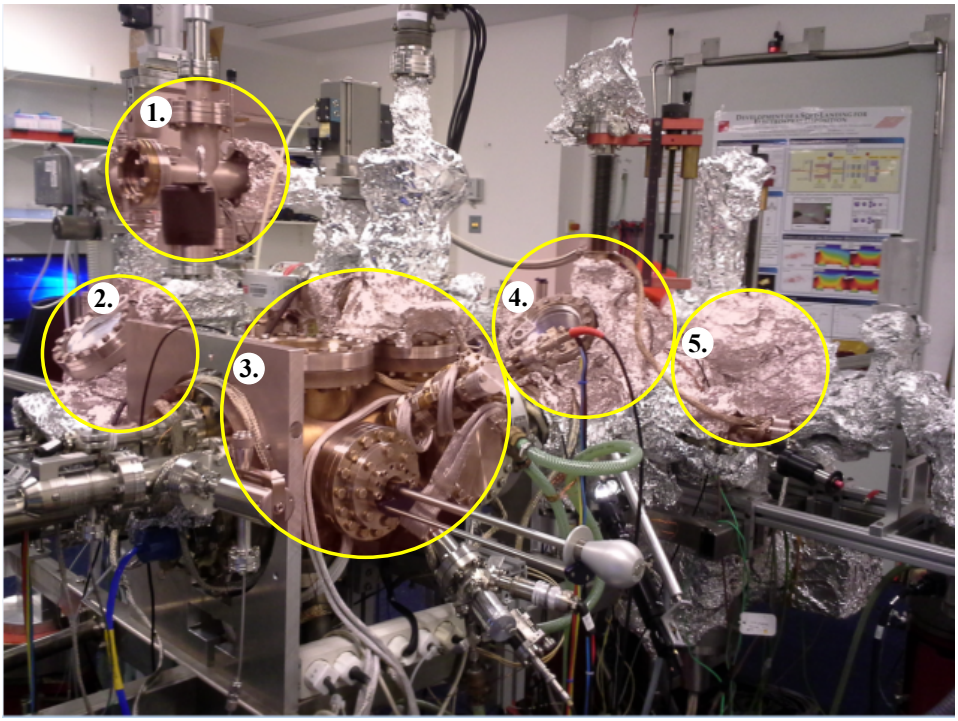

Figure 4.3: Photograph of the vacuum chamber with the variable-temperature STM setup. The individual chambers are marked with circles: 1. load lock, 2. storage chamber, 3. preparation chamber, 4. STM chamber, and 5. electrospray-deposition chamber. Figure adapted from [235].

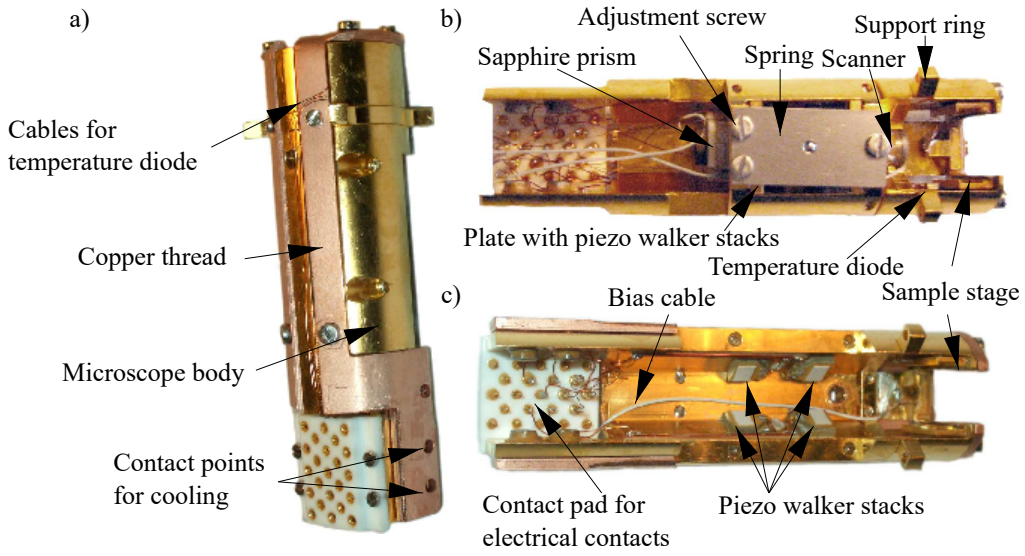

Figure 4.4: Photographs of the variable-temperature STM body from multiple angles. The back view is presented in a). The front view is presented with b) and without c) mounted scanner. Figure and caption adapted from [237].

of large molecules, which cannot be sublimated from a Knudsen cell [17]. This chamber is also connected to a load lock used to connect a UHV suitcase for sample transport between different UHV systems. In the other preparation chamber, all further preparation procedures can be done, such as Ar-ion sputtering, annealing, thermal sublimation of molecules, and e-beam evaporation of metals. A filament, mountable on the transfer rod, enables the deposition of metals and molecules at elevated sample temperatures. Attached to this chamber is a small chamber with a storage carrousel, followed by another small load-lock chamber for the introduction of evaporators, tips, and substrates.

Images of the STM body from different angles are presented in Figure 4.4. It is cooled by a flow cryostat and capable of measurements in a temperature range of 18 K up to 300 K. The flow of helium can be adjusted by a needle valve to control the temperature. A heater is used to stabilize the temperature of the STM at a fixed value, and a metal shield cooled by the backflow of the liquid helium reduces the heat input by radiation.

To minimize electronic noise, the STM is galvanically isolated from the vacuum chamber. To reduce mechanical noise, the STM is mechanically decoupled from the chamber by means of springs and an eddy-current damping stage. Additionally, the whole system is mounted on a rigid metal frame supported by four passive damping legs. The STM chamber is pumped by a combination of an ion getter and a non-evaporable getter pump to minimize vibrations. All other chambers are pumped by turbo pumps backed up by a rotary vane pump.

5 $[\text{Co-Sal}]_n$ on $GdAu_2$ Surface Alloy

Surface alloys are an interesting branch of two-dimensional materials offering a great variety of properties. In the past, the majority of research in this field concentrated on combinations of two transition metals [238], transition metals with rare earth metals [239, 240], and transition metals with noble metals [241]. Recently, surface alloys of rare earth metals with noble metals began to attract an increasing amount of interest [104, 105, 242, 243]. These surfaces combine weak ferromagnetism with the capability to catalyze on-surface Ullmann reactions. A study by Que *et al.* showed that a $TbAu_2$ surface alloy can support purely organic molecules, i.e. graphene nanoribbons, while pertaining their electronic states almost as in the free-standing molecule [105]. In the present chapter, the properties of the $GdAu_2$ surface alloy will be introduced, followed by details on the preparation procedure for the surface itself, the STM tip, and the single Br_2Co–Sal molecules and $[Co–Sal]_n$ chains on the substrate. Afterward, the findings concerning the electronic and magnetic properties of the system will be presented.

5.1 $GdAu_2$ Surface Alloy

While bulk $GdAu_2$ crystals [244] and thin amorphous layers of Au alloyed with Gd [245] are known for several years, well-defined single or double layer $GdAu_2$ surface alloys on Au(111) are a recent discovery. $GdAu_2$ as a two-dimensional surface alloy was first synthesized in 2010 by Corso *et al.* [242, 246]. They deposited Gd atoms by molecular-beam evaporation onto a Au(111) substrate held at a temperature of 550 K. Depending on the deposited amount of Gd atoms, they found

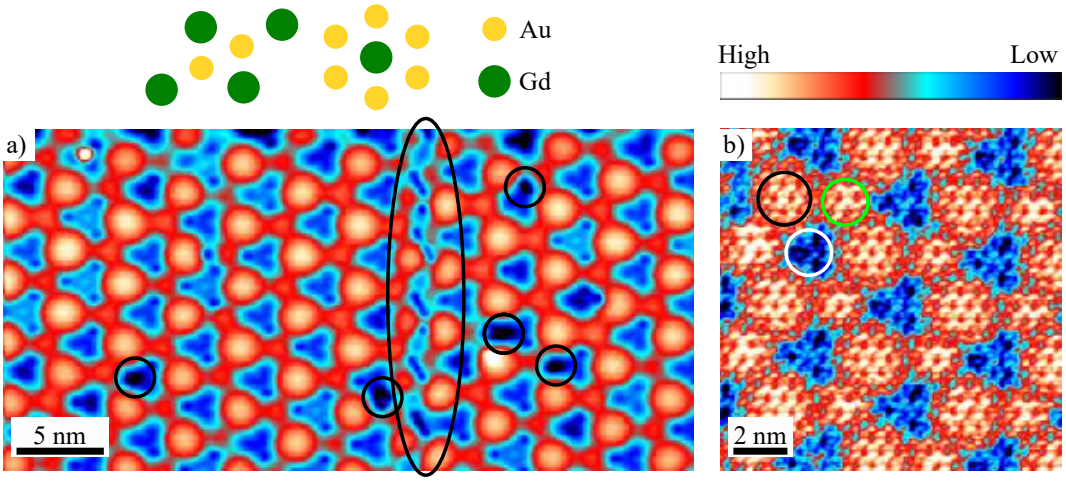

Figure 5.1: Topographic STM images of a single layer of the $GdAu_2$ surface alloy on Au(111). The moiré pattern can be seen clearly in both images. The topography image in a) shows two areas separated by a dislocation line. The dislocation line and several point defects are marked by black ovals. The topography image in b) shows the surface resolved with atomic resolution. The Au atoms are imaged as protrusions. Here, three different regions of the moiré pattern are marked by colored circles. The regions will be referred to according to reference [243]: TOP (white circle), HCP (black circle), and FCC (green circle). Above the STM images the unit cells of the Gd and Au sublattices are shown.
Tunneling parameters: a) $U = 3000\,\mathrm{mV}$; $I_{\mathrm{stab}} = 1\,\mathrm{nA}$; $z-$range $= 0.98\,\text{Å}$; b) $U = 50\,\mathrm{mV}$; $I_{\mathrm{stab}} = 50\,\mathrm{nA}$; $z-$range $= 1.13\,\text{Å}$.

different phases of the GdAu alloy [242]. At low concentrations, the discommensuration lines of the herringbone reconstruction are modified: First to a pattern of alternating straight and zigzag lines, then to a regular network of trigons with wave-like borders. With increased concentrations of Gd atoms, island growth of the $GdAu_2$ surface alloy, as shown in Figure 5.1, is initialized. After the growth of a full monolayer of $GdAu_2$ surface alloy, Corso *et al.* saw a sharp transition in their ARPES data indicating the growth of a second layer of $GdAu_2$ in a layer-by-layer fashion.

The structure of the $GdAu_2$ surface alloy corresponds to a (110) surface of the bulk $GdAu_2$ alloy and is characterized by a moiré pattern interrupted by dislocation lines, as seen in Figure 5.1 a) [247]. By choosing certain bias voltages, one can

easily image the Gd or the Au atoms of the surface individually. This simplifies imaging with atomic resolution. An example of a topography image with atomic resolution is presented in Figure 5.1 b). In this figure, the Au atoms are imaged as protrusions and the Gd atoms as hollow sites. As one can see in this image, the Au atoms form a honeycomb structure with six Au atoms surrounding one Gd atom.

The moiré pattern is caused by a lattice mismatch between the $GdAu_2$ layer and the Au(111) substrate. Therefore, three different regions are created as indicated in Figure 5.1 b): One with the Gd atoms on top of a Au atom in the layer beneath (TOP), another with the Gd atoms in an hexagonal close packed (hcp) position (HCP), and the third with the Gd atoms in a face centered cubic (fcc) position (FCC) [243]. Because of these variations in the adsorption sites, the moiré pattern has a corrugation of roughly 0.6 Å [242]. Its unit cell is rotated by $(30.8 \pm 0.15)^\circ$ in relation to the atomic unit cell of the Gd sublattice [247]. A mismatch of the moiré unit cell and the atomic unit cell causes the moiré pattern to be incommensurate.

The LDOS of the $GdAu_2$ surface alloy is characterized by a state at 600 meV, attributed to Au-5d and Au-6s states, and two states at 2500 meV and 3200 meV, attributed to Gd-5d states [247]. This can be seen from the SP-STS data in Figure 5.2 a) and from the DFT data in Figure 5.3. However, the local geometric structure, responsible for the moiré pattern, induces variations in the electronic structure of the different regions, as has been investigated thoroughly by Correa *et al.* [243]. Their results can be summarized in three major observations, all caused by an offset in the vertical position of the Gd atoms in the TOP regions relative to the first layer of the Au(111) substrate [243]. While the FCC and HCP regions do not show any differences in their electronic structure, the aforementioned offset of the Gd atoms induces an energy gap of 500 meV at Fermi energy in the TOP regions. Additionally, it causes a change in the hybridization of the Gd-pd orbitals with the Au-sp orbitals. Finally, also the energy of the Gd-4f states is affected by the local displacement of the Gd atoms.

Despite these local variations in the electronic structure, the magnetic properties of the $GdAu_2$ surface alloy are homogenous with respect to the moiré pattern, as

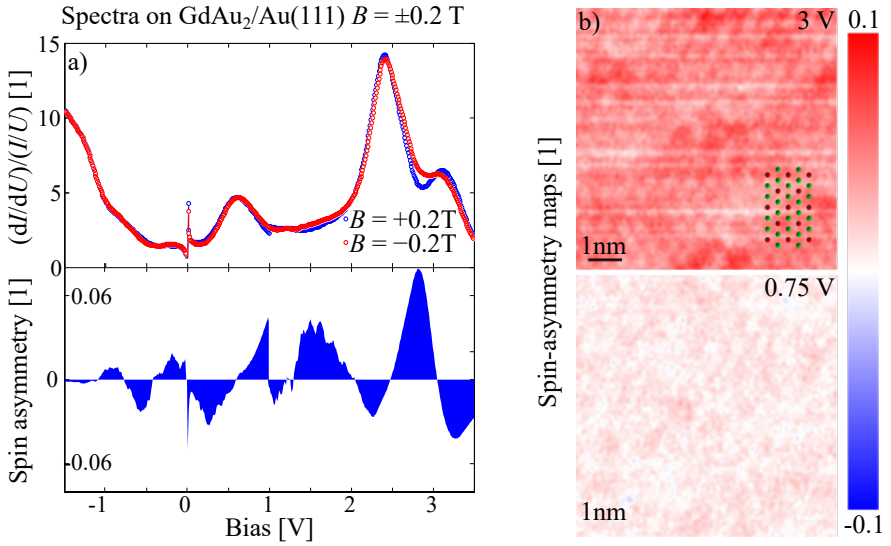

Figure 5.2: SP-STS data obtained on a single layer of the $GdAu_2$ surface alloy on Au(111) with in-plane magnetic fields. In a), normalized spin-polarized point-tunneling spectroscopy (SP-PTS) data obtained at the center of a HCP region and the corresponding spin asymmetry derived from the spin-resolved dI/dU curves are presented. In b), spin-asymmetry maps for energies corresponding to Gd ($U = 3000\,\mathrm{mV}$) and Au states ($U = 750\,\mathrm{mV}$) are shown. A model of the surface alloy is overlaid on top of the maps.
Reprinted figure with permission from [247].Copyright 2019 by the American Physical Society.

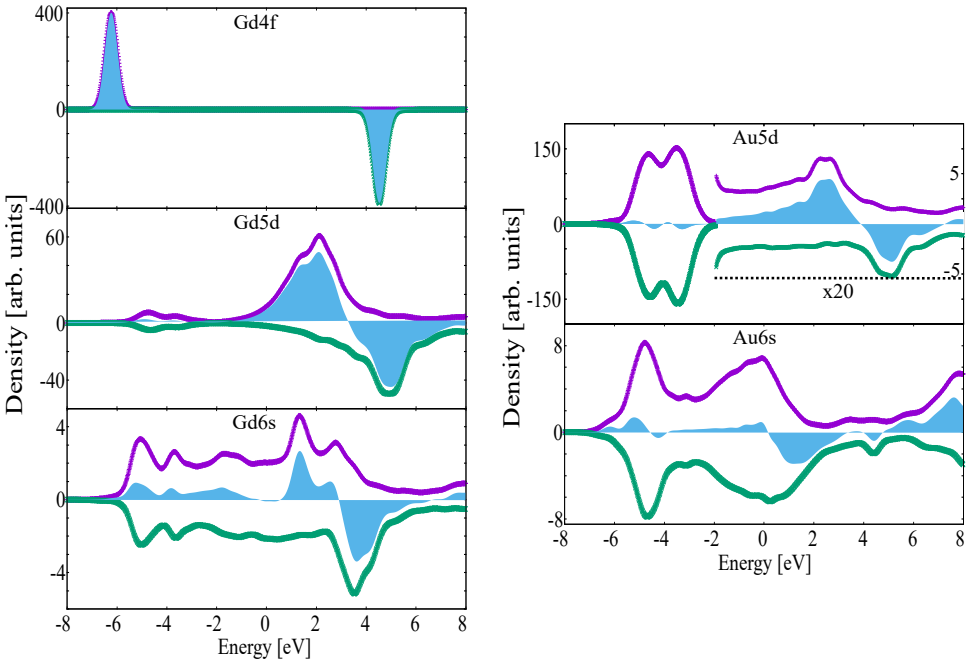

Figure 5.3: DFT-calculated partial density of states (PDOS) for different surface atoms and their electronic states. Each plot shows violet and green curves for the opposing spin channels and the corresponding spin asymmetry (filled blue). In the data for the Au 5d orbitals, the scale is enhanced for the energy range above −2000 meV for clarity.
Figure and caption adapted under permission from [247].

can be seen in Figure 5.2 b) [247]. While bulk $GdAu_2$ is antiferromagnetic [248, 249], the $GdAu_2$ surface alloy on top of Au(111) is ferromagnetic with an in-plane easy axis [247, 250]. This is caused by a difference in the packing resulting in a larger distance between the Gd atoms [246]. Because of the larger distance, the RKKY coupling, which is responsible for the magnetic ordering in the $GdAu_2$ alloy, changes its sign from ferromagnetic to antiferromagnetic. The same effect has also been observed for nearest neighbor coupling in amorphous thin-layer alloys of Gd and Au [245]. With a relatively low coercive field, varying between roughly 1.5 mT [251] and 17.5 mT [247] depending on the density of dislocation lines, the $GdAu_2$ surface alloy is a soft magnet. The ferromagnetic ordering persists up to a Curie temperature of $T_C = 19\,K$ [252].

As the spin-polarized DFT calculations presented in Figure 5.3 show, the magnetism of the system is mainly caused by the 4f states of the Gd atoms. However, the 4f states are relatively far from the Fermi energy with roughly 4.5 eV for the unoccupied and −6 eV for the occupied 4f states.[1] Additionally, they are strongly localized at the Gd atoms and decay rapidly into the vacuum [247]. Therefore, they are hardly accessible for SP-STS. Nonetheless, the SP-STS data in Figure 5.2 show spin asymmetry across the whole energy range from −1000 meV to 3500 meV. Particular high asymmetry can be seen for the aforementioned states at 600 meV, attributed to Au-5d and Au-6s states, and at 2500 meV and 3200 meV, attributed to Gd-5d states. This indicates that the spin polarization extends also to the Gd-5d and Gd-6s states as well as to the conduction electrons of the Au-5d and Au-6s states. The latter is responsible for the ferromagnetic RKKY interaction.

The polarization of the Gd-5d and Gd-6s states was also observed for $GdAu_2$ bulk systems and other Gd compounds [244, 249]. It was accounted responsible for the increased magnetic moment of the Gd atoms in alloy systems, which is larger than the value for a free Gd ion of $7\,\mu_B$. The investigation of larger-scale areas revealed that the dislocation lines interrupting the moiré pattern serve as anchors for the magnetic moment [247]. Neighboring areas divided by such a dislocation line are coupled antiferromagnetically. This explains the variations in the coercive field among different samples and the dependence on the density of dislocation lines since smaller areas have a higher coercive field.

Compared to other ferromagnetic substrates, the $GdAu_2$ surface is relatively inert because of the trivalent state of the Gd atoms [104]. Therefore, it is possible to prepare clean surfaces without contamination by impurities such as H_2, O_2, and C_2, which is a frequently encountered issue on other magnetic layers. Additionally, it promises low hybridization of molecular structures deposited onto this substrate. This was confirmed in a study by Abadia *et al.* who presented angular resolved photoemission spectroscopy data indicating chemisorption of $4,4''$-dibromo-p-terphenyl molecules on the $GdAu_2$ surface alloy [104]. In this study, they showed that the $GdAu_2$ substrate enables Ullmann-coupling reactions and

[1] 3.5 eV for the unoccupied and −8 eV for the occupied 4f states, according to supplementary data of reference [243].

that the ferromagnetic behavior of the substrate persists after covering it with organic molecules. The only change observed by Abadia *et al.* after the formation of polymeric chains from $4,4''$-dibromo-p-terphenyl molecules is a lowered Curie temperature of $T_C = 12.8\,\mathrm{K}$. This change was accounted to the formation of Br–Gd complexes.

Opposed to these findings, promising a low hybridization of molecules adsorbed on $GdAu_2$, a study by Farnesi Camellone *et al.* [253], following their investigations of the moiré pattern, found indications that the local variations in the electronic structure of $GdAu_2$ can influence adsorbed hydrogen-phthalocyanines. Next to differences in the adsorption energy depending on the adsorption site, they observed a site-selective dehydrogenation upon annealing of the sample. These variations are explained by the interaction between the cavities of the molecules, formed by N atoms, and substrate Gd atoms. In distinct positions of the moiré pattern, this distance is smaller and the Gd atoms are more accessible for the H atoms.[2]

5.2 Sample Preparation and Characterization

The Au(111) single crystal used during this thesis has been used for the growth of the $GdAu_2$ surface alloy multiple times. Therefore, at the start of the experiments it was already poisoned with Gd atoms that diffused into the bulk of the crystal. However, it was still possible to create a clean Au(111) surface by repeated cycles of Ar-ion sputtering and consecutive annealing. For Ar-ion sputtering, the crystal was kept in the focus of the ion source for 60 minutes with a base pressure of $4 \times 10^{-6}\,\mathrm{mbar}$ to $6 \times 10^{-6}\,\mathrm{mbar}$ and an acceleration energy of $0.8\,\mathrm{keV}$ for the ion beam. To heal the surface of the Au(111) crystal, it was heated for 20 minutes to a maximum temperature of about $855\,\mathrm{K}$. In the final cycle, the duration for the sputtering was reduced to 30 minutes.

[2] As mentioned earlier in Chapter 2.3.2, dehydrogenation is limited by H transfer from the molecule to the catalyzing substrate atoms. Therefore, it is reasonable that a larger separation of the molecule from the metal hinders the dehydrogenation.

A $GdAu_2$ layer was obtained by vapor deposition of Gd from an e-beam evaporator onto the Au(111) crystal kept in the temperature range of 608 K to 613 K. With these parameters, the resulting $GdAu_2$ surface is pervaded by dislocation lines. This gives access to areas of opposite magnetization direction for small external fields. Gd was deposited for 5 minutes to obtain close to one full monolayer coverage of $GdAu_2$. Lower coverages lead to a preferred adsorption of the Co–Sal molecules on areas of Au(111), especially at elevated sample temperatures needed for the Ullmann coupling. In addition, the few remaining areas of Au(111) are welcome for the *in situ* manipulation and characterization of the STM tip.

Because of the soft magnetism of the $GdAu_2$ surface alloy, an antiferromagnetic Cr-bulk tip was used for the measurements. This guaranties the possibility to obtain spin-polarized data without influencing the sample with the tip's stray field, as it is possible for ferromagnetic tips. The Cr-bulk tips were chemically etched in two-molar sodium hydroxide (NaOH) from a 0.5 mm thick wire and cleaned by consecutive annealing cycles at temperatures of roughly 900 K for 10 minutes. Since the spin contrast of a perfectly shaped antiferromagnetic tip depends only on the atom sitting at the apex of the tip, the spin contrast can be changed by manipulating the tip geometry *in situ*.

After the growth of the $GdAu_2$ layer, the sample has to cool down for the deposition of the molecules. To get single molecules, the deposition was started at temperatures below 373 K. For the growth of the $[Co–Sal]_n$ chains, the sample was held at 483 K to 493 K during the deposition. The $Br_2Co–Sal$ molecules were deposited from a crucible heated to a temperature of 533 K to 538 K for 15 minutes to 30 minutes. An overview of a sample with single molecules and a sample with $[Co–Sal]_n$ chains is presented in Figure 5.4. For the single molecules, it can be seen that the molecules avoid the HCP and FCC regions of the moiré pattern. Some isolated molecules can be found at adsorption sites similar to the ones reported for phthalocyanines on $GdAu_2$ [253]. However, opposed to these results, $Br_2Co–Sal$ does not cover equivalent adsorption sites until all of these sites are occupied, but instead the molecules tend to adsorb preferably in small clusters covering the TOP regions of the moiré pattern.

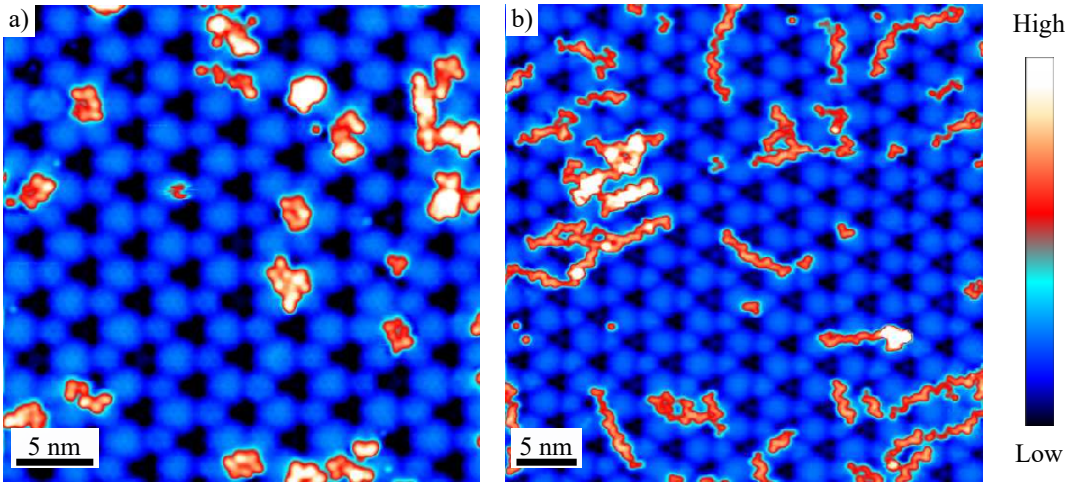

Figure 5.4: STM topographs of Co–Sal molecules on the $GdAu_2$ surface alloy on Au(111). Data on a sample of single Br_2Co–Sal molecules after deposition onto the substrate held at room temperature are presented in a), while $[\text{Co–Sal}]_n$-chains after deposition onto the substrate held at an elevated temperature are shown in b).
Tunneling parameters: a) $U = 500\,\text{mV}$; $I_{\text{stab}} = 100\,\text{pA}$; $z-$range $= 2.1\,\text{Å}$; b) $U = 100\,\text{mV}$; $I_{\text{stab}} = 100\,\text{pA}$; $z-$range $= 3.1\,\text{Å}$.

After deposition onto the substrate held at elevated temperatures most of the molecules have formed chains of random length. Opposed to $[\text{Co–Sal}]_n$ chains grown on Au(111), where the chains follow the discommensuration lines and are very straight, here, many of the chains are bent. It can be seen that a big fraction of the chains also adsorb on the HCP and FCC regions. One could assume that this is only because the chains are too long to fit into TOP regions exclusively, but this would not explain why some chains are positioned on HCP and FCC regions along the whole length of the chain. Another more likely reason are local changes in the adsorption energy due to deformations of the substrate and the molecules induced by the elevated temperature. Further hints toward the latter interpretation will be seen in the course of this chapter.

5.3 Electronic Properties

The results presented by Correa *et al.* and Camelloni *et al.* considering the local variations in the electronic structure and their influence on adsorbed molecules indicate difficulties when interpreting the electronic structure of molecules adsorbed on the $GdAu_2$ suface alloy on Au(111) [243, 253]. For example, a typical normalization technique for PTS data on molecules, as suggested by Wahl *et al.*, is not possible [254]. In this normalization procedure, PTS data obtained on the bare surface are subtracted from PTS data obtained on the molecule to separate molecular features from substrate and tip features. Because of the variations in the local electronic structure of the substrate, this procedure is not possible on the $GdAu_2$ surface alloy. Instead, the assignment of spectroscopic features has to be done carefully. To identify tip-induced features, the tip was characterized on areas of the clean $GdAu_2$ surface before each set of measurements on molecules.

Figure 5.5 shows STS data obtained on two single Br_2Co–Sal molecules on $GdAu_2$. This data was measured by Maciej Bazarnik.[3] The point spectra on both molecules show two features in the positive energy range. One feature at about 650 meV is very close to the state at 600 meV of the $GdAu_2$ surface alloy. Anyway, the deviation from the spectroscopy on the bare surface indicates the presence of a molecular state at this energy, which is the LUMO. The second feature caused by the LUMO+1 and higher order unoccupied molecular orbitals is very broad. A maximum can only be seen for one of the molecules, represented by the blue curve, at 1870 meV. The red curve only shows the onset of this state since the lock-in amplifier was registering an overload in the signal.

For the negative energy range, a striking difference between the molecules becomes apparent. While the red curve hardly deviates from the data obtained on the bare substrate, the other molecule shows a clear state with a maximum at −1230 meV. The difference can also be seen in the $\mathrm{d}I/\mathrm{d}U$ maps obtained at an energy of −1000 meV. Only the $\mathrm{d}I/\mathrm{d}U$ map corresponding to the blue curve shows a feature positioned at the center of the molecule, where also the Co atom is positioned.

[3] Dept. of Physics, University of Hamburg, D-20355 Hamburg, Germany; Institute of Physics, Poznan University of Technology, 60-965 Poznan, Poland

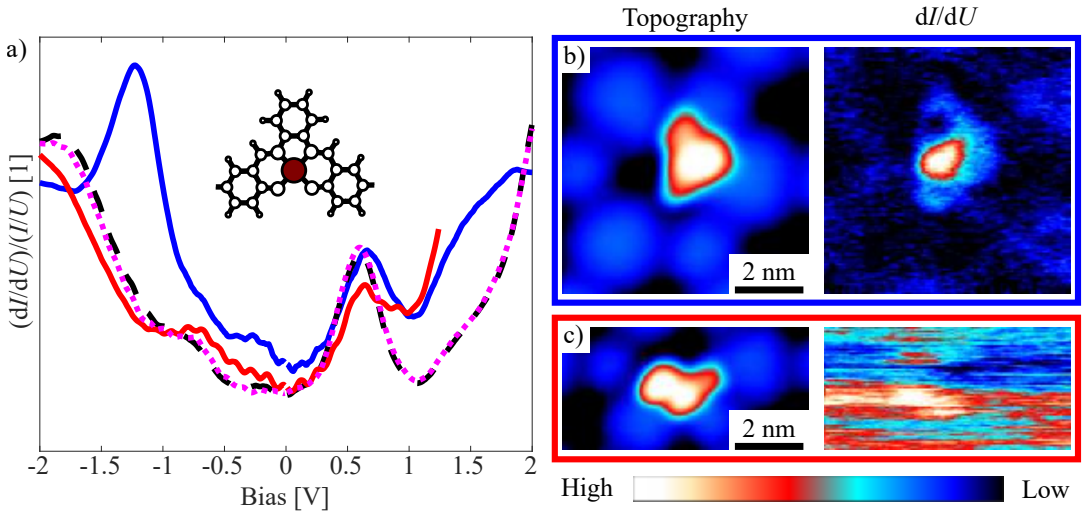

Figure 5.5: STS data on single Br_2Co–Sal molecules on $GdAu_2$ on Au(111). In a), PTS data obtained on two different molecules (red and blue curve) and corresponding spectra taken on the bare substrate with the same tip (pink and black curve) are presented. The red curve was cut at 1.1 V since the lock-in amplifier registered an overload of the signal. A dark red dot on a schematic of the molecule indicates the position at which the spectra were obtained. In b), topography images and corresponding $\mathrm{d}I/\mathrm{d}U$ maps of the molecules are shown. The borders around the images indicate which set belongs to which curve. The lower $\mathrm{d}I/\mathrm{d}U$ map is of inferior quality since the scanning speed was too high for the set time constant on the lock-in amplifier.
Tunneling parameters: a) $U_{\mathrm{stab}} = -1000\,\mathrm{mV}$; $I_{\mathrm{stab}} = 75\,\mathrm{pA}$; $U_{\mathrm{mod}} = 50\,\mathrm{mV}$; b) top: $U = -1000\,\mathrm{mV}$; $I_{\mathrm{stab}} = 100\,\mathrm{pA}$; $U_{\mathrm{mod}} = 50\,\mathrm{mV}$; $z-$range $= 1.64\,\text{Å}$; bottom: $U = -1000\,\mathrm{mV}$; $I_{\mathrm{stab}} = 750\,\mathrm{pA}$; $U_{\mathrm{mod}} = 50\,\mathrm{mV}$; $z-$range $= 1.64\,\text{Å}$.

Since the adsorption positions of both molecules are equal, the differences in the electronic structure cannot be caused by the adsorption position.

Figure 5.6 shows data obtained on $[\text{Co–Sal}]_n$ chains. Here, the two features in the positive energy range can be observed as well. Only the onset of the state positioned at above 1000 meV appears in the spectra because of the limited energy range. The energies at which the maxima of the LUMO states are observed vary within the range from 550 meV to 750 meV for the individual members of the chain. Additionally, when comparing the $\mathrm{d}I/\mathrm{d}U$ maps at 1450 meV and 1750 meV, it appears that the LUMO+1 states contributing to the feature above 1000 meV have maxima at different energies. At 1450 meV the central member shows the highest intensity of the $\mathrm{d}I/\mathrm{d}U$ signal and at 1750 meV the molecule on the left shows the highest signal. These variations in the positions in energy of the electronic states were not observed for $[\text{Co–Sal}]_n$ chains on Au(111) [15] or Ag(111) [17]. This indicates that the differences are induced by the substrate and its locally varying electronic structure.

To support the earlier claim that the features around 600 meV in the PTS data obtained on the molecules are indeed caused by the LUMO, one can take a look at the $\mathrm{d}I/\mathrm{d}U$ map at 650 meV in Figure 5.6 b). Here, a signal comparable to the level of the surrounding substrate can be seen at the positions of the Co atoms of the $[\text{Co–Sal}]_n$ chain, while the signal is suppressed for the areas covered by C atoms. This indicates a MO with a main contribution of the Co atoms at this energy, which causes the feature in the PTS data. The LUMO+1 is characterized by two bright features flanking each of the bridges of the individual members. Because of this characteristic appearance, it can be assigned to the ligand state, which was identified as the LUMO in the DFT calculations of Co–Sal, as presented in Chapter 3.6. However, the $\mathrm{d}I/\mathrm{d}U$ map at 1750 meV shows that, instead of a nodal plane cutting through the symmetry axis of the left member, there is also a large signal on the Co center of this member. This is likely caused by a MO with a Co-3d-orbital contribution, which is lowered in energy. For the other two members, the expected node can be observed in the map obtained at 1450 meV. These observations suggest significant hybridization of the molecules with the substrate. In particular, the Co centers are hybridized, leading to an

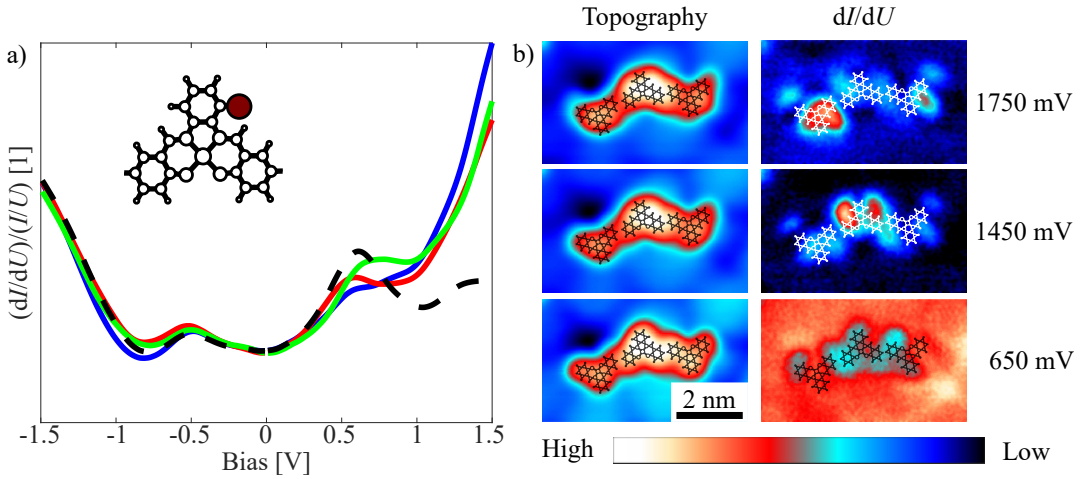

Figure 5.6: STS data obtained on $[\text{Co–Sal}]_n$ chains on $GdAu_2$ on Au(111). In a) PTS data obtained on various positions on top of a chain and one curve taken on the bare substrate with the same tip (black curve) are presented. A dark red dot on a schematic of the molecule indicates the position at which the spectra were obtained. In b) topography images and corresponding $\mathrm{d}I/\mathrm{d}U$ maps of a $[\text{Co–Sal}]_n$ chain at different energies are shown. A model of the Co–Sal molecule is superimposed to indicate the positions of the chain's individual members.
Tunneling parameters: a) $U_{\text{stab}} = -1500\,\text{mV}$; $I_{\text{stab}} = 200\,\text{pA}$; $U_{\text{mod}} = 100\,\text{mV}$; b) $I_{\text{stab}} = 100\,\text{pA}$; $U_{\text{mod}} = 100\,\text{mV}$; $z-$range $= 2.55\,\text{Å}$.

energy shift of the unoccupied MOs with a strong contribution of Co-3d orbitals toward Fermi energy.

For negative energies, the signal obtained on the molecules hardly differs from the signal obtained on the substrate, as it was the case for the data on single molecules. Comparing the $\mathrm{d}I/\mathrm{d}U$ maps over the energy range of $-450\,\mathrm{meV}$ to $-1050\,\mathrm{meV}$ in the middle column of Figure 5.7 with those from Figure 5.6, confirms that the $\mathrm{d}I/\mathrm{d}U$ signal barely differs between the substrate and the molecules. Additionally, the maps in the middle column of Figure 5.7, which are plotted with an adjusted scale, show that no individual states can be identified. The signal takes different shapes around the location of each individual member of the $[\mathrm{Co–Sal}]_n$ chain. This signal is continuous over the whole energy range. Together with the variations of the position in energy for the unoccupied states, the band-like structure for negative energies indicates strong hybridization of the system. Similar effects were observed for cobalt-phthalocyanine molecules on thin Fe films on W(110) [255]. In this study, Brede *et al.* presented DFT calculations showing that hybridization can lead to drastic changes in the electronic structure of adsorbed molecules and that the molecular states can be broadened up to an extent where they form band-like structures.

A possible reason for the strong hybridization is the tendency of the Co–Sal molecule to coordinate additional nucleophilic ligands along the z-axis to the Co atom [144, 228, 256]. This is also supported by the disappearance of the HOMO state that was observed at $-1000\,\mathrm{meV}$ for some of the single molecules, which indicates an electron transfer from the molecule toward the sample. Additionally, the appearance of the ligand state in the STS data obtained on the chain shows that the hybridization is concentrated on the Co atom since this state is only shifted in energy due to the electron transfer but has still its typical appearance.

It is remarkable that after polymerization there were no molecules found which showed the state that was observed at $-1000\,\mathrm{meV}$ for single molecules. This indicates that not only the adsorption site of the molecules controls the hybridization since the length of the chains forces molecules into all kinds of adsorption positions. Instead, it suggests that the heating of the sample changes the interaction of the

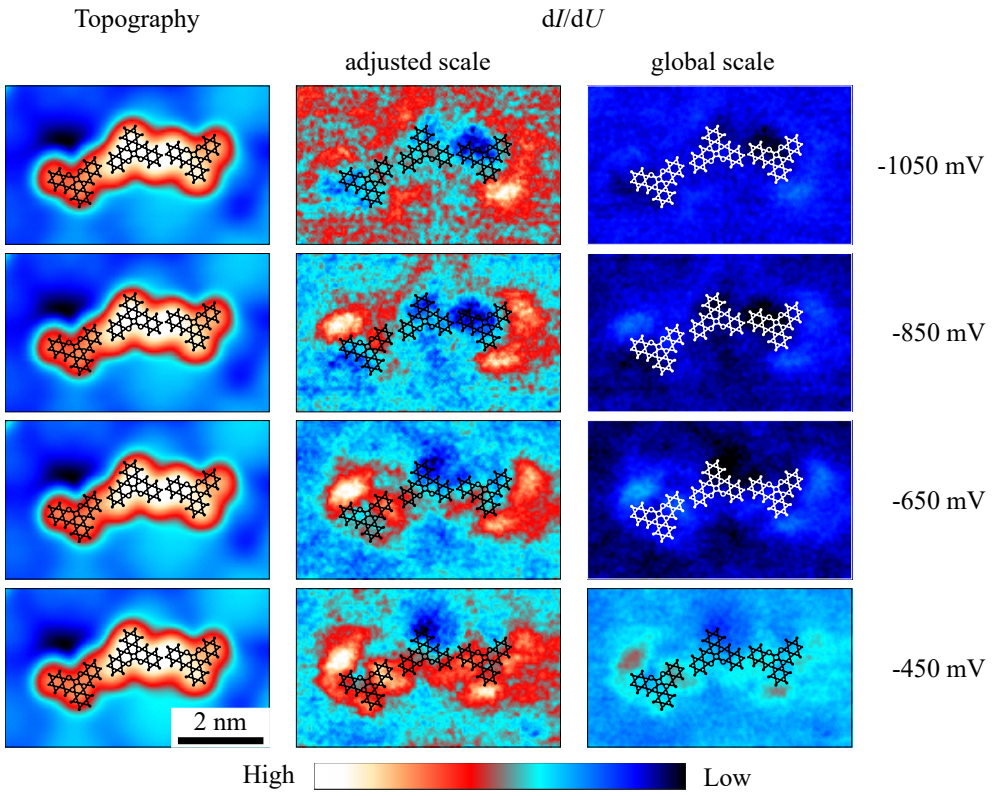

Figure 5.7: STS data obtained on $[\text{Co–Sal}]_n$ chains on $GdAu_2$ on Au(111). The left column shows topography images of a $[\text{Co–Sal}]_n$ chain at different energies. In the middle column corresponding $\mathrm{d}I/\mathrm{d}U$ maps with the color scale adjusted to observe the features of the molecule–substrate hybrid system. $\mathrm{d}I/\mathrm{d}U$ maps with the same scale as used in Figure 5.6 are shown in the right column. A model of the Co–Sal molecule is superimposed to indicate the positions of the individual members. Tunneling parameters: $I_{\mathrm{stab}} = 100\,\mathrm{pA}$; $U_{\mathrm{mod}} = 100\,\mathrm{mV}$; $z-$range $= 2.55\,\text{Å}$.

molecules and the substrate. It is likely that, due to the additional mobility of the substrate atoms, Gd atoms, which are most likely to interact with the Co atoms of the molecules, can change their vertical position to optimize the interaction with the molecules. In return, the Co atoms of the molecules can reposition to further optimize the distance between Gd and Co atoms, and a bond can be created.

5.4 Magnetic Properties

To determine whether the magnetism of the molecules and the substrate is preserved after the growth of $[\text{Co–Sal}]_n$ chains on top of the $GdAu_2$ surface alloy, XMCD experiments were performed. These were followed by an investigation of the local magnetic properties by means of SP-STS, revealing the intramolecular magnetic properties. For the XMCD experiments, the substrates were prepared with a coverage close to a full monolayer to get a sufficient signal. In the STM experiments, the coverage was limited to 0.2 to 0.4 monolayers to be able to investigate individual chains.

5.4.1 XMCD

The XMCD data presented here were obtained at the X-Treme beamline of the Swiss light source (SLS) of the Paul Scherrer Institut [257]. All experiments were performed by M. Bazarnik[3] and J. Dreiser[4] who also extracted the results presented in Table 5.1 from the data. During the experiments, the sample had a temperature of 1.5 K to 3.0 K. The data presented in Figure 5.8 were obtained with a normal incidence of the X-ray beam.[5] Therefore, they provide information about the out-of-plane magnetic properties of the sample. After the polymerization of the molecules, the XAS signal and the resulting XMCD measured for the L_{II} and L_{III} edges of Co is diminished because of the lower amount of molecules left on the sample. In the magnetization curves obtained for the Gd-M_{V} edge with a field

[4]Swiss Light Source, Paul Scherrer Institut, CH-5232 Villigen PSI, Switzerland
[5]The external magnetic field was always aligned collinear with the incident X-ray beam.

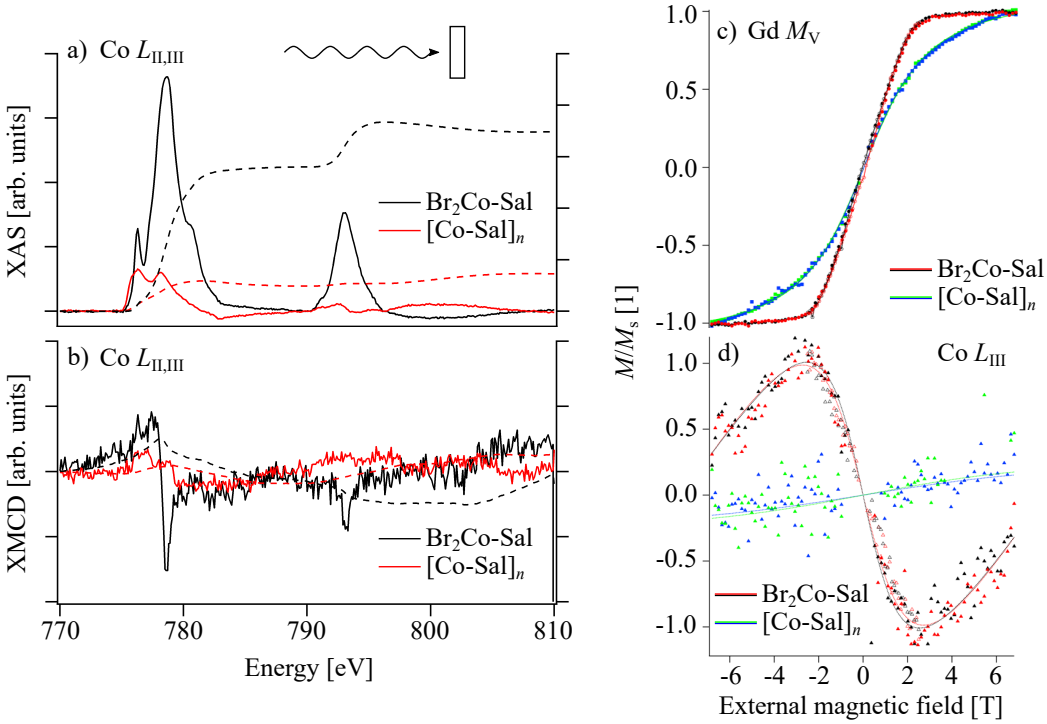

Figure 5.8: XAS and XMCD data with normal incidence of the X-ray beam for Co–Sal molecules on $GdAu_2$/Au(111). In a), XAS data on single Br_2Co–Sal molecules (black) and on [Co–Sal]$_n$ chains (red) for an out-of-plane external field of 6.8 T is presented. The dotted lines indicate the background signal that was subtracted to get the pure XAS signal. In b), the extracted XMCD signal is plotted. On the right hand side, the normalized field dependent magnetization is shown for Gd atoms c), measured at the M_V edge, and for Co atoms d), measured at the L_{III} edge. Red and black data show the results for single Br_2Co–Sal molecules, green and blue data indicate the results for samples with [Co–Sal]$_n$ chains.

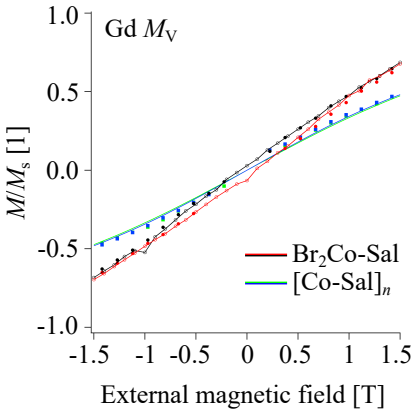

Figure 5.9: Out-of-plane magnetization curve obtained for Gd atoms at the M_V edge for a field range of ±1.5 T. Data for single Br_2Co–Sal molecules on $GdAu_2$/Au(111) are presented in black and red, and for [Co–Sal]$_n$ chains in blue and green.

range of ±6.5 T, no hysteresis can be seen. At the same time, the magnetization curve obtained for a smaller field range of ±1.5 T, presented in Figure 5.9, shows a non-zero hysteresis at the Gd-M_V edge for the sample with single molecules. However, after the Ullmann reaction the hysteresis disappears and the substrate behaves paramagnetic.

Comparison between the out-of-plane magnetization curves obtained for the Co-L_{III} edge and the Gd-M_V edge, before the Ullmann reaction, shows that the Co centers of the single Br_2Co–Sal molecules interact antiferromagnetically with the substrate. Only for magnetic fields above 2 T, the magnetization starts to align toward the field direction. This is the same field strength at which the substrate magnetization is saturated. Usually, antiferromagnetic coupling of paramagnetic molecules with a magnetic substrate is attributed to a 180° superexchange interaction mediated by the organic ligand. For the present system, however, an immediate pathway via an electronic bond formed between the Co atom and Gd atoms of the substrate must be considered. Antiferromagnetic coupling also has been reported for Co clusters of mono-atomic height on the $GdAu_2$ surface, where no ligand is available to mediate a superexchange pathway [250, 252, 258]. Remarkably, Fernandez *et al.* found that the antiferromagnetic coupling of this system goes hand in hand with the development of an to out-of-plane anisotropy after

the deposition of the Co clusters. They attribute this change to the formation of a $Co_n/GdAu_2$ system with unique properties [250]. Since no XMCD data was obtained on the clean $GdAu_2$ substrate in the here presented experiment, it cannot be judged whether the deposition of single Br_2Co–Sal molecules causes such local changes of the anisotropy. A direct comparison of the data presented in Figures 5.8 and 5.9 with the data presented by Garcia-Fernandéz *et al.* [250] should be handled with care since the magnetic properties of the $GdAu_2$ surface alloy can vary with the local atomic structure of the surface, as mentioned above.

In the case of Co clusters, the anisotropy changes back to in-plane anisotropy when either the height of the clusters is increased or with the start of coalescence of neighboring Co-clusters, initializing the formation of larger Co islands [252]. For Co–Sal on $GdAu_2$, these situations are inaccessible. However, after the polymerization reaction the antiferromagnetic coupling of the Co atoms and the substrate disappears. At the same time, the Gd loses its ferromagnetic behavior and behaves paramagnetic instead, with an increased saturation field.

The in-plane data presented in Figure 5.10 shows the same reduction in the signal strength after polymerization as the out-of-plane data. Here, the magnetization curve obtained from the Gd-M_V edge for the large field range shows clear hysteresis before the Ullmann reaction. This shows that the easy axis of the substrate on average remains in-plane after the deposition of Br_2Co–Sal, and only those Gd atoms interacting with a Co atom might have changed to an out-of-plane anisotropy. Surprisingly, the in-plane magnetization curve obtained from the Co-L_{III} edge for single Br_2Co–Sal molecules has the same sign as the magnetization curve for the substrate. In contrast to the data on Co clusters on $GdAu_2$, no antiferromagnetic coupling with the substrate is observed for the in-plane magnetic moment of single Br_2Co–Sal molecules.

From the XMCD data, the element-specific spin and orbital magnetic moments can be calculated using the sum rules introduced in Section 2.2.2. The results are summarized in Table 5.1, with an estimated error of 10 %. It has to be noted that the in-plane data will have an additional out-of-plane component due to the grazing incidence of the X-ray beam and the collinear alignment between the

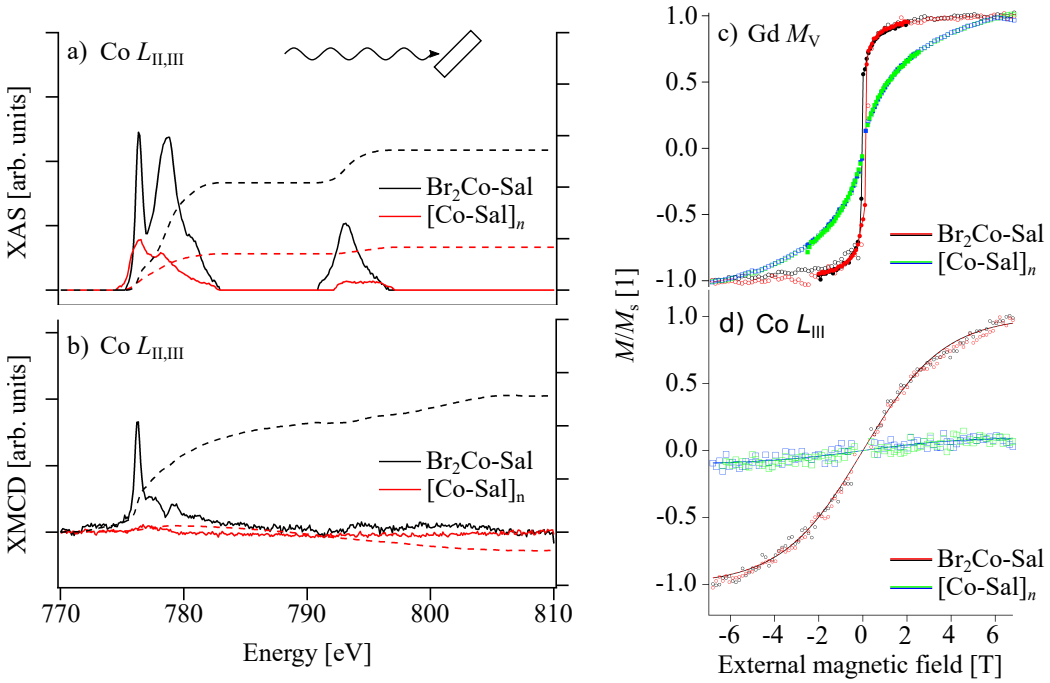

Figure 5.10: XAS and XMCD data with grazing incidence of the X-ray beam for Co–Sal molecules on $GdAu_2$/Au(111). The incidence angle of the X-ray beam was 60° off the surface normal. In a), XAS data on single Br_2Co–Sal molecules (black) and on [Co–Sal]$_n$ chains (red) for an external field of 6.8 T aligned collinear with the incident beam is presented. The dotted lines indicate the background signal that was subtracted to get the pure XAS signal. In b), the extracted XMCD signal is plotted. On the right hand side, the normalized field dependent magnetization is shown for Gd atoms c), measured at the M_V edge, and for Co atoms d), measured at the L_{III} edge. Red and black data show the results for single Br_2Co–Sal molecules, green and blue data indicate the results for samples with [Co–Sal]$_n$ chains.

Table 5.1: Calculated magnetic moments of Co and Gd before and after the polymerization by Ullmann reaction:

	out-of-plane incidence [μ_B]		grazing incidence [μ_B]	
	Br_2Co–Sal	$[Co–Sal]_n$	Br_2Co–Sal	$[Co–Sal]_n$
Co:$\boldsymbol{M}_{\mathbf{S}\|\|,\mathrm{eff}}$	−0.28	0.12	−0.66	−0.06
Co:$\boldsymbol{M}_{\mathbf{L}\|\|}$	0.12	0.09	−0.57	−0.04
Gd:$\boldsymbol{M}_{\mathbf{S}\|\|,\mathrm{eff}}$	−6.67	−5.95	−6.91	−6.20
Gd:$\boldsymbol{M}_{\mathbf{L}\|\|}$	−0.72	−0.29	−1.74	−0.62

external magnetic field and the incident X-ray beam. Furthermore, the shown values of the effective spin magnetic moments contain the magnetic dipole term, as mentioned in Section 2.2.2. This term is small enough to be neglected in cubic systems but has to be considered in systems of low dimensionality as the present system [259].

The values for the Co-effective spin magnetic moment are below the expected value of $1\,\mu_B$ in all cases. This can be explained by a combination of three different effects: First, the applied field might not be sufficient to completely align the magnetic moment of the molecules with the incident beam, second, the additional contribution due to the magnetic dipole operator can reduce the effective spin magnetic moment, and, third, an electron transfer between molecules and substrate due to hybridization can reduce the total spin magnetic moment of the molecules. In agreement with the results by Qu *et al.*, who calculated a magnetic anisotropy energy of $D \approx -2.4\,\mathrm{meV}$ for Br_2Co–Sal [229], the in-plane magnetic moments are considerably higher than the out-of-plane moments for the single molecules. Therefore, it is plausible that the out-of-plane behavior of the magnetization in an out-of-plane external field is dominated by the antiferromagnetic interaction with the substrate, while the in-plane behavior is governed by the interaction with the external magnetic field aligned at 60° off the surface normal because of the larger magnetic moment in this direction. The orbital magnetic moments are of the same order of magnitude as the spin magnetic moments in almost all cases. Only the out-of-plane component of the orbital magnetic moment for single molecules is

less than 50 % of the spin magnetic moment, and the two magnetic moments are aligned antiparallelly.

The spin magnetic moments of the Gd atoms of roughly $7\,\mu_B$ in-plane as well as out-of-plane before the polymerization corresponds to the electronic configuration of a half-filled 4f shell. However, this configuration would suggest zero orbital magnetic moment, which is not reflected in the data. Additionally, it should not be forgotten that it is the effective spin magnetic moment which is shown in the data. The large in-plane anisotropy of the Gd-orbital magnetic moment suggests that it is the reason for the overall in-plane anisotropy of the $GdAu_2$ surface. This influence of the orbital magnetic moment on the anisotropy of magnetic films has been reported for 3d-transition metal thin films [260, 261].

All magnetic moments are reduced after the polymerization, especially the in-plane components for the Co atoms, which are almost zero. The lower magnetic moments of the Co and the Gd atoms, as well as the lower relative magnetization observed in the magnetization curves of the Co atoms, both after the Ullmann reaction, can have different reasons. One possible reason is that due to increased hybridization and an accompanying electron transfer from the molecule to the substrate the magnetic moments of molecules and substrate atoms are reduced. In this case, the interruption of the ferromagnetically ordered $GdAu_2$ layer by the locally formed Co–Gd hybrid systems would be an explanation for the paramagnetic behavior of Gd after the polymerization. The residual magnetization of the Co atoms would be caused by a partial occupation of the molecules by an unpaired electron or by molecules remaining weakly hybridized. Note that this explanation agrees with the findings resulting from the discussion of the electronic properties, which indicated an increase in hybridization between molecules and substrate upon heating of the sample. Another possible reason is the antiferromagnetic coupling within the chains, which leads to even-membered $[\text{Co–Sal}]_n$ chains having a zero net magnetic moment, while odd-membered chains would have a total magnetic moment of $1\,\mu_B$. Therefore, the average magnetic moment per Co atom would be drastically reduced. In the latter case, however, it remains unanswered why the substrate itself loses its ferromagnetic order.

5.4.2 Local Magnetism Measured by STM/STS

To determine whether the changes in the magnetic properties of the sample upon polymerization are due to the formation of antiferromagnetically coupled chains or due to an increase in hybridization of the system, the local magnetic structure was investigated by means of SP-PTS and SP-STS. The experiments were performed in the low-temperature STM described in Chapter 4.1. All experiments were focused on odd-membered $[\text{Co–Sal}]_n$ chains (n odd). Since antiferromagnetic coupling of the individual centers within a chain is expected, chains with an even number should have a net magnetic moment of $0\,\mu_\text{B}$ and therefore should not respond to external magnetic fields. Odd-membered chains, instead, are expected to have a net magnetic moment close to $1\,\mu_\text{B}$.

To pinpoint energy regions in which the $[\text{Co–Sal}]_n$ chains show spin contrast, SP-PTS data were obtained. For this purpose, a PTS experiment is made with an applied external magnetic field. Then the direction of the field is inverted and the spectroscopy is repeated in the exact same spot. Afterward, the field direction is inverted again, and another spectroscopy is made. The spin asymmetry can then be calculated according to Equation 2.18 by use of the data obtained within external magnetic fields of opposite directions. Additionally, the error of the measurement can be estimated by calculating the asymmetry between the data obtained within fields of the same direction before and after the field switches.

This procedure is called A-B-A measurement and turned out to be very challenging for the present system. In all cases, the spectra recorded within external fields of the same direction showed deviations of similar size as the spectra within opposite fields, indicating that either the tip or the sample changed during the measurement. Possible reasons for the instability of the system are Br atoms left on the substrate after the Ullmann reaction. These atoms might cause changes in the tunneling barrier by changing their position during the experiment. The Br atoms are cleaved from the $\text{Br}_2\text{Co–Sal}$ molecules during the Ullman reaction. They are desorbing from the GdAu_2 surface at temperatures of 750 K [104], which are not reached during the Ullmann reaction. Heating the sample to this temperature to remove

the Br atoms bears the danger that the $[\text{Co–Sal}]_n$ chains or the $GdAu_2$ layer are destroyed and the Gd atoms are buried deeper in the Au(111) crystal.

Recently Que *et al.* suggested an alternative approach for the preparation of graphene nanoribbons on the rare earth transition metal alloy $TbAu_2$, by intercalating Tb after the creation of the nanoribbons [105]. On Au(111), Br atoms are desorbed at temperatures of 620 K [104]. Therefore, this procedure should enable the preparation of Br-free samples of $[\text{Co–Sal}]_n$ chains on $GdAu_2$. However, for such an experiment it would be necessary to ensure that the $[\text{Co–Sal}]_n$ chains are not altered during the growth of the $GdAu_2$ surface alloy, for example by replacement of the Co centers with Gd atoms. Another possible reason for the errors observed in the SP-PTS data is the modification of the molecule–substrate hybrid system by the tip, which is influencing the vertical position of a part of the molecule, as for example the Co atom and, therefore, the interaction between molecule and the substrate.

The most promising PTS data are presented in Figure 5.11. Looking only at the normalized data, the red curves deviate from the blue curves at different regions. However, the plots of the asymmetry and the calculated error show that the results are not trustworthy since the error is of the same order of magnitude as the asymmetry. The deviations between the two spectra obtained in equal fields are less visible in the plots of the SP-STS spectra in Figure 5.11 a)-c) because of the line width. Only the marked region in the data obtained on the bare $GdAu_2$ substrate shows a spin asymmetry significantly higher than the error, starting at 440 meV. These data agree with the SP-STS data from reference [247], presented previously in Figure 5.2. They show the spin-split state with a maximum at ≈ 600 meV that was attributed to Au-5d and Au-6s states. In addition, a spin-polarized feature is observed with a maximum and an accompanying zero crossing in the spin asymmetry at ≈ 1300 meV. When comparing these data with the DFT data presented above, this feature can be attributed to Gd-6s and Gd-5d states. These states show the first large peak in their asymmetry at this energy, as shown in Figure 5.3. For negative energies, the spin-polarized states are outside of the measured energy range.

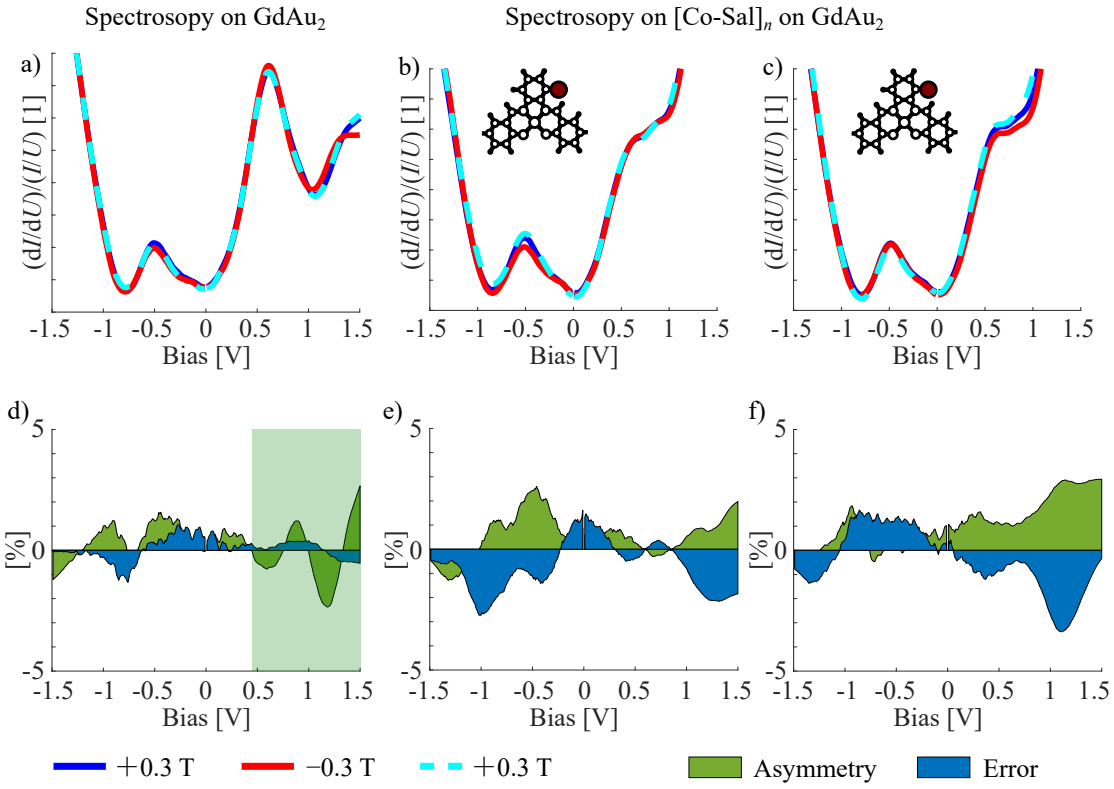

Figure 5.11: SP-STS data for $[\text{Co–Sal}]_n$ chains on $GdAu_2$/Au(111) with in-plane external magnetic fields applied. The spin-polarized point spectra were obtained on a) bare $GdAu_2$ and on b), c) two equivalent positions on two different members of a $[\text{Co–Sal}]_n$ chain. In d-f), corresponding spin-asymmetry (green) and error (blue) plots, calculated from the PTS data, are presented. The area in the spin asymmetry measured on bare $GdAu_2$ marked by a green overlay indicates an energy range, where the measured spin asymmetry is considerably higher than the error.
Tunneling-parameters: $U_{\text{stab}} = -1500\,\text{mV}$; $I_{\text{stab}} = 200\,\text{pA}$; $U_{\text{mod}} = 100\,\text{mV}$.

Table 5.2: Overviews of energies and fields probed for spatial spin asymmetry:

U [V]	Out-of-plane field [mT]					U [V]	In-plane field [mT]			
	200	500	1000	1500	2000		5	50	300	500
−1.05		x				−1.95	x			
−1.00					x	−1.30	x	x		
−0.95		x				−1.00		x		
−0.80	x				x	−0.80			x	
−0.60					x	−0.25	x	x		
−0.40					x	0.75	x	x		x
−0.20					x	1.00				x
0.50		x				1.35	x	x		
0.60		x				3.00	x	x	x	x
0.85	x	x	x	x	x					
3.00					x					

A-B-A measurements following the same procedure can also be performed for spatially resolved $\mathrm{d}I/\mathrm{d}U$ data. Because of the failure of the SP-PTS data to reveal spin-polarized energy regions for the molecules, different energies and magnetic fields were tested for in-plane and out-of-plane contrast. An overview of the tested settings can be found in Table 5.2.

Data obtained for in-plane fields is presented in Figure 5.12. In all images, spin contrast can clearly be observed for the substrate. At the same time, the error plots show only a background of low noise. This proves that the tip is magnetic. The signal in the asymmetry map at −400 meV is low compared to the maps at 750 meV and 1000 meV. This is in agreement with the PTS data which showed only small spin contrast for negative energies. The contrast observed at 750 meV and 1000 meV can be attributed to the Au states, as discussed earlier. The expected antiferromagnetic coupling within the chains was not observed for in-plane fields. The data show that the $[\mathrm{CoSal}]_n$ chains only have marginal influence on the measured spin asymmetry. The asymmetry maps obtained at −400 meV and 1000 meV show a constant asymmetry over the whole scan frame. Only the data at

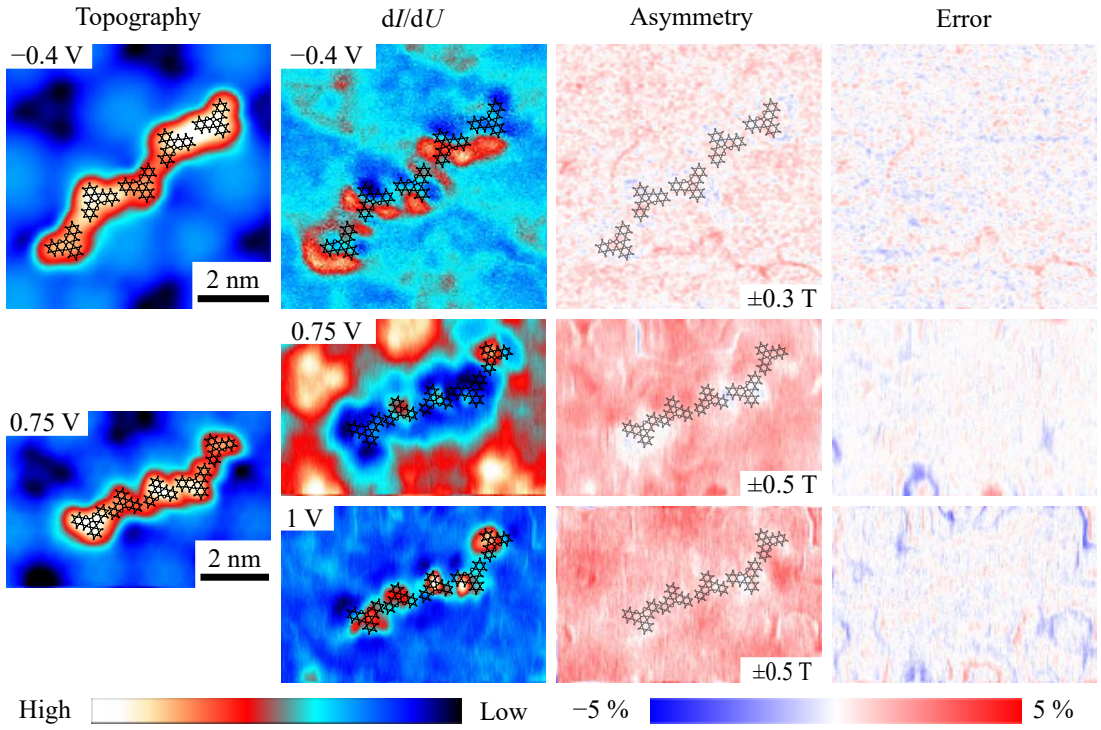

Figure 5.12: Spatially resolved SP-STS data for $[\text{Co–Sal}]_n$-chains on $GdAu_2/Au(111)$ obtained with in-plane external magnetic fields. Topography images and dI/dU maps obtained at three different energies and corresponding spin-asymmetry and error maps are presented. A model of the molecule superimposed on the images indicates the positions of the individual members within the $[\text{Co–Sal}]_n$ chain.
Tunneling-parameters: $I_{\text{stab}} = 100\,\text{pA}$; $U_{\text{mod}} = 100\,\text{mV}$; $z-\text{range} = 2.55\,\text{Å}$.

750 meV shows a decrease in signal at positions of individual molecular members of the chain.

This decrease can either be caused by the chain hindering tunneling from the tip into the substrate or by an actual loss of spin-polarization of the substrate due to the hybridization with the chain. In the first case, the presence of the molecule prevents electrons with an energy in the range of $\pm\frac{U_{\text{mod}}}{2}$ around bias energy to tunnel from the tip into the substrate. The tunneling current is then caused by electrons of lower energy, which do not contribute to the dI/dU signal. The second

case would further strengthen the interpretation of the XMCD data that the average magnetic moments of substrate and molecules are lowered after the Ullmann reaction because of stronger hybridization. This hybridization causes an electron transfer between the molecule and the substrate. Therefore, the magnetic moment of the substrate is locally reduced by the additional electrons in the minority states. Since the effect is observed close to the energy of the molecules' LUMO which is mainly located on the Co atom, this indicates that the hybridization is strongest between the Co atoms and the substrate. The areas where the molecule does not cause a decrease of the measured asymmetry, coincide with TOP regions of the $GdAu_2$/Au(111) substrate. These regions were observed to be the preferred adsorption position for single Co–Sal molecules. Since these molecules in part showed weaker hybridization and the TOP regions are known to have the Gd atoms located deeper within the substrate, it is reasonable that the chain hybridizes less with the substrate at these positions.

The out-of-plane data agree with the in-plane data and give no further results. Because of the clear contrast obtained on the substrate, the tip's out-of-plane spin-polarization is confirmed. However, intramolecular antiferromagnetic coupling is not observed. The inversion of the contrast from blue to red between the map at $-200\,\mathrm{meV}$ and the maps at $-800\,\mathrm{meV}$ and $-1000\,\mathrm{meV}$ indicates a zero crossing in the spin asymmetry between $-200\,\mathrm{meV}$ and $-800\,\mathrm{meV}$. The same can be observed for the maps at $100\,\mathrm{meV}$ and $850\,\mathrm{meV}$. These maps also show the same reduction of the spin asymmetry induced by the $[\mathrm{Co–Sal}]_n$ chain, as observed for the in-plane data.

Except for the data obtained at $100\,\mathrm{meV}$, the spin-asymmetry maps presented in Figure 5.13 show noise surrounding the area of the chain. This noise can also be seen in the error plots. It is caused by an unstable adsorbate either on the tip or on the substrate. For a bias energy of $100\,\mathrm{meV}$, the noise disappears for the area around the molecule but can still be seen at the position of another adsorbate in the lower right corner of the scan frame. Therefore, it is more likely that the noise is caused by an adsorbate on the tip, which is more stable at this bias energy. As can be seen in the $\mathrm{d}I/\mathrm{d}U$ maps, the LDOS is very low in the border regions of the chain where the noise is observed. Therefore, the tip is closer to

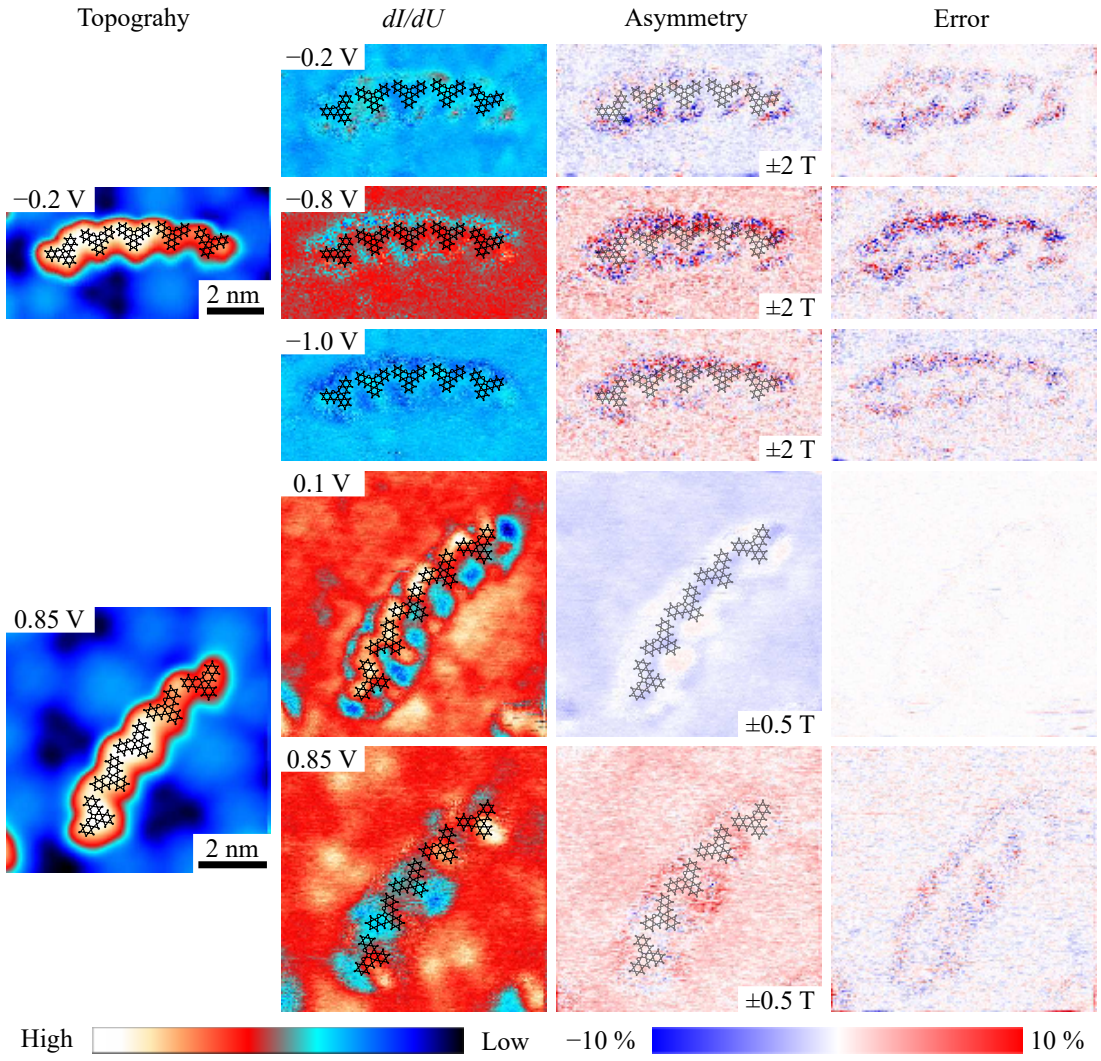

Figure 5.13: Spatially resolved SP-STS data for $[\text{Co–Sal}]_n$-chains on $GdAu_2/Au(111)$ obtained with out-of-plane external magnetic fields. Topography images and $\mathrm{d}I/\mathrm{d}U$ maps obtained at three different energies and corresponding spin-asymmetry and error maps are presented. A model of the molecule superimposed on the images indicates the positions of the individual members within the $[\text{Co–Sal}]_n$ chain.
Tunneling-parameters: $I_{\text{stab}} = 100\,\text{pA}$; $U_{\text{mod}} = 100\,\text{mV}$; $z-\text{range} = 2.55\,\text{Å}$.

the sample in these regions and the adsorbate starts vibrating, which causes the noise. However, at the center of the chain, the LDOS is increased again and a clear signal is visible indicating that the spin asymmetry is the same as on the bare substrate. Only in the spin-asymmetry map obtained at 100 meV the same decrease in the spin-asymmetry signal is observed as for the in-plane data. At the other energies, the effect might also occur but is then covered by the noise in the signal. Interestingly, an influence of the TOP region on the measured spin-asymmetry signal, as observed for the in-plane data, is not present. The chain is equally hybridized with the substrate across its full length.

5.5 Summary and Conclusion

In summary, investigations of the electronic properties of single Br_2Co–Sal molecules on $GdAu_2$ showed different degrees of hybridization between individual molecules and the substrate. Elevated temperatures, needed for Ullmann coupling of the molecules, lead to an increase in the degree of hybridization. Due to the higher mobility of molecules and substrate atoms, the Co atoms of the Co–Sal molecules can form bonds with the substrate Gd atoms. The HOMO state, observed for a fraction of single Br_2Co–Sal molecules, disappeared after the polymerization, and the $[\text{Co–Sal}]_n$ chains formed hybrid systems with a band-like electronic structure. In the observed energy range, only the LUMO and LUMO+1 states are preserved upon polymerization. Additionally, locally varying energy shifts of these states indicate the influence of the inhomogeneity of the substrate's electronic structure on the hybrid system.

These findings are confirmed by the XMCD data, which show a general reduction of the average magnetic moment of substrate and molecules after the polymerization. This reduction is caused by the electron transfer between molecules and substrate, accompanying the hybridization. It leads to a loss of magnetic order, especially for high coverages of molecules, that is reflected in the paramagnetic behavior of the substrate and the disappearance of antiferromagnetic coupling between molecules

and substrate as well as the general reduction of magnetic moments. Local investigations of the magnetic properties rule out the possibility of antiferromagnetic intramolecular coupling, which also could have explained the loss of magnetic moment after the polymerization. Furthermore, the reduction of the spin asymmetry can be observed locally by SP-STM.

These findings damp the hopes that the $GdAu_2$ surface alloy is a good template for magnetic metal–organic compounds, which should preserve the magnetic properties of the molecules and at the same time stabilize the orientation of the molecular magnetic moments. However, the focus of hybridization effects on the Co atoms suggests that $GdAu_2$ might serve as a better template for purely organic systems such as graphene nanoribbons. Additionally, the recent study by Que *et al.* suggests an alternative route for the sample preparation by first introducing the Ullmann reaction, followed by the growth of the surface alloy by intercalation. This way, the hybridization might be reduced since the XMCD data suggests that the hybridization increases because of the additional mobility of molecules and substrate atoms during the Ullmann reaction.

6 [Co-Sal]$_n$ on Co-intercalated Graphene on Ir(111) (Gr/Co/Ir(111))

The term graphene describes a monoatomic layer of sp^2-hybridized C atoms. As a monolayer of graphite, graphene has been the topic of theoretical investigations since the 1940s [262, 263]. In the early 2000s, the interest in graphene as one of the first realizations of a two-dimensional material increased drastically and persists until today [264]. The reasons for the large interest are the unique mechanical and electronic properties of graphene, for example, a high charge carrier mobility combined with low intrinsic spin-orbit coupling [265]. In addition, the laterally extended π-electron system of graphene exhibits metal-like electronic properties along the plane, and molecule-like properties perpendicular to the plane.

The properties of graphene can be tuned by altering the supporting substrate system. In particular, intercalation with molecules or single atoms serves as a technique to alter the properties of graphene layers [266, 267] or earlier of graphite [268, 269]. In the present study, graphene was used as a buffer to reduce the hybridization of Br_2Co–Sal molecules deposited onto a ferromagnetic substrate. An introduction to the Gr/Co/Ir(111) substrate system will be given in the first section of this chapter, followed by a description of the preparation of [Co–Sal]$_n$ chains on the substrate, and a presentation of the results obtained during the investigation of the electronic and magnetic properties of the sample. Afterward, a study of [Co–Sal]$_n$ chains on pristine graphene on Ir(111) (Gr/Ir(111)) will be presented to elucidate the influence of the substrate on the properties of the molecular chains. The chapter will close with a study on *in situ* metalation of Br_2H_2–Sal molecules with Fe and Cr and consecutive formation of molecular chains on Gr/Co/Ir(111).

6.1 Intercalated Graphene

Originally, the process of intercalation has been aimed at creating graphite monolayers by exfoliation from graphite, which also resulted in the discovery of new multi-layer materials [263, 264, 269]. While different intercalation processes have been developed, the most commonly used for the preparation of graphite intercalation systems is the so-called two-zone vapor transport method [269]. In this method, a heated graphite sample is exposed to a vapor of the desired interlayer material, also called the intercalant.

With the boom of the graphene topic in the 2000s, the interest in the intercalation of graphite monolayers, now labeled graphene, shifted toward the control of the electronic properties of graphene. This research has been focused on limiting the interaction between graphene and its substrate to access the unique properties of pristine graphene [267, 270, 271]. At this time, high-quality epitaxially grown graphene became accessible by chemical vapor deposition (CVD) on metal substrates such as Ru(0001), Pt(111), Ir(111), and Ni(111) [272–274]. For this method, a hot metal substrate is exposed to a vapor of carbon-containing molecules like methane or ethene. This leads to the decomposition of the molecules on the hot surface and the growth of graphene patches.

Such epitaxially grown graphene can be intercalated with metal layers via two routes: Either the metal atoms are deposited from an e-beam heater onto the graphene sample held at an elevated temperature, or the sample is post-annealed after room temperature deposition of the metal. First studies on the intercalation mechanism suggested penetration of the graphene layer at preexisting defects and at point defects created by the metal during the penetration [267, 275, 276]. It was found that the intercalation process does not influence the quality of the graphene layer. This means that any created defects will be healed at the end of the penetration process. A study by Vlaic *et al.* from 2014 showed that regions of graphene curvature, like wrinkles or graphene covered step edges, enhance the possibility of Co atoms to penetrate the graphene layer [277]. Therefore, intercalation starts preferably at graphene covered step edges or in the vicinity of wrinkles in the graphene layer.

The growth of graphene on Ni(111) and the subsequent intercalation with Fe by Weser *et al.* showed that ferromagnetic materials in contact with graphene induce magnetic moments in the C atoms because of the hybridization of the graphene π states and the transition metal 3d states [278, 279]. Since Fe has a larger magnetic moment than Ni, the intercalation with Fe induces a larger magnetic moment in the graphene layer. These results promised the creation of interesting, novel magnetic materials by intercalating graphene with Co, Fe, or Ni. Studies by Rougemaille *et al.* and Coraux *et al.* on intercalation of multilayers of Co at the Gr/Ir(111) interface showed further that, in return, the graphene layer affects the magnetism of the transition metal [280, 281]. In particular, the graphene layer leads to a stabilization of the out-of-plane anisotropy for thin Co layers and increases the range of Co layer thickness with out-of-plane anisotropy. Furthermore, the surface of the transition metal layer is passivated by the graphene layer on top, and the adsorption of impurities is hindered.

In 2013, Decker *et al.* conducted a thorough investigation of the properties of a single Co layer intercalated at the Gr/Ir(111) interface [271]. Analogue studies of Fe- and Ni-intercalated graphene on Ir(111) showed similar properties for these systems [282, 283]. However, opposed to the other two systems and to graphene directly grown on Ni(111), an intercalated Ni layer does not induce a magnetic moment in the graphene layer.

When intercalating less then a full monolayer of Co at the Gr/Ir(111) interface, intercalation areas can be mainly found at step edges or around wrinkles because of the facilitated penetration of the graphene layer in those regions. The resulting sample system is characterized by two different moiré patterns, which both can be seen in Figure 6.1 a). One, with a small corrugation of 0.41 Å, is observed in the regions of graphene directly on the Ir(111) crystal and the second, with a larger corrugation of 1.2 Å to 1.8 Å, in the areas of Co intercalation.[1] Both patterns are caused by the mismatch in the lattice constants of the graphene and the underlying metal layer. Because of the pseudomorphic growth of the Co layer at the Gr/Ir(111) interface, both moiré patterns have the same lattice constant of typi-

[1] The theoretical value for the corrugation at the intercalated areas obtained from DFT calculations is 1.27 Å.

cally ≈ 25 Å. However, this value can vary depending on the rotational orientation between the graphene and the metal lattice and can range from 20 Å to 30 Å [284]. In 2008, N'Diaye *et al.* reported a distribution of the observed rotational domains around the most common orientation leading to a lattice constant of 25.3 Å [273]. One year later, they reported the possibility of tuning the rotational orientation by using specific preparation methods [285]. While the Gr/Ir(111) as well as the Gr/Co/Ir(111) system is incommensurate, a single unit cell of the moiré pattern in the most common orientation is formed by 10×10 unit cells of graphene on top of 9×9 unit cells of the metal [272].

The two moiré patterns can be further divided into three different regions, depending on the positions of the C atoms relative to the lattice of the top three metal layers, as can be seen in Figure 6.1 b) and c) for a Co-intercalated area. In the top regions, the center of a C hexagon is positioned right on top of an atom of the topmost metal layer, in the hcp regions the C hexagons are centered at an atom of the second metal layer, and in the fcc regions at an atom in the third metal layer [286]. The interaction of the graphene layer with the substrate varies between the intercalated and the non-intercalated regions. On Ir(111), mainly van-der-Waals interactions act between Ir and graphene, leading to a total binding energy of 50 meV per C atom, according to DFT calculations [286]. Weak chemical bonds between C and Ir atoms are only formed in the fcc and hcp regions. Therefore, the electronic properties of the graphene are close to those of free-standing graphene [287] but vary slightly between the different regions of the moiré pattern. This leads, for example, to preferred adsorption sites for metal clusters on the moiré pattern [272].

The Co interlayer, however, strongly interacts with the graphene, which is also the reason for the increased corrugation. The average binding energy, still mainly caused by van-der-Waals interactions, was calculated to 102 meV per C atom [271]. Additionally, strong chemical bonds are formed at the fcc and hcp regions leading to a distance of 2.02 Å between the C and Co atoms. This goes hand in hand with a charge transfer between C and Co atoms responsible for the already mentioned magnetic moment induced in the graphene layer. In the top regions, instead, only the van-der-Waals interactions act between the graphene and the Co atoms, and

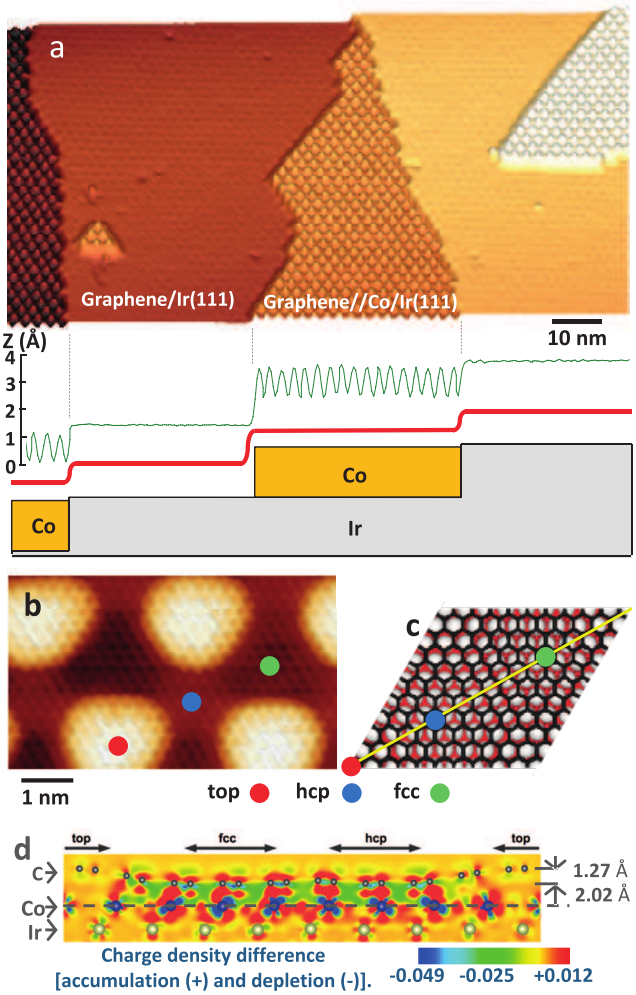

Figure 6.1: Structure of Gr/Co/Ir(111). A topography image of the Gr/Co/Ir(111) surface is presented in a). The line profile taken at the bottom of the topograph illustrates the difference between the Gr/Ir(111)- and the Gr/Co/Ir(111)-moiré corrugations. The high resolution STM topograph presented in b) shows the graphene atomic lattice and the moiré pattern at a cobalt intercalation region. Panel c) shows a model of one unit cell of Gr/Co/Ir(111). Graphene is presented in black, Co atoms in white, and Ir atoms in red. In d), a side view of a charge-density-difference plot of Gr/Co/Ir(111), cut along the yellow plane in c), is presented. The values of the colorbar are given in $e/\text{Å}^3$.
Tunneling parameters: a) $U = -700\,\text{mV}$, $I_{\text{stab}} = 1\,\text{nA}$; b) $U = -100\,\text{mV}$, $I_{\text{stab}} = 4\,\mu\text{A}$
Reprinted figure with permission from [271]. Copyright 2013 by the American Physical Society.

the distance between the C and Co atoms reaches a maximum of 3.29 Å. This behavior is also reflected in the charge-density-difference plot in Figure 6.1 d). In the fcc and hcp regions, the C atoms are closer to the Co layer, and the large charge density indicates the chemical bonds. Later these results have been confirmed in an XPS study by Pacilé *et al.* [288]. They found two different peaks for C atoms interacting differently with the Co layer depending on their distance from the Co layer.

As mentioned earlier, the graphene layer hardens the out-of-plane anisotropy of the Gr/Co/Ir(111) system compared to pure Co on Ir(111). Therefore, the system is a hard magnet with an out-of-plane anisotropy. In their study, Decker *et al.* found magnetic contrast for out-of-plane magnetic fields but not for in-plane fields [271]. They observed that out-of-plane fields of 6.5 T were not sufficient to align all intercalated areas of their sample with the external field [271]. On average, a field of about 4.5 T was sufficient to align 50 % of the intercalated areas with the external field. This value is significantly larger than the 3 T found in an analogue experiment for monolayer islands of Co on Ir(111) [289].

Locally, the varying hybridization between graphene and Co leads to variations of the dipole moments in the different regions of the moiré pattern. For the ferromagnetic Co layer, the dipole moments are parallel and vary only slightly with magnetic moments of $+1.92\,\mu_B$, $+1.88\,\mu_B$, and $2.08\,\mu_B$ in the hcp, fcc, and top regions, respectively [271]. Surprisingly, spin-asymmetry maps obtained on Gr/-Co/Ir(111), as presented in Figure 6.2 b), show that the top regions have a spin polarization with opposite sign compared to the hcp and fcc regions. This indicates complex magnetic properties of the graphene layer. The total magnetic moment of the graphene layer was calculated to be antiparallelly aligned to the Co layer magnetic moment [271]. This was later confirmed in an XMCD experiment by Vita *et al.* [290]. According to the DFT calculations by Decker *et al.*, one graphene unit cell acquires a total magnetic moment of $-1.36\,\mu_B$ for C atoms in fcc and hcp regions, antiparallelly aligned to the Co layer beneath. At the same time, a unit cell of graphene has a much smaller total magnetic moment of $+0.14\,\mu_B$ for C atoms in the top region, parallelly aligned to the Co layer. This magnetic structure is depicted in Figure 6.2 c) on a DFT-calculated model of Gr/Co/Ir(111) provided

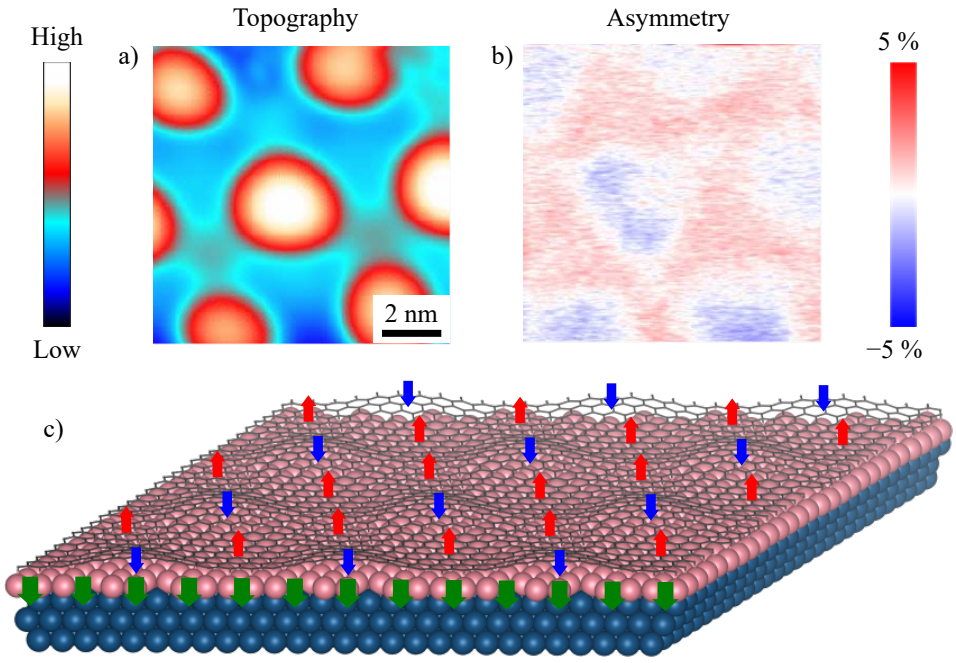

Figure 6.2: Overview of the magnetic structure of Gr/Co/Ir(111). A topography image of Gr/Co/Ir(111) is presented in a), the corresponding asymmetry map in b). A DFT-calculated model of Gr/Co/Ir(111) is shown in c). Arrows indicate the local magnetization directions. Green arrows indicate the magnetization of the ferromagnetic Co layer, blue arrows indicate the magnetization of the C atoms in the graphene top regions, parallel to the magnetization of the Co layer, and red arrows indicate the magnetization of the C atoms in the graphene's hcp and fcc regions, antiparallel to the Co layer.

by N. Atodiresei.[2] These results were qualitatively confirmed in a DFT study by Vita *et al.*, yet they found smaller values for the spin polarization induced in the graphene layer [290].

The magnetic properties of Gr/Co/Ir(111) are summarized in the model in Figure 6.2 c). The Co layer is ferromagnetic and induces a magnetic moment in the graphene layer. Within the graphene layer, the magnetic moments of the C atoms vary with the moiré pattern. C atoms in the top regions of the moiré pattern carry

[2]Peter Grünberg Institut (PGI-1) and Institute for Advanced Simulation (IAS-1), Forschungszentrum Jülich GmbH, Jülich, 52425, Germany

a small magnetic moment parallel to the Co layer, while C atoms in fcc and hcp regions carry a bigger magnetic moment antiferromagnetically coupled with the Co layer.

Various studies investigated the adsorption of metals and molecules on graphene moiré patterns of different corrugations. N'Diaye *et al.* showed that Ir atoms deposited onto Gr/Ir(111) form clusters preferably adsorbed on hcp regions, with a lower chance to occupy fcc regions and total avoidance of top regions [272]. The binding of the clusters was attributed to the formation of a chemical bond of Ir atoms with C atoms sitting atop a threefold coordinated hcp position in the Ir(111) layer below. C atoms in these positions can form additional bonds since their direct neighbors form weak chemical bonds with the Ir atoms directly below. This leads to an electron transfer between graphene and the Ir(111) substrate and a disturbance in the sp^2 hybridization of the graphene layer.

Presel *et al.* investigated the desorption of CO molecules and Ar atoms from Gr/Co/Ir(111) and Gr/Ir(111) [291]. They found that these non-metallic species also adsorb preferably on hcp and fcc regions but can be adsorbed on top regions as well, when higher coverages are reached. In their studies, the binding energies were only caused by van-der-Waals interactions, mainly with the metal layer below the graphene. They suggested that the graphene is translucent to the van-der-Waals forces imposed by the metal onto the adsorbant. The main reason for the lower binding energy in the top regions, according to their results, is the larger distance of the adsorbant toward the underlying metal layer, caused by the buckling of the graphene.

An additional mechanism influencing the adsorption of polarizable molecules was found by Zhang *et al.* [292]. They showed that in-plane dipole moments, induced in the graphene layer by strain effects, can create preferred adsorption sites on the moiré pattern trapping the molecules within local electric fields. The adsorption of metal–organic molecules on graphene was investigated in a study by Bazarnik *et al.* [284]. They deposited Co-phthalocyanine molecules onto Fe- and Co-intercalated graphene on Ir(111) and pristine Gr/Ir(111). Also in this study, the preferred adsorption on the fcc and hcp regions of the intercalated areas was

confirmed. Additionally, the study showed that intermolecular interactions can influence the adsorption configurations. However, this influence was mainly observed on pristine Gr/Ir(111), where the molecule–substrate interactions are weaker.

The above results suggest that metal–organic molecules are held on graphene substrates by van-der-Waals interactions of the organic ligand with the substrate and by covalent bonds formed between the metal centers of the molecules and graphene C atoms in the fcc and hcp regions. The chemical bond can also influence the electronic and magnetic properties of the molecules and allow for magnetic interaction pathways only possible via covalent bonds. Depending on the polarizability of the molecules, the in-plane dipole moments of the graphene layer will additionally modify the preferred adsorption site together with intermolecular interactions.

Epitaxially grown graphene on Fe, Co, or Ni, either produced by intercalation or directly grown on the metal, has been widely used to stabilize the magnetic moment of paramagnetic molecules. These substrates were perceived as ideal for molecular systems since they are expected to preserve the intrinsic properties of the molecules, which should be interacting mainly by van-der-Waals interactions because of the graphene layer [293]. At the same time, the magnetic moment of the molecules will be stabilized by interaction with the substrate. The reduction of hybridization by the graphene layer was shown by Hermanns *et al.* in an XAS study of Co–octaethylporphyrin (CoOEP) molecules on Gr/Ni/W(110) compared to the same molecules directly on Ni/W(110) and in a bulk molecular sample [293].

For the magnetic interactions between molecules and an intercalated-graphene substrate, ferromagnetic as well as antiferromagnetic coupling has been found for different systems. In their study of CoOEP on Gr/Ni/W(110), Hermanns *et al.* found antiferromagnetic coupling between the molecules and the Ni layer. The coupling was attributed to superexchange coupling mediated by the graphene layer and the ligand. About one year later, Candini *et al.* found ferromagnetic coupling for Fe–phthalocyanine molecules adsorbed on Gr/Ni(111) [294]. They suggested a more direct interaction pathway between the molecule Fe atoms and the substrate Ni atoms, only mediated by the graphene layer. It has to be noted that this in-

teraction is not a superexchange mechanism since the graphene carries a magnetic moment, induced by the hybridization with the underlying Ni layer.

In another thorough study on Fe–, Cu–, and Mn–phthalocyanines (Pcs) on a Gr/-Co/Ir(111) substrate, Avvisati *et al.* found antiferromagnetic coupling for Fe– and Mn–Pcs, and ferromagnetic coupling for Cu–Pcs [295–297]. They suggested the same ligand-mediated coupling pathways for all three species. The different coupling for Cu–Pcs was attributed to a 90° superexchange mechanism because of the in-plane character of the magnetic Cu-$d_{x^2-y^2}$ orbital, while the other two species couple via a 180° superexchange mechanism.[3] Another interesting result by Avvisati *et al.* is the dependence of the magnetic coupling on the relative orientation of the easy axes of the substrate and the molecule magnetization. They compared results obtained on Fe–Pc, with an in-plane easy magnetization axis, and Co–Pc, with an out-of-plane easy magnetization axis, each adsorbed on a substrate system with an out-of-plane and one with an in-plane easy axis. These samples were obtained by intercalating a single Co layer at the graphene on Ir(111) interface, for an out-of-plane easy axis of the substrate magnetization, and six Co layers for an in-plane easy axis. This comparison showed that a parallel alignment of the easy magnetization axes of molecule and substrate enhances the magnetic coupling.

All these studies were based on the surface averaging XMCD. Possible local variations in the coupling are therefore neglected. Only theoretical investigations by DFT calculations have been employed to account for this drawback. This changed with a study by Sierda *et al.*, in which the local magnetic moments of single Br_2Co–Sal molecules on Gr/Fe/Ir(111) have been investigated by SP-STM [230]. In this study, it was revealed that the magnetic coupling between Br_2Co–Sal molecules and the Gr/Fe/Ir(111) substrate can vary depending on the adsorption configuration of the molecule. Collinear alignment between the molecular and the substrate magnetic moment, either antiparallel or parallel, was observed for strongly interacting molecules. For weakly interacting molecules, intermediate orientations

[3] For the Fe–Pcs Avvisati *et al.* admitted the possibility of an additional direct interaction pathway due to the hybridization of the Fe-d_{z^2} orbital and the graphene π-orbitals, adding to the antiferromagnetic coupling.

have been observed. However, it has to be mentioned that the adsorption sites of Br_2Co–Sal molecules are more variable than those of metal–Pcs because of the smaller size of Br_2Co–Sal. Another result of this study was magnetic contrast measured on individual Br_2Co–Sal molecules independently of the substrate magnetic orientation. This was accomplished by bending the canted magnetic moment of a weakly, antiferromagnetically coupled molecule within a field range too low to influence the substrate magnetic moment.

6.2 Sample Preparation and Characterization

The Ir(111) crystal used during the experiment was cleaned by repeated cycles of Ar-ion sputtering and O_2 annealing. For the Ar-ion sputtering, the crystal was kept in the focus of the ion source for 30 minutes. During this process, the base pressure was kept at 4×10^{-6} mbar to 6×10^{-6} mbar, and the acceleration energy of the ion beam was set to 800 eV. The annealing was done in an O_2 atmosphere with a pressure of 10^{-8} mbar, at a temperature of roughly 1000 K. Finally, the sample was flashed after two to three cycles of sputtering and annealing. For this purpose, the crystal was heated to ≈ 1400 K for about 3 minutes.

The growth procedure of the graphene layer followed the one introduced by N'Diaye *et al.* [273]. While being kept in an atmosphere of ethene with a base pressure of 3×10^{-8} mbar to 3.5×10^{-8} mbar, the crystal was annealed to a temperature of about 1300 K. This self-limiting growth method led to a full monolayer coverage with graphene after 20 minutes of growth. After this time, the chamber was pumped down to a pressure of roughly 2×10^{-9} mbar, followed by a final flash to ≈ 1400 K for about 3 minutes. Then the sample was cooled down slowly over the course of 10 minutes with reduced heat input. For the intercalation, Co was deposited from an e-beam evaporator onto the sample heated to a temperature of 613 K to 618 K for 3 to 5 minutes. The resulting coverage with Co intercalated graphene is about $0.5 - 0.7$ monolayers.

After the intercalation, the sample was cooled down to room temperature before molecules were deposited. STM topographs presented in Figure 6.3 give an impres-

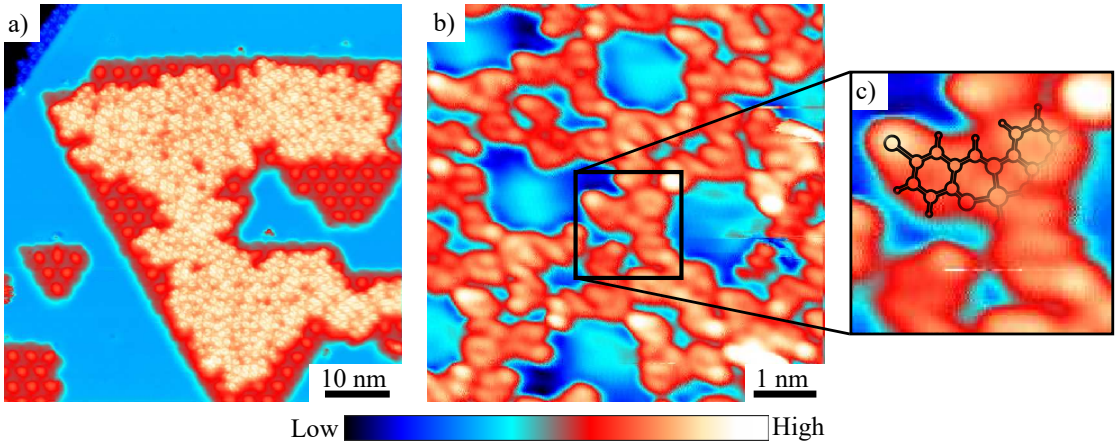

Figure 6.3: Topographic STM images of Br_2Co–Sal molecules on Gr/Co/Ir(111). In a), a large-scale topography image of single Br_2Co–Sal molecules after deposition onto the substrate held at room temperature is presented. The image area contains mainly one big island of intercalation underneath graphene on a single Ir(111) terrace and some smaller islands of intercalation in the lower left corner. A graphene covered step edge toward a lower Ir(111) terrrace can be seen in the top left corner. A zoomed-in topography image, presented in b), shows submolecular resolution. A further enlarged area with a superimposed model of the molecule in c) allows easy identification of the molecule's structure. Tunneling parameters: a) $U = 1000\,\mathrm{mV}$; $I_{\mathrm{stab}} = 100\,\mathrm{pA}$; $z-$range $= 7.9\,\text{Å}$; (b,c) $U = 50\,\mathrm{mV}$; $I_{\mathrm{stab}} = 50\,\mathrm{pA}$; $z-$range $= 1.4\,\text{Å}$.

sion of a sample prepared with single Br_2Co–Sal molecules. The molecules cover only areas of intercalated graphene, avoiding the top regions of the moiré pattern. A zoomed in image in Figure 6.4 b) shows submolecular resolution obtained on the molecules. Further enlarging one Br_2Co–Sal molecule, enhances the details that can be observed in the image. One can clearly identify the Br atoms on the sides of the molecule, the Co atom in the center, and the three benzene rings.

The main focus of the present chapter lies on $[\text{Co–Sal}]_n$ chains on Gr/Co/Ir(111). These can be created from *ex situ* metalated Br_2Co-Sal molecules by depositing minute amounts of Co onto a sample of the molecules on Gr/Co/Ir(111) kept at an elevated temperature. However, for the present study, Br_2H_2–Sal molecules on Gr/Co/Ir(111) were metalated *in situ*. For this purpose, Br_2H_2–Sal molecules were deposited from a crucible at a temperature of 410 K onto the sample kept

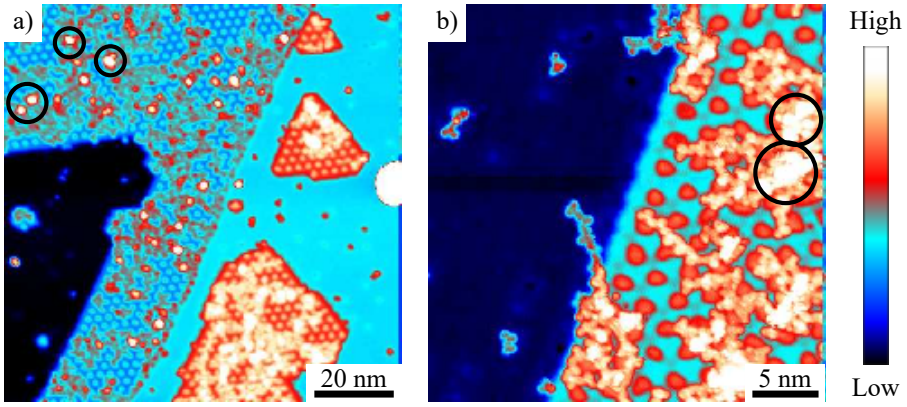

Figure 6.4: Topographic STM images of $[\text{Co–Sal}]_n$ chains on Gr/Co/Ir(111). The large-scale topography image in a) shows two graphene covered terraces of the Ir(111) crystal. Islands of Co intercalation can be seen on the upper terrace in the lower right corner and a large intercalated area along the step edge on the lower terrace. The intercalated areas are decorated by $[\text{Co–Sal}]_n$ chains and Co clusters. Some of the latter are indicated by black circles. A few Co clusters can also be found on the Gr/Ir(111) areas. In b), a topography image centered on a step edge between an intercalated and a non-intercalated area is presented. Chains and Co clusters can be mainly found on the intercalated area. One $[\text{Co–Sal}]_n$ chain starts at the intercalated area and protrudes into the area of pristine Gr/Ir(111).
Tunneling parameters: a) $U = 500\,\text{mV}$; $I_{\text{stab}} = 10\,\text{pA}$; $z-$range $= 5.65\,\text{Å}$; b) $U = 500\,\text{mV}$; $I_{\text{stab}} = 10\,\text{pA}$; $z-$range $= 3.75\,\text{Å}$.

at room temperature. Deposition times of 2 minutes resulted in coverages ranged from $0.3 - 0.5$ monolayers. Finally, minute amounts of Co were deposited onto the sample to metalate the molecules and induce the Ullmann reaction for the creation of the $[\text{Co–Sal}]_n$ chains. The best results were obtained by using a two-step process. For the first step, in which the molecules are metalated, some Co is deposited onto the sample kept at $\approx 410\,\text{K}$ for 20 seconds. In the second step, Co is deposited for another 20 seconds with a higher sample temperature of $\approx 600\,\text{K}$, which induces the Ullmann reaction. The validity of the metalation process was thoroughly investigated and the results are published in reference [80].

An overview of a sample after the full preparation process is presented in Figure 6.4. Most of the molecules are adsorbed on the intercalated areas, but some molecules

as well as Co clusters can be found on pristine Gr/Ir(111). One $[\text{Co–Sal}]_n$ chain starts on an intercalated area and protrudes onto pristine Gr/Ir(111). It can be seen that almost all molecules created chains or at least dimers. Many of the chains are connected to larger Co clusters. The thereby formed knots indicate a strong interaction between molecules and Co clusters. This interaction hinders the creation of longer chains. Attempts to lower the amount of Co deposited for metalation and polymerization, however, resulted in a failure of the Ullmann reaction. Since isolated chains without connection to other chains and clusters can be found, the samples are adequate for the experiments discussed here.

As mentioned before, Gr/Co/Ir(111) is a hard magnet with a switching field in the range of 4 T to 6 T. Therefore, Fe-coated W tips were used for the experiments focusing on the magnetic properties. These tips already switch at fields of roughly 500 mT. Pure W tips were used for the experiments on electronic properties. These experiments were conducted with the variable-temperature STM setup described in Section 4.2, at a temperature of ≈ 25 K. Experiments focusing on the magnetic properties were performed with the low-temperature setup described in Section 4.1, at 6.5 K. Electrochemically etched W tips were cleaned by 15 minutes of annealing in an O_2 atmosphere, followed by repeated cycles of flash annealing for 15 seconds. For the spin-polarized experiments, the tip was coated with ≈ 50 monolayers of Fe by depositing Fe from an e-beam evaporator onto the tip for 45 minutes. During the deposition the tip was heated to ≈ 470 K to obtain a uniform coating. To judge the quality of the Fe-coated W tips, they were tested on Co islands deposited onto Ir(111) before the preparation of the actual sample.

6.3 Electronic Properties

As discussed earlier, the graphene layer of the Gr/Co/Ir(111) substrate reduces the hybridization of adsorbed molecules with the substrate. Therefore, opposed to the experiments on $GdAu_2$, individual molecular states can be identified by STS measurements on the present sample system. The data presented in this section were partly published in reference [80]. PTS data obtained at various positions on

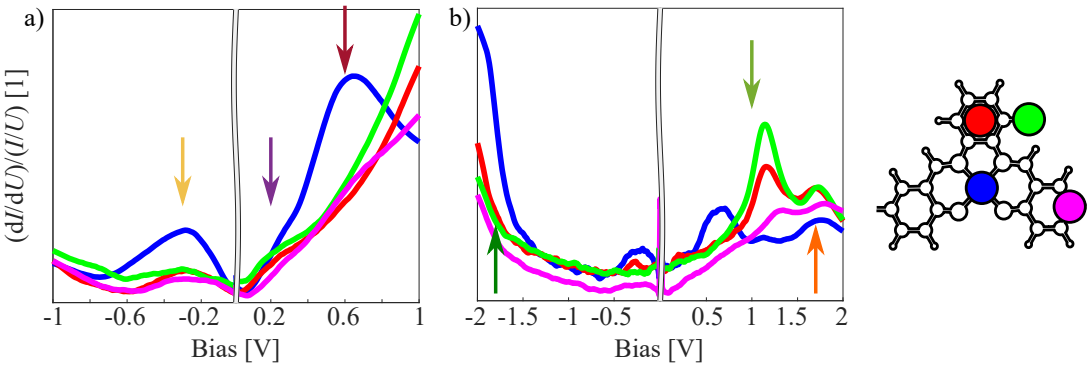

Figure 6.5: STS data on $[\text{Co–Sal}]_n$ chains on Gr/Co/Ir(111). PTS data obtained on various positions of a molecule for an energy range of a) ±1 eV and b) ±2 eV. The positions of the spectra are indicated by the color coded marks on the model of the molecule on the right. The color coded arrows in a) and b) indicate energies for which spatially resolved $\mathrm{d}I/\mathrm{d}U$ data are presented in Figure 6.6 for arrows pointing down and Figure 6.7 for arrows pointing up.
Tunneling-parameters: a) $U = -1000\,\mathrm{mV}$; $I_{\mathrm{stab}} = 20\,\mathrm{pA}$; $U_{\mathrm{mod}} = 50\,\mathrm{mV}$; $T \approx 25\,\mathrm{K}$; b) top: $U = -2000\,\mathrm{mV}$; $I_{\mathrm{stab}} = 20\,\mathrm{pA}$; $U_{\mathrm{mod}} = 50\,\mathrm{mV}$; $T \approx 25\,\mathrm{K}$.
Figure reprinted with permission from supporting information of [80].

top of a Co–Sal molecule are presented in Figure 6.5. The spectra in Figure 6.5 a), with the lower energy range, show the states close to the Fermi energy, while the data presented in b) makes states at higher energies visible. The energy values given in the following will not directly correspond to the presented data, but are the average values obtained from analyzing 160 STS spectra.

Because of the different spatial appearances of individual molecular states, the spectra obtained at different positions do not show the same number of features. Although the features in the spectra overlap with each other due to their broad appearance, their positions can be identified in the normalized $\mathrm{d}I/\mathrm{d}U$ data presented here. The broadening of the features is caused by multiple factors: The finite lifetimes of the electrons in the molecular states, the temperature broadening at 25 K, and the modulation voltage of 50 mV, necessary to obtain the $\mathrm{d}I/\mathrm{d}U$ signal. Additionally, broadening of the features due to residual hybridization with the substrate is possible.

The STS data obtained on the Co center for the ±1 eV energy range clearly deviates from the other spectra obtained at different positions on the ligand. For negative energies, the HOMO appears most prominently in the spectroscopy obtained on the Co center. It is positioned at an energy of −267 meV. In the positive energy range, the LUMO+1 causes a large feature at 670 meV in the data obtained on the Co center. In the other data, it causes only small shoulders. The LUMO appears at an energy of 245 meV. It is better visible in the spectra obtained on the ligand than in the data obtained on the Co center. This is caused by the fact that the large feature caused by the LUMO+1 covers up the feature caused by the LUMO.

In Figure 6.5 b), also the LUMO+2 appears at an energy of 1138 meV and the LUMO+3 at 1683 meV. Both of these states are prominent in all spectra obtained on the ligand, but the height and the position in energy of the feature caused by the LUMO+2 are varying. The STS data obtained on the Co center shows peaks at the same energies but they have a smaller height. Especially the LUMO+2 has little to no contribution by the Co center. A HOMO−1 state is indicated by a pronounced shoulder in the Co center spectroscopy at −1785 eV. In the spectra obtained on the ligand positions, an onset of a large peak can still be seen in the ±2 eV energy range.

To visualize the spatial appearance of the individual states, $\mathrm{d}I/\mathrm{d}U$ maps were obtained at various energies. The arrows in Figure 6.5 indicate energies at which $\mathrm{d}I/\mathrm{d}U$ maps were obtained that show the identified states. They are presented in Figure 6.6 for arrows pointing down and Figure 6.7 for arrows pointing up. For the states presented in Figure 6.6, the corresponding DFT-calculated MOs could be identified and are shown below the maps. The MOs are labeled with a combination of the spin state (α or β) and the Co-3d orbital contributing to the MO or with LS for the ligand states, which have no contribution of the Co atom. For the DFT-calculated MOs, the square of the calculated electron wave function is plotted, which corresponds to the probability density of an electron in this orbital. This probability density directly correlates to the LDOS at the energy of the MO and, therefore, to the spatially resolved $\mathrm{d}I/\mathrm{d}U$ signal. The attribution between measured and calculated states was done based on their position in energy

and their spatial appearance. The energies of the MOs shown in Figure 6.6 are presented in Table 6.1. Because of the finite energy resolution of STS, the $\mathrm{d}I/\mathrm{d}U$ signal of a single measured state can be composed of contributions by multiple MOs having a similar energy eigenvalue. Therefore, multiple DFT-calculated MOs have been attributed to each map.

Remarkable are the ligand states, as defined in Section 3.6, marked by the light green color. These can easily be attributed because of the nodal plane cutting through the bridge benzene ring and the Co center, accompanied by almost zero probability density on the Co atom. This shape is clearly resembled by the LUMO+2 state. The HOMO, marked by the yellow color, can just as easily be attributed since there are only two MOs with their energy eigenvalues within the respective energy range, as can be seen in Figure 6.8. One of these MOs consists almost exclusively of a Co-$3\mathrm{d}_{z^2}$ orbital, with only minor contributions of the ligand. The other MO consists of a Co-$3\mathrm{d}_{yz}$ orbital and ligand π-orbitals. Both MOs are attributed to the HOMO since they are very close in energy, and the measured signal shows a large intensity at the position of the Co atom but also extends onto the ligand atoms.

The attribution of the LUMO and the LUMO+1 to the corresponding MOs is challenging. Arguably, the large spread over the surrounding ligand of the signal peak centered on the Co center, observed for the LUMO+1, nicely resembles the Co-$3d_{xy}$ orbital, strongly hybridizing with the in-plane π-orbitals of the surrounding N and O atoms. At the same time, the LUMO state shows a more confined signal peak at the Co center, fitting to the Co-$3\mathrm{d}_{xz}$ orbital. The last mentioned is the minority component of the SOMO, as discussed in Section 3.6. The additional MOs attributed to LUMO and LUMO+1, respectively, have a very similar contribution of the ligand atoms and explain the constant contrast on the ligand further away from the Co center.[4]

The two states that are presented in Figure 6.7 could not be related to any of the calculated MOs unequivocally. Since they can still be observed clearly in the PTS

[4]It has to be noted at this point that the $\mathrm{d}_{x^2y^2}$ orbital attributed to the LUMO+1 appears distorted in plots of the calculated electron wavefunction.

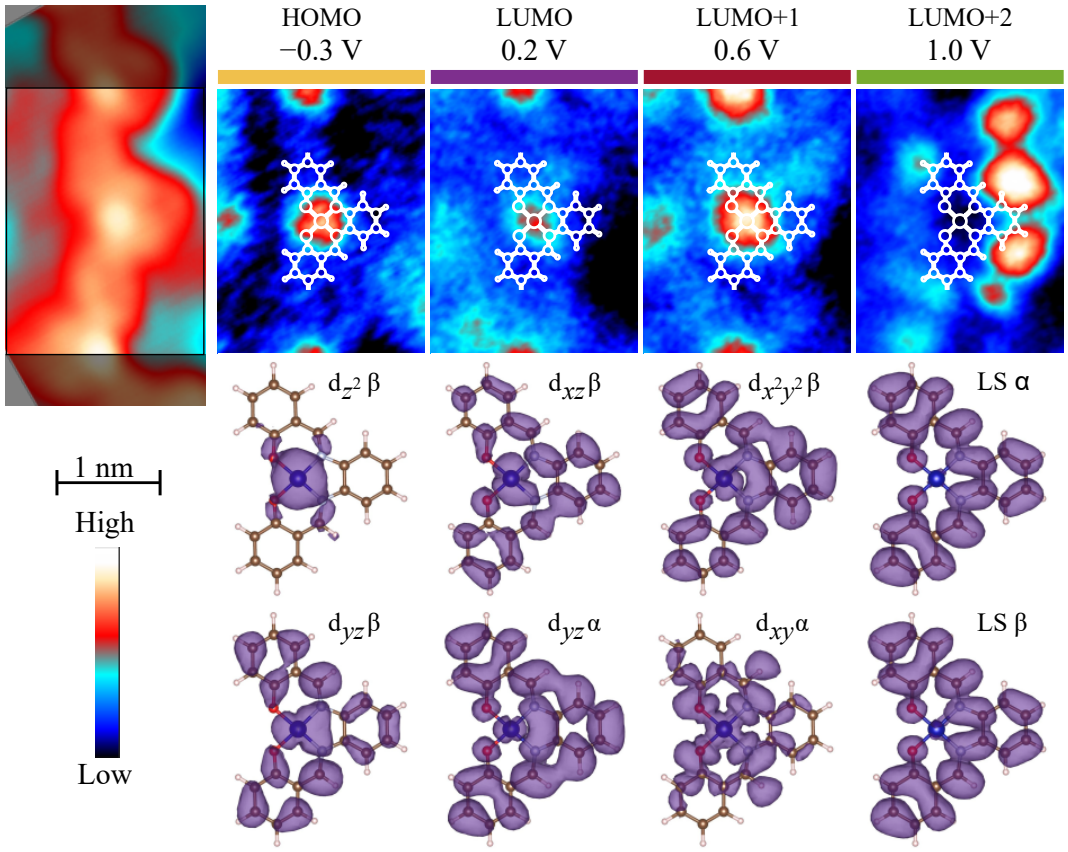

Figure 6.6: Comparison between molecular states, as imaged by STM, and DFT calculated MOs. A topography image with submolecular resolution on the left hand side, obtained at $U = 50\,\mathrm{mV}$, indicates the frame presented in the $\mathrm{d}I/\mathrm{d}U$ maps. Above each $\mathrm{d}I/\mathrm{d}U$ map a color coded bar and the bias voltage is given. A model of the Co–Sal molecule, superimposed on each $\mathrm{d}I/\mathrm{d}U$ map, indicates the position of the molecule. Below each $\mathrm{d}I/\mathrm{d}U$ map the squared electron wave functions of the DFT-calculated MOs attributed to the $\mathrm{d}I/\mathrm{d}U$ map are shown. The MOs are labeled with the contributing 3d orbital of the Co atom or with LS in case of the ligand state and with the label for the spin state α or β.
Tunneling-parameters: $I_{\mathrm{stab}} = 20\,\mathrm{pA}$; $U_{\mathrm{mod}} = 50\,\mathrm{mV}$; $T \approx 25\,\mathrm{K}$.
Figure reprinted with permission from [80].

Table 6.1: Energies of the LDOS plots shown in Figure 6.6:

MO	$d_{yz}\beta$	$d_{z^2}\beta$	$d_{yz}\alpha$	$d_{xz}\beta$	$d_{xy}\alpha$	$d_{x^2y^2}\beta$	LS β	LS α
energy [meV]	−602	−530	951	997	1169	1171	531	604

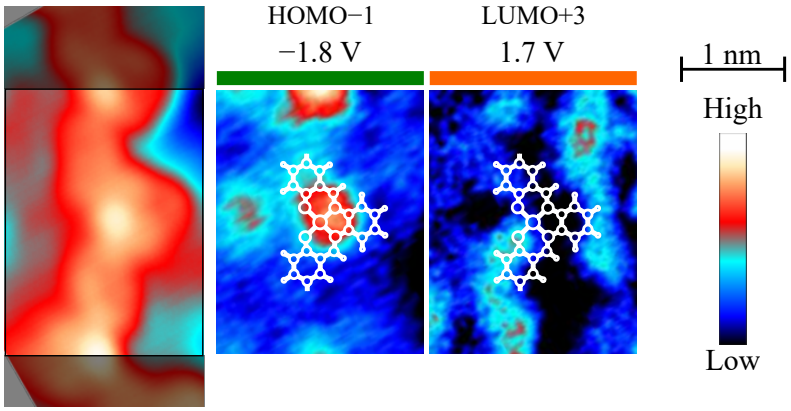

Figure 6.7: Molecular states as imaged by STM which could not unequivocally be attributed to DFT-calculated MOs. A topography image with submolecular resolution on the left hand side, obtained at $U = 50\,\mathrm{mV}$, indicates the frame presented in the $\mathrm{d}I/\mathrm{d}U$ maps. Above each $\mathrm{d}I/\mathrm{d}U$ map, a color coded bar and the bias voltage is given. A model of the Co–Sal molecule, superimposed on each $\mathrm{d}I/\mathrm{d}U$ map, indicates the position of the molecule.
Tunneling-parameters: $I_{\mathrm{stab}} = 20\,\mathrm{pA}$; $U_{\mathrm{mod}} = 50\,\mathrm{mV}$; $T \approx 25\,\mathrm{K}$.

measurements and the spatially resolved $\mathrm{d}I/\mathrm{d}U$ maps, they are presented here for completeness. The HOMO−1 also shows a large signal peak on the Co center, extending widely onto the ligand. This explains the faster rising onset in the PTS data obtained on the Co center than in the data obtained on the ligand. Opposed to this, the LUMO+3 state seems to be mainly composed of ligand contributions.

A comparison between the measured energies of the molecular states and the DFT-calculated energies for the MOs is presented in Figure 6.8. The experimental values are those given in the text above, obtained from analyzing the peak positions in the STS data. Plotted are the mean values of the energies with the standard deviations given as errors. For the DFT-calculated MOs, the energy eigenvalues are plotted, as already presented in Figure 3.7 in Section 3.6. The colors connect those states that were attributed to each other by comparing the spatial $\mathrm{d}I/\mathrm{d}U$ data and the calculated electron-probability densities, as shown in Figure 6.6.

When comparing the energies extracted from the STS data with the DFT-calculated energies, a striking difference can be seen for the ligand states, repre-

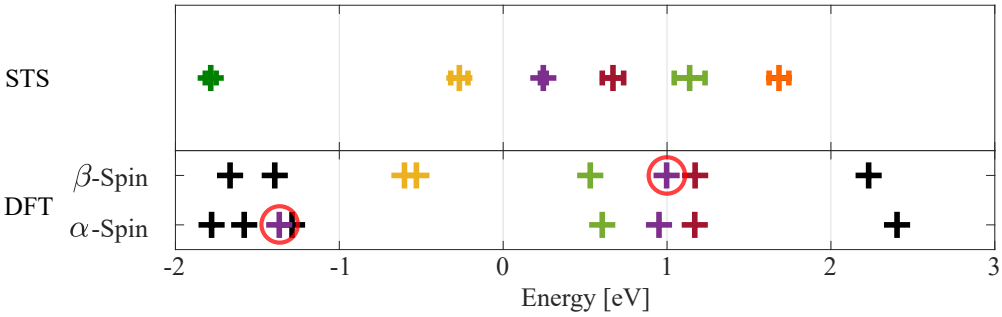

Figure 6.8: Comparison between energies of molecular states, as measured by STM, and DFT-calculated MOs. The color code assigns corresponding states from experimental data and DFT data. The color code of the experimental data also corresponds to the color code in the previous figures. Majority and minority component of the SOMO in the DFT data are marked by red circles.

sented by the light green color. These states could be clearly attributed because of their spatial appearance, as discussed above. However, the energy eigenvalues of the calculated ligand states lie at 531 meV and 604 meV, below the energy of those MOs with a Co-3d-orbital component. At the same time, the energy of the measured ligand states lies at 1138 meV, above the states with a strong signal at the Co center position. Additionally, the energies of the LUMO and LUMO+1 extracted from the experiment are lower than the energies of the attributed DFT-calculated MOs. This goes hand in hand with a reduced HOMO–LUMO gap for the measured data, of (469 ± 88) meV, as compared to the DFT-calculated gap of 1061 meV. The differences can have two possible reasons: Either the DFT calculations attribute a wrong position in energy to these states, or the hybridization between the molecule and the substrate causes an energy shift of the states.

As discussed in Section 3.6, DFT calculations of various independent studies by different research groups, using different basis sets and simulation packages, led to similar results concerning the spatial appearances of the MOs [15, 16, 80, 223, 227, 228]. Also the energy of the ligand state is lying between 500 meV and 1000 meV in all studies presenting this state. However, while in most of the studies, the ligand state was calculated to be the LUMO, in the study by DiLullo *et al.*, the SUMO

was calculated to have the lowest energy with $\approx 300\,\mathrm{meV}$.[5] Since this study is the only one considering a Au(111) substrate in the calculations, this points to the interpretation that hybridization of the Co center with the substrate lowers the energy of states with a contribution of the Co-3d orbitals. This was also observed for Co–Sal on $GdAu_2$, as described in Section 5.3. This shows that, against expectations, the graphene layer does not completely suppress hybridization between Co–Sal molecules and the substrate.

An aforementioned study by N'Diaye *et al.* showed that hybridization guides the adsorption of metal clusters on pristine Gr/Ir(111) [272]. In this study, it was found that C atoms sitting directly on top of Ir atoms in the hcp regions of the moiré hybridize with the Ir atoms. Therefore, the nearest neighbors of these C atoms can, in return, hybridize with metal atoms on top of the graphene layer. This effect will be even stronger for Gr/Co/Ir(111) due to the stronger hybridization between graphene and the Co layer. In combination with the tendency of the Co center of Co–Sal to coordinate additional axial ligands, hybridization is likely the explanation for the discrepancy between DFT data and experimental data. Signs of hybridization between Co intercalated graphene and adsorbed Fe–Pcs have also been found in an XPS study by Avvisati *et al.* [295]. While the hybridization of the Co atoms with the substrate will not directly affect the energy of the ligand state, which has no contribution by the metal orbitals, it will instead cause a lowering of the molecular states that have a large contribution by the Co-3d orbitals. This, in return, can also affect the energy of the ligand state.

In summary, differences in the energies of the MOs suggest that the hybridization is not completely suppressed by the graphene layer. Instead, it is only reduced compared to the hybridization of a Co–Sal adsorbed on a pure metal substrate. This is evident from the comparison of STS data of Co–Sal on Gr/Co/Ir(111) compared to data of Co–Sal adsorbed on the $GdAu_2$ surface alloy. Despite the residual hybridization between Co-Sal and the Gr/Co/Ir(111) substrate, individual states could be identified by analyzing normalized $\mathrm{d}I/\mathrm{d}U$ data, and their spatial appearance was resolved by $\mathrm{d}I/\mathrm{d}U$ mapping. Additionally, the experimentally

[5] The study by Kochem *et al.* does not show the ligand state, and all presented unoccupied MOs have a Co-d-orbital contribution [228].

identified states could be related to the MOs from DFT calculations. Because of the low grade of hybridization, it is likely that the molecules' magnetic moments are preserved and can be investigated by SP-STM and SP-STS measurements.

6.4 Magnetic Properties

Asymmetry maps obtained for two $[\text{Co–Sal}]_n$ chains from $\mathrm{d}I/\mathrm{d}U$ maps measured at 450 meV with external fields of ± 0.75 T are presented in Figure 6.12. In these maps, the contrast is caused by a switch of the tip magnetic moment. The upper panel shows a five-membered chain, adsorbed on the most commonly observed orientational domain of Gr/Co/Ir(111) with a lattice constant of 24 Å for the moiré pattern. The typical magnetic contrast of the moiré pattern, with spin polarization of opposite sign for top regions compared to fcc and hcp regions, can be seen. For the data on the six-membered chain in the lower panel, the moiré pattern has a significantly smaller lattice constant of 14.7 Å. Here, the contrast due to the substrate's spin polarization is very small. Only the fcc and hcp areas show a light blue shading, while the top areas show no spin polarization. An exception are two top sites in the lower right of the image, which show a clear spin polarization indicated by the red color in the asymmetry map. In the topography image, one of these sites appears higher and one appears lower than the average top site. This indicates anomalies in the graphene layer at these positions.

For both $[\text{Co–Sal}]_n$ chains, magnetic contrast can be observed at the positions of each individual member of the chain. This indicates clearly that all members of the chain still obtain a magnetic moment. Under the assumption that all molecules have the same electronic structure, the spin-polarized electrons tunnel for each member into the same state, of either minority or majority spin. In this case, a second conclusion can be drawn from the asymmetry maps: The expected antiferromagnetic coupling between individual Co centers within a $[\text{Co–Sal}]_n$ is not obtained for these chains adsorbed on Gr/Co/Ir(111). Instead, for the first chain, the two members on the left show a positive asymmetry, while the three members on the right show a negative spin asymmetry. For the second chain, the first and

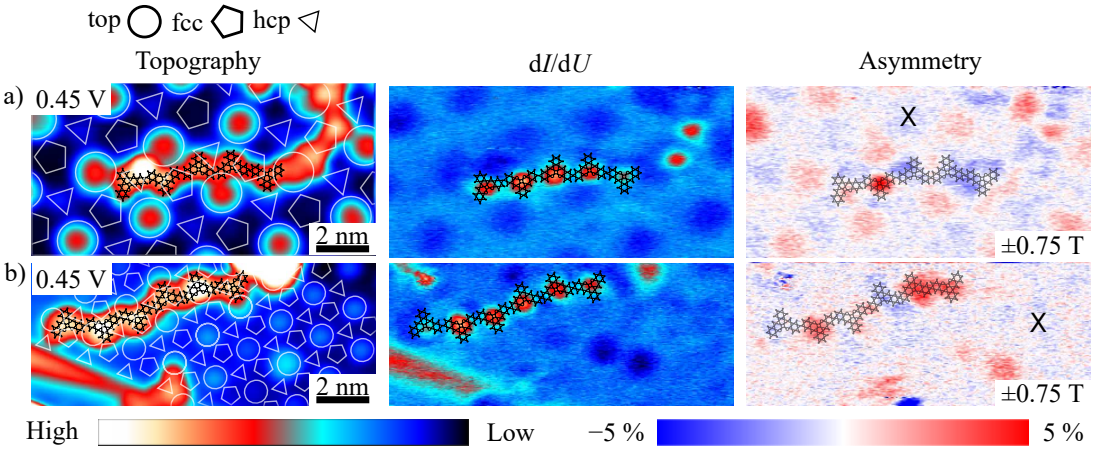

Figure 6.9: Spatially resolved SP-STS data for $[\text{Co–Sal}]_n$ chains on Gr/Co/Ir(111), obtained for out-of-plane external fields. The figure shows topography images, corresponding $\mathrm{d}I/\mathrm{d}U$ maps, and corresponding spin asymmetry maps obtained at 450 meV for two $[\text{Co–Sal}]_n$-chains. Panel a) shows a five-membered chain and panel b) a six-membered chain. A model of the molecule, superimposed on the images, indicates the positions of the individual molecules within the $[\text{Co–Sal}]_n$ chains. In the topography images, also the different areas of the moiré pattern are shown. The black 'x' symbols in the asymmetry maps indicate the positions at which magnetization curves for the substrate, presented in Figure 6.10 and 6.11, were obtained.
Tunneling-parameters: $I_{\text{stab}} = 50\,\text{pA}$; $U_{\text{mod}} = 50\,\text{mV}$; $z-\text{range} = 2.0\,\text{Å}$.

the fourth member from the left show negative spin asymmetry, while the others show positive spin asymmetry

Multiple explanations can be considered for the unexpected behavior of the individual magnetic moments within the chain. For the magnetic moments of single Br_2Co–Sal molecules on Gr/Co/Ir(111), different behaviors have been found depending on the molecules' adsorption configurations [230]. Both ferromagnetic and antiferromagnetic coupling of the molecular magnetic moments to the substrate has been observed. Therefore, one possible explanation for the different behaviors of the individual Co centers within a chain is the varying interaction of the centers with the substrate, depending on the adsorption site. In this case, the intramolecular magnetic coupling between the Co centers would be weak compared to the coupling between the Co centers and the substrate.

The adsorption sites of the members of both chains can be judged by looking at the topography images in Figure 6.9. The five-membered chain is almost exclusively adsorbed on fcc and hcp regions, which are only distinguished by the relative lateral position between the C atoms of the graphene layer and the Ir atoms in the layer below the Co layer. Only the member on the far left is positioned on a top region of the moiré pattern with the outer benzene ring. Most studies on transition metal intercalated graphene on Ir(111) and on pristine graphene on Ir(111) showed that fcc and hcp regions can be assumed to be equivalent. Only the study by N'Diaye *et al.* on adsorption of Ir clusters on Gr/Ir(111) showed a preferred adsorption of the clusters on the hcp areas [272]. Additionally, the second and the third member from the left have very similar adsorption sites while showing opposite spin asymmetry.

For the six-membered chain, the data has to be interpreted cautiously. The moiré pattern cannot be seen at the position of the chain. Therefore, the moiré pattern in the lower right corner was extended over the area of the molecule. However, since the pattern on the other side of the chain is not visible, this procedure may be flawed. Additionally, the wrinkle in the graphene layer, which can be seen in the lower left corner of the image, might cause distortions in the graphene layer. The chain covers all three regions of the moiré pattern, including the top regions. However, the adsorption sites of the individual Co centers cannot be related to the differences in the spin asymmetry.

Differences in the electronic structure of individual molecular members within a chain also could explain the differences in the measured spin polarization. As it was seen for the SP-STS data on $GdAu_2$, presented in section 5.1, the spin-polarization switches its sign for different energies. Therefore, different spin polarizations would be measured for individual members at the same energy if their electronic states are positioned at different energies. Such differences in the electronic structure could be caused either by the interaction with other adsorbates in vicinity to the chain or, again, by the adsorption configuration of the individual members. Indeed, for both chains adsorbates can be found close to the chains. For the five-membered chain, an adsorbate positioned between the first and second member from the left can be seen, and for the six-membered chain a large cluster is adsorbed next

to the member on the far right of the chain. Neither of these adsorbates shows any magnetic contrast. Therefore, a magnetic interaction between the chains and the respective adsorbate can be ruled out. However, in both cases the adsorbate could cause a change in the electronic structure of the neighboring molecules. For the six-membered chain, this interaction could only influence the far right member of the chain. This, however, cannot explain the spin asymmetry found for the different members along the whole chain. For the five-membered chain, the adsorbate is positioned directly between the two members showing different spin asymmetry compared to the other members. In the $\mathrm{d}I/\mathrm{d}U$ map at 450 meV this adsorbate causes a depletion of the measured signal. Therefore, it cannot be ruled out that this defect causes the observed differences in the spin asymmetry, while the three members on the right are ferromagnetically coupled, either via intramolecular coupling or because of interactions with the substrate.

A third possible reason is constituted by multiple competing interaction pathways, causing non-collinear behavior instead of collinear antiferromagnetic coupling. At first thought, the DM interaction causing a spiral-like spin structure within a $[\mathrm{Co–Sal}]_n$ chain seems likely to produce the observed spin polarization. In his original publication about the DM interaction, Moriya showed that in an inversion symmetric system the DM interaction will be zero [181]. The symmetry of a $[\mathrm{Co–Sal}]_2$ dimer on a surface depends on the relative orientation of the bridges of the individual members. If they are aligned parallelly, there is no inversion symmetry, but if the bridges are aligned antiparallelly, the dimer will be inversion symmetric. In the here investigated $[\mathrm{Co–Sal}]_n$ chains, both situations occur, but, considering the hybridization between the Co centers and the graphene layer, it has to be taken into account that also the graphene takes part in the interaction. Therefore the system loses its inversion symmetry in both possible orientations, as often observed in interface systems [298, 299]. However, the spin-orbit coupling for 3d transition metals is rather low. In this case, the interaction only causes canting of interacting magnetic moments by a few degrees, which, alone, would preserve an antiferromagnetic behavior of the individual members and cannot explain the observed contrast [208, 300].

Theoretical predictions showed an in-plane anisotropy for Co–Sal molecules [229]. A competition between out-of-plane antiferromagnetic coupling between molecules and substrate and in-plane antiferromagnetic coupling between Co centers could explain a non-collinear arrangement of the individual magnetic moments of the Co centers. Both effects, the DM interaction and the competing contributions by anisotropy and external field, may complement each other to create the observed spin asymmetry.

To gain deeper insight into the magnetic behavior of the two $[\text{Co–Sal}]_n$ chains, magnetization curves on the individual Co centers of both chains were obtained with SP-STS, according to the procedure presented in reference [230]. First, the sample was magnetized by a full field sweep [$0.75\,\text{T} \rightarrow 6.0\,\text{T} \rightarrow -6.0\,\text{T} \rightarrow -0.75\,\text{T}$]. Then the field sweep was repeated in steps of 0.75 T and a $\mathrm{d}I/\mathrm{d}U$ map was obtained at each field, with a bias voltage of 450 mV. To extract the magnetization curves from the data, the positions of the Co centers were manually selected in each $\mathrm{d}I/\mathrm{d}U$ map. Using the 'find' function implemented in MATLAB, the exact coordinates of the local maximum in the $\mathrm{d}I/\mathrm{d}U$ signal close to the selected position is determined. A fixed point on the substrate is defined by its position relative to one of the Co centers. Thereby it is guaranteed that the selected position does not change because of the varying position of the scan frame. In the end, the $\mathrm{d}I/\mathrm{d}U$ signal is averaged over a fixed area centered on the calculated positions, and the averaged signal is plotted versus the magnetic field for each point. This signal is proportional to the projection of the local magnetic moment of the sample onto the magnetic moment of the tip. The results are shown in Figures 6.10, 6.11, and 6.12.

Magnetization curves obtained on the five-membered chain are presented in Figure 6.10. Individual members are numbered from left to right and color coded to identify the corresponding magnetization curve. The asymmetry map in Figure 6.9 corresponds to the difference between the data points at $+0.75\,\text{T}$ and $-0.75\,\text{T}$, coming from $+6\,\text{T}$. Next to the signal changes induced by the switch of the tip magnetic moment, large, simultaneous signal changes can also be seen for most of the molecules and the substrate between $\pm 4.5\,\text{T}$ and $\pm 5.25\,\text{T}$. These changes are caused by the switch of the magnetic moment of the substrate and indicate magnetic coupling of molecules and substrate.

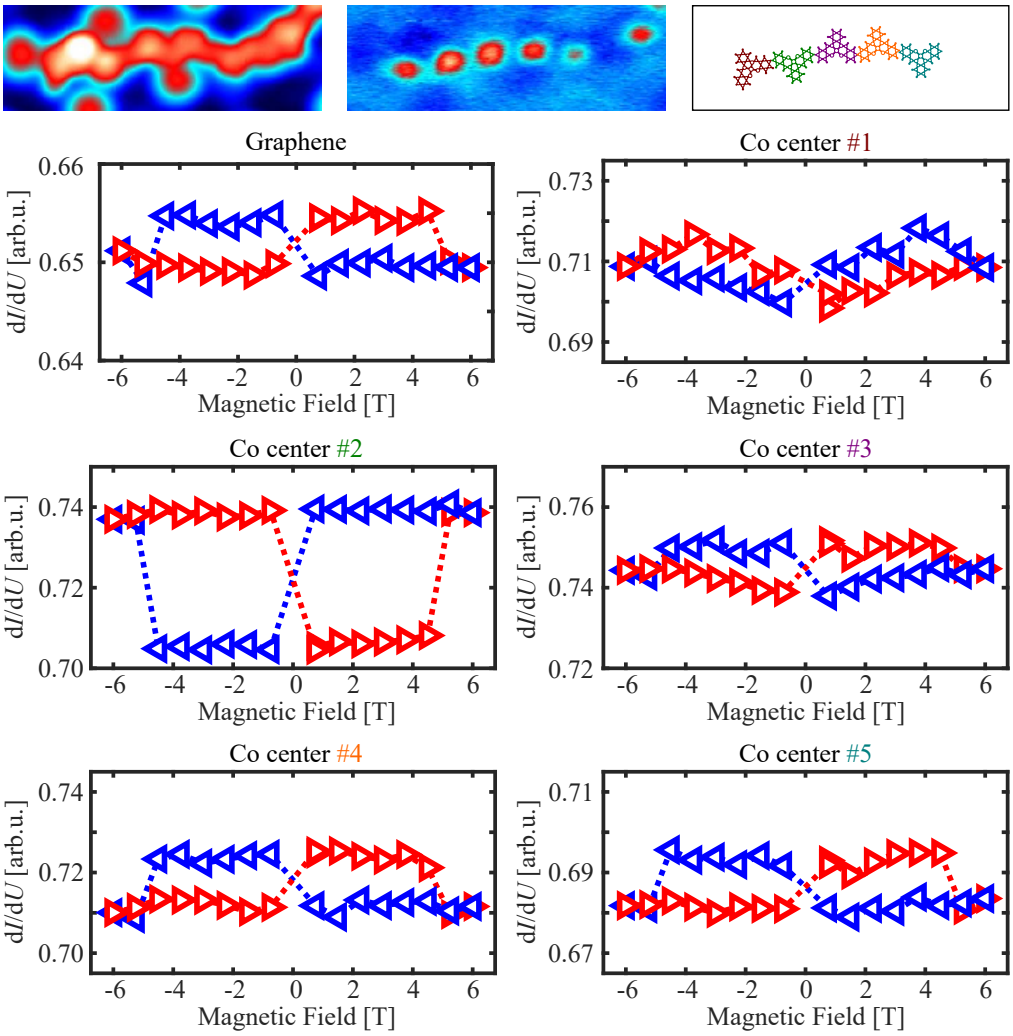

Figure 6.10: Magnetization curves for individual Co centers within a $[\text{Co–Sal}]_5$ chain and for an fcc region of the Gr/Co/Ir(111) substrate. At the top of the image, a topograph, a $\mathrm{d}I/\mathrm{d}U$ map, and a model of the chain are shown. These data are presented in more detail in Figure 6.9. The colors in the model of the chain link the members to their respective magnetization curves. The starting field was chosen at 0.75 T. The direction and color of the triangles, representing individual measurement points, indicate the direction of the field sweep: Red color for increasing field strength and blue color for decreasing fields.

The coupling between molecules and substrate is less clear in the data for the six-membered chain on a different rotational domain of Gr/Co/Ir(111), presented in Figures 6.11 and 6.12. It has to be noted that during the recording of the data for the magnetization curve on the six-membered chain, the tip changed. These changes cause artifacts in the magnetization curves. Therefore, the curve obtained on the substrate, shown in Figure 6.11, is not closed, and the end point strongly deviates from the starting point. However, general observations, like the switching of the tip and the sample magnetization can be clearly observed in the data. In this data of the six-membered chain, the simultaneous switching events of molecules take place already at lower fields, between $\pm 3.75\,\mathrm{T}$ and $\pm 4.5\,\mathrm{T}$. The substrate switches over a larger field range, starting at $3\,\mathrm{T}$ and reaching saturation at $5.25\,\mathrm{T}$. This behavior is uncommon for the Gr/Co/Ir(111)-substrate, but can probably be caused by the extreme orientation of the orientational domain, indicated by the small lattice constant of the moiré pattern. Also the wrinkle in close vicinity to the chain could induce such atypical behavior.

Up to this point, the discussion was limited to the linkage between the behaviors of the magnetic moments of substrate, Co centers, and tip, but their orientation in space was not discussed. Since the Fe-coated W tip is a weak magnet, its magnetic moment will be aligned with the applied external field. It may, however, have a small additional component perpendicular to the field direction, due to canting. This could cause a gradual behavior of the tip magnetic moment in an external field. Such a gradual change of the tip magnetic moment would cause gradual changes in all magnetization curves simultaneously, which has not been observed. The Gr/Co/Ir(111) substrate magnetic moment will be aligned antiparallelly to the external field for increasing absolute field strengths up to the local coercive field. Then it will flip parallel and stay parallel until the direction of the external field is inverted, and the coercive field is reached again.

To judge the spatial orientation of the Co-center magnetic moments, a more detailed interpretation of the magnetization curves is needed. In the five-membered chain, three of the Co centers show clear hysteresis. For Co center #2, the signal behaves opposite to the signal measured on the substrate, while Co center #4 and #5 show the same behavior as the substrate. Co center #1, which is parallel

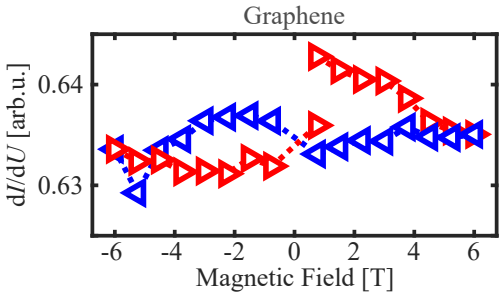

Figure 6.11: Magnetization curve obtained on Gr/Co/Ir(111) next to the six-memberd $[\text{Co–Sal}]_n$ chain. The starting field was chosen at 0.75 T. The direction and color of the triangles, representing individual measurement points, indicate the direction of the field sweep: Red color for increasing field strength and blue color for decreasing fields.

to Co center #2, according to the asymmetry map, and Co center #3, which is parallel to the remaining two Co centers, show only small signal changes at the fields at which the substrate magnetization switches. For decreasing absolute field strengths, both of these Co centers show a gradual change in the $\mathrm{d}I/\mathrm{d}U$ signal. Co center #1 also shows a gradual change for increasing field strengths. Such gradual changes can only be caused by bending of a canted magnetic moment in the changing external field. Since no gradual changes can be seen in the data obtained on the substrate, the gradual changes can only be caused by the Co-center magnetic moments, while the direction of the tip's magnetic moment stays constant. This supports the theory of a non-collinear spin structure within the $[\text{Co–Sal}]_n$ chains.

Small gradual changes of the $\mathrm{d}I/\mathrm{d}U$ signal can also be seen for Co center #5, although these are not as clear as those for the other two Co centers. Since the spin-polarized $\mathrm{d}I/\mathrm{d}U$ signal is proportional to the cosine of the angle between the magnetic moments of tip and sample, the gradual changes in the signal, induced by the bending, will be larger the closer this angle is to 90°. As mentioned above, the tip magnetic moment is aligned out-of-plane, parallelly to the external magnetic field. Therefore, it follows that Co centers #2 and #4 have an out-of-plane magnetic moment, Co center #5 has a mainly out-of-plane magnetic moment with only a small in-plane component, and Co centers #1 and #3 have a large in-plane component in their magnetic moments.

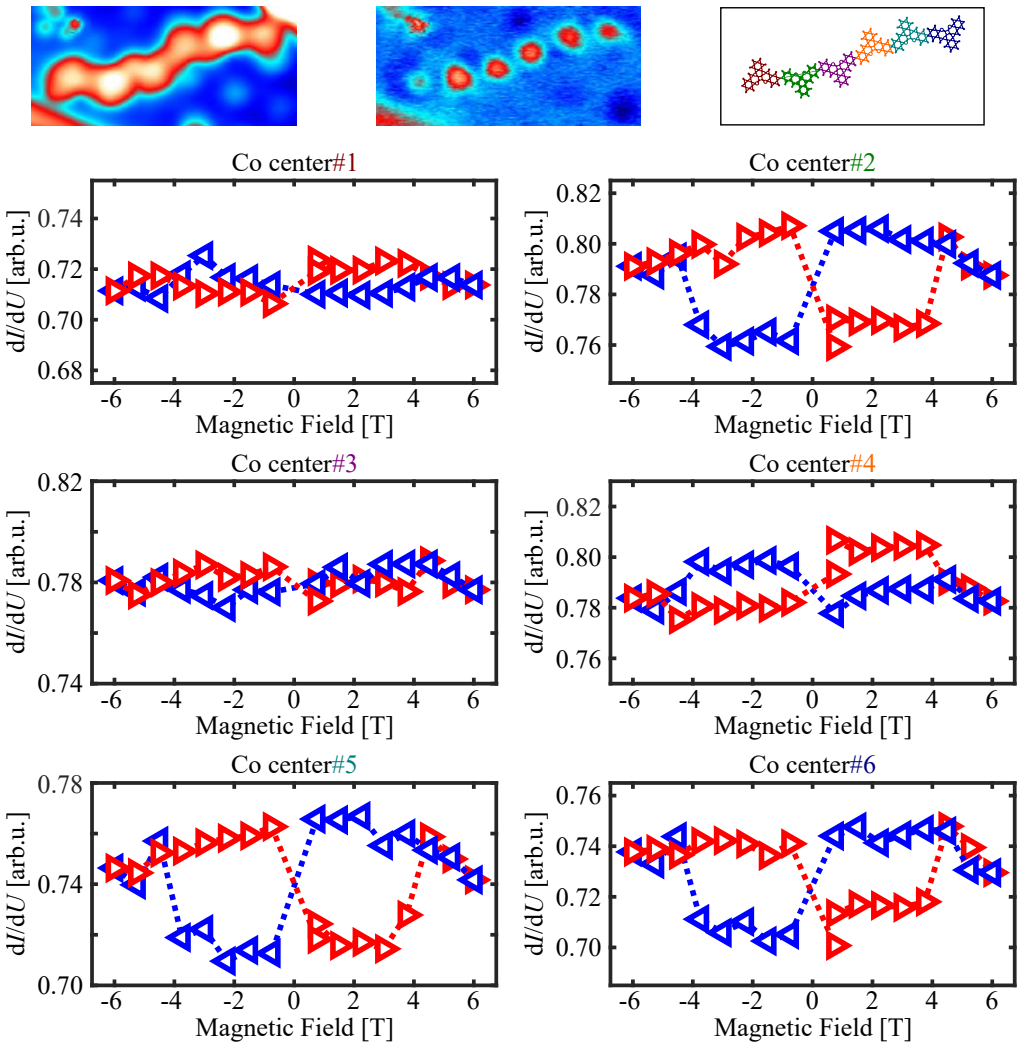

Figure 6.12: Magnetization curves for individual Co centers within a $[\text{Co–Sal}]_6$ chain. At the top of the image, a topograph, a $\mathrm{d}I/\mathrm{d}U$ map and a model of the chain are shown. This data are presented in more detail in Figure 6.9. The colors in the model of the chain link the members to their respective magnetization curves. The starting field was chosen at 0.75 T. The direction and color of the triangles, representing individual measurement points, indicate the direction of the field sweep: Red color for increasing field strength and blue color for decreasing fields.

As mentioned above, the out-of-plane magnetic moments of Co centers #1 and #2 are considered to be aligned parallelly with each other, while those of the other Co centers are also aligned parallelly with each other, but antiparallelly with the aforementioned. Note that this is only true under the assumption that all individual members of the chain have the same electronic structure. To identify which of the Co centers couple ferromagnetically to the substrate and which antiferromagnetically, we can analyze the directions of the gradual changes for Co centers #1, #3, and #5. Co center #3 shows a gradually decreasing $\mathrm{d}I/\mathrm{d}U$ signal for decreasing fields after reaching the maximum field. This behavior can be described by a magnetic moment aligned antiparallelly with the substrate magnetic moment. At the starting field, the out-of-plane component of the magnetic moment is aligned parallelly with the external field but it has a large in-plane component. When the external field becomes large enough to switch the substrate magnetic moment, the Co-center magnetic moment is forced into the direction opposite to the external field because of the antiferromagnetic coupling. Upon further increase of the field strength, the external field forces the canted moment into a position with an even larger in-plane component. When the field strength is reduced, the magnetic moment of the Co center #3 gradually rotates into its equilibrium position and the same behavior is repeated for negative fields.

Co center #5 behaves similarly. Here, the out-of-plane component of the magnetic moment is assumed to be oriented parallelly to the external magnetic field at the start of the magnetization curve. When the external field is increased, the canted magnetic moment rotates further into the field direction because of its in-plane component. After the inversion of the substrate magnetic moment, the Co-center magnetic moment is forced to align antiparallel to the external field. It stays in this position until zero external field is reached, and the same procedure is repeated for negative fields.

The behavior of Co center #1 is more complicated. It is assumed to have a magnetic moment with an out-of-plane component aligned parallelly to the substrate magnetic moment and a large in-plane component, indicated by the gradual changes. The alignment of the out-of-plane component is deduced from the fact that the $\mathrm{d}I/\mathrm{d}U$ signal measured on this Co center behaves opposite to that of Co

centers #3 and #5. These were, according to the previous discussion, found to be coupled antiferromagnetically to the substrate. Therefore, the canted magnetic moment is rotated further into an in-plane orientation when the external field is increased. Thereby, the out-of-plane component, antiparallel to the tip magnetic moment, is shrinking, and the $\mathrm{d}I/\mathrm{d}U$ signal increases. Upon the inversion of the substrate magnetic moment, the $\mathrm{d}I/\mathrm{d}U$ signal measured on Co center #1 shows only a marginal change, indicating its almost complete in-plane alignment. Surprisingly, the $\mathrm{d}I/\mathrm{d}U$ signal increases further for decreasing external fields, until a field of 3.75 T is reached. Only then the $\mathrm{d}I/\mathrm{d}U$ signal decreases again, which would be expected since the magnetic moment can relax into its original position, only with an inverted out-of-plane component. However, the increase between 6 T and $3,75$ T cannot be explained by the obtained data.

An analogue discussion of the data obtained for the six-membered chain has to be done with care because of the changes in the tip during the experiments. However, hysteresis can be observed clearly for four of the Co centers, i.e. #2, #4, #5, and #6. The other two Co centers showed contrast in the asymmetry map presented in Figure 6.9, but the signal is low compared to the other Co centers, which is also reflected in the magnetization curves. Therefore, it cannot be ruled out that these changes in the $\mathrm{d}I/\mathrm{d}U$ signal are due to the changes of the tip.

Following the previous arguments that the tunneling electrons always probe the same spin-polarized state of the individual members, the relative orientation of the magnetic moments of Co centers #2, #4, #5, and #6 can be judged by comparing their hysteresis curves with those of the five-membered chain. In this case, the behaviors of Co centers #2, #5, and #6 are clear. Their out-of-plane magnetic moments are aligned antiparallelly with the external field at the start of the magnetization curve, stabilized by ferromagnetic coupling with the substrate. For increasing fields, the $\mathrm{d}I/\mathrm{d}U$ signal stays constant up to a field of 0.75 T. At this field the magnetic moment of the Co centers switches, and they are aligned parallelly with the external field. Co center #4 shows exactly opposite behavior compared to the aforementioned Co centers.

Interestingly, while the substrate magnetic moment is inverted over a field range of 2.25 T, the Co-center magnetic moments flip abruptly between 3.75 T and 4.5 T. This hints toward intramolecular coupling since still all Co centers switch simultaneously. However, it is also possible that the substrate magnetization reaches a threshold that causes the simultaneous changes. For the other two Co centers, #1 and #3, the data cannot be interpreted safely because of the changes in the tip. Gradual changes of the $\mathrm{d}I/\mathrm{d}U$ signal can be observed for the two Co centers #2 and #5, which show a clear hysteresis. Usually, such gradual changes would be expected for the Co centers which are showing small hysteresis since these are expected to have an in-plane oriented magnetic moment. For both Co centers, gradual changes can be observed for decreasing absolute fields. The $\mathrm{d}I/\mathrm{d}U$ signal is continually increasing until the magnetic moment of the tip is inverted. After the switch of the tip magnetic moment the signal is constant until the molecules switch again.

For now, the discussion was focused on the spatial resolution of the spin asymmetry. To resolve the spin asymmetry in energy, a SP-PTS experiment was performed on the five-membered $[\mathrm{Co–Sal}]_5$ chain. Since the spin polarization is concentrated on the Co centers, the spectra were obtained at their positions. Normalized STS spectra obtained with out-of-plane external fields of 2.25 T and 6 T, before and after the flip of the sample magnetic moment, are presented in Figure 6.13. Asymmetry plots deduced from these data are presented as well.

To exclude artificial contrast caused by different tip–sample distances in the parallel and antiparallel case, usually, the tip is stabilized above a non-spin-polarized area and kept at constant height while moving it to the position of the SP-PTS measurement. Since no non-spin-polarized area can be found in the vicinity of the $[\mathrm{Co–Sal}]_5$ chain, the tip was stabilized on top of Gr/Co/Ir(111) at a bias voltage of $-800\,\mathrm{mV}$, at which the substrate shows low spin polarization. This way, an artificial contribution cannot be completely excluded but is reduced to a minimum. According to the investigation of the electronic properties, the SOMO is positioned below $-2\,\mathrm{eV}$. PTS experiments at such energies are risky for the tip and the molecules and, therefore, have to be avoided. The SUMO was found within the $\pm 1\,\mathrm{eV}$ energy range. For the energy ranges from 1 eV to 2 eV and from $-1\,\mathrm{eV}$

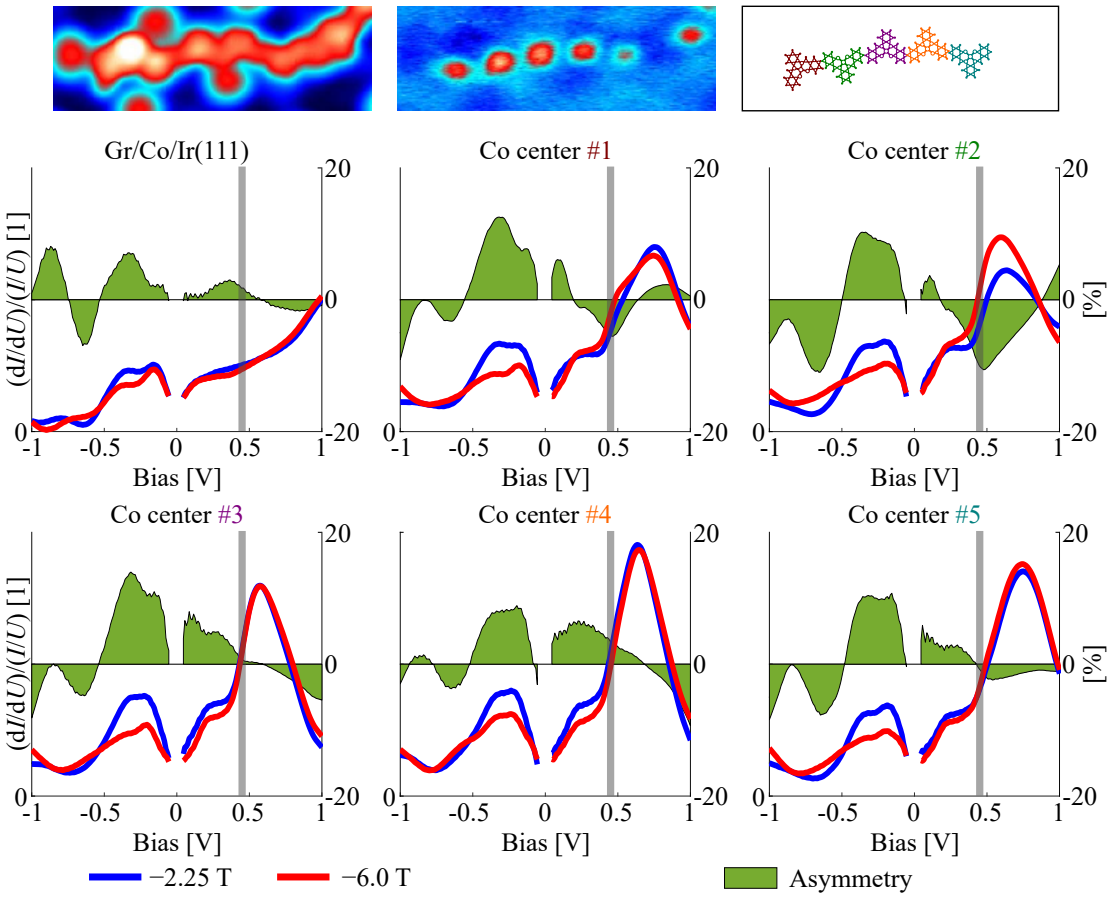

Figure 6.13: SP-PTS data for a $[\text{Co–Sal}]_5$ chain on Gr/Co/Ir(111) obtained with out-of-plane external fields. At the top of the image, a topograph, a $\mathrm{d}I/\mathrm{d}U$ map, and a model of the chain are shown. The colors in the model of the chain link the Co centers to their respective PTS data. SP-PTS data on an fcc area of the Gr/Co/Ir(111) substrate and on the Co centers were measured at $-2.25\,\mathrm{T}$ (blue) and at $-6\,\mathrm{T}$ (red). Corresponding spin-asymmetry plots (green) were calculated from the SP-PTS data. The gray bars indicate the energy at which the magnetization curves were obtained. The energy range of $\pm 50\,\mathrm{meV}$ around Fermi energy was cut out in the plots.
Tunneling-parameters: $U_{\mathrm{stab}} = -800\,\mathrm{mV}$; $I_{\mathrm{stab}} = 50\,\mathrm{pA}$; $U_{\mathrm{mod}} = 50\,\mathrm{mV}$.

to −2 eV, no relevant states concerning the magnetic properties of the molecule are expected. Therefore, the energy range was chosen to be ±1 eV. The plots are cut out in the energy range of ±50 meV around Fermi energy to remove an artificial peak due to the normalization of the data over I/U.

For the negative energy range, the SP-PTS data obtained on Co centers and substrate look very similar. Only at the lower border of the energy range, the spin asymmetries of the Co centers show an onset of a negative feature, while the substrate spin asymmetry shows a positive peak at −869 meV. The feature causing the negative spin asymmetry for the Co centers is outside of the measured energy range. An interesting feature can be seen around −250 meV for the substrate and all Co centers. Here, all spin-asymmetry plots show a broad feature of positive sign. This is the energy at which the HOMO of the Co–Sal molecules was found. According to the analysis of the electronic properties in Section 6.3, the HOMO is composed of two MOs with minority spin. However, since substrate and Co centers show spin asymmetry at this energy, a quantitative analysis would be needed to extract information about the Co-center magnetic moments from the spin asymmetry at this energy. Such an analysis is not possible because of the inadequate stabilization procedure for the tip, which cannot completely exclude a different tip–sample distance for the SP-PTS data obtained at different fields. Nonetheless, the similarity in sign and energy of the spin-asymmetry peak indicates hybridization between the molecule and the substrate at this energy, which could cause ferromagnetic coupling between molecules and substrate, according to the results by Candini *et al.* [294].

In the positive energy range, there are clear differences between the spectra obtained on the Co centers and the data obtained on the substrate. Additionally, the spectra obtained on Co centers #1 and #2 deviate from those on Co centers #3, #4, and #5, which agrees with the observations in the spin-asymmetry maps and the magnetization curves. For Co centers #1 and #2, the spin asymmetry has a negative peak at 467 meV and 477 meV, respectively. This asymmetry seems to be caused by a spin splitting of the LUMO+1, similar to the observations reported by Schwöbel *et al.* for the LUMO of $TbPc_2$ on Gr/Ir(111) [301]. In the present case, according to the discussion of Section 6.3, the LUMO+1 is composed

of two MOs of opposite spin. These cannot be resolved individually by non-spin-polarized STS. In the case of spin-polarized tunneling, however, the probability of the spin-polarized electrons to tunnel from the tip into the majority-spin MO is higher when the magnetic moment of the MO is parallel to the tip magnetic moment. For antiparallel alignment, tunneling into the minority-spin MO has a higher probability. This is reflected in the appearance of an additional shoulder at around 540 meV for Co center #1 and in a shift of the LUMO+1 state from 630 meV to 590 meV for Co center #2.

For Co centers #3 and #4, a peak of positive sign is observed in the spin-asymmetry plots, with a maximum at $\approx$ 250 meV. This is the energy at which the LUMO was observed, which is composed of the SUMO and another MO of opposite spin. Co centers #1 and #2 also show a small feature at this energy but of negative sign. In these asymmetry plots, the features are hard to see because of their small size and since they are partly covered by the large features of the LUMO+1, discussed before. Close to this energy, at 360 meV, the substrate shows a spin-asymmetry peak of positive sign as well. Therefore, the additional contribution by tunneling directly from the tip into the substrate can cause an increase in the measured spin-asymmetry for Co centers #3 and #4 and a decrease for the negative features for Co centers #1 and #2. Interestingly, Co center #5 shows a mixture of both behaviors. On the one hand side, it shows the same positive feature as Co centers #3 and #4, at $\approx$ 250 meV, but, on the other hand, it also shows a small negative spin-asymmetry peak at 540 meV. In summary, the SP-PTS data does not provide information on whether electrons tunnel into majority or minority states at certain energies. It shows differing features between molecules coupled ferromagnetically or antiferromagnetically to the substrate. However, these differences cannot be linked to the adsorption sites of the Co centers and are rather caused by the magnetic behavior of the molecules than by differences in hybridization.

It can be concluded at this point that the individual Co centers of [Co–Sal]$_n$ chains on Gr/Co/Ir(111) preserve a magnetic moment. A coupling between the magnetic properties of the chain and the substrate is also found unequivocally. Additionally, there are strong indications for a non-collinear behavior of the Co centers.

This non-collinear behavior can be explained by a combination of intramolecular DM-type interaction between the individual Co centers in combination with a competition between the collinear coupling with the substrate magnetic moment and the in-plane anisotropy of the molecules. However, other explanations for the observed behavior are conceivable, and no clear evidence for intramolecular magnetic coupling within a $[\text{Co–Sal}]_n$ chain was found. The differences in the behaviors of the individual magnetic moments might be caused by a varying interaction with the substrate. To exclude such an influence of the substrate on the behavior of the Co-center magnetic moments, investigations of chains on top of pristine Gr/Ir(111) are an interesting approach. In addition to the exclusion of magnetic molecule–substrate interactions, the hybridization and, therefore, the influence of the adsorption position should be further reduced.

6.5 $[\text{Co–Sal}]_n$ on pristine Graphene on Ir(111) (Gr/Ir(111))

$[\text{Co–Sal}]_n$ chains on Gr/Co/Ir(111) are preferably adsorbed on the intercalated areas. Only on rare occasions, $[\text{Co–Sal}]_n$ chains are adsorbed on pristine Gr/Ir(111), if they are trapped between wrinkles in the graphene layer. However it is possible to manipulate individual $[\text{Co–Sal}]_n$ chains and reposition them on the surface by utilizing the STM tip. For this purpose, the tip is positioned next to the chain that is to be manipulated, preferably at an fcc or hcp area of the moiré pattern. Then the tip is stabilized with an active feedback-loop at a bias voltage of $U_{\text{stab}} = 10\,\text{mV}$ and a current in the nA regime to bring it close to the surface. After the tip is stabilized, the feedback loop is turned off and the tip is moved slowly across the chain, at a speed of about $\approx 50\frac{\text{pm}}{\text{s}}$. Then the feedback-loop is turned on, the usual tunneling parameters are restored, and an image is started to observe the resulted state of the area.

Such a process is depicted in Figure 6.14. In the beginning, the chain is adsorbed on an area of Gr/Co/Ir(111) along a step edge of a higher lying terrace of the Ir(111) crystal. After two manipulation experiments, the chain is positioned such that

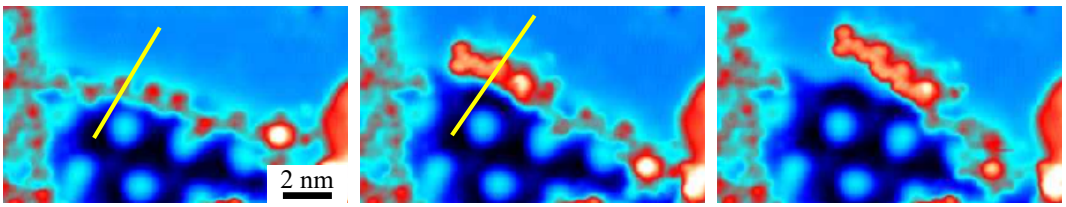

Figure 6.14: Three topography images, indicating the stepwise manipulation of a $[\text{Co–Sal}]_n$ chain to position it on the border between intercalated Gr/Co/Ir(111) and pristine Gr/Ir(111). In the first two images, a yellow line indicates the lateral movement of the tip, inducing the repositioning of the molecular chain.
Tunneling-parameters: $U = 500\,\text{mV}$; $I_{\text{stab}} = 10\,\text{pA}$; $z-\text{range} = 3.0\,\text{Å}$.

three members are positioned completely on the pristine Gr/Ir(111), one member is positioned on the step edge, and two members remain on Gr/Co/Ir(111). Positioning the chain this way, with two members remaining on the intercalated Gr/Co/Ir(111), serves two purposes. On one hand, the adsorption position of the chain is stabilized by the larger adsorption energy on the intercalated graphene compared to pristine Gr/Ir(111). On the other hand, the magnetic moments of the chain are also stabilized by the magnetic interaction of the two members with the Gr/Co/Ir(111) substrate. At the same time, the magnetic moments of the Co centers positioned on pristine Gr/Ir(111) should be influenced solely by the intramolecular coupling with their neighbors. The substrate can influence the coupling between these Co centers only by providing an additional superexchange pathway. However, this effect should be small because of the expected weak hybridization of molecules on pristine Gr/Ir(111).

It should be mentioned that for the manipulation of the chains a molecular tip had to be used. This means that molecules or Co clusters entangled with molecules had to be picked up with the tip apex. Attempting a manipulation experiment with a purely metallic tip always led to the chain being adsorbed on the tip apex. In some cases the chain could be recovered on the surface by applying voltage pulses to the tunnel junction. Similar problems occur also when performing STS or SP-STS experiments with a metallic tip on a $[\text{Co–Sal}]_n$ chain adsorbed partly on pristine Gr/Ir(111). Because of the attractive forces between the molecules and

the metallic tip, in combination with the low adsorption energy of the molecules on pristine Gr/Ir(111), the molecules tend to adsorb on the tip or are moved around during the measurements. Under these circumstances the collection of reliable results is impossible. Therefore, molecular functionalized tips have been employed for further experiments.

PTS data are presented in Figure 6.15 a). The data were not normalized by dividing over I/U since the current is too low for this normalization procedure. Higher currents could not be used during the measurements, as this would cause changes in the adsorption configuration of the $[\text{Co–Sal}]_n$ chain. The data show a larger HOMO–LUMO gap for Co–Sal adsorbed on pristine Gr/Ir(111) than it was found for Co–Sal on intercalated Gr/Co/Ir(111). Judging solely from the PTS data, the HOMO would have its maximum at $-1120\,\text{meV}$ and the LUMO at $1840\,\text{meV}$. However, the $\text{d}I/\text{d}U$ maps obtained at $-600\,\text{meV}$ and $-500\,\text{meV}$, presented in Figure 6.15 b) and c), respectively, clearly show molecular states at these energies. This also agrees with the results of the DFT calculations, predicting two occupied MOs at energies of $-602\,\text{meV}$ and $-529\,\text{meV}$. Therefore, the actual energy of the HOMO is assumed to be at $\approx -500\,\text{meV}$.

Also for positive energies, an additional state is observed at $1650\,\text{meV}$, below the energy at which the maximum is observed in the PTS data. The spatial appearance of this state, presented in Figure 6.15 c), is characterized by a large feature positioned at the Co centers. The state observed at $1850\,\text{meV}$ has the characteristic appearance of the ligand state with two large intensities next to the bridge benzene rings and low contribution of the Co center. Therefore, the order of the individual states in energy for $[\text{Co–Sal}]_n$ chains on Gr/Ir(111) better resembles the results obtained by DFT calculations compared to $[\text{Co–Sal}]_n$ chains on Gr/-Co/Ir(111). However, the ligand state is still placed at slightly higher energies than the LUMO, which is still represented by a state with a large contribution of the Co center. This indicates that also on pristine Gr/Ir(111), hybridization with the substrate alters the electronic structure of Co–Sal. Interestingly, the energies of the ligand state and the LUMO are higher than DFT calculations predict. This results in a HOMO–LUMO gap of $\approx 2150\,\text{meV}$ for Co–Sal on Gr/Ir(111), which is twice the value of $1061\,\text{meV}$ obtained by DFT calculations.

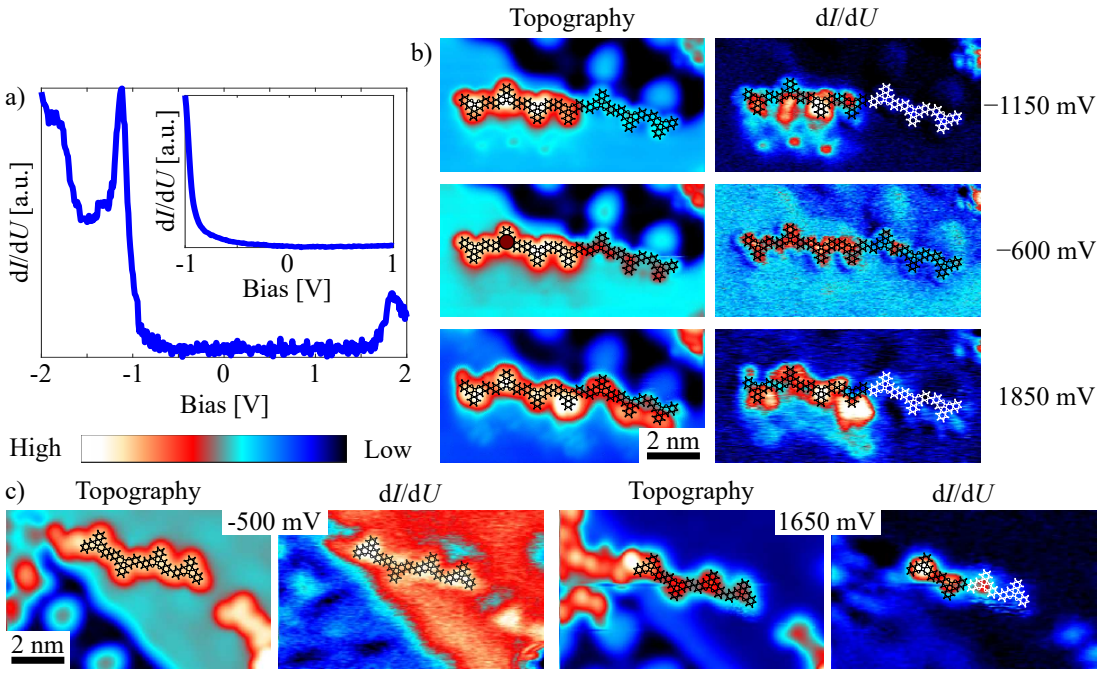

Figure 6.15: STS data for $[\text{Co–Sal}]_n$ chains on pristine Gr/Ir(111). PTS data obtained on a Co center for an energy range of ±2 V and for an energy range of ±1 V (inset), are presented in a). For the same chain, topography images and corresponding $\mathrm{d}I/\mathrm{d}U$ maps, obtained at different energies, are shown in b). The red dot in the topography obtained at −600 mV indicates the position at which the PTS data were obtained. In c), Topography images and corresponding $\mathrm{d}I/\mathrm{d}U$ maps of another $[\text{Co–Sal}]_n$ chain are presented. The $\mathrm{d}I/\mathrm{d}U$ data obtained at −1150 meV and −1850 meV were not corrected for artifacts caused by the scan direction. A model of Co–Sal is superimposed on the images to indicate the positions of the individual members of the chains.
Tunneling-parameters: a) $U_{\text{stab}} = -2\,\text{V}$; ($U_{\text{stab}} = -1\,\text{V}$ inset); $I_{\text{stab}} = 80\,\text{pA}$; $U_{\text{mod}} = 50\,\text{mV}$. b) $I_{\text{stab}} = 30\,\text{pA}$; $U_{\text{mod}} = 50\,\text{mV}$; $z-$range = 3.9 Å. c) $I_{\text{stab}} = 50\,\text{pA}$; $U_{\text{mod}} = 50\,\text{mV}$; $z-$range = 3.0 Å.

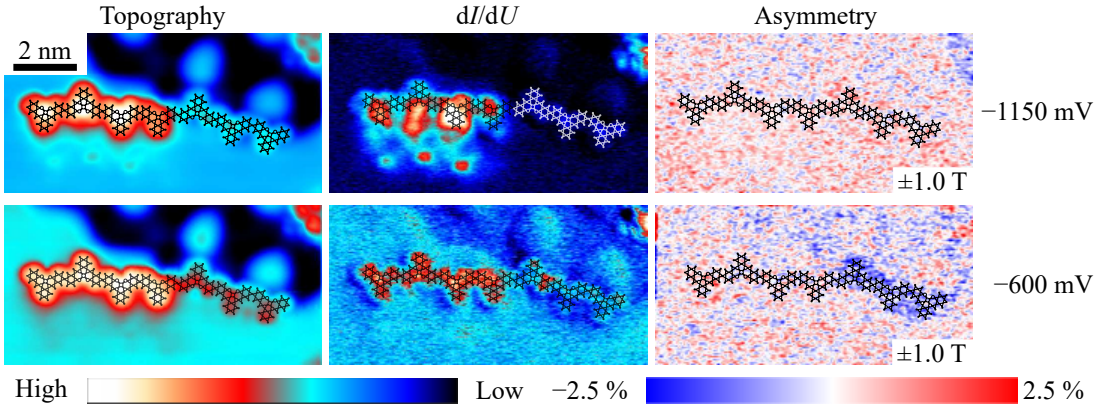

Figure 6.16: SP-STS data for a $[\text{Co–Sal}]_n$ chain on pristine Gr/Ir(111). Topography images, corresponding dI/dU maps, and corresponding asymmetry-maps of a $[\text{Co–Sal}]_n$ chain at different energies are presented. A model of Co–Sal is superimposed on the images to indicate the positions of the individual members within the chain. Tunneling-parameters: $I_{\text{stab}} = 30\,\text{pA}$; $U_{\text{mod}} = 50\,\text{mV}$; $z-$range $= 3.9\,\text{Å}$.

Usually, for SP-STM experiments, metallic tips bearing a magnetic moment are used, like Cr bulk tips or W tips coated with a magnetic material. As already mentioned, the purely metallic Fe-coated W tips used during the experiments were found to move the $[\text{Co–Sal}]_n$ chains on pristine Gr/Ir(111) or even picking up the chains from the surface. However, it was possible to create molecular terminated tips showing spin-polarized contrast on the substrate. A drawback of these tips is their undefined shape leading to artificial features in topography images and dI/dU maps. These artificial features are observed mainly when imaging $[\text{Co–Sal}]_n$ chains on pristine Gr/Ir(111) at higher energies. At these energies, the molecules obtain states protruding far into the z-direction, which allows additional tunneling paths between the molecule and tip features next to the tip apex. This can be seen for example in Figure 6.15 b).

Spin-asymmetry maps obtained for the $[\text{Co–Sal}]_n$ chain from Figure 6.15 a,b) are presented in Figure 6.16. The map obtained at $-600\,\text{meV}$ clearly shows contrast on the intercalated Gr/Co/Ir(111) area in the top right corner of the scan frame. At the position of the three members of the chain positioned on the intercalated area the asymmetry of the substrate is enhanced. This agrees with the energy

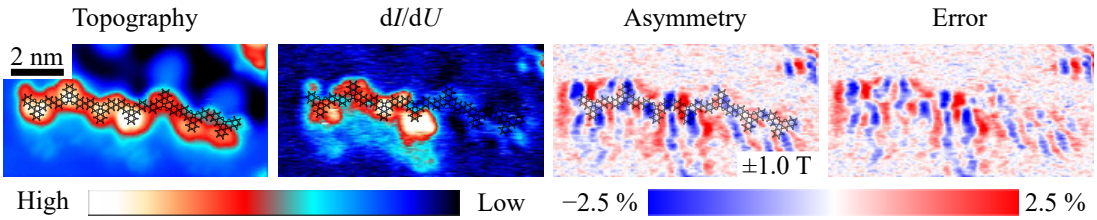

Figure 6.17: SP-STS data for $[\text{Co–Sal}]_n$ on pristine Gr/Ir(111). Topography images, corresponding $\mathrm{d}I/\mathrm{d}U$ maps, asymmetry maps, and error plots of a $[\text{Co–Sal}]_n$ chain, obtained at 1850 meV, are presented. A model of Co–Sal is superimposed on the images to indicate the positions of the individual members within the chain.
Tunneling-parameters: $I_{\text{stab}} = 30\,\text{pA}$; $U_{\text{mod}} = 50\,\text{mV}$; $z-$range $= 3.9\,\text{Å}$.

resolved SP-STS data presented previously, which showed that at these energies the Gr/Co/Ir(111) and molecules adsorbed on it show a spin asymmetry of the same sign. However, for the pristine Gr/Ir(111) and the molecules adsorbed on this area no spin contrast is observed at this energy. Also the asymmetry map at $-1150\,\text{meV}$ shows no sign of spin polarization. For this data, however, it has to be mentioned that the artificial contrast due to the imperfect shape of the tip might influence the results. No convincing data could be obtained for positive energies.

Not only the shape of the tip can hinder the measurement of spin-polarized data but also the tendency of the molecular tips to be unstable during the measurements. Already small changes in the tip can induce artificial contrast in the spin-asymmetry maps. For example, it has been observed that molecular tips bent into one direction when scanning from left to right over a molecule and into the other direction for the backward scan. This causes contrast of alternating sign, as can be seen in Figure 6.17. In these data, the asymmetry map and the error plot show the same contrast, caused by the movement of the tip apex while scanning over the molecule.

6.6 On-Surface Metalation of H_2-Sal with Fe and Cr

As discussed earlier, Co–Sal has only one unpaired electron causing a small magnetic moment of $1\,\mu_B$. Larger magnetic moments are more accessible for external fields and lead to larger contrast in SP-STS data. To obtain larger magnetic moments, the salophen ligand can be metalated with different transition metals. As discussed earlier in Chapter 2.3.2, the metalation of organic ligands with metal atoms can be a challenging task, especially if done in solution. On-surface metalation provides an alternative pathway with several advantages. In the experiments performed for this thesis, Br_2H_2–Sal was on-surface metalated with Co, Fe, and Cr. The results were published in reference [80]. The success of the on-surface metalation was proven by XAS data and by comparison of STS data obtained on Co–Sal metalated in solution with data obtained for on-surface metalated Co–Sal. The XAS data showed that the metalation occurs in multiple steps. A two-step process was identified for the metalation with Fe: In the first step, the metal atom bonds to the O atoms of the central O_2N_2 entity, and the asymmetry inherent to the Br_2H_2–Sal ligand is removed, in the second step, the bonds between the Fe and the N atoms are formed, which completes the metalation reaction. For Cr, the metal occupies the cavity of the central O_2N_2 entity in an additional step before the bond formation.

For the resulting salophenatoiron(II) (Fe–Sal) and salophenatochromium(II) (Cr–Sal) molecules, Qu *et al.* predicted magnetic moments of $2\,\mu_B$ and $4\,\mu_B$, respectively [229]. These results were also confirmed by the DFT study published in [80]. A drawback of Fe–Sal and Cr–Sal molecules is their lower magnetic anisotropy which was also predicted by Qu *et al.*. However, this is not relevant if their magnetic moments are stabilized by interaction with a magnetic substrate. In the following, the results of the STS experiments and the DFT calculations on the metalation of Br_2H_2–Sal with Fe and Cr will be discussed. Analogue data on the on-surface metalated Co–Sal has been presented above in Section 6.3. The data were obtained on molecular chains to guarantee higher stability of the molecules during the experiments. At the end of this section, a comparison of all three transition metal–salophen complexes will be presented.

PTS data obtained on Fe-metalated Br_2H_2–Sal are presented in Figure 6.18. Five features related to electronic states of the molecule can be identified in the data and are marked by arrows. Two additional features marked by the gray circles are caused by the electronic structure of the tip. This becomes clear when looking at the spatially resolved STS data at the respective energies, presented in Figure 6.19 c). The HOMO at $\approx -164\,\mathrm{meV}$ and the LUMO at $\approx 196\,\mathrm{meV}$ can be observed in the spectra with a $\pm 1\,\mathrm{eV}$ energy range. As for Co–Sal, the spectra obtained on the different positions show different features. The HOMO is observed mainly in the PTS data obtained on the Fe center and the outer benzene rings, which are connected to the neighboring members but not on the bridge position. The LUMO also causes a clear peak in the spectroscopy on the Fe center. At the other positions, the LUMO causes a shoulder in the spectra instead of a peak. For the larger energy range, the HOMO-1 and LUMO$+1$ become apparent at $\approx -1885\,\mathrm{meV}$ and $\approx 1239\,\mathrm{meV}$, respectively. Additionally, the LUMO$+2$, with a lower intensity, can be observe at $\approx 1799\,\mathrm{meV}$. While the LUMO$+1$ and the LUMO$+2$ appear at all positions with varying peak height and position of the maximum, the HOMO-1 is only visible in the spectroscopy on the Fe center.

The spatially resolved data on the electronic states presented in Figure 6.19 allows assigning the DFT-calculated MOs to the individual states, as previously done for the Co–Sal data. The energy eigenvalues for the DFT-calculated MOs are given in table 6.2. In the $\mathrm{d}I/\mathrm{d}U$ map at $-200\,\mathrm{meV}$, the HOMO appears with a high-intensity feature centered on the Fe center. Additionally, this feature reaches over the ligand, especially on the side of the O atoms. Therefore, the MO with a contribution of the Fe $\mathrm{d}_{x^2y^2}$ orbital is attributed to this state. Taking into account the signal measured on the benzene rings, the MO with the Fe d_{yz} orbital is added. Next to their spatial appearances, also their positions in energy can be used to identify corresponding states from DFT calculations and experiment. Both MOs attributed to the HOMO have very similar energy eigenvalues with $-489\,\mathrm{meV}$ for the MO with a d_{yz} orbital contribution and $-415\,\mathrm{meV}$ for the MO with a $\mathrm{d}_{x^2y^2}$ orbital contribution. Additionally, they are the only MOs in the range of $-1000\,\mathrm{meV}$ up to Fermi energy. The LUMO has a spatial appearance similar to that of the HOMO. However, the bright feature at the Fe center position is

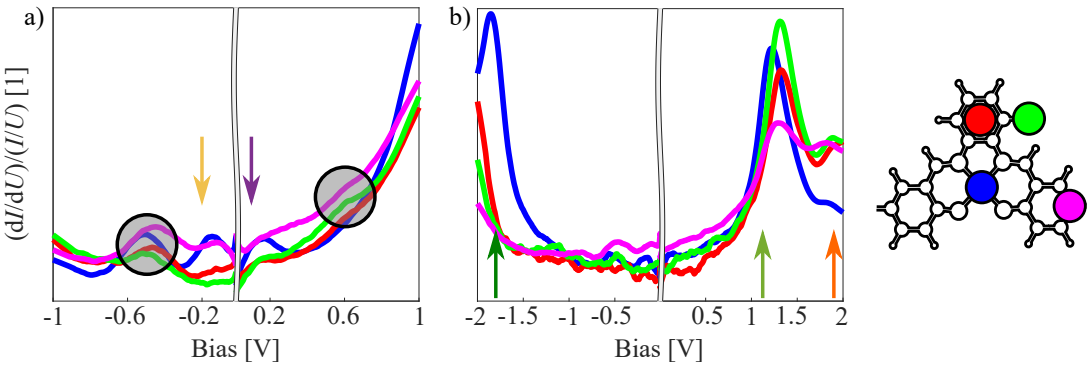

Figure 6.18: STS data obtained on $[\text{Fe–Sal}]_n$ chains on Gr/Co/Ir(111). PTS data were obtained on various positions of a molecule for an energy range of a) ±1 eV and b) ±2 eV. The positions of the spectra are indicated by the color-coded marks on the model of the molecule on the right. The color-coded arrows in (a) and (b) indicate energies for which spatially resolved $\mathrm{d}I/\mathrm{d}U$ data are presented in Figure 6.19. Grey circles indicate energies at which features can be observed in the PTS data that are caused by the tip and, therefore, are not reflected in the spatially resolved data.
Tunneling-parameters: (a) $U_{\text{stab}} = -1\,\text{V}$; $I_{\text{stab}} = 50\,\text{pA}$; $U_{\text{mod}} = 50\,\text{mV}$; $T \approx 25\,\text{K}$; (b) top: $U_{\text{stab}} = -2\,\text{V}$; $I_{\text{stab}} = 50\,\text{pA}$; $U_{\text{mod}} = 50\,\text{mV}$; $T \approx 25\,\text{K}$.
Figure reprinted with permission from supporting information of [80].

Table 6.2: Energies of the LDOS plots shown in Figure 6.19:

MO	$d_{x^2y^2}\beta$	$d_{yz}\beta$	$d_{xy}\alpha$	$d_{yz}\beta$	$d_{yz}\alpha$	$d_{xz}\beta$	$d_{z^2}\beta$	LS α	LS β
E [meV]	−415	−489	1265	1100	879	2046	1798	546	414

more confined, while the overall signal is higher and spreads even further across the benzene rings of the ligand than observed for the HOMO. Considering this in combination with position in energy of the states, three calculated MOs can be attributed to this state, i.e. the states with an Fe-d_{xz} orbital contribution of both spins and the d_{xy} orbital with an α spin.

In comparison with Co–Sal and Cr–Sal, the spatial appearance of the LUMO+1 of Fe–Sal is noteworthy. It shows the two pronounced features next to the bridge typical for the ligand state. However, it also shows a feature at the Fe center position. Therefore, in addition to the two ligand states, two MOs are attributed to the LUMO+1, one with a contribution of the Fe d_{xz} orbital and one with a d_{z^2}-orbital contribution. It has to be noted that also the ligand states themselves show a small contribution of the Fe-d_{z^2} orbital, which is neither the case for Co–Sal nor for Cr–Sal. This, however, would not be sufficient to explain the feature observed in the dI/dU map and the high peak in the PTS data in figure 6.18.

The HOMO−1 observed at an energy of −1885 meV in the PTS data obtained on the Fe center is shown in Figure 6.19 b). However, this state could not be correlated unequivocally with the DFT-calculated MOs. The LUMO+2, observed at ≈ 1799 meV in the PTS data, could not be resolved spatially. This is due to the high density of states observed for the LUMO+1 and its large extension into the z-direction. In constant-current mode, this causes relatively high tip–sample distances in the region of the molecule at bias voltages above the energy of the LUMO+1. Therefore, the LUMO+2, with a lower density of states, cannot be observed in a constant-current image. For the sake of completeness, also maps obtained at −500 meV and 600 meV are presented in Figure 6.19 c). These data clearly show that no molecular states are positioned at the respective energies, despite the features observed in the PTS data.

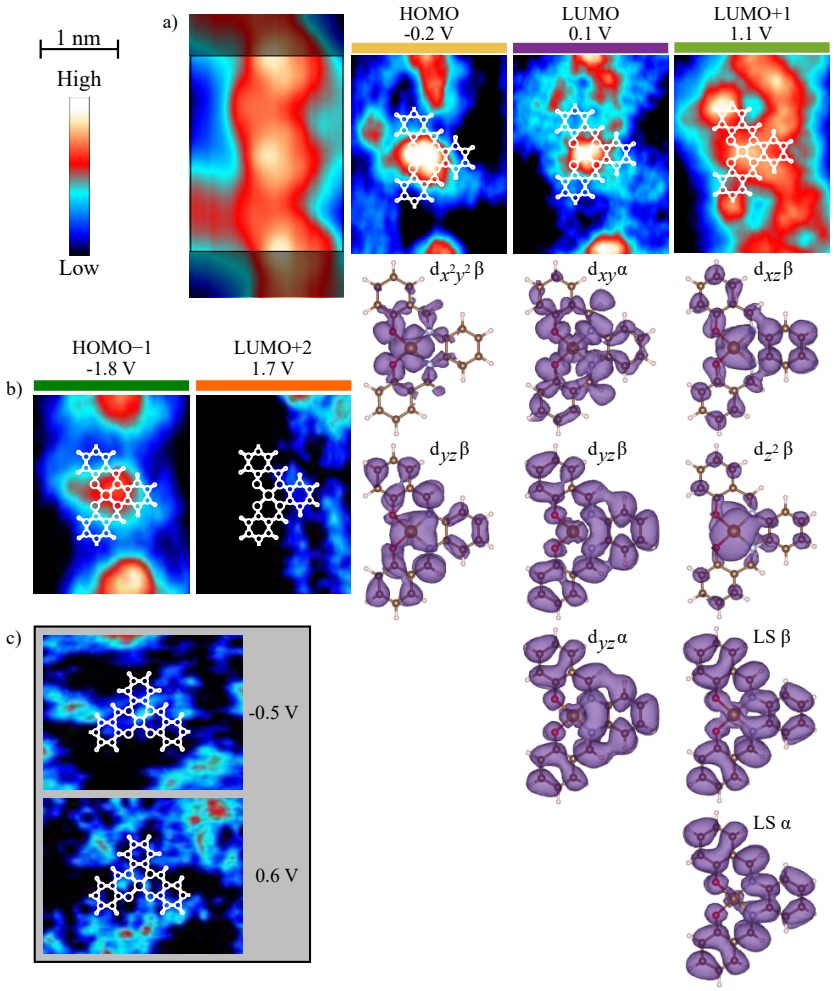

Figure 6.19: Comparison between experimental and DFT-calculated data for Fe–Sal on Gr/Co/Ir(111). Panel a) presents a topography image with submolecular resolution obtained at $U = 50\,\mathrm{mV}$ and indicates the frame presented in the $\mathrm{d}I/\mathrm{d}U$ maps. Above each $\mathrm{d}I/\mathrm{d}U$ map, the bias voltage is given. A model of the Fe–Sal molecule superimposed on each $\mathrm{d}I/\mathrm{d}U$ map indicates the molecule's position. Below each $\mathrm{d}I/\mathrm{d}U$ map the squared electron wave functions of the DFT-calculated MOs attributed to the $\mathrm{d}I/\mathrm{d}U$ map are shown. The MOs are labeled with their spin state and the contributing 3d orbital of the Fe atom or LS for the ligand states. Panel b) shows a $\mathrm{d}I/\mathrm{d}U$ map of the HOMO−2. In c), $\mathrm{d}I/\mathrm{d}U$ maps obtained at energies where the PTS data showed tip induced features are shown.
Tunneling-parameters: $I_{\mathrm{stab}} = 25\,\mathrm{pA}$; $U_{\mathrm{mod}} = 50\,\mathrm{mV}$; $T \approx 25\,\mathrm{K}$.
Figure reprinted with permission from [80].

Fe(+II) has one electron less in its d shell than Co(+II). In combination with a small energy splitting of the Fe-3d orbitals in the square-planar salophen ligand,[6] this leads to two singly occupied MOs for Fe–Sal: One with a d_{xz}-orbital contribution of the Fe atom, which is the same as for Co–Sal, and an additional one with a d_{z^2}-orbital contribution of the Fe atom. According to this, the two SUMOs are the MOs attributed to the LUMO+1 state in addition to the two ligand states. The two SOMOs are outside of the measured energy range below −2 eV.

PTS data for Cr–Sal are presented in Figure 6.20. Here, next to the HOMO and LUMO, also the HOMO−1 can be found in the ±1 eV-range data. The HOMO causes a peak with a maximum at ≈ −106 meV in the spectra at all four positions. Interestingly, the HOMO−1, observed at −552 meV, is most pronounced in the PTS data obtained next to the bridge benzene ring. When looking at the spatially resolved data, presented in Figure 6.21, this state shows an intensity peak at the Cr center's position but also extends over the other parts of the molecule. Therefore, the highest intensity should be observed for the spectroscopy on the Cr center. In the positive energy range, the LUMO is visible at all four positions, indicated by a feature with a maximum at ≈ 250 meV. In the larger energy range, the HOMO−2, at 1728 meV, and the LUMO+1, at 1277 meV, are visible.[7] Both are observed at all four positions, but the LUMO+1 has a significantly lower intensity in the spectroscopy on top of the Cr center. Additionally, a shoulder at ≈ 1877 meV in each of the spectra indicates the LUMO+2, which is spread over the whole molecule.

Spatially resolved $\mathrm{d}I/\mathrm{d}U$ maps of $[\text{Cr–Sal}]_n$ chains on Gr/Co/Ir(111) together with the attributed DFT-calculated MOs are presented in Figure 6.21. The energy eigenvalues for the DFT-calculated MOs are given in Table 6.3. The HOMO−1 is characterized by a confined maximum centered at the Cr center position and extends onto the rest of the molecule, especially onto the N atoms. This appearance

[6] An exception is the $d_{x^2-y^2}$ orbital which is strongly separated in energy from the other orbitals. This orbital is usually not occupied for transition metals with less then seven electrons in the 3d shell, leading to the low spin state for Co–Sal [144, 302].

[7] Note that for this energy range the HOMO−1 is more pronounced at the Cr-center position and the bridge position. This indicates the relevance of the exact positioning of the tip for the PTS experiments and the stabilization parameters, and underlines the importance to interpret spatially resolved and energy-resolved STS data in combination with DFT.

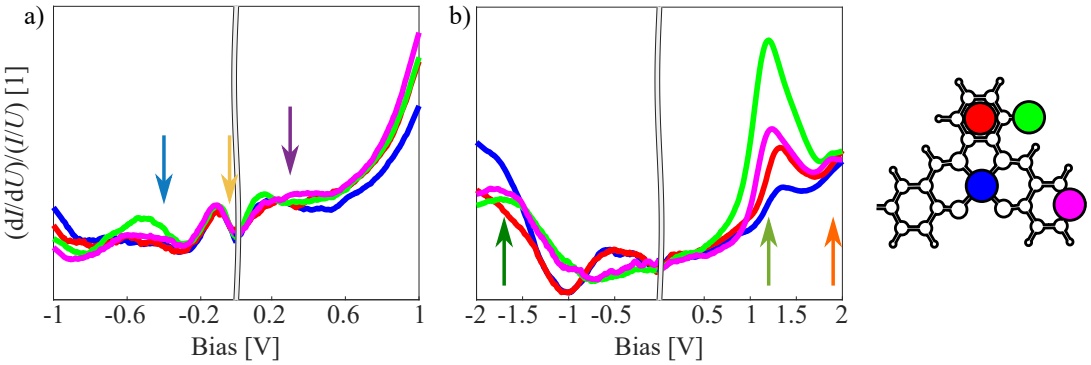

Figure 6.20: STS data obtained on $[\text{Cr–Sal}]_n$ chains on Gr/Co/Ir(111). PTS data was obtained on various positions of a molecule for energy ranges of a) $\pm 1\,\text{eV}$ and b) $\pm 2\,\text{eV}$. The positions of the spectra are indicated by the color-coded marks on the model of the molecule on the right. The color-coded arrows in a) and b) indicate energies for which spatially resolved $\mathrm{d}I/\mathrm{d}U$ data are presented in Figure 6.21.
Tunneling-parameters: (a) $U_{\text{stab}} = -1000\,\text{mV}$; $I_{\text{stab}} = 50\,\text{pA}$; $U_{\text{mod}} = 50\,\text{mV}$; $T \approx 25\,\text{K}$; (b) top: $U_{\text{stab}} = -2000\,\text{mV}$; $I_{\text{stab}} = 50\,\text{pA}$; $U_{\text{mod}} = 50\,\text{mV}$; $T \approx 25\,\text{K}$.
Figure reprinted with permission from supporting information of [80].

fits ideally to the MO with an Fe-d_{z^2}-orbital contribution. The HOMO is more evenly spread over the whole molecule and has only a slight intensity peak on the Cr center position. This, in combination with the order in energy of the MOs, indicates that the HOMO corresponds to the MO with the d_{xz}-orbital contribution of the Cr center.

Two MOs of opposite spin are attributed to the LUMO. They can be identified by the large density of states on the C atoms of the bridge benzene ring. In the $\mathrm{d}I/\mathrm{d}U$ maps, these features are reflected in a c-shaped feature around the bridge benzene ring. As already observed for Co–Sal and Fe–Sal, the LUMO+1 is characterized by two large intensities next to the bridge benzene ring and corresponds to the ligand states. Opposed to Fe–Sal, the LUMO+1 has a nodal plane cutting through the bridge and the Cr center, as observed for the LUMO+1 of Co–Sal. The HOMO−2 and the LUMO+2, presented in Figure 6.21 b), could not be attributed to MOs unequivocally.

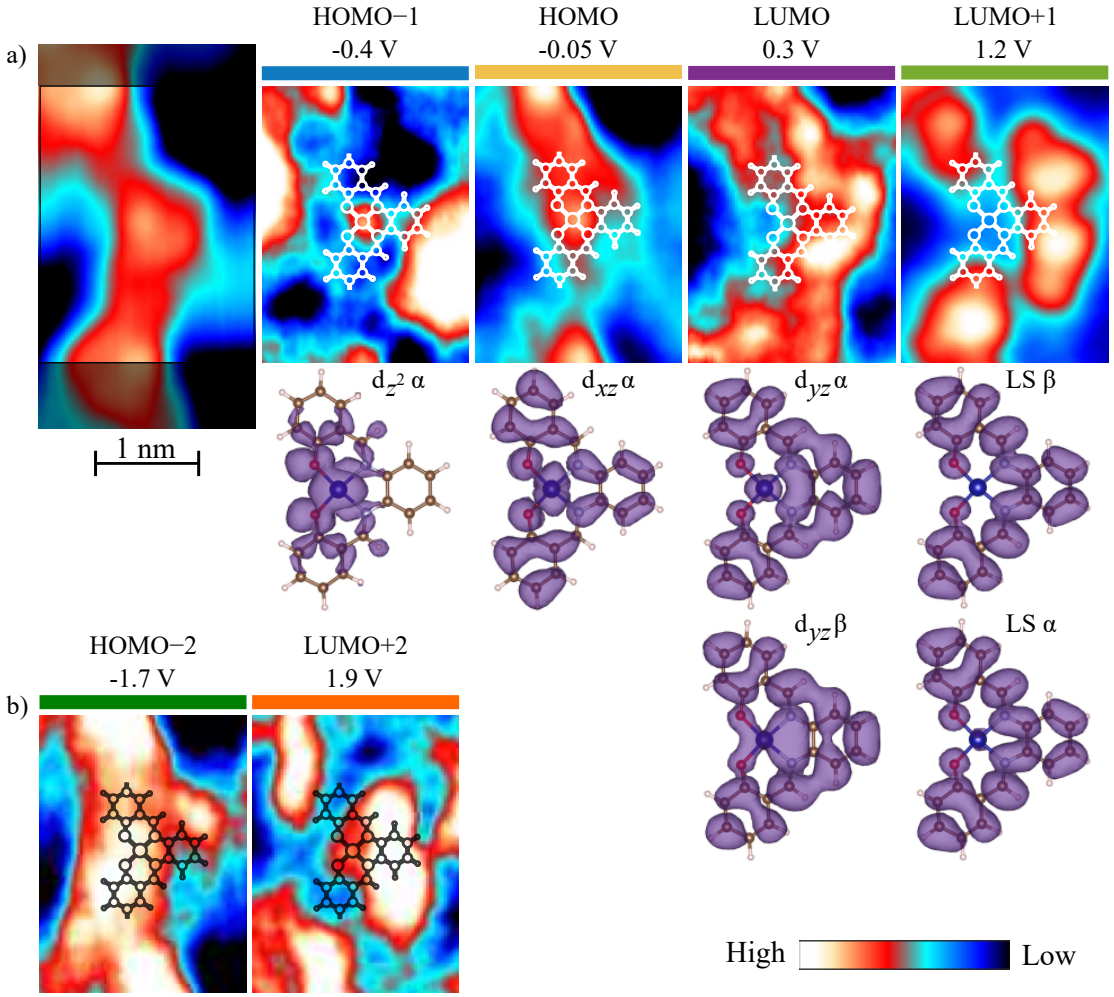

Figure 6.21: Comparison between experimental and DFT-calculated data for Cr–Sal on Gr/Co/Ir(111). Panel a) presents a topography image with submolecular resolution obtained at $U_{set} = 50\,mV$ and indicates the frame presented in the dI/dU maps. Above each dI/dU map, the bias voltage is given. A model of the Cr–Sal molecule superimposed on each dI/dU map indicates the molecule's position. Below each dI/dU map the squared electron wave functions of the DFT-calculated MOs attributed to the dI/dU map are shown. The MOs are labeled with their spin state and the contributing 3d orbital of the Cr atom or LS for the ligand states. Panel b) shows dI/dU maps of the HOMO−2 and the LUMO+2, to which no DFT-calculated MOs could be attributed unequivocally.
Tunneling-parameters: $I_{\mathrm{stab}} = 50\,\mathrm{pA}$; $U_{\mathrm{mod}} = 50\,\mathrm{mV}$; $T \approx 25\,\mathrm{K}$.
Figure reprinted with permission from [80].

Table 6.3: Energies of the LDOS plots shown in Figure 6.21:

MO	$d_{z^2}\alpha$	$d_{xz}\alpha$	$d_{yz}\beta$	$d_{yz}\alpha$	LS β	LS α
energy [meV]	−1085	−773	714	1053	531	604

Compared to Co(+II), Cr(+II) has three electrons less in its d shell, two less than Fe(+II). Because of the previously discussed electronic structure caused by the square-plane ligand field, this leads to four SOMOs in Cr–Sal. Two of these have the same contribution of the metal-3d orbitals as for Fe–Sal, i.e. a d_{xz}-orbital contribution and a d_{z^2}-orbital contribution of the Cr center. The additional SOMOs have a d_{xy}-orbital contribution and a d_{yz}-orbital contribution of the Cr center. Since the DFT data is limited to the energy range of −2 eV to 3 eV and some of the SOMOs and SUMOs are outside of this range, they cannot be identified unequivocally. Of course, the ligand state can be excluded for the magnetic orbitals since both, α and β ligand state are unoccupied. The same holds for the states with the d_{yz}-orbital contribution, which are both attributed to the LUMO identified in the experimental data. The HOMO was shown to have a d_{xz}-orbital contribution and the HOMO−1 to have a d_{z^2}-orbital contribution. Since both of these are singly occupied for Fe–Sal, this is likely also the case for Cr–Sal

A comparison of all three transition metal–Sal molecules is presented in Figure 6.22. It shows all energies at which states were observed in the STS and the PTS data in panel a) and the energy eigenvalues of the DFT-calculated MOs in b). As mentioned before for the experimental data, multiple point-tunneling spectra obtained on different molecules for each transition metal have been analyzed to obtain statistically significant data. To exclude features caused by the tip or the substrate, the energy-resolved data was compared with spatially resolved data. The differences in the number of states observed in experiment and calculation are due to the limited energy resolution in the experiment.

In the case of Co–Sal, data for *ex situ* as well as *in situ* prepared molecules is presented. The good agreement between these data proves the success of the on-surface metalation process. Comparing the DFT-calculated data with the spatially resolved STS data, it becomes clear why for Cr–Sal two states are visible in the

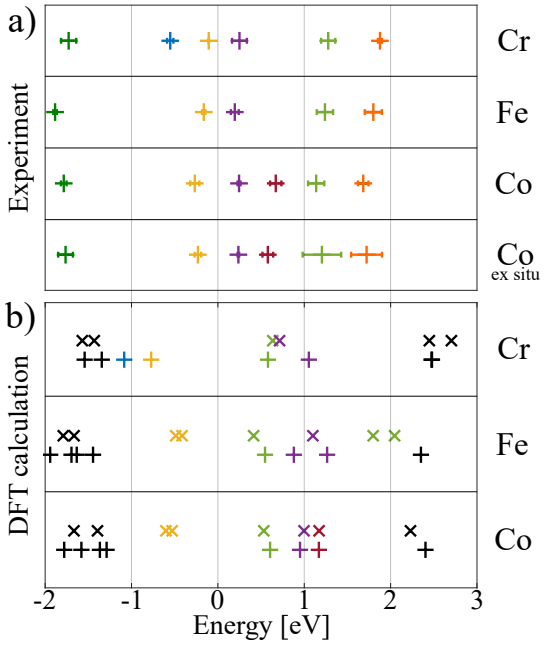

Figure 6.22: Energy positions of electronic states with respect to the Fermi level for metal–salophen complexes as a) measured by STS on Gr/Co/Ir(111) and b) calculated by DFT for the gas phase. The experimental data has been obtained for chains of salophen molecules on Gr/Co/Ir(111), metalated *in situ* with Cr, Fe, or Co. Data for [Co–Sal]$_n$ chains, metalated *ex situ*, are provided for comparison. The energies are extracted from normalized dI/dU curves. In the calculated data, majority spin states are marked by '+' symbols and minority spin states by 'x' symbols. The energies are the eigenvalues of the calculated wave functions. Corresponding states from the measurements and calculations are marked with the same color. A calculated state marked in a specific color contributes to a feature measured in the STS experiment at the energy marked by the same color. The states marked in black could not be assigned unequivocally.
Figure reprinted with permission from [80].

negative energy range of the ±1 eV data. For Cr–Sal the two states in this range, which had very similar energy eigenvalues for Co–Sal and Fe–Sal, are further apart from each other at −1085 meV and −773 meV. Therefore, they can be resolved individually by PTS, and only a single DFT-calculated MO can be attributed to each state, as presented in Figure 6.21. For Co–Sal, an additional state compared to the other complexes was found for ≈ 670meV. Here, the distance between the states in the DFT calculations is not considerably larger than for Fe–Sal and Cr–Sal. However, each of the states is cause by two MOs, one of α and one of β spin, which are very close in energy. This might be a reason, why they are more confined and can be resolved individually in the STS data.

As mentioned in Section 3.6, the transition metal–salophen complexes can be identified by the ligand state, which has a characteristic spatial appearance for all complexes. Only for Fe–Sal the ligand states have an additional feature centered on the Fe-center position. However, the two features next to the bridge benzene rings are clearly visible. For all complexes, the ligand state is shifted to higher energies in the STS data compared to the DFT calculations. This indicates that for all complexes the metal center hybridizes with the substrate, as discussed for Co–Sal in more detail.

In conclusion, on-surface metalation of the salophen ligand with different transition metals was done successfully. The method gives access to salophen complexes with higher magnetic moments, which are less accessible from solution. The individual complexes can be distinguished based on their characteristic electronic structures, summarized in Figure 6.22. However, as reported by Avvisati *et al.* the different nature of the SOMOs might influence the intramolecular magnetic coupling of the resulting chains [296, 297]. Additionally, for systems with spin moments larger than 1 μ_B per center, higher order terms may play a role for the inter-center magnetic coupling [177].

6.7 Summary and Conclusions

In summary, a combined STS and DFT study on the electronic properties of [Co–Sal]$_n$ chains on Gr/Co/Ir(111) was presented. The electronic states close to Fermi energy and their constitution of ligand and Co-3d states could be identified. It was found that, although the hybridization is limited because of the decoupling graphene layer, unoccupied MOs with a contribution of Co-3d states are shifted closer to Fermi energy. At the same time, the so-called ligand states are shifted to higher energies. Individual members of the [Co–Sal]$_n$ chains show no variations in their electronic structure, apart from slight shifts in energy of the individual states.

An investigation of the local magnetic properties by SP-STS revealed spin polarization for all Co centers in multiple [Co–Sal]$_n$ chains and a coupling of the chains' magnetic moments to the substrate. A non-collinear arrangement of the individual Co-center magnetic moments could be deduced from their different behaviors in external magnetic fields, occurring independently from the substrate magnetic moment. However, the results are not sufficient to exclude the possibility that the equilibrium orientations of the individual magnetic moments at zero external fields are caused solely by local differences in the magnetic coupling with the substrate. The existence of such an influence of the adsorption configuration on the magnetic coupling between molecules and substrate is evident from an earlier study on single Co–Sal molecules on Gr/Fe/Ir(111) [230].

To further elucidate the influence of the substrate on the magnetic properties of [Co–Sal]$_n$ chains, the creation of longer chains was attempted. Longer chains should show a periodicity in the contrast variations if these are caused by intramolecular interactions. According to the literature, the usage of Co as a catalyst for the Ullmann reaction leads to the formation of relatively stable intermediate metal–organic structures [96]. This is reflected in the here presented experiments by the formation of clusters consisting of Co and entangled molecular chains. This behavior hinders the formation of longer chains. To obtain longer chains, the deposition of a different metal as the catalyst should suppress the formation of intermediate metal–organic compounds. On Au(111) substrates no metal–organic

intermediates are observed [15, 98]. Therefore, Au would be a promising candidate as a catalyst.

Another approach to elucidate the substrate's influence on the intramolecular magnetic coupling is the reduction of the substrate's influence on the chain to a minimum. To this end, $[\text{Co–Sal}]_n$ chains were repositioned with the STM tip on the border between Gr/Co/Ir(111) and Gr/Ir(111). This way, the chains were anchored physically and magnetically by some members of the chain positioned on Gr/Co/Ir(111), while those members on the pristine Gr/Ir(111) are solely coupled via intramolecular magnetic interactions. However, because of the instability of the $[\text{Co–Sal}]_n$ chains on pristine Gr/Ir(111), no conclusive data could be obtained. Also here, the creation of longer chains could help to overcome these difficulties. This would allow anchoring the chains on Gr/Co/Ir(111) at both ends while crossing an area of pristine Gr/Ir(111). Thereby, the chain should be more resilient against tip-induced changes of its adsorption position.

An alternative route to obtain reliable spin-polarized data on $[\text{Co–Sal}]_n$ chains on pristine Gr/Ir(111) are well-defined molecular functionalized tips. Examples were recently suggested for inelastic electron tunneling spectroscopy experiments [303, 304]. In these studies, the exchange interaction between a magnetic moment of the sample and the magnetic moment of a nickelocene molecule adsorbed at the tip apex of a non-magnetic tip could be measured simultaneously with the local spin polarization around Fermi energy. However, the deposition of another molecule would further complicate the already complex preparation procedure of the samples.

On-surface metalation provides another approach to obtain more conclusive SP-STS data. In this approach transition-metal–Sal complexes with larger magnetic moments are prepared. These are easier to address by external magnetic fields and lead to larger contrast in SP-STS experiments. However, the nature of the SOMOs in the new complexes might change the pathways of the intramolecular magnetic coupling. Furthermore, in the intramolecular interaction of magnetic moments larger than $1\,\mu_\text{B}$, additional, higher-order interactions play a role in the coupling

of the individual transition-metal centers, which constitutes new challenges in possible future SP-STS experiments.

7 Closure and Outlook

Two surfaces were tested as possible substrates for a spintronic device based on $[\text{Co–Sal}]_n$ chains. To this end, on both surfaces, chains were synthesized from single *in situ* metalated Br_2Co–Sal molecules by an Ullmann reaction. On the $GdAu_2$ surface alloy, the reaction is catalyzed by substrate atoms at an elevated temperature of $\approx 485\,\text{K}$, while on Gr/Co/Ir(111), additional Co atoms had to be deposited to activate the reaction at a temperature of $\approx 600\,\text{K}$. Thorough SP-STS studies of the local electronic and magnetic properties of the $[\text{Co–Sal}]_n$ chains were performed on both substrates.

The system with $[\text{Co–Sal}]_n$ chains on the $GdAu_2$ surface alloy, as prepared in the present study, could be excluded as a potential system for spintronic devices. While purely organic molecules showed only weak hybridization with the substrate [105], the Co–Sal molecule hybridizes with the substrate, especially after the Ullmann reaction. The hybridization can be explained with the affinity of Co–Sal to coordinate additional atoms along the z-direction. Thereby, the electronic structure of the molecules is altered, and it loses its magnetic moment almost completely. For energies below Fermi energy, the chain–substrate complex showed a band-like electronic structure. Additionally, the Br atoms remaining on the substrate up to high temperatures cause difficulties in SP-STS experiments.

A possible strategy to avoid the hybridization and the remaining Br atoms on the surface is the inversion of the preparation process. As suggested recently by Que *et al.* [105] for graphene nanoribbons on a $TbAu_2$ surface alloy, the alloy could be created after the polymerization of the $[\text{Co–Sal}]_n$ chains, by intercalating Gd atoms after the Ullmann reaction. This way, the Br atoms can be desorbed by heating slightly above the temperature needed for the Ullmann reaction, as observed by Abadia *et al.* [104]. Furthermore, since XMCD data suggests that the

hybridization between Co–Sal and the substrate is increased upon the Ullmann reaction, this preparation procedure might prevent the increased hybridization.

On Gr/Co/Ir(111), the hybridization is much weaker, and the Co–Sal molecules preserve their magnetic moment. Therefore, a comparison of the results with DFT calculations of the free-standing Co–Sal molecule is possible. However, the electronic structure of the molecules is still altered, which is reflected by a shift in energy of the unoccupied states close to Fermi energy. The expected antiferromagnetic coupling was not observed in the SP-STS study. Instead, the chains showed a non-collinear magnetic structure. If this non-collinear behavior is caused by intramolecular magnetic interactions, utilization of the chains as spin leads in a spintronic device is possible. To this end, however, the influences of intramolecular and molecule–substrate interactions need to be further elucidated.

Attempts to investigate the magnetic properties of $[\text{Co–Sal}]_n$ chains independently of molecule–substrate interactions by repositioning the chains onto pristine Gr/Ir(111) were not successful. The instability of the system did not allow for reliable SP-STS studies. The stability possibly could be increased by the growth of longer chains by using a different metal as the catalyst for the Ullmann reaction. Successful on-surface metalation of the Br_2H_2–Sal ligand with Fe and Cr led to molecules with larger magnetic moments. This provides perspectives for future experiments on new systems, more accessible by external fields and magnetic STM tips.

Bibliography

[1] M. C. Petty, T. Nagase, H. Suzuki, and H. Naito, „Molecular electronics“, in *Springer handbook of electronic and photonic materials*, edited by S. Kasap and P. Capper (Springer International Publishing, Cham, 2017).

[2] P. T. Mathew and F. Fang, „Advances in molecular electronics: a brief review“, Engineering **4**, 760–771 (2018).

[3] S. Sanvito, „Molecular spintronics“, Chem. Soc. Rev. **40**, 3336–3355 (2011).

[4] J. Atulasimha and S. Bandyopadhyay, „Introduction to spintronic and nanomagnetic computing devices“, in *Nanomagnetic and spintronic devices for energy-efficient memory and computing* (John Wiley & Sons, Ltd, 2016).

[5] E. Coronado, „Molecular magnetism: from chemical design to spin control in molecules, materials and devices“, Nat. Rev. Mater. **5**, 87–104 (2020).

[6] B. C. Guha and W. G. Penney, „Magnetic properties of some paramagnetic crystals at low temperatures“, Proc. R. Soc. London, Ser. A **206**, 353–373 (1951).

[7] B. Bleaney and K. D. Bowers, „Anomalous paramagnetism of copper acetate“, Proc. R. Soc. London, Ser. A **214**, 451–465 (1952).

[8] P. J. Hay, J. C. Thibeault, and R. Hoffmann, „Orbital interactions in metal dimer complexes“, J. Am. Chem. Soc. **97**, 4884–4899 (1975).

[9] O. Kahn and B. Briat, „Exchange interaction in polynuclear complexes. Part 1.—Principles, model and application to the binuclear complexes of chromium(III)“, J. Chem. Soc., Faraday Trans. 2 **72**, 268–281 (1976).

[10] G. Christou, D. Gatteschi, D. N. Hendrickson, and R. Sessoli, „Single-molecule magnets“, MRS Bull. **25**, 66–71 (2000).

[11] A. Gaita-Ariño, F. Luis, S. Hill, and E. Coronado, „Molecular spins for quantum computation“, Nat. Chem. **11**, 301–309 (2019).

[12] B. E. C. Bugenhagen and M. H. Prosenc, „Direct C–C coupling of two Ni-salphen complexes to yield dinickel-disalphen complexes with symmetric and non-symmetric substitution-patterns“, Dalton Trans. **45**, 7460–7468 (2016).

[13] T. Glaser, M. Heidemeier, and T. Lügger, „The novel triplesalen ligand bridges three Ni^{II}-salen subunits in a *meta*-phenylene linkage“, Dalton Trans., 2381–2383 (2003).

[14] T. Glaser, „Rational design of single-molecule magnets: a supramolecular approach“, Chem. Commun. **47**, 116–130 (2011).

[15] A. DiLullo, S.-H. Chang, N. Baadji, K. Clark, J.-P. Klöckner, M.-H. Prosenc, S. Sanvito, R. Wiesendanger, G. Hoffmann, and S.-W. Hla, „Molecular Kondo chain“, Nano Lett. **12**, 3174–3179 (2012).

[16] M. Bazarnik, B. Bugenhagen, M. Elsebach, E. Sierda, A. Frank, M. H. Prosenc, and R. Wiesendanger, „Toward tailored all-spin molecular devices“, Nano Lett. **16**, 577–582 (2016).

[17] M. Elsebach, „Electronic properties of tailored Co-salophene based building blocks on Ag(111)“, Master Thesis (2016).

[18] G. Binnig, H. Rohrer, C. Gerber, and E. Weibel, „Tunneling through a controllable vacuum gap“, Appl. Phys. Lett. **40**, 178–180 (1982).

[19] G. Binnig and H. Rohrer, „Scanning tunneling microscopy—from birth to adolescence“, Rev. Mod. Phys. **59**, 615–625 (1987).

[20] *Creative commons legal code*, German, version 2.0, Creative Commons, Sept. 30, 2016.

[21] R. Wiesendanger, „Scanning tunneling microscopy (STM)“, in *Scanning probe microscopy and spectroscopy: methods and applications* (Cambridge University Press, Cambridge, Sept. 1994), pp. 11–209.

[22] J. Bardeen, „Tunnelling from a many-particle point of view“, Phys. Rev. Lett. **6**, 57–59 (1961).

[23] T. Fujita, H. Nakai, and H. Nakatsuji, „*Ab initio* molecular orbital model of scanning tunneling microscopy“, J. Chem. Phys. **104**, 2410–2417 (1996).

[24] A. D. Gottlieb and L. Wesoloski, „Bardeen's tunnelling theory as applied to scanning tunnelling microscopy: a technical guide to the traditional interpretation“, Nanotechnology **17**, R57 (2006).

[25] J. R. Oppenheimer, „Three notes on the quantum theory of aperiodic effects“, Phys. Rev. **31**, 66–81 (1928).

[26] J. Tersoff and D. R. Hamann, „Theory and application for the scanning tunneling microscope“, Phys. Rev. Lett. **50**, 1998–2001 (1983).

[27] J. Tersoff and D. R. Hamann, „Theory of the scanning tunneling microscope“, Phys. Rev. B **31**, 805–813 (1985).

[28] C. J. Chen, „Tunneling matrix elements in three-dimensional space: the derivative rule and the sum rule“, Phys. Rev. B **42**, 8841–8857 (1990).

[29] C. J. Chen, *Introduction to scanning tunneling microscopy* (Oxford University Press, New York, 1993).

[30] J. H. Brede, „Spin-polarized scanning tunneling microscopy and spectroscopy of phthalocyanine molecules on surfaces“, PhD thesis (2011).

[31] S. Matencio, E. Barrena, and C. Ocal, „Coming across a novel copper oxide 2D framework during the oxidation of Cu(111)“, Phys. Chem. Chem. Phys. **18**, 33303–33309 (2016).

[32] N. D. Lang, „Spectroscopy of single atoms in the scanning tunneling microscope“, Phys. Rev. B **34**, 5947–5950 (1986).

[33] I. Fernández Torrente, „Local spectroscopy of bi-molecular self-assemblies“, PhD thesis (2008).

[34] H. J. W. Zandvliet and A. van Houselt, „Scanning tunneling spectroscopy“, Annu. Rev. Anal. Chem. **2**, 37–55 (2009).

[35] P. K. Dixon and L. Wu, „Broadband digital lock-in amplifier techniques“, Rev. Sci. Instrum. **60**, 3329–3336 (1989).

[36] V. A. Ukraintsev, „Data evaluation technique for electron-tunneling spectroscopy“, Phys. Rev. B **53**, 11176–11185 (1996).

[37] R. M. Feenstra, J. A. Stroscio, and A. P. Fein, „Tunneling spectroscopy of the Si(111)2 × 1 surface“, Surf. Sci. **181**, 295–306 (1987).

[38] A. H. Carim, M. M. Dovek, C. F. Quate, R. Sinclair, and C. Vorst, „High-resolution electron microscopy and scanning tunneling microscopy of native oxides on silicon“, Science **237**, 630–633 (1987).

[39] M. C. Gallagher, M. S. Fyfield, J. P. Cowin, and S. A. Joyce, „Imaging insulating oxides: scanning tunneling microscopy of ultrathin MgO films on Mo(001)“, Surf. Sci. **339**, L909–L913 (1995).

[40] J.-P. Launay and M. Verdaguer, „The mastered electron: molecular electronics and spintronics, molecular machines“, in *Electrons in molecules: from basic principles to molecular electronics* (Oxford University Press, Oxford, 2017).

[41] J. Nieminen, S. Lahti, S. Paavilainen, and K. Morgenstern, „Contrast changes in STM images and relations between different tunneling models“, Phys. Rev. B **66**, 165421 (2002).

[42] D. T. Pierce, „Spin-polarized electron microscopy“, Phys. Scr. **38**, 291–296 (1988).

[43] R. Wiesendanger, H.-J. Güntherodt, G. Güntherodt, R. J. Gambino, and R. Ruf, „Observation of vacuum tunneling of spin-polarized electrons with the scanning tunneling microscope“, Phys. Rev. Lett. **65**, 247–250 (1990).

[44] J. Stöhr, „X-ray magnetic circular dichroism spectroscopy of transition metal thin films“, J. Electron Spectrosc. Relat. Phenom. **75**, 253–272 (1995).

[45] M. Julliere, „Tunneling between ferromagnetic films“, Phys. Lett. A **54**, 225–226 (1975).

[46] M. Bode, „Spin-polarized scanning tunnelling microscopy“, Rep. Prog. Phys. **66**, 523–582 (2003).

[47] E. C. Stoner, „Collective electron ferromagnetism“, Proc. R. Soc. London, Ser. A **165**, 372–414 (1938).

[48] J. C. Slonczewski, „Conductance and exchange coupling of two ferromagnets separated by a tunneling barrier“, Phys. Rev. B **39**, 6995–7002 (1989).

[49] D. Wortmann, S. Heinze, P. Kurz, G. Bihlmayer, and S. Blügel, „Resolving complex atomic-scale spin structures by spin-polarized scanning tunneling microscopy“, Phys. Rev. Lett. **86**, 4132–4135 (2001).

[50] D. Wortmann, P. Kurz, S. Heinze, K. Hirai, G. Bihlmayer, and S. Blügel, „Resolving noncollinear magnetism by spin-polarized scanning tunneling microscopy“, J. Magn. Magn. Mater. **240**, 57–63 (2002).

[51] A. R. Smith, „Atomic-scale spin-polarized scanning tunneling microscopy and atomic force microscopy: a review“, J. Scanning Probe Microsc. **1**, 3–20 (2006).

[52] R. Wiesendanger, „Spin mapping at the nanoscale and atomic scale“, Rev. Mod. Phys. **81**, 1495–1550 (2009).

[53] J. Brede and R. Wiesendanger, „Spin-resolved imaging and spectroscopy of individual molecules with sub-molecular spatial resolution“, MRS Bull. **39**, 608–613 (2014).

[54] S.-h. Phark and D. Sander, „Spin-polarized scanning tunneling microscopy with quantitative insights into magnetic probes“, Nano Convergence **4**, 10.1186/s40580-017-0102-5 (2017).

[55] H. Wende, „Recent advances in x-ray absorption spectroscopy“, Rep. Prog. Phys. **67**, 2105–2181 (2004).

[56] E. Beaurepaire, H. Bulou, F. Scheurer, and J.-P. Kappler, eds., *Magnetism: a synchrotron radiation approach* (Springer Berlin Heidelberg, Berlin, Heidelberg, 2006).

[57] I. A. Kowalik, „Element specific magnetometry combining x-ray circular with linear dichroism: fundamentals and applications“, Acta Phys. Pol., A **127**, 831–849 (2015).

[58] E. Beaurepaire, H. Bulou, F. Scheurer, and K. Jean-Paul, eds., *Magnetism and synchrotron radiation* (Springer Berlin Heidelberg, Berlin, Heidelberg, 2010).

[59] S. Calvin, *XAFS for everyone* (CRC press, Boca Raton, 2013).

[60] C. M. Praetorius, „Ce M4,5 XAS and XMCD as local probes for Kondo and heavy fermion materials - a study of CePt5/Pt(111) surface intermetallics -“, PhD thesis (Universität Würzburg, 2015).

[61] H. Wende and C. Antoniak, „X-ray magnetic dichroism“, in Magnetism and synchrotron radiation, edited by E. Beaurepaire, H. Bulou, F. Scheurer, and K. Jean-Paul (2010), pp. 145–167.

[62] H. G. Pfeiffer and H. A. Liebhafsky, „The origins of Beer's law“, J. Chem. Educ. **28**, 123 (1951).

[63] M. N. Berberan-Santos, „Beer's law revisited“, J. Chem. Educ. **67**, 757 (1990).

[64] J. Als-Nielsen and D. McMorrow, *Elements of modern x-ray physics* (John Wiley & Sons, Incorporated, Hoboken, United Kingdom, 2011).

[65] T. Eelbo, „Interaction of transition metal adatoms and dirac materials investigated by scanning tunneling microscopy and x-ray magnetic circular dichroism“, PhD thesis (2013).

[66] Y. Joly, „Interaction of polarized light with matter“, in Magnetism and synchrotron radiation, edited by E. Beaurepaire, H. Bulou, F. Scheurer, and K. Jean-Paul (2010), pp. 77–125.

[67] D. Sébilleau, „X-ray and electron spectroscopies: an introduction“, in *Magnetism: a synchrotron radiation approach*, edited by E. Beaurepaire, H. Bulou, F. Scheurer, and J.-P. Kappler (Springer Berlin Heidelberg, Berlin, Heidelberg, 2006), pp. 15–57.

[68] J. Stöhr, *NEXAFS spectroscopy*, Vol. 25 (Springer-Verlag Berlin Heidelberg, 1992).

[69] J. L. Erskine and E. A. Stern, „Calculation of the M_{23} magneto-optical absorption spectrum of ferromagnetic nickel“, Phys. Rev. B **12**, 5016–5024 (1975).

[70] G. Schütz, W. Wagner, W. Wilhelm, P. Kienle, R. Zeller, R. Frahm, and G. Materlik, „Absorption of circularly polarized x rays in iron“, Phys. Rev. Lett. **58**, 737–740 (1987).

[71] J. Stöhr and Y. Wu, „X-ray magnetic circular dichroism: basic concepts and theory for 3d transition metal atoms“, in *New directions in research with third-generation soft x-ray synchrotron radiation sources*, edited by A. S. Schlachter and F. J. Wuilleumier (Springer Netherlands, Dordrecht, 1994), pp. 221–250.

[72] I. Krug, „Magnetic proximity effects in highly-ordered transition metal oxide heterosystems studied by soft x-ray photoemission electron microscopy“, en, PhD thesis (Apr. 2008).

[73] B. T. Thole, P. Carra, F. Sette, and G. van der Laan, „X-ray circular dichroism as a probe of orbital magnetization“, Phys. Rev. Lett. **68**, 1943–1946 (1992).

[74] P. Carra, B. T. Thole, M. Altarelli, and X. Wang, „X-ray circular dichroism and local magnetic fields“, Phys. Rev. Lett. **70**, 694–697 (1993).

[75] A. Rogalev, F. Wilhelm, N. Jaouen, J. Goulon, and J.-P. Kappler, „X-ray magnetic circular dichroism: historical perspective and recent highlights“, in *Magnetism: a synchrotron radiation approach*, edited by E. Beaurepaire, H. Bulou, F. Scheurer, and J.-P. Kappler (Springer Berlin Heidelberg, Berlin, Heidelberg, 2006), pp. 71–93.

[76] C. T. Chen, Y. U. Idzerda, H.-J. Lin, N. V. Smith, G. Meigs, E. Chaban, G. H. Ho, E. Pellegrin, and F. Sette, „Experimental confirmation of the x-ray magnetic circular dichroism sum rules for iron and cobalt“, Phys. Rev. Lett. **75**, 152–155 (1995).

[77] G. A. Somorjai and Y. Li, „Impact of surface chemistry“, Proc. Natl. Acad. Sci. U. S. A. **108**, 917–924 (2011).

[78] J. V. Barth, „Molecular architectonic on metal surfaces“, Annu. Rev. Phys. Chem. **58**, 375–407 (2007).

[79] J. V. Barth, „Fresh perspectives for surface coordination chemistry“, Surf. Sci. **603**, 1533–1541 (2009).

[80] M. Elsebach, E. Sierda, J. J. Goedecke, L. Bignardi, M. Hermanowicz, M. Rohde, R. Wiesendanger, and M. Bazarnik, „*In Situ* synthesis of metal–salophene complexes on intercalated graphene“, J. Phys. Chem. C **124**, 4279–4287 (2020).

[81] F. Ullmann and J. Bielecki, „Ueber Synthesen in der Biphenylreihe“, Ber. Dtsch. Chem. Ges. **34**, 2174–2185 (1901).

[82] J. Hassan, M. Sévignon, C. Gozzi, E. Schulz, and M. Lemaire, „Aryl-aryl bond formation one century after the discovery of the Ullmann reaction“, Chem. Rev. **102**, 1359–1470 (2002).

[83] M. Xi and B. E. Bent, „Iodobenzene on Cu(111): formation and coupling of adsorbed phenyl groups“, Surf. Sci. **278**, 19–32 (1992).

[84] M. Xi and B. E. Bent, „Mechanisms of the Ullmann coupling reaction in adsorbed monolayers“, J. Am. Chem. Soc. **115**, 7426–7433 (1993).

[85] M. Lackinger and W. M. Heckl, „A STM perspective on covalent intermolecular coupling reactions on surfaces“, J. Phys. D: Appl. Phys. **44**, 464011 (2011).

[86] R. Lindner and A. Kühnle, „On-surface reactions“, ChemPhysChem **16**, 1582–1592 (2015).

[87] L. Dong, P. N. Liu, and N. Lin, „Surface-activated coupling reactions confined on a surface“, Acc. Chem. Res. **48**, 2765–2774 (2015).

[88] Q. Shen, H.-Y. Gao, and H. Fuchs, „Frontiers of on-surface synthesis: from principles to applications“, Nano Today **13**, 77–96 (2017).

[89] L. Talirz, P. Ruffieux, and R. Fasel, „On-surface synthesis of atomically precise graphene nanoribbons“, Adv. Mater. **28**, 6222–6231 (2016).

[90] P. A. Held, H. Fuchs, and A. Studer, „Covalent-bond formation via on-surface chemistry“, Chem. Eur. J **23**, 5874–5892 (2017).

[91] S.-W. Hla, L. Bartels, G. Meyer, and K.-H. Rieder, „Inducing all steps of a chemical reaction with the scanning tunneling microscope tip: towards single molecule engineering“, Phys. Rev. Lett. **85**, 2777–2780 (2000).

[92] L. Grill, M. Dyer, L. Lafferentz, M. Persson, M. V. Peters, and S. Hecht, „Nano-architectures by covalent assembly of molecular building blocks“, Nat. Nanotechnol. **2**, 687–691 (2007).

[93] A. Basagni, L. Ferrighi, M. Cattelan, L. Nicolas, K. Handrup, L. Vaghi, A. Papagni, F. Sedona, C. D. Valentin, S. Agnoli, and M. Sambi, „On-surface photo-dissociation of C–Br bonds: towards room temperature ullmann coupling“, Chem. Commun. **51**, 12593–12596 (2015).

[94] W.-J. Yoo, T. Tsukamoto, and S. Kobayashi, „Visible light-mediated Ullmann-type C–N coupling reactions of carbazole derivatives and aryl iodides“, Org. Lett. **17**, 3640–3642 (2015).

[95] S. Kawai, A. Sadeghi, T. Okamoto, C. Mitsui, R. Pawlak, T. Meier, J. Takeya, S. Goedecker, and E. Meyer, „Organometallic bonding in an Ullmann-type on-surface chemical reaction studied by high-resolution atomic force microscopy“, Small **12**, 5303–5311 (2016).

[96] E. A. Lewis, C. J. Murphy, A. Pronschinske, M. L. Liriano, and E. C. H. Sykes, „Nanoscale insight into C–C coupling on cobalt nanoparticles“, Chem. Commun. **50**, 10035–10037 (2014).

[97] L. Lafferentz, V. Eberhardt, C. Dri, C. Africh, G. Comelli, F. Esch, S. Hecht, and L. Grill, „Controlling on-surface polymerization by hierarchical and substrate-directed growth“, Nat. Chem. **4**, 215–220 (2012).

[98] M. Di Giovannantonio, M. Tomellini, J. Lipton-Duffin, G. Galeotti, M. Ebrahimi, A. Cossaro, A. Verdini, N. Kharche, V. Meunier, G. Vasseur, Y. Fagot-Revurat, D. F. Perepichka, F. Rosei, and G. Contini, „Mechanistic picture and kinetic analysis of surface-confined Ullmann polymerization“, J. Am. Chem. Soc. **138**, 16696–16702 (2016).

[99] S. Zint, D. Ebeling, T. Schlöder, S. Ahles, D. Mollenhauer, H. A. Wegner, and A. Schirmeisen, „Imaging successive intermediate states of the on-surface Ullmann reaction on Cu(111): role of the metal coordination“, ACS Nano **11**, 4183–4190 (2017).

[100] M. Di Giovannantonio, M. El Garah, J. Lipton-Duffin, V. Meunier, L. Cardenas, Y. Fagot Revurat, A. Cossaro, A. Verdini, D. F. Perepichka, F. Rosei, and G. Contini, „Insight into organometallic intermediate and its evolution to covalent bonding in surface-confined Ullmann polymerization“, ACS Nano **7**, 8190–8198 (2013).

[101] E. A. Lewis, C. J. Murphy, M. L. Liriano, and E. C. H. Sykes, „Atomic-scale insight into the formation, mobility and reaction of Ullmann coupling intermediates“, Chem. Commun. **50**, 1006–1008 (2014).

[102] B. Cirera, J. Björk, R. Otero, J. M. Gallego, R. Miranda, and D. Ecija, „Efficient lanthanide catalyzed debromination and oligomeric length-controlled Ullmann coupling of aryl halides“, J. Phys. Chem. C **121**, 8033–8041 (2017).

[103] A. Rastgoo Lahrood, J. Björk, W. M. Heckl, and M. Lackinger, „1,3-diiodobenzene on Cu(111) – an exceptional case of on-surface Ullmann coupling“, Chem. Commun. **51**, 13301–13304 (2015).

[104] M. Abadía, M. Ilyn, I. Piquero-Zulaica, P. Gargiani, C. Rogero, J. E. Ortega, and J. Brede, „Polymerization of well-aligned organic nanowires on a ferromagnetic rare-earth surface alloy“, ACS Nano **11**, 12392–12401 (2017).

[105] Y. Que, B. Liu, Y. Zhuang, C. Xu, K. Wang, and X. Xiao, „On-surface synthesis of graphene nanoribbons on two-dimensional rare earth–gold intermetallic compounds“, J. Phys. Chem. Lett. **11**, 5044–5050 (2020).

[106] M. Kittelmann, P. Rahe, M. Nimmrich, C. M. Hauke, A. Gourdon, and A. Kühnle, „On-surface covalent linking of organic building blocks on a bulk insulator“, ACS Nano **5**, 8420–8425 (2011).

[107] J. M. Gottfried, K. Flechtner, A. Kretschmann, T. Lukasczyk, and H.-P. Steinrück, „Direct synthesis of a metalloporphyrin complex on a surface“, J. Am. Chem. Soc. **128**, 5644–5645 (2006).

[108] W. Auwärter, A. Weber-Bargioni, S. Brink, A. Riemann, A. Schiffrin, M. Ruben, and J. V. Barth, „Controlled metalation of self-assembled porphyrin nanoarrays in two dimensions“, ChemPhysChem **8**, 250–254 (2007).

[109] T. E. Shubina, H. Marbach, K. Flechtner, A. Kretschmann, N. Jux, F. Buchner, H.-P. Steinrück, T. Clark, and J. M. Gottfried, „Principle and mechanism of direct porphyrin metalation: joint experimental and theoretical investigation“, J. Am. Chem. Soc. **129**, 9476–9483 (2007).

[110] Y. Bai, F. Buchner, M. T. Wendahl, I. Kellner, A. Bayer, H.-P. Steinrück, H. Marbach, and J. M. Gottfried, „Direct metalation of a phthalocyanine monolayer on Ag(111) with coadsorbed iron atoms“, J. Phys. Chem. C **112**, 6087–6092 (2008).

[111] J. M. Gottfried, „Surface chemistry of porphyrins and phthalocyanines“, Surf. Sci. Rep. **70**, 259–379 (2015).

[112] J. Li, C. Wäckerlin, S. Schnidrig, E. Joliat, R. Alberto, and K.-H. Ernst, „On-surface metalation and 2D self-assembly of pyrphyrin molecules into metal-coordinated networks on Cu(111)“, Helv. Chim. Acta **100**, e1600278 (2017).

[113] M. Schmid, M. Zugermeier, J. Herritsch, B. P. Klein, C. K. Krug, L. Ruppenthal, P. Müller, M. Kothe, P. Schweyen, M. Bröring, and J. M. Gottfried, „On-surface synthesis and characterization of an iron corrole“, J. Phys. Chem. C **122**, 10392–10399 (2018).

[114] A. Weber-Bargioni, J. Reichert, A. P. Seitsonen, W. Auwärter, A. Schiffrin, and J. V. Barth, „Interaction of cerium atoms with surface-anchored porphyrin molecules“, J. Phys. Chem. C **112**, 3453–3455 (2008).

[115] F. Bischoff, K. Seufert, W. Auwärter, A. P. Seitsonen, D. Heim, and J. V. Barth, „Metalation of porphyrins by lanthanide atoms at interfaces: direct observation and stimulation of cerium coordination to 2H-TPP/Ag(111)“, J. Phys. Chem. C **122**, 5083–5092 (2018).

[116] H. Marbach, „Surface-mediated *in Situ* metalation of porphyrins at the solid–vacuum interface“, Acc. Chem. Res. **48**, 2649–2658 (2015).

[117] A. Goldoni, C. A. Pignedoli, G. Di Santo, C. Castellarin-Cudia, E. Magnano, F. Bondino, A. Verdini, and D. Passerone, „Room temperature metalation of 2H-TPP monolayer on iron and nickel surfaces by picking up substrate metal atoms“, ACS Nano **6**, 10800–10807 (2012).

[118] A. Sperl, J. Kröger, and R. Berndt, „Controlled metalation of a single adsorbed phthalocyanine“, Angew. Chem., Int. Ed. **50**, 5294–5297 (2011).

[119] M. Chen, X. Feng, L. Zhang, H. Ju, Q. Xu, J. Zhu, J. M. Gottfried, K. Ibrahim, H. Qian, and J. Wang, „Direct synthesis of nickel(II) tetraphenylporphyrin and its interaction with a Au(111) surface: a comprehensive study“, J. Phys. Chem. C **114**, 9908–9916 (2010).

[120] L. Zhang, A. J. Patil, L. Li, A. Schierhorn, S. Mann, U. Gösele, and M. Knez, „Chemical infiltration during atomic layer deposition: metalation of porphyrins as model substrates“, Angew. Chem., Int. Ed. **48**, 4982–4985 (2009).

[121] A. C. Papageorgiou, S. Fischer, S. C. Oh, Ö. Sağlam, J. Reichert, A. Wiengarten, K. Seufert, S. Vijayaraghavan, D. Écija, W. Auwärter, F. Allegretti, R. G. Acres, K. C. Prince, K. Diller, F. Klappenberger, and J. V. Barth, „Self-terminating protocol for an interfacial complexation reaction *in Vacuo* by metal–organic chemical vapor deposition“, ACS Nano **7**, 4520–4526 (2013).

[122] J. Nowakowski, C. Wäckerlin, J. Girovsky, D. Siewert, T. A. Jung, and N. Ballav, „Porphyrin metalation providing an example of a redox reaction facilitated by a surface reconstruction“, Chem. Commun. **49**, 2347–2349 (2013).

[123] D. Écija, W. Auwärter, S. Vijayaraghavan, K. Seufert, F. Bischoff, K. Tashiro, and J. V. Barth, „Assembly and manipulation of rotatable cerium porphyrinato sandwich complexes on a surface“, Angew. Chem., Int. Ed. **50**, 3872–3877 (2011).

[124] D.-L. Bao, Y.-Y. Zhang, S. Du, S. T. Pantelides, and H.-J. Gao, „Barrierless on-surface metal incorporation in phthalocyanine-based molecules“, J. Phys. Chem. C **122**, 6678–6683 (2018).

[125] C. Wang, Q. Fan, S. Hu, H. Ju, X. Feng, Y. Han, H. Pan, J. Zhu, and J. M. Gottfried, „Coordination reaction between tetraphenylporphyrin and nickel on a TiO2(110) surface“, Chem. Commun. **50**, 8291–8294 (2014).

[126] C. Wang, Q. Fan, Y. Han, J. I. Martínez, J. A. Martín-Gago, W. Wang, H. Ju, J. M. Gottfried, and J. Zhu, „Metalation of tetraphenylporphyrin with nickel on a TiO2(110)-1 × 2 surface“, Nanoscale **8**, 1123–1132 (2016).

[127] J. D. Baran, J. A. Larsson, R. A. J. Woolley, Y. Cong, P. J. Moriarty, A. A. Cafolla, K. Schulte, and V. R. Dhanak, „Theoretical and experimental comparison of SnPc, PbPc, and CoPc adsorption on Ag(111)“, Phys. Rev. B **81**, 075413 (2010).

[128] C. M. Doyle, J. P. Cunniffe, S. A. Krasnikov, A. B. Preobrajenski, Z. Li, N. N. Sergeeva, M. O. Senge, and A. A. Cafolla, „Ni–Cu ion exchange observed for Ni(ii)–porphyrins on Cu(111)“, Chem. Commun. **50**, 3447–3449 (2014).

[129] J.-P. Launay and M. Verdaguer, „Basic concepts“, in *Electrons in molecules: from basic principles to molecular electronics* (Oxford University Press, Oxford, 2017).

[130] J.-P. Launay and M. Verdaguer, „The localized electron: magnetic properties“, in *Electrons in molecules: from basic principles to molecular electronics* (Oxford University Press, Oxford, 2017).

[131] O. Kahn, *Molecular magnetism wiley-vch* (Weinhem, 1993).

[132] C. Benelli and D. Gatteschi, *Introduction to molecular magnetism* (Wiley-VCH Verlag GmbH & Co, 2015).

[133] M. Born and J. R. Oppenheimer, „On the quantum theory of molecules“, Annalen der Physik **84**, 457 (1927).

[134] P. Echenique and J. L. Alonso, „A mathematical and computational review of Hartree–Fock SCF methods in quantum chemistry“, Mol. Phys. **105**, 3057–3098 (2007).

[135] F. Hund, „Atomtheoretische Deutung des Magnetismus der seltenen Erden“, Zeitschrift für Physik **33**, 855–859 (1925).

[136] W. Kutzelnigg and J. D. Morgan, „Hund's rules“, Zeitschrift für Physik D Atoms, Molecules and Clusters **36**, 197–214 (1996).

[137] H. Bethe, „Termaufspaltung in Kristallen“, Ann. Phys. **395**, 133–208 (1929).

[138] J. S. Griffith and L. E. Orgel, „Ligand-field theory“, Q. Rev. Chem. Soc. **11**, 381–393 (1957).

[139] J. Zuckerman, „Crystal field splitting diagrams“, J. Chem. Educ. **42**, 315 (1965).

[140] B. W. Pfennig, „Structure, bonding, and spectrocsopy of coordination compounds“, in *Principles of inorganic chemistry* (John Wiley & Sons, 2015), pp. 509–572.

[141] R. H. Crabtree, *The organometallic chemistry of the transition metals* (John Wiley & Sons, 2009).

[142] Y. Nishida and S. Kida, „Splitting of d-orbitals in square planar complexes of copper(II), nickel(II) and cobalt(II)“, Coord. Chem. Rev. **27**, 275–298 (1979).

[143] M. A. Hitchman, „Electronic structure of low-spin cobalt(II) Schiff base complexes“, Inorg. Chem. **16**, 1985–1993 (1977).

[144] A. Ceulemans, M. Dendooven, and L. G. Vanquickenborne, „Unusual ligand field effects in square-planar cobalt(II) complexes of quadridentate Schiff bases“, Inorg. Chem. **24**, 1159–1165 (1985).

[145] C. C. J. Roothaan, „New developments in molecular orbital theory“, Rev. Mod. Phys. **23**, 69–89 (1951).

[146] C. K. Jo/rgensen, R. Pappalardo, and H.-H. Schmidtke, „Do the “ligand field” parameters in lanthanides represent weak covalent bonding?“, J. Chem. Phys. **39**, 1422–1430 (1963).

[147] C. E. Schäffer and C. K. Jørgensen, „The angular overlap model, an attempt to revive the ligand field approaches“, Mol. Phys. **9**, 401–412 (1965).

[148] P. Bertrand, „The electron paramagnetic resonance phenomenon“, in *Electron paramagnetic resonance spectroscopy: fundamentals* (Springer International Publishing, Cham, 2020), pp. 3–30.

[149] W. Koch and M. C. Holthausen, „Electron density and hole functions“, in *A chemist's guide to density functional theory* (John Wiley & Sons, Ltd, 2001) Chap. 2, pp. 19–28.

[150] R. O. Jones and O. Gunnarsson, „The density functional formalism, its applications and prospects“, Rev. Mod. Phys. **61**, 689–746 (1989).

[151] W. Kohn, „Nobel lecture: electronic structure of matter—wave functions and density functionals“, Rev. Mod. Phys. **71**, 1253–1266 (1999).

[152] L. H. Thomas, „The calculation of atomic fields“, Math. Proc. Cambridge Philos. Soc. **23**, 542–548 (1927).

[153] E. Fermi, „Eine statistische Methode zur Bestimmung einiger Eigenschaften des Atoms und ihre Anwendung auf die Theorie des periodischen Systems der Elemente“, Zeitschrift für Physik **48**, 73–79 (1928).

[154] R. G. Parr, „Density functional theory of atoms and molecules“, in Horizons of quantum chemistry, edited by K. Fukui and B. Pullman (1980), pp. 5–15.

[155] W. Koch and M. C. Holthausen, *A chemist's guide to density functional theory* (John Wiley & Sons, Ltd, 2001).

[156] P. Hohenberg and W. Kohn, „Inhomogeneous electron gas“, Phys. Rev. **136**, B864–B871 (1964).

[157] W. Kohn and L. J. Sham, „Self-consistent equations including exchange and correlation effects“, Phys. Rev. **140**, A1133–A1138 (1965).

[158] W. Koch and M. C. Holthausen, „Elementary quantum chemistry“, in *A chemist's guide to density functional theory* (John Wiley & Sons, Ltd, 2001) Chap. 1, pp. 3–18.

[159] W. Koch and M. C. Holthausen, „The Kohn-Sham approach“, in *A chemist's guide to density functional theory* (John Wiley & Sons, Ltd, 2001) Chap. 5, pp. 41–64.

[160] W. Koch and M. C. Holthausen, „The quest for approximate exchange-correlation functionals“, in *A chemist's guide to density functional theory* (John Wiley & Sons, Ltd, 2001) Chap. 6, pp. 65–91.

[161] R. Stowasser and R. Hoffmann, „What do the Kohn-Sham orbitals and eigenvalues mean?“, J. Am. Chem. Soc. **121**, 3414–3420 (1999).

[162] D. P. Chong, O. V. Gritsenko, and E. J. Baerends, „Interpretation of the Kohn–Sham orbital energies as approximate vertical ionization potentials“, J. Chem. Phys. **116**, 1760–1772 (2002).

[163] G. Zhang and C. B. Musgrave, „Comparison of DFT methods for molecular orbital eigenvalue calculations“, J. Phys. Chem. A **111**, 1554–1561 (2007).

[164] R. van Meer, O. V. Gritsenko, and E. J. Baerends, „Physical meaning of virtual Kohn–Sham orbitals and orbital energies: an ideal basis for the description of molecular excitations“, J. Chem. Theory Comput. **10**, 4432–4441 (2014).

[165] Y. Orimoto, Y. Aoki, and A. Imamura, „Extraction of one-handed helical frontier orbital in even [n]cumulenes by breaking mirror images of right- and left-handed helical orbitals: theoretical study“, J. Phys. Chem. C **123**, 11134–11139 (2019).

[166] W. Koch and M. C. Holthausen, „The basic machinery of density functional programs“, in *A chemist's guide to density functional theory* (John Wiley & Sons, Ltd, 2001) Chap. 7, pp. 93–116.

[167] Q. Peng, A. Obolda, M. Zhang, and F. Li, „Organic light-emitting diodes using a neutral π radical as emitter: the emission from a doublet“, Angew. Chem., Int. Ed. **54**, 7091–7095 (2015).

[168] J. C. Dobrowolski and G. Karpińska, „Substituent effect in the first excited triplet state of monosubstituted benzenes“, ACS Omega **5**, 9477–9490 (2020).

[169] K. Momma and F. Izumi, „*Vesta3* for three-dimensional visualization of crystal, volumetric and morphology data“, J. Appl. Cryst. **44**, 1272–1276 (2011).

[170] D. M. Ceperley and B. J. Alder, „Ground state of the electron gas by a stochastic method“, Phys. Rev. Lett. **45**, 566–569 (1980).

[171] M. Mostafanejad, „Basics of the spin Hamiltonian formalism“, Int. J. Quantum Chem. **114**, 1495–1512 (2014).

[172] M. H. L. Pryce, „A modified perturbation procedure for a problem in paramagnetism“, Proc. Phys. Soc. A **63**, 25–29 (1950).

[173] S. Tripathi, A. Dey, M. Shanmugam, R. S. Narayanan, and V. Chandrasekhar, „Cobalt(II) complexes as single-ion magnets“, in *Organometallic magnets*, edited by V. Chandrasekhar and F. Pointillart (Springer International Publishing, Cham, 2019), pp. 35–75.

[174] L. Noodleman, „Valence bond description of antiferromagnetic coupling in transition metal dimers“, J. Chem. Phys. **74**, 5737–5743 (1981).

[175] A. Bencini and F. Totti, „A few comments on the application of density functional theory to the calculation of the magnetic structure of oligo-nuclear transition metal clusters“, J. Chem. Theory Comput. **5**, 144–154 (2009).

[176] C. J. Cramer and D. G. Truhlar, „Density functional theory for transition metals and transition metal chemistry“, Phys. Chem. Chem. Phys. **11**, 10757–10816 (2009).

[177] J. P. Malrieu, R. Caballol, C. J. Calzado, C. de Graaf, and N. Guihéry, „Magnetic interactions in molecules and highly correlated materials: physical content, analytical derivation, and rigorous extraction of magnetic Hamiltonians“, Chem. Rev. **114**, 429–492 (2014).

[178] J.-M. Mouesca, J. L. Chen, L. Noodleman, D. Bashford, and D. A. Case, „Density functional/Poisson-Boltzmann calculations of redox potentials for iron-sulfur clusters“, J. Am. Chem. Soc. **116**, 11898–11914 (1994).

[179] S. Sinnecker, F. Neese, L. Noodleman, and W. Lubitz, „Calculating the electron paramagnetic resonance parameters of exchange coupled transition metal complexes using broken symmetry density functional theory: application to a Mn^{III}/Mn^{IV} model compound“, J. Am. Chem. Soc. **126**, 2613–2622 (2004).

[180] I. Dzyaloshinsky, „A thermodynamic theory of “weak” ferromagnetism of antiferromagnetics“, J. Phys. Chem. Solids **4**, 241–255 (1958).

[181] T. Moriya, „Anisotropic superexchange interaction and weak ferromagnetism“, Phys. Rev. **120**, 91–98 (1960).

[182] C. Iacovita, M. V. Rastei, B. W. Heinrich, T. Brumme, J. Kortus, L. Limot, and J. P. Bucher, „Visualizing the spin of individual cobalt-phthalocyanine molecules“, Phys. Rev. Lett. **101**, 116602 (2008).

[183] N. Ballav, C. Wäckerlin, D. Siewert, P. M. Oppeneer, and T. A. Jung, „Emergence of on-surface magnetochemistry“, J. Phys. Chem. Lett. **4**, 2303–2311 (2013).

[184] P. W. Anderson, „Antiferromagnetism. Theory of superexchange interaction“, Phys. Rev. **79**, 350–356 (1950).

[185] P. W. Anderson, „New approach to the theory of superexchange interactions“, Phys. Rev. **115**, 2–13 (1959).

[186] A. V. Ushakov, D. A. Kukusta, A. N. Yaresko, and D. I. Khomskii, „Magnetism of layered chromium sulfides $\boldsymbol{M}CrS_2$ ($\boldsymbol{M}$ = Li, Na, K, Ag, and Au): A first-principles study“, Phys. Rev. B **87**, 014418 (2013).

[187] S. Kobayashi, H. Ueda, C. Michioka, and K. Yoshimura, „Competition between the direct exchange interaction and superexchange interaction in layered compounds $LiCrSe_2$, $LiCrTe_2$, and $NaCrTe_2$ with a triangular lattice“, Inorg. Chem. **55**, 7407–7413 (2016).

[188] C. David Sherrill and H. F. Schaefer, „The configuration interaction method: advances in highly correlated approaches“, in , Vol. 34, edited by P.-O. Löwdin, J. R. Sabin, M. C. Zerner, and E. Brändas, Advances in Quantum Chemistry (Academic Press, 1999), pp. 143–269.

[189] I. Shavitt, „The history and evolution of configuration interaction“, Mol. Phys. **94**, 3–17 (1998).

[190] C. J. Calzado, J. Cabrero, J. P. Malrieu, and R. Caballol, „Analysis of the magnetic coupling in binuclear complexes. I. Physics of the coupling“, J. Chem. Phys. **116**, 2728–2747 (2002).

[191] J. W. Verhoeven, „Glossary of terms used in photochemistry (IUPAC Recommendations 1996)“, Pure Appl. Chem. **68**, 2223–2286 (1996).

[192] J. B. Goodenough, „An interpretation of the magnetic properties of the perovskite-type mixed crystals $La_{1-x}Sr_xCoO_{3-\Lambda}$“, J. Phys. Chem. Solids **6**, 287–297 (1958).

[193] J. Kanamori, „Superexchange interaction and symmetry properties of electron orbitals“, J. Phys. Chem. Solids **10**, 87–98 (1959).

[194] P. W. Anderson, „Theory of magnetic exchange interactions: exchange in insulators and semiconductors“, in , Vol. 14, edited by F. Seitz and D. Turnbull, Solid State Physics (Academic Press, 1963), pp. 99–214.

[195] V. H. Crawford, H. W. Richardson, J. R. Wasson, D. J. Hodgson, and W. E. Hatfield, „Relation between the singlet-triplet splitting and the copper-oxygen-copper bridge angle in hydroxo-bridged copper dimers“, Inorg. Chem. **15**, 2107–2110 (1976).

[196] P. De Loth, P. Cassoux, J. P. Daudey, and J. P. Malrieu, „Ab initio direct calculation of the singlet-triplet separation in cupric acetate hydrate dimer“, J. Am. Chem. Soc. **103**, 4007–4016 (1981).

[197] J. A. McCleverty and M. D. Ward, „The role of bridging ligands in controlling electronic and magnetic properties in polynuclear complexes“, Acc. Chem. Res. **31**, 842–851 (1998).

[198] T. Glaser, H. Theil, and M. Heidemeier, „Spin-polarization in 1,3,5-trihydroxybenzene-bridged first-row transition metal complexes“, C. R. Chim. **11**, 1121–1136 (2008).

[199] D. Bhattacharya, S. Shil, A. Misra, and D. J. Klein, „Intramolecular ferromagnetic coupling in bis-oxoverdazyl and bis-thioxoverdazyl diradicals with polyacene spacers“, Theor. Chem. Acc. **127**, 57–67 (2010).

[200] M. Castellano, F. R. Fortea-Pérez, S.-E. Stiriba, M. Julve, F. Lloret, D. Armentano, G. De Munno, R. Ruiz-García, and J. Cano, „Very long-distance magnetic coupling in a dicopper(II) metallacyclophane with extended π-conjugated diphenylethyne bridges“, Inorg. Chem. **50**, 11279–11281 (2011).

[201] S. Motomura, M. Nakano, H. Fukui, K. Yoneda, T. Kubo, R. Carion, and B. Champagne, „Size dependences of the diradical character and the second hyperpolarizabilities in dicyclopenta-fused acenes: relationships with their aromaticity/antiaromaticity“, Phys. Chem. Chem. Phys. **13**, 20575–20583 (2011).

[202] D. Chylarecka, C. Wäckerlin, T. K. Kim, K. Müller, F. Nolting, A. Kleibert, N. Ballav, and T. A. Jung, „Self-assembly and superexchange coupling of magnetic molecules on oxygen-reconstructed ferromagnetic thin film“, J. Phys. Chem. Lett. **1**, 1408–1413 (2010).

[203] A. Lodi Rizzini, C. Krull, T. Balashov, J. J. Kavich, A. Mugarza, P. S. Miedema, P. K. Thakur, V. Sessi, S. Klyatskaya, M. Ruben, S. Stepanow, and P. Gambardella, „Coupling single molecule magnets to ferromagnetic substrates“, Phys. Rev. Lett. **107**, 177205 (2011).

[204] E. Coulaud, N. Guihéry, J.-P. Malrieu, D. Hagebaum-Reignier, D. Siri, and N. Ferré, „Analysis of the physical contributions to magnetic couplings in broken symmetry density functional theory approach“, J. Chem. Phys. **137**, 114106 (2012).

[205] T. Steenbock, J. Tasche, A. I. Lichtenstein, and C. Herrmann, „A Green's-function approach to exchange spin coupling as a new tool for quantum chemistry“, J. Chem. Theory Comput. **11**, 5651–5664 (2015).

[206] A. Fert, V. Cros, and J. Sampaio, „Skyrmions on the track“, Nat. Nanotechnol. **8**, 152–156 (2013).

[207] N. Romming, C. Hanneken, M. Menzel, J. E. Bickel, B. Wolter, K. von Bergmann, A. Kubetzka, and R. Wiesendanger, „Writing and deleting single magnetic skyrmions“, Science **341**, 636–639 (2013).

[208] P. Ferriani, K. von Bergmann, E. Y. Vedmedenko, S. Heinze, M. Bode, M. Heide, G. Bihlmayer, S. Blügel, and R. Wiesendanger, „Atomic-scale spin spiral with a unique rotational sense: Mn monolayer on W(001)“, Phys. Rev. Lett. **101**, 027201 (2008).

[209] P. Mahata, D. Sarma, and S. Natarajan, „Magnetic behaviour in metal-organic frameworks—Some recent examples“, J. Chem. Sci. **122**, 19–35 (2010).

[210] H. De Raedt, S. Miyashita, K. Michielsen, and M. Machida, „Dzyaloshinskii-Moriya interactions and adiabatic magnetization dynamics in molecular magnets“, Phys. Rev. B **70**, 064401 (2004).

[211] M. A. Ruderman and C. Kittel, „Indirect exchange coupling of nuclear magnetic moments by conduction electrons“, Phys. Rev. **96**, 99–102 (1954).

[212] T. Kasuya, „Electrical resistance of ferromagnetic metals“, Prog. Theor. Phys. **16**, 58–63 (1956).

[213] K. Yosida, „Magnetic properties of Cu-Mn alloys“, Phys. Rev. **106**, 893–898 (1957).

[214] P. Wahl, P. Simon, L. Diekhöner, V. S. Stepanyuk, P. Bruno, M. A. Schneider, and K. Kern, „Exchange interaction between single magnetic adatoms“, Phys. Rev. Lett. **98**, 056601 (2007).

[215] N. Tsukahara, S. Shiraki, S. Itou, N. Ohta, N. Takagi, and M. Kawai, „Evolution of Kondo resonance from a single impurity molecule to the two-dimensional lattice“, Phys. Rev. Lett. **106**, 187201 (2011).

[216] F. Meier, L. Zhou, J. Wiebe, and R. Wiesendanger, „Revealing magnetic interactions from single-atom magnetization curves“, Science **320**, 82–86 (2008).

[217] A. A. Khajetoorians, J. Wiebe, B. Chilian, and R. Wiesendanger, „Realizing all-spin–based logic operations atom by atom“, Science **332**, 1062–1064 (2011).

[218] E. Sierda, M. Abadia, J. Brede, M. Elsebach, B. Bugenhagen, M. H. Prosenc, M. Bazarnik, and R. Wiesendanger, „On-surface oligomerization of self-terminating molecular chains for the design of spintronic devices“, ACS Nano **11**, 9200–9206 (2017).

[219] K. Chichak, U. Jacquemard, and N. R. Branda, „The construction of (salophen)ruthenium(II) assemblies using axial coordination“, Eur. J. Inorg. Chem. **2002**, 357–368 (2002).

[220] A. Dalla Cort, P. De Bernardin, G. Forte, and F. Yafteh Mihan, „Metal–salophen-based receptors for anions“, Chem. Soc. Rev. **39**, 3863–3874 (2010).

[221] A. K. Crane and M. J. MacLachlan, „Portraits of porosity: porous structures based on metal salen complexes“, Eur. J. Inorg. Chem. **2011**, 17–30 (2012).

[222] R. M. Clarke and T. Storr, „The chemistry and applications of multimetallic salen complexes“, Dalton Trans. **43**, 9380–9391 (2014).

[223] C. García-Fernández, E. Sierda, M. Abadía, B. Bugenhagen, M. H. Prosenc, R. Wiesendanger, M. Bazarnik, J. E. Ortega, J. Brede, E. Matito, and A. Arnau, „Exploring the relation between intramolecular conjugation and band dispersion in one-dimensional polymers“, J. Phys. Chem. C **121**, 27118–27125 (2017).

[224] H.-C. Zhang, W.-S. Huang, and L. Pu, „Biaryl-based macrocyclic and polymeric chiral (salophen)Ni(II) complexes: synthesis and spectroscopic study“, J. Org. Chem. **66**, 481–487 (2001).

[225] F. Thomas, O. Jarjayes, C. Duboc, C. Philouze, E. Saint-Aman, and J.-L. Pierre, „Intramolecularly hydrogen-bonded *versus* copper(ii) coordinated mono- and bis-phenoxyl radicals“, Dalton Trans., 2662–2669 (2004).

[226] J. A. Castro-Osma, K. J. Lamb, and M. North, „Cr(salophen) complex catalyzed cyclic carbonate synthesis at ambient temperature and pressure“, ACS Catal. **6**, 5012–5025 (2016).

[227] J. Oldengott, A. Stammler, H. Bögge, and T. Glaser, „Enhancing the ferromagnetic coupling in extended phloroglucinol complexes by increasing the metal SOMO–ligand overlap: synthesis and characterization of a trinuclear Co_3^{II} triplesalophen complex“, Dalton Trans. **44**, 9732–9735 (2015).

[228] A. Kochem, H. Kanso, B. Baptiste, H. Arora, C. Philouze, O. Jarjayes, H. Vezin, D. Luneau, M. Orio, and F. Thomas, „Ligand contributions to the electronic structures of the oxidized cobalt(II) salen complexes“, Inorg. Chem. **51**, 10557–10571 (2012).

[229] J. Qu and J. Hu, „Engineering giant magnetic anisotropy in single-molecule magnets by dimerizing heavy transition-metal atoms“, Appl. Phys. Express **11**, 055201 (2018).

[230] E. Sierda, M. Elsebach, R. Wiesendanger, and M. Bazarnik, „Probing weakly hybridized magnetic molecules by single-atom magnetometry“, Nano Lett. **19**, 9013–9018 (2019).

[231] C. Wittneven, R. Dombrowski, S. H. Pan, and R. Wiesendanger, „A low-temperature ultrahigh-vacuum scanning tunneling microscope with rotatable magnetic field“, Rev. Sci. Instrum. **68**, 3806–3810 (1997).

[232] J. Wiebe, A. Wachowiak, F. Meier, D. Haude, T. Foster, M. Morgenstern, and R. Wiesendanger, „A 300 mK ultra-high vacuum scanning tunneling microscope for spin-resolved spectroscopy at high energy resolution“, Rev. Sci. Instrum. **75**, 4871–4879 (2004).

[233] S. Pan, „Piezoelectric motor“, WO/1993/019494 (Sept. 30, 1993).

[234] O. Pietzsch, A. Kubetzka, D. Haude, M. Bode, and R. Wiesendanger, „A low-temperature ultrahigh vacuum scanning tunneling microscope with a split-coil magnet and a rotary motion stepper motor for high spatial resolution studies of surface magnetism“, Rev. Sci. Instrum. **71**, 424–430 (2000).

[235] J. J. Goedecke, „Metalation and polymerization of 5,5'-dibromosalophene adsorbed on au(111) and co-intercalated graphene“, Master Thesis (2018).

[236] S. Kuck, J. Wienhausen, G. Hoffmann, and R. Wiesendanger, „A versatile variable-temperature scanning tunneling microscope for molecular growth“, Rev. Sci. Instrum. **79**, 083903 (2008).

[237] S. Kuck, „Scanning tunneling microscopy and spectroscopy of magnetic molecules on surfaces“, PhD thesis (2009).

[238] F. Pfeifer and C. Radeloff, „Soft magnetic Ni-Fe and Co-Fe alloys - some physical and metallurgical aspects“, J. Magn. Magn. Mater. **19**, 190–207 (1980).

[239] Y. Li, C. Polaczyk, F. Mezei, and D. Riegel, „Magnetic properties of Gd/Fe and Fe/Gd bilayer systems“, Phys. B **234-236**, 489–491 (1997).

[240] T. M. Danh, N. H. Duc, and N. P. Thuy, „Exchange interactions in amorphous Gd–Fe alloys“, J. Magn. Magn. Mater. **185**, 105–108 (1998).

[241] M. Kitada, „Annealing behaviour and magnetic properties of Co/Pt and Fe/Pt bilayer thin films“, Thin Solid Films **146**, 21–26 (1987).

[242] M. Corso, L. Fernández, F. Schiller, and J. E. Ortega, „Au(111)-based nanotemplates by Gd alloying“, ACS Nano **4**, 1603–1611 (2010).

[243] A. Correa, M. F. Camellone, A. Barragan, A. Kumar, C. Cepek, M. Pedio, S. Fabris, and L. Vitali, „Self-texturizing electronic properties of a 2-dimensional $GdAu_2$ layer on Au(111): the role of out-of-plane atomic displacement“, Nanoscale **9**, 17342–17348 (2017).

[244] L. R. Sill, S. R. Snow, and A. J. Fedro, „Magnetic properties of some rare-earth gold compounds“, AIP Conf. Proc. **10**, 1060–1064 (1973).

[245] T. R. McGuire and R. J. Gambino, „Magnetic and transport properties of rare-earth Au and Cu amorphous alloys“, J. Appl. Phys. **50**, 7653–7655 (1979).

[246] M. Corso, M. J. Verstraete, F. Schiller, M. Ormaza, L. Fernández, T. Greber, M. Torrent, A. Rubio, and J. E. Ortega, „Rare-earth surface alloying: a new phase for $GdAu_2$“, Phys. Rev. Lett. **105**, 016101 (2010).

[247] M. Bazarnik, M. Abadia, J. Brede, M. Hermanowicz, E. Sierda, M. Elsebach, T. Hänke, and R. Wiesendanger, „Atomically resolved magnetic structure of a Gd-Au surface alloy“, Phys. Rev. B **99**, 174419 (2019).

[248] A. Saccone, M. L. Fornasini, D. Macciò, and S. Delfino, „Phase equilibria in the GdAu system“, Intermetallics **4**, 111–119 (1996).

[249] J. Szade and M. Neumann, „Electronic structure investigation of Gd intermetallics“, J. Phys.: Condens. Matter **11**, 3887–3896 (1999).

[250] L. Fernández, M. Blanco-Rey, M. Ilyn, L. Vitali, A. Magaña, A. Correa, P. Ohresser, J. E. Ortega, A. Ayuela, and F. Schiller, „Co nanodot arrays grown on a $GdAu_2$ template: substrate/nanodot antiferromagnetic coupling“, Nano Lett. **14**, 2977–2981 (2014).

[251] M. Ormaza, L. Fernández, M. Ilyn, A. Magaña, B. Xu, M. J. Verstraete, M. Gastaldo, M. A. Valbuena, P. Gargiani, A. Mugarza, A. Ayuela, L. Vitali, M. Blanco-Rey, F. Schiller, and J. E. Ortega, „High temperature ferromagnetism in a $GdAg_2$ monolayer“, Nano Lett. **16**, 4230–4235 (2016).

[252] A. Cavallin, L. Fernández, M. Ilyn, A. Magaña, M. Ormaza, M. Matena, L. Vitali, J. E. Ortega, C. Grazioli, P. Ohresser, S. Rusponi, H. Brune, and F. Schiller, „Magnetism and morphology of Co nanocluster superlattices on $GdAu_2$/Au(111)–(13×13)“, Phys. Rev. B **90**, 235419 (2014).

[253] M. Farnesi Camellone, A. Correa, A. Barragán, M. Pedio, S. Fabris, C. Cepek, and L. Vitali, „Can atomic buckling control a chemical reaction? The case of dehydrogenation of phthalocyanine molecules on $GdAu_2$/Au(111)“, J. Phys. Chem. C **123**, 6496–6501 (2019).

[254] P. Wahl, L. Diekhöner, M. A. Schneider, and K. Kern, „Background removal in scanning tunneling spectroscopy of single atoms and molecules on metal surfaces“, Rev. Sci. Instrum. **79**, 043104 (2008).

[255] J. Brede, N. Atodiresei, S. Kuck, P. Lazić, V. Caciuc, Y. Morikawa, G. Hoffmann, S. Blügel, and R. Wiesendanger, „Spin- and energy-dependent tunneling through a single molecule with intramolecular spatial resolution“, Phys. Rev. Lett. **105**, 047204 (2010).

[256] C. W. Anson, S. Ghosh, S. Hammes-Schiffer, and S. S. Stahl, „Co(salophen)-catalyzed aerobic oxidation of *p*-hydroquinone: mechanism and implications for aerobic oxidation catalysis“, J. Am. Chem. Soc. **138**, 4186–4193 (2016).

[257] C. Piamonteze, U. Flechsig, S. Rusponi, J. Dreiser, J. Heidler, M. Schmidt, R. Wetter, M. Calvi, T. Schmidt, H. Pruchova, J. Krempasky, C. Quitmann, H. Brune, and F. Nolting, „X-Treme beamline at SLS: X-ray magnetic circular and linear dichroism at high field and low temperature“, J. Synchrotron Rad. **19**, 661–674 (2012).

[258] L. Fernández, M. Corso, F. Schiller, M. Ilyn, M. Holder, and J. E. Ortega, „Self-organized growth of high density magnetic Co nanodot arrays on a moiré template“, Appl. Phys. Lett. **96**, 013107 (2010).

[259] D. Schmitz, C. Schmitz-Antoniak, A. Warland, M. Darbandi, S. Haldar, S. Bhandary, O. Eriksson, B. Sanyal, and H. Wende, „The dipole moment of the spin density as a local indicator for phase transitions“, Sci. Rep. **4**, 5760–5766 (2014).

[260] P. Bruno, „Tight-binding approach to the orbital magnetic moment and magnetocrystalline anisotropy of transition-metal monolayers“, Phys. Rev. B **39**, 865–868 (1989).

[261] D. Weller, J. Stöhr, R. Nakajima, A. Carl, M. G. Samant, C. Chappert, R. Mégy, P. Beauvillain, P. Veillet, and G. A. Held, „Microscopic origin of magnetic anisotropy in Au/Co/Au probed with x-ray magnetic circular dichroism“, Phys. Rev. Lett. **75**, 3752–3755 (1995).

[262] P. R. Wallace, „The band theory of graphite“, Phys. Rev. **71**, 622–634 (1947).

[263] D. R. Dreyer, R. S. Ruoff, and C. W. Bielawski, „From conception to realization: an historial account of graphene and some perspectives for its future“, Angew. Chem., Int. Ed. **49**, 9336–9344 (2010).

[264] A. K. Geim and K. S. Novoselov, „The rise of graphene“, in *Nanoscience and technology* (Co-Published with Macmillan Publishers Ltd, UK), pp. 11–19.

[265] K. S. Novoselov, V. I. Fal'ko, L. Colombo, P. R. Gellert, M. G. Schwab, and K. Kim, „A roadmap for graphene“, Nature **490**, 192–200 (2012).

[266] A. M. Shikin, D. Farías, and K. H. Rieder, „Phonon stiffening induced by copper intercalation in monolayer graphite on Ni(111)“, Europhys. Lett. (EPL) **44**, 44–49 (1998).

[267] L. Huang, Y. Pan, L. Pan, M. Gao, W. Xu, Y. Que, H. Zhou, Y. Wang, S. Du, and H.-J. Gao, „Intercalation of metal islands and films at the interface of epitaxially grown graphene and Ru(0001) surfaces“, Appl. Phys. Lett. **99**, 163107 (2011).

[268] L. B. Ebert, „Intercalation compounds of graphite“, Annu. Rev. Mater. Sci. **6**, 181–211 (1976).

[269] M. S. Dresselhaus and G. Dresselhaus, „Intercalation compounds of graphite“, Adv. Phys. **51**, 1–186 (2002).

[270] D. Farías, A. M. Shikin, K.-H. Rieder, and Y. S. Dedkov, „Synthesis of a weakly bonded graphite monolayer on Ni(111) by intercalation of silver“, J. Phys.: Condens. Matter **11**, 8453–8458 (1999).

[271] R. Decker, J. Brede, N. Atodiresei, V. Caciuc, S. Blügel, and R. Wiesendanger, „Atomic-scale magnetism of cobalt-intercalated graphene“, Phys. Rev. B **87**, 041403 (2013).

[272] A. T. N'Diaye, S. Bleikamp, P. J. Feibelman, and T. Michely, „Two-dimensional Ir cluster lattice on a graphene moiré on Ir(111)“, Phys. Rev. Lett. **97**, 215501 (2006).

[273] A. T. N'Diaye, J. Coraux, T. N. Plasa, C. Busse, and T. Michely, „Structure of epitaxial graphene on Ir(111)“, New J. Phys. **10**, 043033 (2008).

[274] Y. Zhang, L. Zhang, and C. Zhou, „Review of chemical vapor deposition of graphene and related applications“, Acc. Chem. Res. **46**, 2329–2339 (2013).

[275] M. Sicot, P. Leicht, A. Zusan, S. Bouvron, O. Zander, M. Weser, Y. S. Dedkov, K. Horn, and M. Fonin, „Size-selected epitaxial nanoislands underneath graphene moiré on Rh(111)“, ACS Nano **6**, 151–158 (2012).

[276] L. Jin, Q. Fu, Y. Yang, and X. Bao, „A comparative study of intercalation mechanism at graphene/Ru(0001) interface“, Surf. Sci. **617**, 81–86 (2013).

[277] S. Vlaic, A. Kimouche, J. Coraux, B. Santos, A. Locatelli, and N. Rougemaille, „Cobalt intercalation at the graphene/iridium(111) interface: influence of rotational domains, wrinkles, and atomic steps“, Appl. Phys. Lett. **104**, 101602 (2014).

[278] M. Weser, Y. Rehder, K. Horn, M. Sicot, M. Fonin, A. B. Preobrajenski, E. N. Voloshina, E. Goering, and Y. S. Dedkov, „Induced magnetism of carbon atoms at the graphene/Ni(111) interface“, Appl. Phys. Lett. **96**, 012504 (2010).

[279] M. Weser, E. N. Voloshina, K. Horn, and Y. S. Dedkov, „Electronic structure and magnetic properties of the graphene/Fe/Ni(111) intercalation-like system“, Phys. Chem. Chem. Phys. **13**, 7534–7539 (2011).

[280] N. Rougemaille, A. T. N'Diaye, J. Coraux, C. Vo-Van, O. Fruchart, and A. K. Schmid, „Perpendicular magnetic anisotropy of cobalt films intercalated under graphene“, Appl. Phys. Lett. **101**, 142403 (2012).

[281] J. Coraux, A. T. N'Diaye, N. Rougemaille, C. Vo-Van, A. Kimouche, H.-X. Yang, M. Chshiev, N. Bendiab, O. Fruchart, and A. K. Schmid, „Air-protected epitaxial graphene/ferromagnet hybrids prepared by chemical vapor deposition and intercalation“, J. Phys. Chem. Lett. **3**, 2059–2063 (2012).

[282] D. Pacilé, P. Leicht, M. Papagno, P. M. Sheverdyaeva, P. Moras, C. Carbone, K. Krausert, L. Zielke, M. Fonin, Y. S. Dedkov, F. Mittendorfer, J. Doppler, A. Garhofer, and J. Redinger, „Artificially lattice-mismatched graphene/metal interface: graphene/Ni/Ir(111)“, Phys. Rev. B **87**, 035420 (2013).

[283] R. Decker, M. Bazarnik, N. Atodiresei, V. Caciuc, S. Blügel, and R. Wiesendanger, „Local tunnel magnetoresistance of an iron intercalated graphene-based heterostructure“, J. Phys.: Condens. Matter **26**, 394004 (2014).

[284] M. Bazarnik, J. Brede, R. Decker, and R. Wiesendanger, „Tailoring molecular self-assembly of magnetic phthalocyanine molecules on Fe- and Co-intercalated graphene“, ACS Nano **7**, 11341–11349 (2013).

[285] J. Coraux, A. T. N'Diaye, M. Engler, C. Busse, D. Wall, N. Buckanie, F.-J. M. zu Heringdorf, R. van Gastel, B. Poelsema, and T. Michely, „Growth of graphene on Ir(111)“, New J. Phys. **11**, 023006 (2009).

[286] C. Busse, P. Lazić, R. Djemour, J. Coraux, T. Gerber, N. Atodiresei, V. Caciuc, R. Brako, A. T. N'Diaye, S. Blügel, J. Zegenhagen, and T. Michely, „Graphene on Ir(111): physisorption with chemical modulation“, Phys. Rev. Lett. **107**, 036101 (2011).

[287] I. Pletikosić, M. Kralj, P. Pervan, R. Brako, J. Coraux, A. T. N'Diaye, C. Busse, and T. Michely, „Dirac cones and minigaps for graphene on Ir(111)“, Phys. Rev. Lett. **102**, 056808 (2009).

[288] D. Pacilé, S. Lisi, I. Di Bernardo, M. Papagno, L. Ferrari, M. Pisarra, M. Caputo, S. K. Mahatha, P. M. Sheverdyaeva, P. Moras, P. Lacovig, S. Lizzit, A. Baraldi, M. G. Betti, and C. Carbone, „Electronic structure of graphene/Co interfaces“, Phys. Rev. B **90**, 195446 (2014).

[289] J. E. Bickel, F. Meier, J. Brede, A. Kubetzka, K. von Bergmann, and R. Wiesendanger, „Magnetic properties of monolayer Co islands on Ir(111) probed by spin-resolved scanning tunneling microscopy“, Phys. Rev. B **84**, 054454 (2011).

[290] H. Vita, S. Böttcher, P. Leicht, K. Horn, A. B. Shick, and F. Máca, „Electronic structure and magnetic properties of cobalt intercalated in graphene on Ir(111)“, Phys. Rev. B **90**, 165432 (2014).

[291] F. Presel, A. Gijón, E. R. Hernández, P. Lacovig, S. Lizzit, D. Alfè, and A. Baraldi, „Translucency of graphene to van der Waals forces applies to atoms/molecules with different polar character“, ACS Nano **13**, 12230–12241 (2019).

[292] H. G. Zhang, J. T. Sun, T. Low, L. Z. Zhang, Y. Pan, Q. Liu, J. H. Mao, H. T. Zhou, H. M. Guo, S. X. Du, F. Guinea, and H.-J. Gao, „Assembly of iron phthalocyanine and pentacene molecules on a graphene monolayer grown on Ru(0001)“, Phys. Rev. B **84**, 245436 (2011).

[293] C. F. Hermanns, K. Tarafder, M. Bernien, A. Krüger, Y.-M. Chang, P. M. Oppeneer, and W. Kuch, „Magnetic coupling of porphyrin molecules through graphene“, Adv. Mater. **25**, 3473–3477 (2013).

[294] A. Candini, V. Bellini, D. Klar, V. Corradini, R. Biagi, V. De Renzi, K. Kummer, N. B. Brookes, U. del Pennino, H. Wende, and M. Affronte, „Ferromagnetic exchange coupling between Fe phthalocyanine and Ni(111) surface mediated by the extended states of graphene“, J. Phys. Chem. C **118**, 17670–17676 (2014).

[295] G. Avvisati, S. Lisi, P. Gargiani, A. Della Pia, O. De Luca, D. Pacilé, C. Cardoso, D. Varsano, D. Prezzi, A. Ferretti, and M. G. Betti, „FePc adsorption on the moiré superstructure of graphene intercalated with a cobalt layer“, J. Phys. Chem. C **121**, 1639–1647 (2017).

[296] G. Avvisati, C. Cardoso, D. Varsano, A. Ferretti, P. Gargiani, and M. G. Betti, „Ferromagnetic and antiferromagnetic coupling of spin molecular interfaces with high thermal stability“, Nano Lett. **18**, 2268–2273 (2018).

[297] G. Avvisati, P. Gargiani, P. Mondelli, F. Presel, A. Baraldi, and M. G. Betti, „Superexchange pathways stabilize the magnetic coupling of MnPc with Co in a spin interface mediated by graphene“, Phys. Rev. B **98**, 115412 (2018).

[298] M. Bode, M. Heide, K. von Bergmann, P. Ferriani, S. Heinze, G. Bihlmayer, A. Kubetzka, O. Pietzsch, S. Blügel, and R. Wiesendanger, „Chiral magnetic order at surfaces driven by inversion asymmetry“, Nature **447**, 190–193 (2007).

[299] A. Crépieux and C. Lacroix, „Dzyaloshinsky–Moriya interactions induced by symmetry breaking at a surface“, J. Magn. Magn. Mater. **182**, 341–349 (1998).

[300] M. Bałanda and R. Pełka, „Magnetism“, in *Molecular magnetic materials* (John Wiley & Sons, Ltd, 2017) Chap. 1, pp. 1–28.

[301] J. Schwöbel, Y. Fu, J. Brede, A. Dilullo, G. Hoffmann, S. Klyatskaya, M. Ruben, and R. Wiesendanger, „Real-space observation of spin-split molecular orbitals of adsorbed single-molecule magnets“, Nat. Comm. **3**, 953 (2012).

[302] S. A. Cantalupo, S. R. Fiedler, M. P. Shores, A. L. Rheingold, and L. H. Doerrer, „High-spin square-planar Co^{II} and Fe^{II} complexes and reasons for their electronic structure“, Angew. Chem., Int. Ed. **51**, 1000–1005 (2012).

[303] B. Verlhac, N. Bachellier, L. Garnier, M. Ormaza, P. Abufager, R. Robles, M.-L. Bocquet, M. Ternes, N. Lorente, and L. Limot, „Atomic-scale spin sensing with a single molecule at the apex of a scanning tunneling microscope“, Science **366**, 623–627 (2019).

[304] G. Czap, P. J. Wagner, F. Xue, L. Gu, J. Li, J. Yao, R. Wu, and W. Ho, „Probing and imaging spin interactions with a magnetic single-molecule sensor“, Science **364**, 670–673 (2019).

List of publications

[1] M. Elsebach, E. Sierda, J. J. Goedecke, L. Bignardi, M. Hermanowicz, M. Rohde, R. Wiesendanger, and M. Bazarnik, „*In Situ* synthesis of metal–salophene complexes on intercalated graphene“, J. Phys. Chem. C **124**, 4279–4287 (2020).

[2] E. Sierda, M. Elsebach, R. Wiesendanger, and M. Bazarnik, „Probing weakly hybridized magnetic molecules by single-atom magnetometry“, Nano Lett. **19**, 9013–9018 (2019).

[3] M. Bazarnik, M. Abadia, J. Brede, M. Hermanowicz, E. Sierda, M. Elsebach, T. Hänke, and R. Wiesendanger, „Atomically resolved magnetic structure of a Gd-Au surface alloy“, Phys. Rev. B **99**, 174419 (2019).

[4] E. Sierda, M. Abadia, J. Brede, M. Elsebach, B. Bugenhagen, M. H. Prosenc, M. Bazarnik, and R. Wiesendanger, „On-surface oligomerization of self-terminating molecular chains for the design of spintronic devices“, ACS Nano **11**, 9200–9206 (2017).

[5] M. Bazarnik, B. Bugenhagen, M. Elsebach, E. Sierda, A. Frank, M. H. Prosenc, and R. Wiesendanger, „Toward tailored all-spin molecular devices“, Nano Lett. **16**, 577–582 (2016).

Contributed Talks

[1] M. Elsebach, J. J. Goedecke, E. Sierda, R. Wiesendanger, and M. Bazarnik, „Sp-sts study of (co-sal)$_n$-chains on co-intercalated graphene on ir(111)“, 2019, 8th International Conference on Scanning Probe Spectroscopy (SPS 2019), Hamburg.

[2] M. Elsebach, J. J. Goedecke, E. Sierda, M. Przychodnia, M. Bazarnik, and R. Wiesendanger, „On-surface metalation of the salophene ligand and investigations of local electronic properties“, Mar. 2018, Frühjarstagung, Deutsche Physikalische Gesellschaft, Berlin, Germany.

[3] M. Elsebach, E. Sierda, B. Bugenhagen, M. H. Prosenc, R. Wiesendanger, and M. Bazarnik, „Electronic properties of tailored co-salophene based building blocks on ag(111)“, Mar. 2017, Frühjarstagung, Deutsche Physikalische Gesellschaft, Dresden, Germany.

Contributed Posters

[1] M. Elsebach, J. J. Goedecke, E. Sierda, B. Bugenhagen, M. Przychodnia, R. Wiesendanger, and M. Bazarnik, „On-surface metalization of the salophen ligand and comparison with ex situ synthesized metal-salophen complexes“, 2018, 654. WE-Heraeus-Seminar on Topical Insights into Nanoscience using Scanning Probes, Bad Honnef, Germany.

[2] D. Schwickert, M. Elsebach, M. Bazarnik, B. Bugenhagen, M. H. Prosenc, and R. Wiesendanger, „Tuning the interaction of magnetic molecules with a metallic substrate via an insulating film“, Mar. 2016, Frühjarstagung, Deutsche Physikalische Gesellschaft, Regensburg, Germany.

[3] M. Elsebach, M. Bazarnik, B. Bugenhagen, A. Frank, M. H. Prosenc, and R. Wiesendanger, „Development of a soft-landing for electrospray deposition“, Mar. 2018, Frühjarstagung, Deutsche Physikalische Gesellschaft, Berlin, Germany.

Acknowledgements

Finally, I would like to thank all the people who contributed to the creation of this thesis in one way or the other.

First, I would like to thank Prof. Dr. Roland Wiesendanger for his advice on the interpretation and presentation of my scientific results, pointing out weaknesses in my argumentation, but always giving me the confidence and reassurance that I can improve and make the best out of my data. Furthermore, I want to thank him for the opportunity to work in his renowned research group and do the research necessary for writing this thesis.

As much thanks go to my mentor Dr. Maciej Bazarnik, who supported me since the very beginning as well as throughout my studies. His guidance helped me to develop the skills and knowledge that went into my research. He was also the one encouraging me to go on this journey, which I am very grateful for.

Many thanks go to my colleagues from the molecular subgroup, in particular Dr. Emil Sierda and Julia Jirapon Goedecke, with whom I had many fruitful discussions. Especially Julia brought many fresh ideas to the table. Together with Dr. Maciej Bazarnik, we spent a lot of time improving the scientific instruments to get the best results out of our STM setups.

I also want to thank the other former and active members of the Wiesendanger group who accompanied me during my time at the institute. They provided an additional hand or a fresh thought whenever it was needed and altogether created a welcoming and productive working atmosphere throughout my time at the institute. They also contributed to many refreshing and amusing moments during lunch breaks, in the evening at the kicker table, or on other occasions, which I remember fondly.

Special thanks go to the staff of the Wiesendanger group and the facilities at the institute, without whom the research of the whole group would not be possible. Among these, the first to mention are the technical staff of the group as well as the secretaries, who were always quick with responses to various requests. They are followed by the liquid-He team, tirelessly working to keep the He liquefier running and keeping our measurement instruments cold. Then there is the team of the mechanical workshop, which always was willing to discuss my requests with me to improve my crude technical drawings, and without hesitating accepted last-minute requests on Friday afternoons. The staff of the electric workshop was always willing to help with repairing electronics or to discuss the development of new electronic setups.

Outside of the institute, I would like to thank, in particular, Dr. Michal Hermanowicz for his reliable and fruitful cooperation. Additionally, I want to thank Dr. Nicolae Atodiresei, Dr. Jens Brede, and Dr. Bernhard E. C. Bugenhagen for their help in optimizing the present thesis and giving quick responses to my questions. More thanks belong to the people who worked on the various publications I was able to contribute to.

For the funding of my position at the University of Hamburg and the resources used during my research, I acknowledge the Office of Naval Research via Grant No. N00014-16-1-2900.

I also owe many thanks to my friends and family outside of the scientific world.

At the Kellertheater Hamburg, I found a place to live up to my love for acting. Here I also found many friends, who always have an open ear for me and with whom I can work on awesome projects.

I also want to mention the Junges Orchester Hamburg although my path led me away from the people there since I needed my time and focus elsewhere. Nevertheless, I will never forget the time I spent with these amazing people.

For helping me to improve my writing, I thank Doris Gebert, who, despite her struggles with the physical terms, gave me a lot of useful input and identified my greatest weakness in this matter: the comma.

I also want to thank Larissa Stark for accompanying me on many walks during the lockdown times and for sharing coffee, thoughts, and cookies with me.

Furthermore, I thank Katrin Joswig and Kevin Juschkat from the CSI:Fuhle. They helped me to escape from everyday life from time to time, especially during the lockdowns.

Special thanks go to my mom, who encouraged me throughout my life to learn and to develop, my father, who always supported my urge to question things, and my sister, who showed me that it is also necessary to take some time to rest.

The greatest thanks go to my beloved girlfriend Maike. I could have never finished this thesis without her enduring support and her love. She best understood the struggles I went through and kept me going with her wise words, her warmth, and her love.